AN ABSTRACT OF THE THESIS OF

Skye Forrest Dorsett for the degree of Doctor of Philosophy in Physics presented on February 27, 2008.

Title: Breaking of spherical symmetry in electronic structure, Free and immersed atoms in an electron gas

Abstract approved: _____

Henri J.F. Jansen

Total electronic energies are calculated numerically for free and singly-ionized He, Li, C, and Ne atoms using density functional theory. Immersion energies are calculated for a single C impurity atom embedded or absorbed into a charge-neutral system composed of a free-electron gas with uniform positive background, also called 'jellium'. Nonspherical effects resulting from the breaking of angular momentum symmetry are taken into account. Previous work has been limited to spherical approximations to these effects. Spin-polarization effects are incorporated through the local spin-density approximation. Solving the resulting coupled equations allows for a direct calculation of the total energy and the dielectric response of the charge cloud to an applied electric field.

For a free carbon atom, we show that the ground state configuration predicted by the local spin density approximation violates Hund's 2nd rule. For free He, C, and Ne atoms in the presence of an applied electric field, we show that the polarizabilities calculated directly are in good agreement with previous results of perturbation theory and with experiment. For a carbon impurity system, phase shifts of the free-electron states are examined. Friedel oscillations and the Friedel sum rule are used for physical verification of the solutions. In the limit of low background density, we show that the impurity atom is affected by the presence of the electron gas and does not necessarily approach the

free atom solution. Particularly, we show that the orbital magnetic quantum number is quenched for a neutral C impurity atom, even at very low background densities, which is again in violation of Hund's 2nd rule. For a neutral carbon impurity system, we show that the immersion energy changes from negative to postive value as the orbital magnetic quantum number is varied from $0 - 1$.

Breaking of Spherical Symmetry in Electronic Structure, Free and Immersed Atoms in an Electron Gas

by

Skye Forrest Dorsett

A THESIS

submitted to

Oregon State University

in partial fulfillment of
the requirements for the
degree of

Doctor of Philosophy

Presented February 27, 2008
Commencement June 2008

Doctor of Philosophy thesis of Skye Forrest Dorsett presented on February 27, 2008

APPROVED:

Major Professor, representing Physics

Chair of the Department of Physics

Dean of the Graduate School

I understand that my thesis will become part of the permanent collection of Oregon State University libraries. My signature below authorizes release of my thesis to any reader upon request.

Skye Forrest Dorsett, Author

ACKNOWLEDGEMENTS

I am indebted to my major professor, Henri J.F. Jansen, for his guidance and assistance throughout this project. His experience and advice was indispensable when I would encounter difficult aspects of my research project and needed to find solution. I am also indebted to David Hamby, William Hetherington, Kenneth Krane, Corinne Manogue, David Roundy, Guenter Schneider and Willian Warren for their patience and willingness to serve as my graduate committee members, even if it was only temporary. I would like to thank all of the Oregon State University physics faculty who instructed me throughout my undergraduate and graduate experience and provided me with the knowledge and ability to perform this work. I would also like to thank my office mates, Jared Stenson and Kenneth Walsh, for the many hours of conversation upon diverse topics in physics that helped develop and enrich my understanding. I would like to give a very large thanks to the faculty of Sisters High School in Sisters, Oregon for giving me a solid foundation upon which to build my formal education. I would also like to thank anyone else with whom I've discussed scientific principles.

I wish to thank my family and friends who have listened to me explain, at length, scientific ideas that may not have been quite as interesting to them as they were to me. There are too many people to name here. My appreciation goes out to Dr. Greg Graffin and the members of Bad Religion, Tiger Army, AFI, and many other bands whose music and lyrics have inspired me and given me a richer appreciation of the world. Last, but certainly not least, I would like to thank the love of my life, Chelsea, for all of her patience in waiting for me to finish this work and her support for me to follow this dream.

TABLE OF CONTENTS

Page

1. INTRODUCTION 1

2. DENSITY FUNCTIONAL THEORY 4

2.1 Formal Justification: The Hohenberg-Kohn Theorem 4

2.1.1 Uniqueness of the external potential in terms of the charge density 5
2.1.2 Energy Minimization and the Variational Principle 6
2.1.3 Hohenberg-Kohn Universal Functional $F_{HK}[n]$ 7

2.2 Implementation of the basic theorem: the Kohn-Sham equations 8

2.2.1 System of non-interacting particles in an external potential leading to the interacting system ground state density 8
2.2.2 Interacting particle system in terms of non-interacting system potential 9
2.2.3 Ground state energy of interacting particle system 11
2.2.4 Spin-polarized systems 11
2.2.5 External electric field 14
2.2.6 Exchange-correlation; spin-polarized LDA 15
2.2.6.1 General form of the exchange-correlation energy functional . 15
2.2.6.2 Exchange-correlation energy of a uniform electron gas 16
2.2.6.3 Interpolation scheme; spin-independent 19
2.2.6.4 Interpolation scheme; spin-dependent 20

3. PROPERTIES OF OUR MODEL SYSTEM 34

3.1 Determination of the Density 36

3.1.1 Continuum States of the Electron Gas 36
3.1.2 Bound States Localized on the Impurity 40

3.2 Determination of the Potential 42

3.2.1 Hartree Potential 42
3.2.2 Exchange-Correlation Potential 44

3.3 Phase Shifts 45

3.3.1 Derivation of phase shifts 45
3.3.2 Induced density of states in terms of phase shifts 48

TABLE OF CONTENTS (Continued)

Page

3.4 Energy calculation 48
3.4.1 Induced kinetic energy 49
3.4.2 Induced electrostatic energy 51
3.4.3 Induced exchange-correlation energy 53
3.5 Friedel oscillations and the Friedel sum rule 54
3.6 Electric polarizability 55

4. NUMERICAL IMPLEMENTATION 58
4.1 Iterative scheme used to find self-consistent solutions 59
4.1.1 Non spin-polarized systems 59
4.1.2 Spin-polarized systems 60
4.2 Potential mixing scheme 61
4.3 Energy eigenvalue search 63
4.3.1 Bound states 63
4.3.2 Scattered states 66
4.4 Numerical errors 67
4.4.1 Real-space mesh 67
4.4.1.1 Mesh parameters 67
4.4.1.2 Oscillation of induced charge 69
4.4.2 Momentum space mesh 70
4.4.3 Cutoff values for l quantum numbers 70
4.4.4 Numerical corrections to the output potential 73

5. RESULTS 84
5.1 Free atom 85
5.1.1 Zero external electric field 85
5.1.2 Non-zero external electric field; atomic polarizability 87
5.2 Impurity System 89
5.2.1 Transient behavior during numerical calculation iterations 90

TABLE OF CONTENTS (Continued)

Page

5.2.2 Friedel Oscillations 91
5.2.3 Low background density; symmetry variation of excited state 91
5.2.3.1 Charge densities and potentials 92
5.2.3.2 Phase shifts and density of induced states 93
5.2.3.3 Immersion energies 94
5.2.4 Low background density; variation of sub-shell population 96
5.2.4.1 Charge densities and potentials 96
5.2.4.2 Phase shifts and density of induced states 97
5.2.4.3 Immersion energies 99
5.2.5 High background density 99
5.2.5.1 Charge densities and potentials 99
5.2.5.2 Phase shifts and density of induced states 101
5.2.5.3 Spin-polarization 101
5.2.5.4 Immersion energies 102

6. DISCUSSION 159

BIBLIOGRAPHY 162

APPENDICES 164

A APPENDIX Rydberg Atomic Units 165

B APPENDIX Boundary conditions for potentials as $r \to 0$ 166

C APPENDIX Singular Value Decomposition (SVD) 168

LIST OF FIGURES

Figure		Page
2.1	High density and low density limits for the average exchange-correlation energy per electron for a homogeneous electron gas	23
2.2	Thomas-Fermi kinetic T_{TF}, exchange ε_x, and correlation ε_c energies per electron as a function of density for a homogeneous electron gas from the parametrization of Hedin and Lundqvist	24
2.3	Exchange v_x and correlation v_c potentials for a homogeneous electron gas as a function of density from the parametrization of Hedin and Lundqvist.	25
2.4	Thomas-Fermi kinetic ε_{TF}, exchange ε_x, and correlation ε_c energies per electron multiplied by the electron density n for a homogeneous electron gas.	26
2.5	Exchange-correlation energy per electron ε_{xc} for a spin-polarized electron gas from the parametrization of von Barth, Hedin, and Lundqvist	27
2.6	Thomas-Fermi kinetic energy per electron $T_{TF} = 2.2099/r_{WS}^2$ for a spin-polarized electron gas	28
2.7	Exchange-correlation energy density $n\varepsilon_{xc}$ for a spin-polarized electron gas from the parametrization of von Barth, Hedin, and Lundqvist	29
2.8	The sum of the exchange-correlation and Thomas-Fermi kinetic energies per electron $\varepsilon_{xc} + T_{TF}$ for a spin-polarized electron gas	30
2.9	The sum of the exchange-correlation and Thomas-Fermi kinetic energy densities for a spin-polarized electron gas	31
2.10	Exchange-correlation potential v_{xc}^{+} for spin up electrons in a spin-polarized electron gas from the parametrization of von Barth, Hedin, and Lundqvist.	32
2.11	Exchange-correlation potential v_{xc}^{-} for spin down electrons in a spin-polarized electron gas from the parametrization of von Barth, Hedin, and Lundqvist.	33
4.1	Iterative scheme used to find self-consistent solutions.	75
4.2	Logarithmic r-mesh	76
4.3	Extrapolation to an infinite number of points to find immersion energies.	77
4.4	Reduction of energy errors caused by finite mesh	78
4.5	Friedel oscillations in the total induced charge	79

LIST OF FIGURES (Continued)

Figure		Page
4.6	Momentum-space mesh for spin up	80
4.7	Momentum-space mesh for spin down	81
4.8	Defects in the spherical component of the output potential	82
4.9	Defects in the nonspherical component of the output potential	83
5.1	LDA violation of Hund's 2nd rule for a free atom	103
5.2	Variation of the $2p^+$ energy eigenvalues and dipole polarizability as M is varied from $0-1$ for a free carbon atom	104
5.3	Variation of the kinetic energy for free and polar carbon atoms as M is varied from $0-1$	105
5.4	Variation of the Coulomb energy and the exchange-correlation energy for free and polar carbon atoms as M is varied from $0-1$	106
5.5	Spherical (monopole) and nonspherical (quadrupole) components of the electron density for a free carbon atom	107
5.6	Spherical (monopole) and nonspherical (dipole and quadrupole) components of the electron density for a free carbon atom in an external electric field	108
5.7	Nonspherical (dipole and quadrupole) components of the electron density for a free carbon atom in an external electric field	109
5.8	Variation of the number of electrons for a carbon impurity at 0.002 background density during the iterative procedure	110
5.9	Behavior of the Friedel oscillations for a carbon impurity for the density range $0.0002-0.001$	111
5.10	Variation in the total electron density as M is varied from $0-1$ at $n_0 = 0.0002$ background density for a neutral carbon impurity.	112
5.11	Variation in the total spin-density as M is varied from $0-1$ at $n_0 = 0.0002$ background density for a neutral carbon impurity.	113
5.12	Variation in the conduction band electron density as M is varied from $0-1$ at $n_0 = 0.0002$ background density for a neutral carbon impurity.	114
5.13	Variation in the conduction band spin-density as M is varied from $0-1$ at $n_0 = 0.0002$ background density for a neutral carbon impurity.	115

LIST OF FIGURES (Continued)

Figure Page

5.14 Variation in the total electron density as M is varied from $0-1$ at $n_0 = 0.0005$ background density for a neutral carbon impurity. 116

5.15 Variation in the total spin-density as M is varied from $0-1$ at $n_0 = 0.0005$ background density for a neutral carbon impurity. 117

5.16 Variation in the conduction band electron density as M is varied from $0-1$ at $n_0 = 0.0005$ background density for a neutral carbon impurity. . 118

5.17 Variation in the conduction band spin-density as M is varied from $0-1$ at $n_0 = 0.0005$ background density for a neutral carbon impurity. 119

5.18 Variation in the total electron density as M is varied from $0-1$ at $n_0 = 0.001$ background density for a neutral carbon impurity. 120

5.19 Variation in the total spin-density as M is varied from $0-1$ at $n_0 = 0.001$ background density for a neutral carbon impurity. 121

5.20 Variation in the conduction band electron density as M is varied from $0-1$ at $n_0 = 0.001$ background density for a neutral carbon impurity. .. 122

5.21 Variation in the conduction band spin-density as M is varied from $0-1$ at $n_0 = 0.001$ background density for a neutral carbon impurity. 123

5.22 Induced electron density for a carbon impurity at low background densities 124

5.23 Induced spin-density for a carbon impurity at low background densities . 125

5.24 Induced density in the conduction band for a carbon impurity at low background densities 126

5.25 Induced spin-density in the conduction for a carbon impurity at low background densities 127

5.26 Phase shifts for $l = 0, 1, 2$ conduction electrons scattered from a neutral carbon impurity at 0.0002 background density with $M = 0$ 128

5.27 Phase shifts for $l = 1$ spin up electrons in the conduction band as M is varied for a neutral carbon impurity at 0.0002 background density..... 129

5.28 Phase shifts for $l = 1$ spin down electrons in the conduction band as M is varied for a neutral carbon impurity at 0.0002 background density 130

5.29 Phase shifts for $l = 0$, $m = 0$ conduction electrons scattered from a neutral carbon impurity with $M = 0$ for low background densities 131

LIST OF FIGURES (Continued)

Figure Page

5.30 Phase shifts for $l = 1$, $m = 0$ conduction electrons scattered from a neutral carbon impurity with $M = 0$ for low background densities 132

5.31 Phase shifts for $l = 1$, $|m| = 1$ conduction electrons scattered from a neutral carbon impurity with $M = 0$ for low background densities 133

5.32 Phase shifts for $l = 2$, $m = 0$ for conduction electrons from a neutral carbon impurity with $M = 0$ at low background densities. 134

5.33 Variation in the immersion energy as M is varied from $0 - 1$ and the background density is varied from $n_0 = 0.0002$ to 0.001 for a neutral carbon impurity 135

5.34 Variation in the kinetic energy and $2p$ spin up energy eigenvalues as M is varied from $0 - 1$ for a neutral carbon impurity at 0.0002 background density 136

5.35 Variation in the kinetic energy and $2p$ spin up energy eigenvalues as M is varied from $0 - 1$ for a neutral carbon impurity at 0.0005 background density 137

5.36 Variation in the Coulomb and Exchange-correlation energies as M is varied from $0 - 1$ at low background densities 138

5.37 Variation in the spin-polarization as M is varied from $0 - 1$ for a neutral carbon impurity at low background densities 139

5.38 Variation of the total electron density as the population of the $2p$ sub-shell is varied for a carbon impurity 140

5.39 Variation of the spin-density as the population of the $2p$ sub-shell is varied for a carbon impurity 141

5.40 Variation of the $2p$ energy eigenvalues for a carbon impurity at 0.0002 background density as the $2p$ population is varied 142

5.41 Variation of the electron density in the conduction band as the population of the $2p$ sub-shell is varied for a carbon impurity 143

5.42 Variation of the spin-density in the conduction band as the population of the $2p$ sub-shell is varied for a carbon impurity 144

5.43 Variation of the $l = 0$ phase shifts as the population of the $2p$ sub-shell is varied for a carbon impurity at 0.0002 background density 145

LIST OF FIGURES (Continued)

Figure Page

5.44 Variation of the $l = 1$ spin up phase shifts as the population of the $2p$ sub-shell is varied for a carbon impurity at 0.0002 background density ... 146

5.45 Variation of the $l = 1$ spin down phase shifts as the population of the $2p$ sub-shell is varied for a carbon impurity at 0.0002 background density ... 147

5.46 Variation of the induced density of states in the conduction band as the population of the $2p$ sub-shell is varied for a carbon impurity at 0.0002 background density ... 148

5.47 Variation of the immersion energy as the $2p$ population is varied for a carbon impurity at 0.0002 background density ... 149

5.48 Variation of the immersion energy as the $2p$ population is varied for a carbon impurity at low background densities ... 150

5.49 Total electron density for a carbon impurity at low to mid-range metallic (background) densities ... 151

5.50 Spin-density for a carbon impurity at low to mid-range metallic (background) densities ... 152

5.51 Induced density in the conduction band for a carbon impurity at low to mid-range metallic (background) densities ... 153

5.52 Spin-density in the conduction band for a carbon impurity at low to mid-range metallic (background) densities ... 154

5.53 Phase shifts for $l = 0, 1$ electrons in the conduction band for a carbon impurity at mid-range metallic (background) densities ... 155

5.54 Induced density of states in the conduction band for a carbon impurity at mid-range metallic (background) densities ... 156

5.55 Variation of the spin-polarization of the ground state for the entire density range studied ... 157

5.56 Variation of the immersion energy for the background density range $0.002 \leq n_0 \leq 0.005$ ... 158

LIST OF TABLES

Table — Page

4.1 Numerical errors associated with the core states can be greatly reduced by calculating the impurity system energy and the free atom energy on the same mesh in real-space. The data shown is for a spin-polarized carbon impurity system at 0.0002 background density with the number of electrons in bound states limited to 6 with structure $1s^2\,2s^2\,2p_1^+\,2p_{-1}^+$. 68

4.2 Oscillation of immersion energy with choice of r-mesh cutoff r_∞. The immersion energy variations are ~ 0.001 Rydbergs. These calculations are for a carbon impurity at 0.0002 background density with 2.9 electrons in the $2p^+$ sub-shell. 600 points were used for the logarithmic r-mesh and 800 points for the linear r-mesh with matching radius $r = 2$. 70

4.3 Immersion energies for a carbon impurity. The immersion energy is accurate to within 0.001 Rydbergs for the number of k-mesh points beyond 120 for a given background density. 600 points for the logarithmic r-mesh and 800 points for the linear r-mesh were used for these calculations. The value of r_∞ used was 100. The calculations shown are for 0.002 background density for a nonspherical, spin-polarized system. 71

5.1 Total energies of free atoms in Rydbergs. It is seen that our results (NS-VBHL) for He, Li, and Ne atoms compare well with experiment and other DFT and Hartree-Fock methods. In the case of a C atom, the energy we found is somewhat lower than the result of Song. 88

5.2 Ionization energies of removing one electron from a free atom, in Rydbergs. It is seen that our results (NS-VBHL) compare well with experiment and with other theoretical approaches, but have much smaller absolute errors than the total energies shown in Table 5.1. This is due to the removal of errors associated with core states since the core density is very similar for neutral and ionized atoms of the same element. 88

5.3 Linear dipole polarizabilities of free atoms (in a_0^3). For He, where exchange effects are more important, configuration interaction and ordinary Hartree-Fock methods give better results than DFT. No theoretical data could be found for C, but our calculation (NS-VBHL) over-estimates the linear dipole polarizbility, but is in reasonable agreement with experiment. 89

BREAKING OF SPHERICAL SYMMETRY IN ELECTRONIC STRUCTURE, FREE AND IMMERSED ATOMS IN AN ELECTRON GAS

1. INTRODUCTION

The understanding of the properties of many-electron systems is of considerable practical interest. The value of such an understanding has been recognized since not long after the discovery of the electron and the beginnings of atomic theory in the early 1900's. All electromagnetic, chemical, and mechanical systems are, in principle, ultimately understood in terms of atomic and electronic structure and the interactions which occur in these systems between the constituent electrons. Knowledge of the form of the governing quantum mechanical equations has been known since the 1920's, but the same equations remain, to this day, rigorously intractable.

Many attempts have been made to deal with the many-body problem. Hartree-Fock theory is one of the more theoretically appealing techniques, but is very difficult to perform for systems with more than a few particles. Second quantization methods could be categorized similarly. From the approach of Thomas and Fermi, it has long been recognized that dealing with the electronic charge density is attractive due to the considerable theoretical simplifications afforded by such a framework. It was in this line of reasoning that density functional theory (DFT) has its beginnings. The (real-valued) charge density becomes the basic quantity studied instead of the (complex-valued) Schrödinger wavefunction. Hohenberg and Kohn published the foundational paper of DFT in 1964 [1], which shows that the ground state energy of an interacting many-particle system can be written as a

unique functional of the charge density. In particular, the problem is reduced to proving the existence of the *universal* Hohenberg-Kohn functional $F_{HK}[n]$, which describes the many-body effects.

The basic formulation of DFT as elucidated by the Hohenberg-Kohn theorem does indeed lead to a new way to access the physics of interacting many-electron systems. This formulation is based solely on the minimization of the energy with respect to the charge density. Essentially, the problem of many-body entanglement is bypassed by dealing directly with the total charge density and the electrostatic potential. However, in almost all situations, the universal functional $F_{HK}[n]$ is impossible to obtain.

Kohn and Sham in 1965 showed [2] a way to calculate the density of an interacting many-electron system based on single-particle orbitals which are solutions to the Schrödinger equation with an appropriate single-particle effective potential. A non-interacting approximation for the kinetic energy is introduced and the many-body effects of the complete interacting system are incorporated into the so-called *exchange-correlation* potential, which is part of the total effective single-particle potential. This single-particle approach reduces the problem of solving N *coupled* Schrödinger equations to solving N *single-particle* Schrödinger equations independently. Though still analytically intractable, the single-particle equations are much easier to solve numerically than the coupled system.

To apply DFT, one must have some suitable model to use for the exchange-correlation effects. The simplest and most common of these is referred to as the *local density approximation* (LDA). The LDA amounts to approximating the variable charge density as a constant, equal to the local density, in the universal functional $F_{HK}[n]$. Another common model used is the *generalized gradient approximation* (GGA), which incorporates the next highest order term(s) in the charge density. In this work, a spin-polarized formulation of the LDA, known as the *local spin-density approximation* (LSDA) is used.

Some of the early applications of DFT were calculations of atomic total energies and

ionization energies by Tong and Sham [3], atomic polarizabilities by Stott and Zaremba [4], and immersion energies of an impurity atom embedded in an electron gas by Puska, Nieminen, and Maninen [5]. In all of these works, spherical approximations were used due to the practical difficulties involved with solving problems of lower symmetry. In [4], atomic polarizabilities were calculated for spherical atoms using perturbation theory. In this work, by solving the coupled equations for a nonspherical system, we apply an external electric field and calculate the actual dipole reponse of the charge cloud. This allows for a direct calcuation of the dipole polarizability. As the dipole response of an atom to an applied electric field is inherently nonspherical, this calculation is not possible without recourse to the coupled equations of the nonspherical system.

For atomic immersions, much of the development can be traced back to the work of Friedel in the 1950's [6] [7] [8]. The relevant theory was discussed in the context of metal alloys, but has application to chemical adsorption and chemical bonding. For the model of an impurity atom in an electron gas (with the 'gas' consisting of plane wave states), two important features Friedel highlighted were the screening of the impurity by the electron gas and its relation to what is now referred to as the Friedel sum rule, and the oscillation of the charge density in the vicinity of the impurity, known as Friedel oscillations. Both of these features are used for verification in this work.

In this work, we solve the coupled equations resulting from the breaking of spherical symmetry due to partially filled angular momentum shells for free and immersed atomic systems. This allows for a study of the nonspherical effects which were previously unavailable without recourse to solving the coupled equations. Within the LSDA, we study the resulting paramagnetic and spin-polarized structures. In particular, we analyze the the magnetic structure and effects on the energy in relation to Hund's rules [9], which govern the magnetic structure of light atoms, where $L - S$ coupling holds [10].

2. DENSITY FUNCTIONAL THEORY

2.1 Formal Justification: The Hohenberg-Kohn Theorem

A system of interacting electrons in an external electrostatic potential $v(\boldsymbol{r})$, is governed by the Hamiltonian

$$\hat{H} = \hat{T} + \hat{V} + \hat{W} \tag{2.1}$$

where $\hat{T}$ is the kinetic energy operator, $\hat{V}$ is the operator associated with the external potential, and $\hat{W}$ is a two-particle interaction, such as the Coulomb interaction. We have, in 2nd quantized notation,

$$\hat{T} = -\frac{\hbar^2}{2m} \sum_{\sigma} \int \hat{\psi}^{\dagger}_{\sigma}(\boldsymbol{r}) \nabla^2 \hat{\psi}_{\sigma}(\boldsymbol{r}) \, \mathrm{d}\boldsymbol{r} \tag{2.2}$$

$$\hat{V} = \sum_{\sigma} \int \hat{\psi}^{\dagger}_{\sigma}(\boldsymbol{r}) v(\boldsymbol{r}) \hat{\psi}_{\sigma}(\boldsymbol{r}) \, \mathrm{d}\boldsymbol{r} \tag{2.3}$$

$$\hat{W} = \frac{1}{2} \sum_{\sigma_1, \sigma_2} \int \hat{\psi}^{\dagger}_{\sigma_1}(\boldsymbol{r}) \hat{\psi}^{\dagger}_{\sigma_2}(\boldsymbol{r}') w(\boldsymbol{r}, \boldsymbol{r}') \hat{\psi}_{\sigma_2}(\boldsymbol{r}') \hat{\psi}_{\sigma_1}(\boldsymbol{r}) \, \mathrm{d}\boldsymbol{r} \, \mathrm{d}\boldsymbol{r}' \tag{2.4}$$

where m is the mass of the electron, σ is the spin index and $w(\boldsymbol{r}, \boldsymbol{r}')$ is a two particle interaction, such as the Coulomb interaction.

The following proof [1] is based on a non-degenerate ground state, but has been extended [11] to the degenerate case. The ground state $|\phi\rangle$ satisfies the Schrödinger equation

$$\hat{H}|\phi\rangle = (\hat{T} + \hat{V} + \hat{W})|\phi\rangle = E_{gs}|\phi\rangle \tag{2.5}$$

with

$$v(\boldsymbol{r}) \in \mathcal{V} \tag{2.6}$$

$$\text{and} \qquad |\phi\rangle \in \Phi. \tag{2.7}$$

We define a map $A : \mathcal{V} \longmapsto \Phi$ from the set of potentials $v(\boldsymbol{r})$ to the set of ground states $|\phi\rangle$. It is important to note that there is no element in Φ not associated with some element

in $\mathcal{V}$, by construction. Since the ground state density can then be calculated from

$$n(\boldsymbol{r}) = \sum_{\sigma} \langle \phi | \hat{\psi}^{\dagger}_{\sigma}(\boldsymbol{r}) \hat{\psi}_{\sigma}(\boldsymbol{r}) | \phi \rangle. \tag{2.8}$$

with

$$n(\boldsymbol{r}) \in \mathcal{N} \tag{2.9}$$

we define a second map $B : \Phi \longmapsto \mathcal{N}$ from the set of ground states $|\phi\rangle$, to the set of ground state densities $n(\boldsymbol{r})$. The map AB indicates that $n(\boldsymbol{r})$ is a functional of $v(\boldsymbol{r})$, or $n = n[v(\boldsymbol{r})]$.

2.1.1 Uniqueness of the external potential in terms of the charge density

To prove that map A is invertible, suppose that two different potentials $v_1(\boldsymbol{r})$ and $v_2(\boldsymbol{r})$ correspond to the same ground state $|\phi\rangle$, then

$$(\hat{T} + \hat{V}_1 + \hat{W})|\phi\rangle = E_1|\phi\rangle \tag{2.10}$$

$$\text{and} \quad (\hat{T} + \hat{V}_2 + \hat{W})|\phi\rangle = E_2|\phi\rangle \tag{2.11}$$

with $\hat{V}_2 \neq \hat{V}_1 + \text{constant}$. (Potentials differing by an additive constant are considered equivalent.) Subtracting one equation from the other, we have

$$(\hat{V}_1 - \hat{V}_2)|\phi\rangle = (E_1 - E_2)|\phi\rangle. \tag{2.12}$$

Because $\hat{V}_1$ and $\hat{V}_2$ are just multiplicative operators, we would have $\hat{V}_1 - \hat{V}_1 = (E_1 - E_2) = \text{constant}$, which contradicts our assumption that the two potentials are not equivalent. Therefore, the only way that two different potentials could lead to the same ground state is *if* they differed only by a constant. More simply, the ground state density $n(\boldsymbol{r})$ uniquely determines the external potential $v(\boldsymbol{r})$ up to an additive constant and, therefore, the map A is invertible.

For map B, assume that two different ground states $|\phi_1\rangle$ and $|\phi_2\rangle$ lead to the *same* ground state density $n(\boldsymbol{r})$. Since $\hat{T}$ and $\hat{W}$ are the same for all systems, we would have

$$\begin{aligned} E_1^{gs} &= \langle\phi_1|\hat{H}_1|\phi_1\rangle < \langle\phi_2|\hat{H}_1|\phi_2\rangle = \langle\phi_2|\hat{H}_2 + \hat{V}_1 - \hat{V}_2|\phi_2\rangle \\ &= E_2^{gs} + \int n(\boldsymbol{r})(v_1(\boldsymbol{r}) - v_2(\boldsymbol{r}))\,\mathrm{d}\boldsymbol{r} \end{aligned}$$

for the first ground state from the Rayleigh-Ritz principle, and

$$\begin{aligned} E_2^{gs} &= \langle\phi_2|\hat{H}_2|\phi_2\rangle < \langle\phi_1|\hat{H}_2|\phi_1\rangle = \langle\phi_1|\hat{H}_1 + \hat{V}_2 - \hat{V}_1|\phi_1\rangle \\ &= E_1^{gs} + \int n(\boldsymbol{r})(v_2(\boldsymbol{r}) - v_1(\boldsymbol{r}))\,\mathrm{d}\boldsymbol{r} \end{aligned}$$

for the second ground state by the same reasoning. Adding these inequalities leads to a physical contradiction, and therefore our assumption must be false. That is, we would have

$$E_1^{gs} + E_2^{gs} < E_1^{gs} + E_2^{gs} \tag{2.13}$$

which is impossible and, therefore, two different ground states $|\phi_1\rangle$ and $|\phi_2\rangle$ must correspond to *different* ground state densities $n_1(\boldsymbol{r})$ and $n_2(\boldsymbol{r})$. The map B is therefore invertible because we have established a one-to-one correspondence from the set of ground states to the set of ground state densities. We have now proved that the ground state expectation value of any observable $\hat{O}$ (including the Hamiltonian $\hat{H}$) is uniquely determined by the ground state density $n(\boldsymbol{r})$ and is therefore a unique functional of the ground state density, i.e.

$$\langle\phi[n(\boldsymbol{r})]|\hat{O}|\phi[n(\boldsymbol{r})]\rangle = O[n]. \tag{2.14}$$

2.1.2 Energy Minimization and the Variational Principle

For a general density n, we have

$$E[n] = \langle\phi|\hat{T} + \hat{V} + \hat{W}|\phi\rangle. \tag{2.15}$$

We have just proved that there is a non-degenerate ground state density $n_{gs}(\boldsymbol{r})$ and ground state energy E_{gs} corresponding to the external potential $v(\boldsymbol{r})$ in (2.15). Therefore, we have

$$E_{gs} < E[n] \quad \text{if} \quad n \neq n_{gs} \tag{2.16}$$

and the actual ground state density is determined by minimizing the energy functional $E[n]$. So,

$$E_{gs} = \min E[n] \tag{2.17}$$

and we must enforce the constraint that

$$\int n(\boldsymbol{r})\,\mathrm{d}\boldsymbol{r} = N \tag{2.18}$$

where N is the total number of electrons.

2.1.3 Hohenberg-Kohn Universal Functional $F_{HK}[n]$

Having shown that the map B is independent of the external potential $v(\boldsymbol{r})$, the total energy functional can be written as

$$\begin{aligned} E[n] &= \langle \phi[n] | \hat{T} + \hat{V} + \hat{W} | \phi[n] \rangle \\ &= F_{HK}[n] + \int v(\boldsymbol{r}) n(\boldsymbol{r})\,\mathrm{d}\boldsymbol{r} \end{aligned} \tag{2.19}$$

with

$$F_{HK}[n] = \langle \phi[n] | \hat{T} + \hat{W} | \phi[n] \rangle. \tag{2.20}$$

It is clear that the *universal* functional $F_{HK}[n]$ does not depend on the external potential $v(\boldsymbol{r})$ and can, in principle, be calculated. Once it has been calculated, the universal functional can therefore be applied to any electronic system including atoms, molecules and solids as the form of the kinetic energy $\hat{T}$ and of the Coulomb interaction $\hat{W}$ is the same for all of these systems, with any number of particles and any external potential.

2.2 Implementation of the basic theorem: the Kohn-Sham equations

The derivation of Kohn and Sham amounts to showing that if n is the density of the *interacting* system with an external potential $v_I(\boldsymbol{r})$, then if one assumes there is an external potential $v_{NI}(\boldsymbol{r})$ for a *non-interacting* system that will give the *same* ground state density n, the uniqueness of the potential $v_{NI}(\boldsymbol{r})$ is assured by the Hohenberg-Kohn theorem (but its existence is assumed).

2.2.1 System of non-interacting particles in an external potential leading to the interacting system ground state density

If we define the external potential $v_{NI}(\boldsymbol{r})$ as the effective potential which leads to the actual ground state density $n(\boldsymbol{r})$ of the *interacting* system, for a system of *non-interacting* particles, the Schrödinger equation for this system of non-interacting particles is

$$\left[\frac{-\hbar^2}{2m}\nabla^2 + v_{NI}(\boldsymbol{r})\right]\psi_i(\boldsymbol{r}) = \epsilon_i\psi_i(\boldsymbol{r}) \tag{2.21}$$

where we have assumed the ground state is non-degenerate. The ground state density is then given by

$$n_{NI}(\boldsymbol{r}) = n_I(\boldsymbol{r}) = n(\boldsymbol{r}) = \sum_{i=1}^{N}|\psi_i(\boldsymbol{r})|^2 \tag{2.22}$$

where i runs over the (lowest) occupied eigenstates.

For a given ground state density $n(\boldsymbol{r})$, the external potential $v_{NI}(\boldsymbol{r})$ is determined uniquely (up to a constant) by the Hohenberg-Kohn theorem. The single-particle, non-interacting wavefunctions $\psi_i(\boldsymbol{r})$ are also unique functionals of the density. The kinetic energy functional is written as

$$T_{NI}[n] = \sum_i \int \psi_i^*(\boldsymbol{r})\left[\frac{-\hbar^2}{2m}\nabla^2\right]\psi_i(\boldsymbol{r})\,\mathrm{d}\boldsymbol{r} \tag{2.23}$$

and so it is also a unique functional of the ground state density. We write the total energy functional for the non-interacting system as

$$E_{NI}[n] = T_{NI}[n] + \int v_{NI}(\boldsymbol{r})n(\boldsymbol{r})\,\mathrm{d}\boldsymbol{r}. \tag{2.24}$$

Now, we use the Euler equation [11] to write $\delta E[n] = 0$, or rather

$$\frac{\delta}{\delta n(\boldsymbol{r})}\left[E_{NI}[n] - \mu_{NI}\int n(\boldsymbol{r})\,\mathrm{d}\boldsymbol{r}\right] = \frac{\delta T_{NI}[n]}{\delta n(\boldsymbol{r})} + v_{NI}(\boldsymbol{r}) - \mu_{NI} = 0 \tag{2.25}$$

with μ_{NI} being a Lagrange multiplier used to enforce the constraint that the total number of particles must be equal to N.

$$\int n(\boldsymbol{r})\,\mathrm{d}\boldsymbol{r} = N \tag{2.26}$$

2.2.2 Interacting particle system in terms of non-interacting system potential

The total energy functional of the complete interacting system was given by (2.19) as

$$E[n] = F_{HK}[n] + \int v_I(\boldsymbol{r})n(\boldsymbol{r})\,\mathrm{d}\boldsymbol{r}.$$

We can *define* the exchange-correlation energy as

$$E_{xc}[n] \equiv F_{HK}[n] - \frac{1}{2}\int n(\boldsymbol{r})w(\boldsymbol{r},\boldsymbol{r}')n(\boldsymbol{r}')\,\mathrm{d}\boldsymbol{r}\,\mathrm{d}\boldsymbol{r}' - T_{NI}[n] \tag{2.27}$$

with $T_{NI}[n]$ being the kinetic energy of the non-interacting system. The total energy functional is then given as

$$E[n] = T_{NI}[n] + \frac{1}{2}\int n(\boldsymbol{r})w(\boldsymbol{r},\boldsymbol{r}')n(\boldsymbol{r}')\,\mathrm{d}\boldsymbol{r}\,\mathrm{d}\boldsymbol{r}' + \int v_I(\boldsymbol{r})n(\boldsymbol{r})\,\mathrm{d}\boldsymbol{r} + E_{xc}[n]. \tag{2.28}$$

We can again use the Euler equation to write

$$\begin{aligned}\frac{\delta}{\delta n(\boldsymbol{r})}&\left[E_I[n] - \mu_I\int n(\boldsymbol{r})\,\mathrm{d}\boldsymbol{r}\right]\\ &= \frac{\delta T_{NI}[n]}{\delta n(\boldsymbol{r})} + v_I(\boldsymbol{r}) + \int n(\boldsymbol{r})w(\boldsymbol{r},\boldsymbol{r}')n(\boldsymbol{r}')\,\mathrm{d}\boldsymbol{r}' + v_{xc}([n];\boldsymbol{r}) - \mu_I = 0\end{aligned} \tag{2.29}$$

with the exchange correlation potential defined as

$$v_{xc}([n];\boldsymbol{r}) \equiv \frac{\delta E_{xc}[n]}{\delta n(\boldsymbol{r})}\,|_{n_0} \tag{2.30}$$

By comparing (2.25) and (2.29), one can see that *if* there exists the potential $v_{NI}(\boldsymbol{r})$ for the non-interacting system that corresponds to the actual ground state density $n(\boldsymbol{r})$ of the interacting system, then

$$\begin{aligned} v_{NI}(\boldsymbol{r}) &= v_I(\boldsymbol{r}) + \int w(\boldsymbol{r}, \boldsymbol{r}')n(\boldsymbol{r}')\,\mathrm{d}\boldsymbol{r}' + v_{xc}([n];\boldsymbol{r}) - (\mu_I - \mu_{NI}) \\ &= v_I(\boldsymbol{r}) + \int w(\boldsymbol{r}, \boldsymbol{r}')n(\boldsymbol{r}')\,\mathrm{d}\boldsymbol{r}' + v_{xc}([n];\boldsymbol{r}) \end{aligned} \tag{2.31}$$

where the second equality comes from the choice of the integration constant in $v_{NI}(\boldsymbol{r})$ to cancel out the term $(\mu_I - \mu_{NI})$.

Putting all of this together, the Kohn-Sham equations [2] can be written as

$$\left[\frac{-\hbar^2}{2m}\nabla^2 + v_I(\boldsymbol{r}) + \int w(\boldsymbol{r}, \boldsymbol{r}')n(\boldsymbol{r}')\,\mathrm{d}\boldsymbol{r}' + v_{xc}([n];\boldsymbol{r})\right]\psi_i(\boldsymbol{r}) = \epsilon_i\psi_i(\boldsymbol{r}) \tag{2.32}$$

where $v_I(\boldsymbol{r})$ is the external potential for the actual interacting system and the density arising from these *single-particle* equations corresponding to the *interacting* system can be written as

$$n(\boldsymbol{r}) = \sum_i^N |\psi_i(\boldsymbol{r})|^2 \tag{2.33}$$

where the sum over i ranges over the lowest (occupied) eigenstates. These equations must be solved self-consistently in that the density obtained from solving (2.32) and (2.33) must then yield the effective potential $v_{NI}(\boldsymbol{r})$ used to derive that density (See chapter 3).

To ensure clarity for the reader, we note that $v(\boldsymbol{r})$ was initially used to denote the external potential of the complete interacting system. This is now denoted as $v_I(\boldsymbol{r})$. For the remainder of the paper after this chapter, we will use $v(\boldsymbol{r})$ to denote the non-interacting effective single-particle potential

$$\begin{aligned} v(\boldsymbol{r}) = v_{NI}([n];\boldsymbol{r}) &= v_I(\boldsymbol{r}) + \int w(\boldsymbol{r}, \boldsymbol{r}')n(\boldsymbol{r}')\,\mathrm{d}\boldsymbol{r}' + v_{xc}([n];\boldsymbol{r}) \\ &= v_{ext}(\boldsymbol{r}) + v_H(\boldsymbol{r}) + v_{xc}(\boldsymbol{r}). \end{aligned} \tag{2.34}$$

2.2.3 Ground state energy of interacting particle system

The ground state energy can be derived by projecting (2.32) onto an eigenstate and integrating,

$$\epsilon_i = \int \psi_i^*(\boldsymbol{r}) \left[\frac{-\hbar^2}{2m}\nabla^2\right] \psi_i(\boldsymbol{r})\,\mathrm{d}\boldsymbol{r} + \int |\psi_i(\boldsymbol{r})|^2 v_{NI}(\boldsymbol{r})\,\mathrm{d}\boldsymbol{r} \tag{2.35}$$

giving

$$T_{NI}[n] = \sum_i^N \epsilon_i - \int n(\boldsymbol{r}) v_{NI}(\boldsymbol{r})\,\mathrm{d}\boldsymbol{r} \tag{2.36}$$

for the total kinetic energy with $v_{NI}(\boldsymbol{r})$ given by (2.34).

Inserting (2.36) into (2.28), the ground state energy $E[n]$ is written as

$$E[n] = \sum_i^N \epsilon_i - \frac{1}{2}\int n(\boldsymbol{r}) w(\boldsymbol{r};\boldsymbol{r}') n(\boldsymbol{r}')\,\mathrm{d}\boldsymbol{r}\,\mathrm{d}\boldsymbol{r}' + E_{xc}[n] - \int v_{xc}(\boldsymbol{r}) n(\boldsymbol{r})\,\mathrm{d}\boldsymbol{r} \tag{2.37}$$

with $E_{xc}[n]$ given by (2.27) and $v_{xc}(\boldsymbol{r})$ given by (2.30).

2.2.4 Spin-polarized systems

In general, magnetic effects are important for a thorough description of electronic systems as the electrons themselves possess an intrinsic magetic moment, or *spin*. Any atomic system with an odd number of electrons and atomic systems with an even number of electrons obeying Hund's 2nd rule (such as atomic carbon) will be spin-polarized in the ground state. In addition, an electron's orbital motion about the nucleus of an atom or lattice site contributes an orbital magnetic moment. The spin magnetic moments interact with one another (spin-spin coupling) and with the orbital moments (spin-orbit coupling) as well as with the magnetic moment of the nucleus, if it exists (spin-nuclear spin coupling). These effects occur even in the absence of an external magnetic field and give rise to fine structure and hyperfine structure of atomic multiplet energy levels. In this work, only spin-spin coupling is considered. In addition, an external magnetic field could be considered or could be vanishingly small. The generalization of the Hohenberg-Kohn theorem to treat spin-polarized systems was first given by von Barth and Hedin [12], Pant

and Rajagopal [13], and Rajagopal and Callaway [14] for relativistic systems. A concise summary of the literature is given in [11]. Here, the formulation of von Barth and Hedin is used to write the Kohn-Sham equations (2.32) for a spin-polarized system in the presence of a finite or vanishing external magnetic field.

The external potential, (2.3), is now extended to

$$\hat{V} = \sum_{\sigma_1\sigma_2} \int \hat{\psi}^\dagger_{\sigma_1}(\boldsymbol{r})[v(\boldsymbol{r})\delta_{\sigma_1\sigma_2} + \mu_B \boldsymbol{B}\cdot\sigma_{\sigma_1\sigma_2}(\boldsymbol{r})]\hat{\psi}_{\sigma_2}(\boldsymbol{r})\,\mathrm{d}\boldsymbol{r} \tag{2.38}$$

where $\mu_B = e\hbar/2mc$ is the Bohr magneton and σ is the vector of Pauli spin matrices.

One can choose to work with the spin density matrix

$$n_{\sigma_1\sigma_2}(\boldsymbol{r}) = \langle\phi|\hat{\psi}^\dagger_{\sigma_1}(\boldsymbol{r})\hat{\psi}_{\sigma_2}(\boldsymbol{r})|\phi\rangle \tag{2.39}$$

or with the total density $n(\boldsymbol{r})$ and magnetization density $\boldsymbol{m}(\boldsymbol{r})$. In either case, there is a total of four independent real-valued functions. In this work, the exchange-correlation potential will be written in terms of the total density and the magnetization density and the Kohn-Sham equations for spin-polarized systems will be written accordingly.

The magnetic moment density operator is written as

$$\hat{\boldsymbol{m}}(\boldsymbol{r}) = -\mu_B \sum_{\sigma_1\sigma_2} \hat{\psi}^\dagger_{\sigma_1}(\boldsymbol{r})\sigma_{\sigma_1\sigma_2}\hat{\psi}_{\sigma_2}(\boldsymbol{r}). \tag{2.40}$$

The total density operator is written as

$$\hat{n}(\boldsymbol{r}) = \hat{n}_+(\boldsymbol{r}) + \hat{n}_-(\boldsymbol{r}) = \sum_\sigma \hat{n}_\sigma(\boldsymbol{r}) = \sum_\sigma \hat{\psi}^\dagger_\sigma(\boldsymbol{r})\hat{\psi}_\sigma(\boldsymbol{r}). \tag{2.41}$$

Using these two expressions, the external potential, (2.38), can be written as

$$\hat{V} = \int [v(\boldsymbol{r})\hat{n}(\boldsymbol{r}) - \boldsymbol{B}\cdot\hat{\boldsymbol{m}}(\boldsymbol{r})]\,\mathrm{d}\boldsymbol{r} \tag{2.42}$$

and the total density and magentization density are written as

$$n(\boldsymbol{r}) = \langle\phi|\hat{n}(\boldsymbol{r})|\phi\rangle \tag{2.43}$$

$$\text{and} \qquad \boldsymbol{m}(\boldsymbol{r}) = \langle\phi|\hat{\boldsymbol{m}}(\boldsymbol{r})|\phi\rangle. \tag{2.44}$$

In this work, it is assumed that the external magnetic field $\boldsymbol{B}(\boldsymbol{r})$ and the magnetization $\boldsymbol{m}(\boldsymbol{r})$ have only a non-vanishing z-component. The magnetization is then written as

$$\boldsymbol{m}(\boldsymbol{r}) = -\mu_B(n_+(\boldsymbol{r}) - n_-(\boldsymbol{r}))\hat{z}. \tag{2.45}$$

The original version of the Hohenberg-Kohn theorem extended to treat spin-polarized systems with a finite or vanishing external magnetic field shows that for the spin-polarized system, two different non-degenerate ground states lead to two different spin-density matrices or, equivalently, to two different sets of $n(\boldsymbol{r}), \boldsymbol{m}(\boldsymbol{r})$ or $n_+(\boldsymbol{r}), n_-(\boldsymbol{r})$.

The variational principle of the Hohenberg-Kohn theorem can now be used to write the Kohn-Sham equations for a spin-polarized system with an external magnetic field $B(\boldsymbol{r})\hat{z}$ and external electrostatic potenial $v(\boldsymbol{r})$ as

$$[-\frac{-\hbar^2}{2m}\nabla^2 + v(\boldsymbol{r}) + \sigma\mu_B B(\boldsymbol{r}) + \int w(\boldsymbol{r},\boldsymbol{r}')n(\boldsymbol{r}')\,\mathrm{d}\boldsymbol{r}' + v^\sigma_{xc}([n_+,n_-];\boldsymbol{r})]\psi^\sigma_i(\boldsymbol{r}) = \epsilon^\sigma_i\psi^\sigma_i(\boldsymbol{r}). \tag{2.46}$$

The total electron density is now given by

$$n(\boldsymbol{r}) = \sum_\sigma \sum_i^{N_\sigma} |\psi^\sigma_i(\boldsymbol{r})|^2 \tag{2.47}$$

where σ denotes + or - for the spin projection along the z-axis and the sums from i to N_s range over the lowest occupied states for a given spin channel and denotes all quantum numbers besides the spin index σ.

The spin-dependent exchange-correlation potential is given by

$$v^\sigma_{xc}([n_+,n_-];\boldsymbol{r}) = \frac{\delta E_{xc}[n_+,n_-]}{\delta n_\sigma(\boldsymbol{r})}\,|_{n_{gs},m_{gs}} \tag{2.48}$$

with the spin-dependent exchange-correlation energy functional given by

$$E_{xc}[n_+,n_-] = F_{HK}[n_+,n_-] - \frac{1}{2}\int n(\boldsymbol{r})w(\boldsymbol{r},\boldsymbol{r}')n(\boldsymbol{r}')\,\mathrm{d}\boldsymbol{r}\,\mathrm{d}\boldsymbol{r}' - T_{NI}[n_+,n_-] \tag{2.49}$$

Finally, the ground state energy can be written, similar to (2.28), as

$$\begin{aligned} E_{gs} &= E[n(\boldsymbol{r}), \boldsymbol{m}(\boldsymbol{r})] = E[n_+(\boldsymbol{r}), n_-(\boldsymbol{r})] \\ &= \sum_\sigma \sum_i^{N_\sigma} \epsilon_i^\sigma - \frac{1}{2} \int n(\boldsymbol{r}) w(\boldsymbol{r}; \boldsymbol{r}') n(\boldsymbol{r}') \, \mathrm{d}\boldsymbol{r} \, \mathrm{d}\boldsymbol{r}' + E_{xc}[n_+, n_-] \\ &- \sum_\sigma \int v_{xc}^\sigma([n_+, n_-]; \boldsymbol{r}) n_\sigma(\boldsymbol{r}) \, \mathrm{d}\boldsymbol{r}. \end{aligned} \tag{2.50}$$

2.2.5 External electric field

In the previous section, the Kohn-Sham equation was presented for a spin-polarized system in the presence of a finite or vanishing external magnetic field, Eq. (2.46). The external potential Eq. (2.3) was extended to Eq. (2.38) or Eq. (2.42). Notice that in the latter expression, Eq. (2.42), the magnetic field $\boldsymbol{B}(\boldsymbol{r})$ is written separately from the external electrostatic potential $v(\boldsymbol{r})$. If we wish to include the effect of an external electric field $\boldsymbol{E}(\boldsymbol{r})$, we first note that the Hamiltonian associated with this field is given by

$$\hat{H}_{Stark} = -\boldsymbol{p} \cdot \boldsymbol{E}. \tag{2.51}$$

If we assume that the field is constant and only has a non-vanishing z-component so that $\boldsymbol{E}(\boldsymbol{r}) = E_0 \hat{z}$, this becomes

$$\hat{H}_{Stark} = -e|E_0| r \cos\theta \tag{2.52}$$

where θ is the angle between the z-axis and the point in question. (The term $\hat{H}_{Stark}$ appears when numerically integrating the Kohn-Sham equation(s) in r-space.) The field can be written in terms of an electrostatic potential $v_E(\boldsymbol{r})$

$$\boldsymbol{E}(\boldsymbol{r}) = -\nabla v_E(\boldsymbol{r}). \tag{2.53}$$

Since the external electrostatic potential $v(\boldsymbol{r})$ in the general formulation was left unspecified, we can associate the addition of the external field $\mathbf{E}(\boldsymbol{r})$ with the potential $v_E(\boldsymbol{r})$ and add this term to the previous external potential term, so that

$$v(\boldsymbol{r}) + v_E(\boldsymbol{r}) \to v(\boldsymbol{r}). \tag{2.54}$$

This justifies the inclusion of the external field $\boldsymbol{E}(\boldsymbol{r})$ without recourse to any further extension of the Kohn-Sham formulation presented so far.

For completeness, we note that the electric polarization can be calculated from

$$\boldsymbol{p} = \int \boldsymbol{r}\rho(\boldsymbol{r})\,\mathrm{d}\boldsymbol{r} = -e\int \boldsymbol{r}n(\boldsymbol{r})\,\mathrm{d}\boldsymbol{r}. \tag{2.55}$$

2.2.6 Exchange-correlation; spin-polarized LDA

Now that the Kohn-Sham equations have been formulated for a spin-polarized system, the problem is reduced to finding a suitable expression for the spin-dependent exchange-correlation potential $v_{xc}^{\sigma}([n_+, n_-]; \boldsymbol{r})$ and the exchange-correlation energy $E_{xc}[n_+, n_-]$, which is the subject of the remainder of the chapter.

2.2.6.1 General form of the exchange-correlation energy functional

By definition, a functional is not locally dependent upon an independent variable, but is globally dependent on an integral over a function of an independent variable. This is what is meant by a functional being 'nonlocal'. It was shown in Sec. 2.1.1 that the ground state properties of an interacting many-electron system are functionals of the ground state density. The energy $E[n]$ is therefore dependent on the entire distribution of charge and, for spin-polarized systems, on the entire distribution of spin-density. First, a non spin-polarized system is considered for the basic outline and is then extended to include spin-polarized systems.

In the general case, the energy functional has the form $E[n] = \int \varepsilon[n(\boldsymbol{r})]\,\mathrm{d}\boldsymbol{r}$ where $\varepsilon[n(\boldsymbol{r})]$ is the energy density per electron of the charge distribution. If the charge density varies slowly, $\varepsilon[n(\boldsymbol{r})]$ can be expanded in a power series in terms of the density gradient.

$$\varepsilon[n(\boldsymbol{r})] = \varepsilon_0(n(\boldsymbol{r})) + \varepsilon_1(n(\boldsymbol{r}))\nabla n(\boldsymbol{r}) + ... \tag{2.56}$$

To employ the LDA is to approximate the energy density $\varepsilon[n(\boldsymbol{r})]$ as only the first term in

the power series so that the exchange-correlation energy functional becomes

$$E_{xc}[n] = \int n(\boldsymbol{r})\varepsilon_{xc}(n(\boldsymbol{r}))\,\mathrm{d}\boldsymbol{r} \qquad \text{(LDA)} \tag{2.57}$$

where $\varepsilon_{xc}(n(\boldsymbol{r}))$ is the exchange-correlation energy density per electron for a homogeneous 'gas' of interacting electrons of density n.

2.2.6.2 Exchange-correlation energy of a uniform electron gas

The properties of the homogeneous electron gas were first derived, as they were initially understood in the context of DFT, in the late 1950's. The 'gas' consists of N interacting electrons in a volume V, which are otherwise free particles, of average density $n_0 = N/V$. Superimposed over the electron gas is a positive background charge density which only interacts with the electrons in the sense that the system is charge neutral, and so the Coulomb, or Hartree, energy is zero. This is often called the *jellium model* of a solid.

Some of the principal results are that the electron density fills a Fermi sphere in k-space and can therefore be related to the Fermi wave vector k_F by

$$n_0 = 2\int \frac{\mathrm{d}\boldsymbol{k}}{(2\pi)^3} = \frac{1}{\pi^2}\int_0^{k_F} k^2\,\mathrm{d}k = \frac{k_F^3}{3\pi^2} \tag{2.58}$$

and that the density is often parametrized in terms of the *Wigner-Seitz radius* r_s through the relation

$$n_0 \frac{4\pi}{3} a_0^3 r_s^3 = 1. \tag{2.59}$$

The total Thomas-Fermi kinetic energy of the gas is given (using Eq. (2.58)) by

$$T_{TF} = 2V\int \frac{\mathrm{d}\boldsymbol{k}}{(2\pi)^3}\frac{\hbar^2 k^2}{2m} = \frac{3}{5}E_F N \tag{2.60}$$

so that the average Thomas-Fermi kinetic energy per electron is

$$\varepsilon_{TF} = \frac{3}{5}E_F = \frac{3}{5}\frac{\hbar^2 k_F^2}{2m} = \frac{2.2099}{r_s^2} \qquad \text{(Ryd)}. \tag{2.61}$$

For an interacting electron gas, the total energy, within the Hartree-Fock model, can be calculated using the exchange term of the self-energy from the Dyson equation [15] because the Hartree energy is zero for a jellium model. This gives, for the exchange energy,

$$E_x(k) = -\frac{e^2 k_F}{\pi}\left(1 + \frac{k_F^2 - k^2}{2k_F k}\ln\left|\frac{k_F + k}{k_F - k}\right|\right) \tag{2.62}$$

For a uniform (non spin-polarized) electron gas, the *average* exchange energy per electron, assuming one spin up and one spin down electron per state, is [15, 16]

$$\varepsilon_x = 2\frac{1}{2N}\sum_k n_k E_x(k) = -\frac{3}{4}\frac{e^2 k_F}{\pi}. \tag{2.63}$$

The exchange contribution to the chemical potential is given by [15]

$$v_x = \mu_x = \frac{\mathrm{d}}{\mathrm{d}n}(n\varepsilon_x) = -\frac{e^2}{\pi}k_F = \frac{4}{3}\varepsilon_x. \tag{2.64}$$

Using the definition of the Wigner-Seitz radius, Eq. (2.59) and using Eq. (2.58) the exchange energy per electron is written as

$$\varepsilon_x = -\frac{3}{4}\frac{e^2 k_F}{\pi} = -\frac{0.9163}{r_s} \quad \text{(Ryd)}. \tag{2.65}$$

In the Hartree-Fock model, the above mentioned 'exchange term' is a quantum mechanical effect directly resulting from enforcing the Pauli exclusion principle for Fermions. It is a repulsive effect between electrons of parallel spin. The Hartree-Fock model fails to include the repulsion between electrons of anti-parallel spin due to Coulomb repulsion. The difference between the exact total energy and the Hartree-Fock energy is called the correlation energy. The total ground state energy per electron is then written as

$$\varepsilon_{gs} = \varepsilon_{TF} + \varepsilon_x + \varepsilon_c \tag{2.66}$$

or as

$$\varepsilon_{gs} = \frac{2.2099}{r_s^2} - \frac{0.9163}{r_s} + \varepsilon_c \quad \text{(Ryd)}. \tag{2.67}$$

Now, the exact definition of the correlation energy, as given above, is not conveninent to calculate. The exchange and correlation terms are classified in terms of the number of internal Coulomb lines in the corresponding Feynman diagrams. The exchange term includes diagrams with 1 internal Coulomb line. The correlation term includes every diagram with 2 or more internal Coulomb lines. Some of these terms have been evaluated in low and high density regimes. For a concise overview, see [15].

The high density limit, $r_s \to \infty$, in the *random phase approximation* (RPA) was first found by Gell-mann and Brueckner [17] and has been verified by several others [18, 19, 20, 21, 22]. Adding a term from Carr and Maradudin [23], the correlation energy is

$$\varepsilon_c = -0.094 + 0.0622 \ln r_s + 0.018 r_s \ln r_s + ... \quad \text{(Ryd)}. \tag{2.68}$$

This formula gives positive values for low densities ($r_s \geq 2.5$), which must be incorrect. The correlation energy must be negative as the correlation effects lower the total energy of the interacting electron system and increase the binding energy [15].

Wigner found [24] that for a jellium model at low density, the total energy is lowered by localization of the electrons. This is referred to as a *Wigner lattice*. This model assumes that there is an electron at the center of a sphere in each unit cell of the lattice. The negative charge of the electron is exactly balanced by the positive background charge and so the electric field is zero outside the sphere. The total energy in this (Wigner-Seitz) model is given by $\sim -1.792/r_s$ [25]. If we subtract the exchange energy, $-0.9163/r_s$, this gives the low density limit of the correlation energy as

$$\varepsilon_c = -\frac{0.8757}{r_s} \quad \text{(Ryd)}. \tag{2.69}$$

The density regimes for which these expressions are individually valid do not span the entire range of actual metallic densities ($\approx 1.8 < r_s < 6$) and so there have been several interpolation schemes employed for acual metallic densities between the low and high density limits.

One of the first interpolation schemes was due to Wigner [24]

$$\varepsilon_c = -\frac{0.88}{r_s + 7.8} \quad \text{(Ryd)}. \tag{2.70}$$

Another, from Nozieres and Pines [20], is

$$\varepsilon_c = -0.115 + 0.031 \ln r_s \quad \text{(Ryd)}. \tag{2.71}$$

Dielectric functions can also be used to calculate the correlation energy. RPA, Thomas-Fermi, Hubbard and Singwi-Sjölander are some of the common models. The Singwi-Sjölander model is commonly used as it gives a positive pair distribution function for most densities [15].

2.2.6.3 Interpolation scheme; spin-independent

The interpolation scheme used in this work was first proposed by Hedin and Lundqvist [26] [25]. It was implemented in the context of the spin-polarized version of DFT of von Barth and Hedin [12]. This model gives

$$v_{xc}(r_s) = v_x(r_s) + v_c(r_s) = \beta(r_s) v_x(r_s) \tag{2.72}$$

where $v_{xc}(r_s)$ is the exchange-correlation contribution to the total effective potential $v_{NI}(\boldsymbol{r})$ for a homogeneous gas of density r_s.

Using the correlation enhancement function

$$\beta(r_s) = 1 + Bx \ln\left(1 + \frac{1}{x}\right) \tag{2.73}$$

and Eq. (2.64), expressions for $v_c(r_s)$ and $\varepsilon_c(r_s)$ are given as

$$v_c(r_s) = -C \ln\left(1 + \frac{1}{x}\right) \quad \text{(Ryd)} \tag{2.74}$$

$$\varepsilon_c(r_s) = -C\left(\left(1 + x^3\right) \ln\left(1 + \frac{1}{x}\right) + \frac{x}{2} - x^2 - \frac{1}{3}\right) \quad \text{(Ryd)} \tag{2.75}$$

where $x = r_s/A$ and $C = 2B((9\pi)/4)^{1/3}/\pi A$. The values of the parameters

$$A = 21.0 \qquad \text{and} \qquad C = 0.045 \tag{2.76}$$

are used to reproduce the results of Singwi *et al.* [27] for $\epsilon_{xc}(r_s)$.

Inspecting the form of Eq. (2.73), it can be seen that $\beta(r_s)$ varies from 1.0 to 1.33 for $0 \leq r_s \leq 6$. This shows that the exchange effect dominates the correlation effects for actual metallic densities.

2.2.6.4 Interpolation scheme; spin-dependent

The extension of the LDA to spin-polarized systems is called the *local spin-density approximation* (LSDA). If the local spin-polarization direction is chosen to be the z-axis, the exchange-correlation energy functional is given by

$$E_{xc}[n_+, n_-] = \int (n_+(\boldsymbol{r}) + n_-(\boldsymbol{r}))\varepsilon_{xc}(n_+(\boldsymbol{r}), n_-(\boldsymbol{r}))\,\mathrm{d}\boldsymbol{r} \tag{2.77}$$

where the spin up and spin down densities $n_+(\boldsymbol{r})$ and $n_-(\boldsymbol{r})$ are related to the total density $n(\boldsymbol{r})$ and the spin-polarization $\zeta(\boldsymbol{r})$ by

$$n(\boldsymbol{r}) = n_+(\boldsymbol{r}) + n_-(\boldsymbol{r}) \tag{2.78}$$

and

$$\zeta(\boldsymbol{r}) = \frac{n_+(\boldsymbol{r}) - n_-(\boldsymbol{r})}{n_+(\boldsymbol{r}) + n_-(\boldsymbol{r})} \tag{2.79}$$

where $n_+(\boldsymbol{r}) - n_-(\boldsymbol{r})$ is the total spin density. The exchange energy is written [11] as

$$E_{x,pol}[n, \zeta] = \frac{1}{2}E_x[(1+\zeta)n] + \frac{1}{2}E_x[(1-\zeta)n]. \tag{2.80}$$

Expanding this in a gradient series expansion gives, to lowest order, the exchange energy per electron as

$$\varepsilon_{x,pol}(\boldsymbol{r}) = \frac{1}{2}\left[(1+\zeta(\boldsymbol{r}))^{4/3} + (1-\zeta(\boldsymbol{r}))^{4/3}\right]\varepsilon_x(\boldsymbol{r}) \tag{2.81}$$

where ε_x is given by Eq. (2.63).

There have been several parametrizations used for spin-polarized systems including that of von Barth and Hedin [12], Gunnarson and Lundqvist [28], and Monte Carlo results

from Ceperley and Alder [29]. A short summary of the details of these schemes is given in [11]. Again, the parametrization of von Barth and Hedin is employed in this work.

The von Barth-Hedin parametrization is based on an interpolation between the paramagnetic, unpolarized ($\zeta = 0$) state and the ferromagnetic, fully polarized ($\zeta = 1$) state. With the exchange-correlation energy per electron written as (suppressing the local dependence on $\boldsymbol{r}$)

$$\varepsilon_{xc}[n,\zeta] = \varepsilon_x[n,\zeta] + \varepsilon_c[n,\zeta] \tag{2.82}$$

the terms take the form

$$\varepsilon_x[n,\zeta] = \varepsilon_x[n,\zeta=0] + f(\zeta)\left(\varepsilon_x[n,\zeta=1] - \varepsilon_x[n,\zeta=0]\right) \tag{2.83}$$

and

$$\varepsilon_c[n,\zeta] = \varepsilon_c[n,\zeta=0] + f(\zeta)\left(\varepsilon_c[n,\zeta=1] - \varepsilon_c[n,\zeta=0]\right). \tag{2.84}$$

The interpolation function is given by

$$f(\zeta) = \frac{(1+\zeta)^{4/3} + (1-\zeta)^{4/3} - 2}{2^{4/3} - 2}. \tag{2.85}$$

In the paramagnetic limit ($\zeta = 0$), the exchange energy $\varepsilon_x(n,\zeta=0)$ is given by Eq. (2.63). In the ferromagnetic limit ($\zeta = 1$), it is given by $\varepsilon_x(n,\zeta=\pm1) = \sqrt[3]{2}\varepsilon_x(n,\zeta=0)$.

In this spin-polarized scheme, the interpolation again follows the Hedin-Lundqvist form, Eq.'s (2.74) and (2.75), with the parameters

$$\begin{aligned} \zeta = 0: &\quad C^P = 0.0504, \quad A^P = 30.0 \\ \zeta = 1: &\quad C^F = 0.0254, \quad A^F = 75.0. \end{aligned} \tag{2.86}$$

Using Eq. (2.48) and Eq. (2.77), the spin-dependent exchange-correlation potential is calculated as

$$v^s_{xc} = \frac{\partial}{\partial n_s}\left[(n_+ + n_-)\varepsilon_{xc}(n_+,n_-)\right]. \tag{2.87}$$

In particular,

$$v_{xc}^{+} = \varepsilon_{xc}(n_+, n_-) + n\frac{\partial \varepsilon_{xc}}{\partial n_+} \tag{2.88}$$

explicitly giving

$$v_{xc}^{+} = \left(\frac{4}{3}\varepsilon_x^{\zeta=0}(n) + \gamma\left(\varepsilon_c^{\zeta=\pm1}(n) - \varepsilon_c^{\zeta=0}(n)\right)\right)(1+\zeta)^{1/3} - C^P \ln\left(1 + \frac{A^P}{r_s}\right) - \gamma\left(\varepsilon_c^{\zeta=\pm1}(n) - \varepsilon_c^{\zeta=0}(n)\right) + \tau f(\zeta) \tag{2.89}$$

with

$$\tau = -C^F \ln\left(1 + \frac{A^F}{r_s}\right) + C^P \ln\left(1 + \frac{A^P}{r_s}\right) - \frac{4}{3}\left(\varepsilon_c^{\zeta=\pm1}(n) - \varepsilon_c^{\zeta=0}(n)\right) \tag{2.90}$$

and

$$\gamma = \frac{4}{3(\sqrt[3]{2} - 1)} \tag{2.91}$$

where $\varepsilon_c(n, \zeta)$ follows the form of Eq. (2.75) with the parameters given by Eq. (2.86). The exchange-correlation potential for spin-down electrons satisfies the symmetric relation $v_{xc}^{+}(\zeta) = v_{xc}^{-}(-\zeta)$.

In summary, the correlation energy for the spin-polarized case uses the Hedin-Lundqvist model which was already presented for the non spin-polarized case. So, even though the parameters are different for the spin-polarized case, the behavior of ε_{xc} and v_{xc} is very similar for the spin-polarized case and the non spin-polarized case. (Compare Fig. 2.2 and Fig. 2.5 along the line $m = 0$.) Similarly, the exchange-correlation potentials are similar for the spin-polarized and non spin-polarized cases. (Compare Fig. 2.3 and Fig.'s 2.10 and 2.11 along the line $m = 0$.)

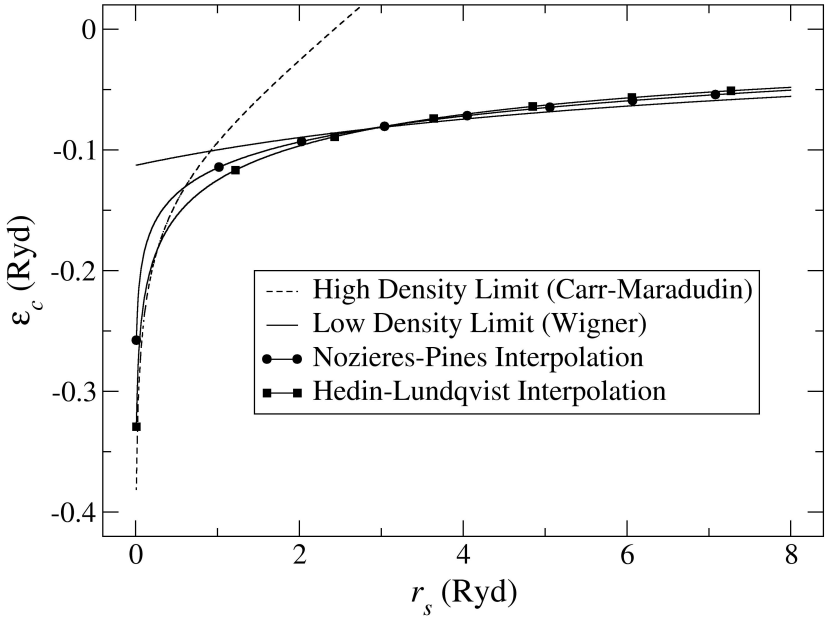

FIGURE 2.1: High density and low density limits for the average exchange-correlation energy per electron for a homogeneous electron gas. Common interpolation schemes between these limits are also shown.

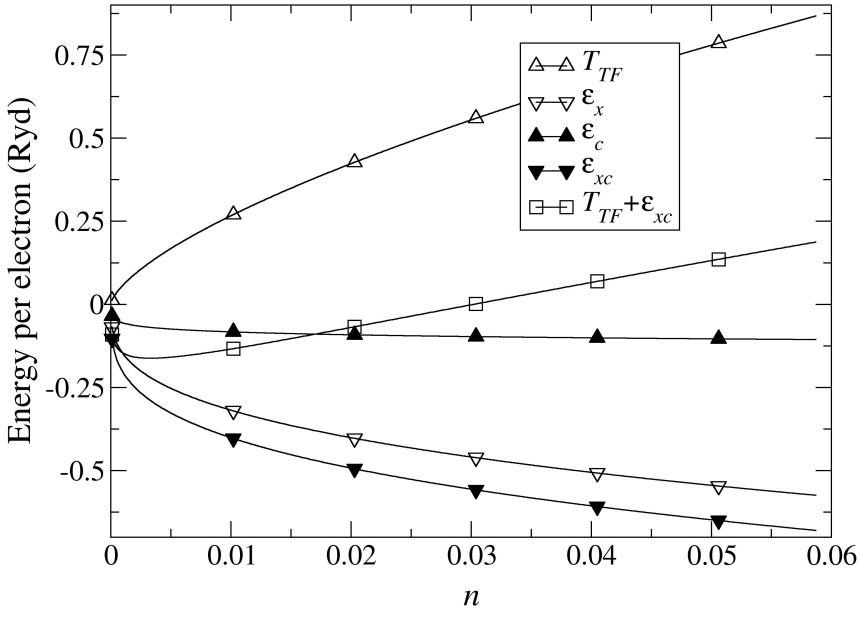

FIGURE 2.2: Thomas-Fermi kinetic T_{TF}, exchange ε_x, and correlation ε_c energies per electron as a function of density for a homogeneous electron gas from the parametrization of Hedin and Lundqvist.

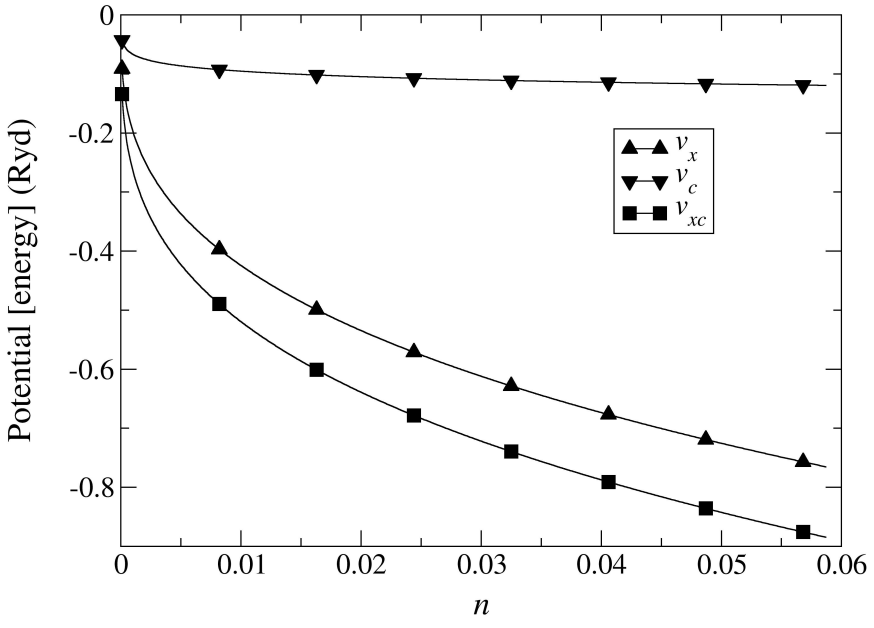

FIGURE 2.3: Exchange v_x and correlation v_c potentials for a homogeneous electron gas as a function of density from the parametrization of Hedin and Lundqvist.

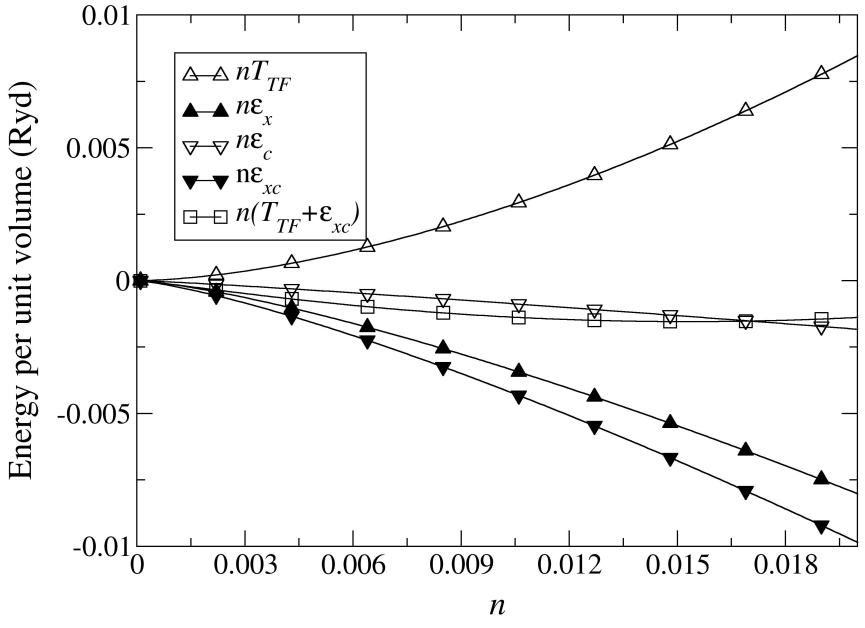

FIGURE 2.4: Thomas-Fermi kinetic ε_{TF}, exchange ε_x, and correlation ε_c energies per electron multiplied by the electron density n for a homogeneous electron gas.

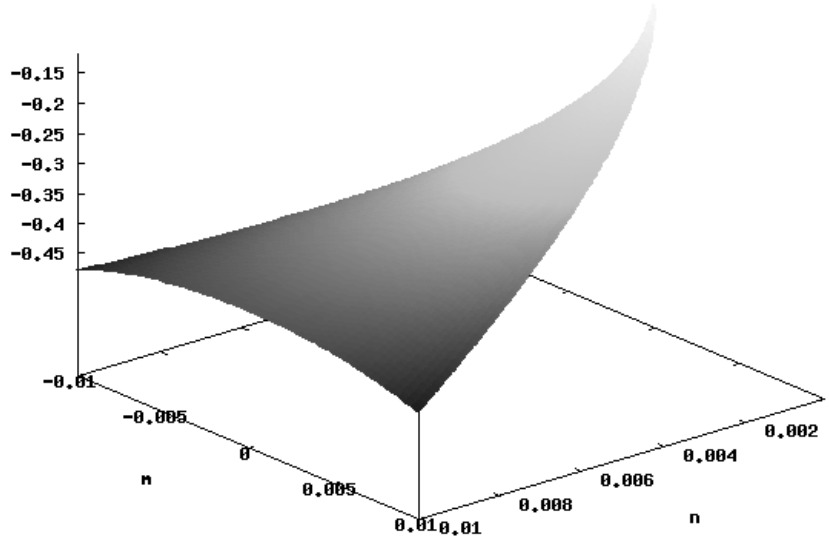

FIGURE 2.5: Exchange-correlation energy per electron ε_{xc} for a spin-polarized electron gas from the parametrization of von Barth, Hedin, and Lundqvist. $m = n\zeta$, where m is the spin-polarization, n is the density and ζ is the relative spin-polarization.

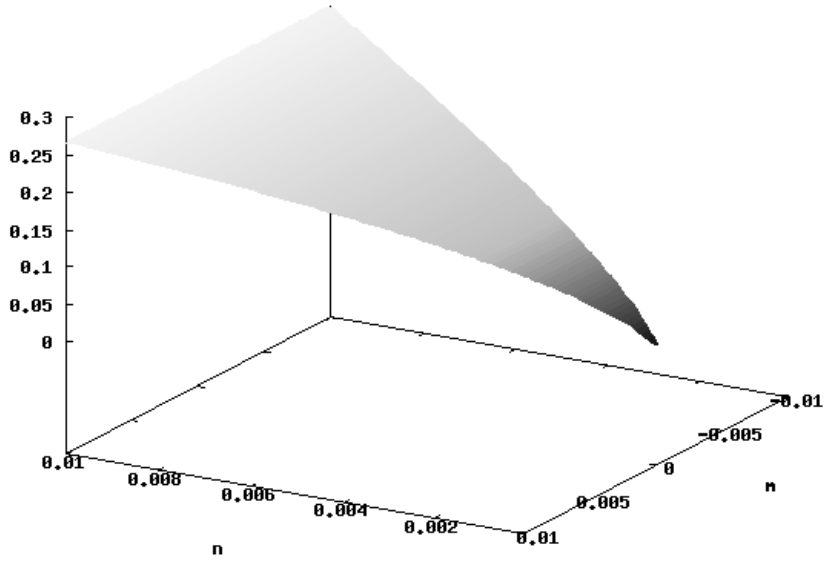

FIGURE 2.6: Thomas-Fermi kinetic energy per electron $T_{TF} = 2.2099/r_{WS}^2$ for a spin-polarized electron gas. There is no difference between spin-polarized and non spin-polarized systems.

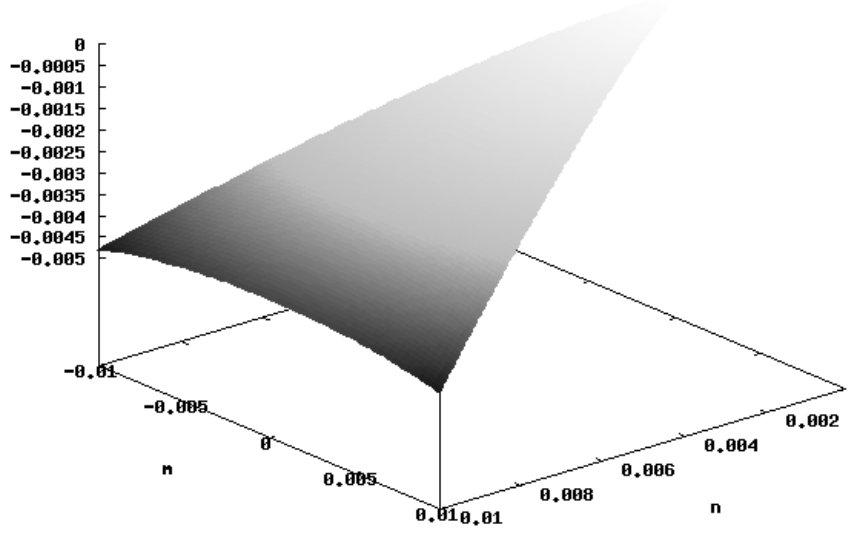

FIGURE 2.7: Exchange-correlation energy density $n\varepsilon_{xc}$ for a spin-polarized electron gas from the parametrization of von Barth, Hedin, and Lundqvist. $m = n\zeta$, where m is the spin-polarization, n is the density and ζ is the relative spin-polarization.

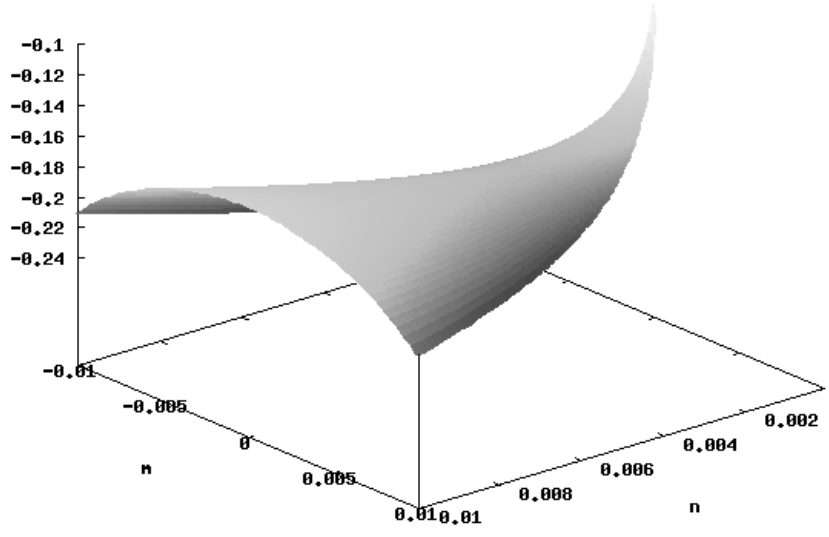

FIGURE 2.8: The sum of the exchange-correlation and Thomas-Fermi kinetic energies per electron $\varepsilon_{xc} + T_{TF}$ for a spin-polarized electron gas where $T_{TF} = 2.2099/r_s^2$.

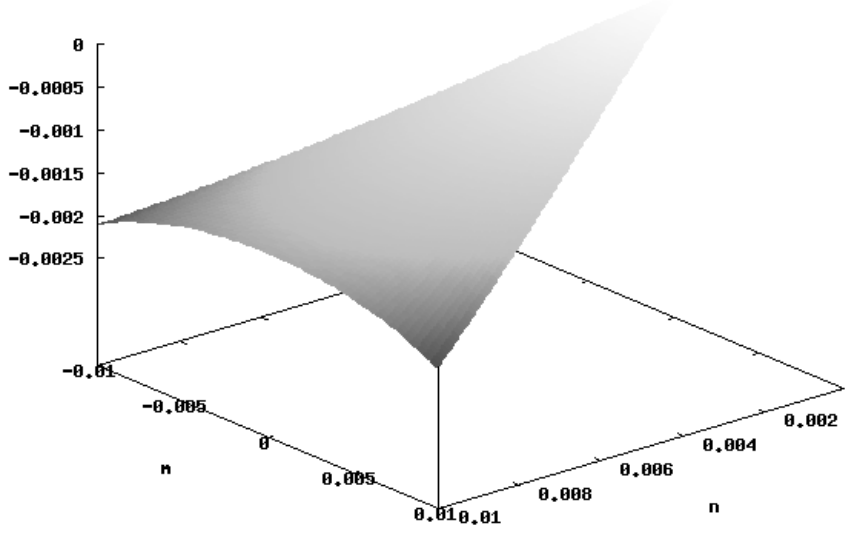

FIGURE 2.9: The sum of the exchange-correlation and Thomas-Fermi kinetic energy densities for a spin-polarized electron gas $n(\varepsilon_{xc} + T_{TF})$ where $T_{TF} = 2.2099/r_s^2$.

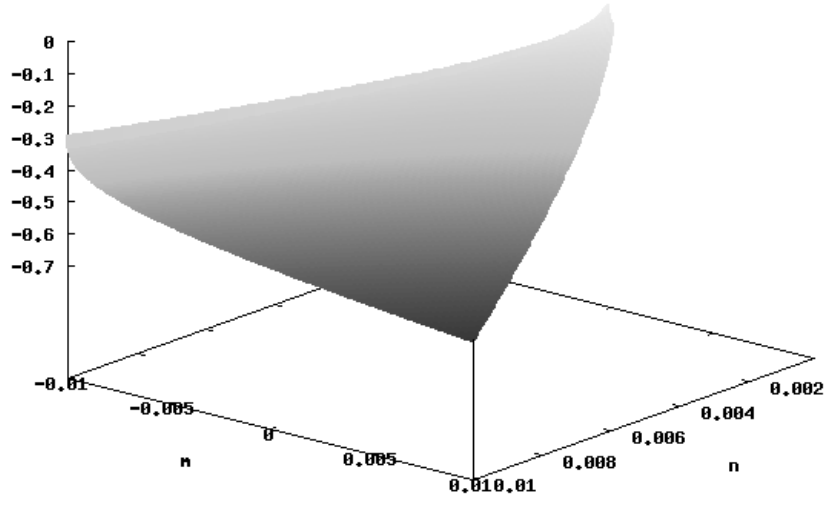

FIGURE 2.10: Exchange-correlation potential v_{xc}^{+} for spin up electrons in a spin-polarized electron gas from the parametrization of von Barth, Hedin, and Lundqvist.

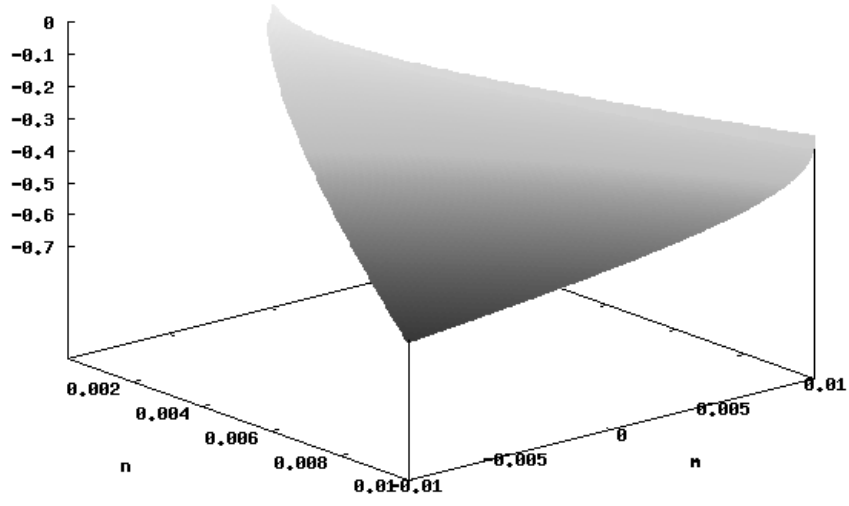

FIGURE 2.11: Exchange-correlation potential v_{xc}^{-} for spin down electrons in a spin-polarized electron gas from the parametrization of von Barth, Hedin, and Lundqvist.

3. PROPERTIES OF OUR MODEL SYSTEM

In this work, we focus on nonspherical free atom calculations and nonspherical immersion calculations. Previous work has primarily focused on spherical systems for immersion calculations [5, 30, 31], while some work has been done for nonspherical systems [32, 33, 34]. Most atoms and molecules as well as almost all solids have nonspherical symmetry, it is therefore important to understand the properties of nonspherical electronic systems. Within the LSDA of the Kohn-Sham scheme, we must solve the single-particle Schrödinger[1] equation of the form

$$[-\nabla^2 + v(\boldsymbol{r}) - \epsilon_i]\psi_i(\boldsymbol{r}) = 0 \tag{3.1}$$

where the total effective potential $v(\boldsymbol{r})$ is the sum of the nuclear Coulomb potential, the Hartree potential, and the exchange-correlation potential as given by Eq. (2.34)

$$v(\boldsymbol{r}) = v_{ext}(\boldsymbol{r}) + v_H(\boldsymbol{r}) + v_{xc}(\boldsymbol{r}).$$

The electronic eigenstates are labelled by the energy index i for bound states and $\boldsymbol{k}$ for scattered states. These can be written in terms of the spherical harmonics as[2]

$$\psi_i(\boldsymbol{r}) = \sum_{lm} \frac{u_{ilm}(r)}{r} Y_{lm}(\hat{\boldsymbol{r}}) \tag{3.2}$$

for bound states, and

$$\psi_{\boldsymbol{k}}(\boldsymbol{r}) = \frac{1}{(2\pi)^{3/2}} \sum_{lm} \frac{u_{lm}(\boldsymbol{k}; r)}{kr} Y_{lm}(\hat{\boldsymbol{r}}) \tag{3.3}$$

[1] When the Schrödinger equation has the effective single-particle potential of the Kohn-Sham scheme inserted into it, we will refer to it as the Kohn-Sham equation(s).

[2] Sums over l quantum numbers appearing in expression for wavefunctions theoretically range from 0 to ∞, but must be limited to a value l_{max} in the numerical calulations in this work; this will be discussed in more detail in chapter 4. Due to the non-spherical symmetry of the systems in this work, there are many 'dummy' l-type indices appearing, symbols used include: l, L, j & λ

for scattered states.[3]

Angular momentum shells in general have cylindrical symmetry. This means that the potentials and densities also have cylindrical symmetry. It also means that m is still a good quantum number. The Kohn-Sham equation(s), Eq. (3.1), can be simplified according to this symmetry.

The cylindrical symmetry of the potential allows an expansion of the form[4]

$$v(\boldsymbol{r}) = v(r,\theta) = \sum_{\nu} v_\nu(r) P_\nu(\cos\theta) \tag{3.4}$$

so that the radial functions $u_{ilm}(r)$ satisfy the following system of coupled equations (for a given value of m)

$$\left[\frac{\mathrm{d}^2}{\mathrm{d}r^2} + \epsilon_i - \frac{l(l+1)}{r^2}\right] u_{ilm}(r) = \sum_{l'} U^m_{ll'}(r) u_{il'm}(r) \tag{3.5a}$$

$$\left[\frac{\mathrm{d}^2}{\mathrm{d}r^2} + k^2 - \frac{l(l+1)}{r^2}\right] u_{lm}(\boldsymbol{k};r) = \sum_{l'} U^m_{ll'} u_{l'm}(\boldsymbol{k};r) \tag{3.5b}$$

for bound and scattered states, respectively, with

$$U^m_{ll'}(r) = \int Y^*_{lm}(\hat{\boldsymbol{r}}) v(r,\theta) Y_{l'm}(\hat{\boldsymbol{r}})\, \mathrm{d}\hat{\boldsymbol{r}}. \tag{3.6}$$

Since the potential becomes a pure Coulomb potential near the nucleus, the components $v_\nu(r)$ of the potential satisfy the following conditions:

$$\lim_{r\to 0} v_\nu(r) \sim \begin{cases} r^\nu & \text{if} \quad \nu \neq 0 \\ -\frac{Z}{r} & \text{if} \quad \nu = 0 \end{cases} \tag{3.7}$$

[3]The factor of $1/(2\pi)^{3/2}$ arises from the inevitability of converting sums over states into integrals and the resulting volume element encountered when normalizing the scattered states in k-space. The factor of $1/k$ is chosen for convenience and is not necessary.

[4]Sums over l quantum numbers appearing in expressions for densities and potentials theoretically range from 0 to ∞, but must be limited to a value of ν_{max} in the numerical calculations performed in this work, which will be different from l_{max} given above. In these cases, the l index will be designated by ν.

3.1 Determination of the Density

3.1.1 Continuum States of the Electron Gas

The continuum solutions of Eq. (3.1), normalized in momentum-space, satisfy the asymptotic relation

$$\psi_{\boldsymbol{k}}(\boldsymbol{r}) \longrightarrow_{r\to\infty} \frac{1}{(2\pi)^{3/2}}[e^{i\boldsymbol{k}\cdot\boldsymbol{r}} + f\,(\boldsymbol{k},\hat{\boldsymbol{r}})\,\frac{e^{ikr}}{r}] \tag{3.8}$$

Due to the nonspherical symmetry of the potential, the radial functions $u_{lm}(\boldsymbol{k};r)$, appearing in Eq. (3.5) depend on the direction $\hat{\boldsymbol{k}}$ of the incident plane wave. Thus, for a given m, we generate a set of linearly independent solutions $u^{(j)}_{lm}(k;r)$ of the system, Eq. (3.5), where l and j both range from 0 to l_{max}.

Using the form of the potential, Eq. (3.7), it can be shown (Appendix B) that there exist solutions of the form

$$u^{(j)}_{lm}(r) \sim_{r\to 0} r^{j+|l-j|+1} \sum_{i=1}^{\infty} b^l_i r^{i-1} \tag{3.9}$$

which is how the integrations of the coupled radial equations are initialized for the outward integration from $r = 0$.

The radial functions $u_{lm}(\boldsymbol{k};r)$ are then given by

$$u_{lm}(\boldsymbol{k};r) = \sum_j \gamma_{jm}(\boldsymbol{k}) u^{(j)}_{lm}(k;r) \tag{3.10}$$

and we expand the angular $\boldsymbol{k}$ dependence as

$$\gamma_{lm}(\boldsymbol{k}) = 4\pi \sum_{l'} i^{l'} \Gamma^m_{ll'}(k) Y^*_{l'm}(\hat{\boldsymbol{k}}) \tag{3.11}$$

where the overall phase is chosen this way for proper normalization. With the solutions $u^{(j)}_{lm}(k;r)$ varying as

$$R^{(j)}_{lm}(k;r) = \frac{u^{(j)}_{lm}(k;r)}{kr} \longrightarrow_{r\to\infty} [A^m_{lj}(k) j_l(kr) + B^m_{lj}(k) n_l(kr)] \tag{3.12}$$

we can take the Wronskian of the radial functions $R_{lm}^{(j)}(k;r)$ with the Bessel functions $n_l(kr)$ and $j_l(kr)$ to calculate the coefficients $A_{lj}^m(k)$ and $B_{lj}^m(k)$. We obtain

$$\mathcal{W}\left[R_{lm}^{(j)}(k;r), n_l(kr_\infty)\right] \rightarrow$$
$$A_{lj}^m(k) = kr_\infty u_{lm}^{(j)}(k;r_\infty)\frac{\mathrm{d}}{\mathrm{d}r}n_l(kr_\infty)$$
$$- r_\infty n_l(kr_\infty)\frac{\mathrm{d}}{\mathrm{d}r}u_{lm}^{(j)}(k;r_\infty) + u_{lm}^{(j)}(k;r_\infty)n_l(kr_\infty) \quad (3.13)$$

and

$$\mathcal{W}\left[R_{lm}^{(j)}(k;r), j_l(kr_\infty)\right] \rightarrow$$
$$B_{lj}^m(k) = kr_\infty u_{lm}^{(j)}(k;r_\infty)\frac{\mathrm{d}}{\mathrm{d}r}j_l(kr_\infty)$$
$$- r_\infty j_l(kr_\infty)\frac{\mathrm{d}}{\mathrm{d}r}u_{lm}^{(j)}(k;r_\infty) + u_{lm}^{(j)}(k;r_\infty)j_l(kr_\infty) \quad (3.14)$$

where r_∞ denotes that the Wronskians are evaluated at the numerical cutoff of the radial mesh, which is the approximation used for infinity in this work. This cutoff will be addressed in more detial in Chapter 4. The $\mathbf{\Gamma}$ coefficient matrix appearing in Eq. (3.11) is defined as [33, 34]

$$\mathbf{\Gamma}^m(k) = [\boldsymbol{A}^m(k) - i\boldsymbol{B}^m(k)]^{-1} \quad (3.15)$$

so that Eq. (3.8) becomes

$$\psi_{\boldsymbol{k}}(\boldsymbol{r}) = \frac{4\pi}{(2\pi)^{3/2}}\frac{1}{kr}\sum_{jl\lambda m} i^\lambda \Gamma_{j\lambda}^m(k)u_{lm}^{(j)}(k;r)Y_{\lambda m}^*(\hat{\boldsymbol{k}})Y_{lm}(\hat{\boldsymbol{r}}). \quad (3.16)$$

To calculate the continuum density, we first needed the continuum Kohn-Sham wavefunctions $\psi_{\boldsymbol{k}}(\boldsymbol{r})$. We can now calculate the continuum density as

$$n_C(\boldsymbol{r}) = \int \psi_{\boldsymbol{k}}^*(\boldsymbol{r})\psi_{\boldsymbol{k}}(\boldsymbol{r})\,\mathrm{d}\boldsymbol{k}. \quad (3.17)$$

Inserting Eq. (3.16) into Eq. (3.17), we have

$$n_C(\boldsymbol{r}) = \int \sum_{jj'll'\lambda\lambda'm} \frac{16\pi^2}{(2\pi)^3 k^2 r^2} i^{\lambda-\lambda'}\Gamma_{j\lambda}^m(k)[\Gamma_{j'\lambda'}^m(k)]^*$$
$$\times Y_{\lambda m}^*(\hat{\boldsymbol{k}})Y_{\lambda' m}(\hat{\boldsymbol{k}})Y_{lm}^*(\hat{\boldsymbol{r}})Y_{l'm}(\hat{\boldsymbol{r}})u_{lm}^{(j)}(k;r)u_{l'm}^{(j')}(k;r)\,\mathrm{d}\boldsymbol{k}. \quad (3.18)$$

We note that the cylindrical symmetry permits an expansion of the density in Legendre polynomials

$$n_C(\boldsymbol{r}) = \sum_\nu n_\nu^C(r) P_\nu(\cos\theta) \tag{3.19}$$

so using

$$\int P_l(\cos\theta) P_{l'}(\cos\theta)\,\mathrm{d}(\cos\theta) = \frac{2}{2l+1}\delta_{l,l'} \tag{3.20}$$

we calculate the components of the continuum density as

$$n_\nu^C(r) = \frac{2\nu+1}{4\pi}\int P_\nu(\cos\theta_r) n_C(\boldsymbol{r})\,\mathrm{d}\hat{\boldsymbol{r}}. \tag{3.21}$$

Inserting Eq. (3.18) into Eq. (3.21), we have

$$n_\nu^C(r) = \frac{2\nu+1}{4\pi}\int \mathrm{d}\hat{\boldsymbol{r}} P_\nu(cos\theta_r)\int \mathrm{d}\boldsymbol{k}\sum_{jj'll'\lambda\lambda'm}\frac{16\pi^2}{(2\pi)^3 k^2 r^2} i^{\lambda-\lambda'}\Gamma^m_{j\lambda}(k)[\Gamma^m_{j'\lambda'}(k)]^* \\ \times Y^*_{\lambda m}(\hat{\boldsymbol{k}}) Y_{\lambda' m}(\hat{\boldsymbol{k}}) Y^*_{lm}(\hat{\boldsymbol{r}}) Y_{l'm}(\hat{\boldsymbol{r}}) u^{(j)}_{lm}(k;r) u^{(j')}_{l'm}(k;r). \tag{3.22}$$

From here, using Wigner $6j$ notation

$$(2L+1)\int Y_{lm}(\hat{r}) P_L(\cos\theta) Y^*_{l'm}(\hat{r})\,\mathrm{d}\hat{\boldsymbol{r}} = \begin{Bmatrix} l & l' & L \\ m & -m & 0 \end{Bmatrix} \tag{3.23}$$

we rewrite Eq. (3.22) as

$$n_\nu^C(r) = \int \sum_{jj'll'\lambda\lambda'm}\frac{4\pi}{(2\pi)^3 k^2 r^2}\begin{Bmatrix} l & l' & \nu \\ m & -m & 0 \end{Bmatrix} \\ \times i^{\lambda-\lambda'}\Gamma^m_{j\lambda}(k)[\Gamma^m_{j'\lambda'}(k)]^* Y^*_{\lambda m}(\hat{\boldsymbol{k}}) Y_{\lambda' m}(\hat{\boldsymbol{k}}) u^{(j)}_{lm}(k;r) u^{(j')}_{l'm}(k;r)\,\mathrm{d}\boldsymbol{k}. \tag{3.24}$$

To show parallel with [33],[34] we use

$$P_0(\cos\theta) = 1 \tag{3.25}$$

to write the total continuum density as

$$n_\nu^C(r) = \int k^2\,\mathrm{d}k \sum_{jj'll'\lambda\lambda'm}\frac{4\pi}{8\pi^3 k^2 r^2}\begin{Bmatrix} l & l' & \nu \\ m & -m & 0 \end{Bmatrix} \\ \times i^{\lambda-\lambda'}\Gamma^m_{j\lambda}(k)[\Gamma^m_{j'\lambda'}(k)]^*\left(\int \mathrm{d}\hat{\boldsymbol{k}} Y^*_{\lambda m}(\hat{\boldsymbol{k}}) Y_{\lambda' m}(\hat{\boldsymbol{k}}) P_0(\cos\theta_k)\right) u^{(j)}_{lm}(k;r) u^{(j')}_{l'm}(k;r)$$

and use Wigner $6j$ notation to rewrite the term in parentheses, giving the total continuum density as

$$n_\nu^C(r) = \frac{2}{(2\pi r)^2} \int \sum_{jj'll'm} \begin{Bmatrix} l & l' & \nu \\ m & -m & 0 \end{Bmatrix} u_{lm}^{(j)}(k;r) u_{l'm}^{(j')}(k;r) \times \sum_{\lambda\lambda'} \begin{Bmatrix} \lambda & \lambda' & 0 \\ -m & m & 0 \end{Bmatrix} i^{\lambda-\lambda'} \Gamma_{j\lambda}^m(k) [\Gamma_{j'\lambda'}^m(k)]^* \, \mathrm{d}k. \quad (3.26)$$

If we define

$$\begin{aligned} \Xi_{jj'}^m(k) &= 2 \sum_{\lambda\lambda'} \begin{Bmatrix} \lambda & \lambda' & 0 \\ -m & m & 0 \end{Bmatrix} i^{\lambda-\lambda'} \Gamma_{j\lambda}^m(k) [\Gamma_{j'\lambda'}^m(k)]^* \\ &= 2 \sum_{\lambda\lambda'} i^{\lambda-\lambda'} \Gamma_{j\lambda}^m(k) [\Gamma_{j'\lambda'}^m(k)]^* \delta_{\lambda\lambda'} \\ &= 2 \sum_{\lambda} \Gamma_{j\lambda}^m(k) [\Gamma_{j'\lambda}^m(k)]^* \end{aligned} \quad (3.27)$$

we have the total continuum density given as

$$n_\nu^C(r) = \frac{1}{(2\pi r)^2} \sum_{jj'll'm} \begin{Bmatrix} l & l' & \nu \\ m & -m & 0 \end{Bmatrix} \int \Xi_{jj'}^m(k) u_{lm}^{(j)}(k;r) u_{l'm}^{(j')}(k;r) \, \mathrm{d}k. \quad (3.28)$$

To calculate the *induced* continuum density $\Delta n_C(\boldsymbol{r}) = n_C(\boldsymbol{r}) - n_0$, we first use the completeness relation

$$\sum_l (2l+1) j_l^2(kr) = 1 \quad (3.29)$$

and the Fermi sphere relation

$$n_0 = 2 \int_0^{k_F} \frac{\mathrm{d}\boldsymbol{k}}{(2\pi)^3} = \frac{1}{\pi^2} \int_0^{k_F} k^2 dk \quad (3.30)$$

to write the homogenous electron gas density as

$$n_0 = \frac{1}{\pi^2} \int_0^{k_F} \sum_l (2l+1) k^2 j_l^2(kr) \, \mathrm{d}k. \quad (3.31)$$

This last step was taken to minimize errors which arise due to the finite cutoff for the l quantum numbers when we calculate the induced density. The change in density $\Delta n(\boldsymbol{r})$ induced by the impurity in the conduction band can then be calculated as

$$\Delta n^C_\nu(r) = \left[\frac{1}{(2\pi r)^2}\sum_{jj'll'm}\begin{Bmatrix} l & l' & \nu \\ m & -m & 0\end{Bmatrix}\int \Xi^m_{jj'}(k)u^{(j)}_{lm}(k;r)u^{(j')}_{l'm}(k;r)\,\mathrm{d}k\right] - \frac{1}{\pi^2}\int\sum_l\left[(2l+1)k^2j_l^2(kr)\right]\,\mathrm{d}k \quad (3.32)$$

which simplifies to

$$\Delta n^C_\nu(r) = \int\sum_{ll'm}\{\frac{1}{(2\pi r)^2}\begin{Bmatrix} l & l' & \nu \\ m & -m & 0\end{Bmatrix}\sum_{jj'}[\Xi^m_{jj'}(k)u^{(j)}_{lm}(k;r)u^{(j')}_{l'm}(k;r)] - \delta_{l,l'}\delta_{\nu,0}\frac{1}{\pi^2}k^2j_l^2(kr)\}\,\mathrm{d}k. \quad (3.33)$$

If we no longer suppress the spin degree of freedom σ, we have the l-th (ν-th) component of the induced continuum density for a single spin-channel as

$$\Delta n^C_{\nu\sigma}(r) = \int\sum_{ll'm}\{\frac{1}{(2\pi r)^2}\begin{Bmatrix} l & l' & \nu \\ m & -m & 0\end{Bmatrix}\sum_{jj'}[\Xi^{m\sigma}_{jj'}(k)u^{(j)}_{lm\sigma}(k;r)u^{(j')}_{l'm\sigma}(k;r)] - \delta_{l,l'}\delta_{\nu,0}\frac{1}{2\pi^2}k^2j_l^2(kr)\}\,\mathrm{d}k. \quad (3.34)$$

3.1.2 Bound States Localized on the Impurity

The bound states can be expanded in the same manner as the continuum states

$$u_{lm}(\epsilon;r) = \sum_j \mu^m_j(\epsilon)u^{(j)}_{lm}(\epsilon;r) \quad (3.35)$$

for the outward integration from $r = 0$ and

$$v_{lm}(\epsilon;r) = \sum_j \eta^m_j(\epsilon)v^{(j)}_{lm}(\epsilon;r) \quad (3.36)$$

for the inward integration from $r = \infty$. We use the asymptotic behavior of the radial functions for large values of r

$$v_{lm}^{(j)}(\epsilon; r) \sim_{r\to\infty} \delta_{lj} e^{-r\sqrt{-2\epsilon}} \tag{3.37}$$

to begin an integration of the radial equations inward from infinity. If a bound state exists, there exists a linear combination of the inner set of solutions that must match up with a linear combination of the outer set of solutions, so that the determinant of the system

$$\sum_j \mu_j^m(\epsilon) u_{lm}^{(j)}(\epsilon; r) = \sum_i \eta_i^m(\epsilon) v_{lm}^{(i)}(\epsilon; r) \tag{3.38a}$$

$$\sum_j \mu_j^m(\epsilon) \frac{\mathrm{d}}{\mathrm{d}r} u_{lm}^{(j)}(\epsilon; r) = \sum_i \eta_i^m(\epsilon) \frac{\mathrm{d}}{\mathrm{d}r} v_{lm}^{(i)}(\epsilon; r) \tag{3.38b}$$

will vanish. Once the bound state energy has been found, the coefficients $\mu_j^m(\epsilon)$ and $\eta_i^m(\epsilon)$ and thus the radial functions $u_{lm}(\epsilon; r)$ can be found from a singular value decomposition (SVD) of the system, Eq. (3.38). See Appendix C for a description of SVD.

Once the bound wavefunctions are known, the electron density from a bound state can be calculated from

$$\begin{aligned} n_i^B(\boldsymbol{r}) &= \psi_i^*(\epsilon_i; \boldsymbol{r}) \psi_i(\epsilon_i; \boldsymbol{r}) \\ &= \frac{1}{r^2} \sum_{ll'm} u_{lm}(\epsilon_i; r) u_{l'm}(\epsilon_i; r) Y_{lm}^*(\hat{\boldsymbol{r}}) Y_{l'm}(\hat{\boldsymbol{r}}). \end{aligned} \tag{3.39}$$

Again, using the expansion

$$n_B(\boldsymbol{r}) = \sum_\nu n_\nu^B(r) P_\nu(\cos\theta) \tag{3.40}$$

and

$$\int P_l(\cos\theta) P_{l'}(\cos\theta)\, \mathrm{d}(\cos\theta) = \frac{2}{2l+1} \delta_{l,l'} \tag{3.41}$$

we have (suppressing the bound state index i)

$$\begin{aligned} n_\nu^B(r) &= \frac{2\nu+1}{4\pi}\int P_\nu(\cos\theta) n_B(\boldsymbol{r})\,\mathrm{d}\hat{\boldsymbol{r}} \\ &= \frac{2\nu+1}{4\pi r^2}\sum_{ll'm}\int Y_{lm}^*(\hat{\boldsymbol{r}})P_\nu(\cos\theta)Y_{l'm}(\hat{\boldsymbol{r}})u_{lm}(\epsilon;r)u_{l'm}(\epsilon;r)\,\mathrm{d}\hat{\boldsymbol{r}} \\ &= \frac{1}{4\pi r^2}\sum_{ll'm}\begin{Bmatrix} l & l' & \nu \\ m & -m & 0 \end{Bmatrix} u_{lm}(\epsilon;r)u_{l'm}(\epsilon;r) \\ &= \frac{1}{4\pi r^2}\sum_{ll'm}\begin{Bmatrix} l & l' & \nu \\ m & -m & 0 \end{Bmatrix} \sum_j \mu_j^m(\epsilon)u_{lm}^{(j)}(\epsilon;r)\sum_{j'}\mu_{j'}^m(\epsilon)u_{l'm}^{(j')}(\epsilon;r). \end{aligned} \tag{3.42}$$

If we no longer suppress the spin degree of freedom, for the total bound electron density for a given ν and a given spin σ, we have

$$n_{\nu\sigma}^B(r) = \frac{1}{4\pi r^2}\sum_{ll'm}\begin{Bmatrix} l & l' & \nu \\ m & -m & 0 \end{Bmatrix} \sum_{jj'}\mu_j^{m\sigma}(\epsilon)\mu_{j'}^{m\sigma}(\epsilon)u_{lm}^{(j)\sigma}(\epsilon;r)u_{l'm}^{(j')\sigma}(\epsilon;r) \tag{3.43}$$

with

$$n_B(\boldsymbol{r}) = \sum_{\nu\sigma} n_{\nu\sigma}^B(r)P_\nu(\cos\theta). \tag{3.44}$$

The total bound electron density can be found by summing the density over all occupied bound states since the Kohn-Sham formulation is a single-particle model.

3.2 Determination of the Potential

3.2.1 Hartree Potential

The Hartree potential is given by the solution to Poisson's equation as

$$v_H(\boldsymbol{r}) = -e\int \frac{\rho_{tot}(\boldsymbol{r}')}{|\boldsymbol{r}-\boldsymbol{r}'|}\,\mathrm{d}\boldsymbol{r}'.$$

where $\rho_{tot}(\boldsymbol{r})$ is the *total* charge density, including the positive 'jellium' background.

$$\begin{aligned} \rho_{total}(\boldsymbol{r}) &= \rho_{0,+} + \rho_{0,-} + \Delta\rho(\boldsymbol{r}) \\ &= e\left(n_0 - n_0 - \Delta n(\boldsymbol{r})\right) \end{aligned} \tag{3.45}$$

where n_0 is the background density and $\Delta n(\boldsymbol{r})$ is the total (bound and scattered) induced electron density due to the presence of the impurity. Since the positive background density is equal in magnitude and opposite in sign to the negative charge of the homogenous electron gas, these two contributions to the Hartree energy cancel out to give

$$v_H(\boldsymbol{r}) = e^2 \int \frac{\Delta n(\boldsymbol{r}')}{|\boldsymbol{r} - \boldsymbol{r}'|}\, \mathrm{d}\boldsymbol{r}'. \tag{3.46}$$

Using the expansion [35]

$$\frac{1}{|\boldsymbol{r} - \boldsymbol{r}'|} = 4\pi \sum_{lm} \frac{1}{2l+1} \frac{r_<^l}{r_>^{l+1}} Y_{lm}(\hat{\boldsymbol{r}}) Y_{lm}^*(\hat{\boldsymbol{r}}') \tag{3.47}$$

and the expansion of the density permitted by cylindrical symmetry

$$\Delta n(\boldsymbol{r}) = \sum_{\nu} \Delta n_\nu(r) P_\nu(\cos\theta) \tag{3.48}$$

we obtain the Hartree potential as

$$v_H(\boldsymbol{r}) = 4\pi e^2 \int \sum_{l\nu m} r'^2 \frac{\Delta n_\nu(r')}{2l+1} \frac{r_<^l}{r_>^{l+1}}\, \mathrm{d}r'\, Y_{lm}(\hat{\boldsymbol{r}}) \int Y_{lm}^*(\hat{\boldsymbol{r}}') P_\nu(\cos\theta')\, \mathrm{d}\hat{\boldsymbol{r}}'. \tag{3.49}$$

Using the fact that [36]

$$P_l(\cos\theta) = \sqrt{\frac{4\pi}{2l+1}} Y_{l0}(\hat{\boldsymbol{r}}) \tag{3.50}$$

the Hartree potential becomes

$$\begin{aligned}
v_H(\boldsymbol{r}) &= 4\pi e^2 \int dr' \sum_{l\nu m} r'^2 \frac{\Delta n_\nu(r')}{2l+1} \sqrt{\frac{2\nu+1}{4\pi}} \frac{r_<^l}{r_>^{l+1}} Y_{lm}(\hat{\boldsymbol{r}}) \int \mathrm{d}\hat{\boldsymbol{r}}' Y_{lm}^*(\hat{\boldsymbol{r}}') Y_{\nu 0}(\hat{\boldsymbol{r}}') \\
&= 4\pi e^2 \int dr' \sum_{l\nu m} r'^2 \frac{\Delta n_\nu(r')}{2l+1} \sqrt{\frac{2\nu+1}{4\pi}} \frac{r_<^l}{r_>^{l+1}} Y_{lm}(\hat{\boldsymbol{r}}) \delta_{l,\nu} \delta_{m,0} \\
&= 4\pi e^2 \int dr' \sum_{\nu} r'^2 \frac{\Delta n_\nu(r')}{2\nu+1} \sqrt{\frac{2\nu+1}{4\pi}} \frac{r_<^\nu}{r_>^{\nu+1}} Y_{\nu 0}(\hat{\boldsymbol{r}}) \\
&= 4\pi e^2 \int dr' \sum_{\nu} r'^2 \frac{\Delta n_\nu(r')}{2\nu+1} \frac{r_<^\nu}{r_>^{\nu+1}} P_\nu(\cos\theta).
\end{aligned} \tag{3.51}$$

It can be seen that the cylindrical symmetry of the Hartree potential arises naturally from the cylindrical symmetry of the density and thus the l-th (ν-th) component is given as

$$v_\nu^H(r) = \frac{4\pi e^2}{2\nu+1} \int r'^2 \Delta n_\nu(r') \frac{r_<^\nu}{r_>^{\nu+1}}\, \mathrm{d}r' \tag{3.52}$$

with the total Hartree potential given as

$$v_H(\boldsymbol{r}) = \sum_\nu v_\nu^H(r) P_\nu(\cos\theta). \tag{3.53}$$

Note that the induced density $\Delta n(\boldsymbol{r})$ and the Hartree potential $v_H(\boldsymbol{r})$ do not depend on the azimuthal coordinate ϕ and are therefore real.

3.2.2 Exchange-Correlation Potential

The exchange-correlation potential $v_{xc}(\boldsymbol{r})$ is proportional to fractional powers of the density and the logarithm of fractional powers of the density and so it is not easy to project out the l-th component, see Eq. (2.89). Thus, for the l-th (ν-th) component, one has to evaluate the integral

$$v_\nu^{xc}(r) = \frac{2\nu+1}{2} \int v_{xc}(\boldsymbol{r})\, P_\nu(\cos\theta)\, \mathrm{d}(\cos\theta). \tag{3.54}$$

However, it is known that $v_{xc}(\boldsymbol{r})$ is cylindrically symmetric, and so it is a polynomial in $\cos\theta$ of order ν_{max} at most from

$$v_{xc}(\boldsymbol{r}) = \sum_\nu v_\nu^{xc}(r) P_\nu\left(\cos\theta\right). \tag{3.55}$$

Therefore, the integrand in (3.54) is a polynomial in $\cos\theta$ of order $2\,\nu_{max}$ at most and is given exactly by a Gauss-Legendre integral of order $\nu_{max}+1$

$$v_\nu^{xc}(r) = \sum_{i=1}^{\nu_{max}+1} \frac{2\nu+1}{2} w_i P_\nu(x_i) v_{xc}(r, \cos^{-1} x_i) \tag{3.56}$$

where w_i and x_i are the weights and pivots, respectively, of a Gauss-Legendre integral of order $\nu_{max}+1$.

Once the Hartree and exchange-correlation potentials have been found, the total effective potential is calculated as

$$v^+(\boldsymbol{r}) = v_{ext}(\boldsymbol{r}) + v_H(\boldsymbol{r}) + v_{xc}^+(\boldsymbol{r}) \tag{3.57}$$

for spin up electrons, and

$$v^{-}(\boldsymbol{r}) = v_{ext}(\boldsymbol{r}) + v_H(\boldsymbol{r}) + v_{xc}^{-}(\boldsymbol{r}) \tag{3.58}$$

for spin down electrons where $v_{ext}(\boldsymbol{r})$ is the external potential from the impurity nucleus, $v_H(\boldsymbol{r})$ is the Hartree potential and $v_{xc}^{+}(\boldsymbol{r})$ and $v_{xc}^{-}(\boldsymbol{r})$ are the exchange-correlation potentials for spin up and spin down electrons, respectively.

3.3 Phase Shifts

3.3.1 Derivation of phase shifts

If we return to the expression for a scattered wave function, Eq. (3.12)

$$R_{lm}^{(j)}(k;r) = \frac{u_{lm}^{(j)}(k;r)}{kr} \longrightarrow_{r\to\infty} [A_{lj}^{m}(k) j_l(kr) + B_{lj}^{m}(k) n_l(kr)]$$

we can use the asymptotic limits [36]

$$j_l(kr) \simeq \frac{1}{kr}\sin(kr - l\frac{\pi}{2}) \qquad \text{for} \quad kr \gg l \tag{3.59a}$$

$$n_l(kr) \simeq \frac{-1}{kr}\cos(kr - l\frac{\pi}{2}) \qquad \text{for} \quad kr \gg l \tag{3.59b}$$

to write

$$\frac{u_{lm}^{(j)}(k;r)}{kr} = A_{lj}^{m}(k)\frac{\sin(kr - l\frac{\pi}{2})}{kr} - B_{lj}^{m}(k)\frac{\cos(kr - l\frac{\pi}{2})}{kr} \qquad \text{for} \quad kr \gg l \tag{3.60}$$

which is identical for the spherical case,

$$\frac{u_l(k;r)}{kr} = A_l(k)\frac{\sin(kr - l\frac{\pi}{2})}{kr} - B_l(k)\frac{\cos(kr - l\frac{\pi}{2})}{kr} \qquad \text{for} \quad kr \gg l. \tag{3.61}$$

This expression can be written as

$$\frac{u_l(k;r)}{kr} \simeq \frac{1}{kr}\sin(kr - l\frac{\pi}{2} + \delta_l(k)) \qquad \text{for} \quad kr \gg l \tag{3.62}$$

with

$$-\tan\delta_l(k) = \frac{B_l(k)}{A_l(k)}. \tag{3.63}$$

Since

$$\frac{u_l(k;r)}{kr} = j_l(kr) \simeq \frac{1}{kr}\sin(kr - l\frac{\pi}{2}) \qquad \text{for} \quad kr \gg l \tag{3.64}$$

is the solution to the radial equations, Eq. (3.5), for $v(\boldsymbol{r}) = 0$, one can see that the effect of the potential $v(\boldsymbol{r})$ is to produce a *phase shift* $\delta_l(k)$ in the radial wavefunction.

To obtain the phase shifts $\delta_{lm}(k)$ for the nonspherical case, we first note that the immersion system can be viewed as a scattering problem. The nonspherical scattering S-matrix can be found from the scattering coefficients obtained previously [33, 34]

$$\boldsymbol{S}^m(k) = [\boldsymbol{A}^m(k) + i\boldsymbol{B}^m(k)]\boldsymbol{\Gamma}^m(k) \tag{3.65}$$

or

$$\boldsymbol{S}^m(k) = [\boldsymbol{A}^m(k) + i\boldsymbol{B}^m(k)][\boldsymbol{A}^m(k) - i\boldsymbol{B}^m(k)]^{-1}. \tag{3.66}$$

If we define the matrix $\boldsymbol{D}^m(k)$ by

$$\boldsymbol{S}^m(k) = e^{-2i\boldsymbol{D}^m(k)} \tag{3.67}$$

the phase shifts $\delta_{lm}(k)$ of the nonspherical continuum states, Eq. (3.8), are the eigenvalues of $\boldsymbol{D}^m(k)$. Equivalently, the phase shifts are equal to the phase of the (complex) eigenvalues of (unitary) $\mathbf{S}^m(k)$. Physically meaningful quantities, such as the density of states induced in the gas by the impurity can be calculated from the phase shifts.

We can show that the definition of the nonspherical phase shift given above reduces to the definition for the spherical case, Eq. (3.63). We first note that if $\boldsymbol{A}^m(k)$ and $\boldsymbol{B}^m(k)$ are diagonal real matrices, that $\boldsymbol{A}^m(k) + i\boldsymbol{B}^m(k)$ is a diagonal complex matrix and therefore $\boldsymbol{\Gamma}^m(k) = [\boldsymbol{A}^m(k) - i\boldsymbol{B}^m(k)]^{-1}$ is a diagonal complex matrix. We can see then that $\boldsymbol{S}^m(k)$ is also a diagonal complex matrix.

We have

$$\boldsymbol{S}^m(k) = \frac{[\boldsymbol{A}^m(k) + i\boldsymbol{B}^m(k)]}{[\boldsymbol{A}^m(k) - i\boldsymbol{B}^m(k)]} \tag{3.68}$$

$$= \frac{[\boldsymbol{A}^m(k) + i\boldsymbol{B}^m(k)]}{[\boldsymbol{A}^m(k) - i\boldsymbol{B}^m(k)]} \frac{[\boldsymbol{A}^m(k) + i\boldsymbol{B}^m(k)]}{[\boldsymbol{A}^m(k) + i\boldsymbol{B}^m(k)]} \tag{3.69}$$

$$= \frac{\boldsymbol{A}^m(k)^2 + 2i\boldsymbol{A}^m(k)\boldsymbol{B}^m(k) - \boldsymbol{B}^m(k)^2}{\boldsymbol{A}^m(k)^2 + \boldsymbol{B}^m(k)^2} \tag{3.70}$$

$$= e^{-2i\boldsymbol{D}^m(k)} \tag{3.71}$$

$$= \cos\left(2\boldsymbol{D}^m(k)\right) - i\sin\left(2\boldsymbol{D}^m(k)\right). \tag{3.72}$$

We can see that

$$\cos 2\boldsymbol{D}^m(k) = \frac{\boldsymbol{A}^m(k)^2 - \boldsymbol{B}^m(k)^2}{\boldsymbol{A}^m(k)^2 + \boldsymbol{B}^m(k)^2} \tag{3.73}$$

and

$$\sin 2\boldsymbol{D}^m(k) = \frac{-2\boldsymbol{A}^m(k)\boldsymbol{B}^m(k)}{\boldsymbol{A}^m(k)^2 + \boldsymbol{B}^m(k)^2}. \tag{3.74}$$

We can then use the double-angle formulas

$$\cos 2\theta = \cos^2\theta - \sin^2\theta \tag{3.75}$$

and

$$\sin 2\theta = 2\cos\theta\sin\theta \tag{3.76}$$

to write

$$\cos \boldsymbol{D}^m(k) = \frac{\boldsymbol{A}^m(k)}{\boldsymbol{A}^m(k)^2 + \boldsymbol{B}^m(k)^2} \tag{3.77}$$

and

$$\sin \boldsymbol{D}^m(k) = \frac{-\boldsymbol{B}^m(k)}{\boldsymbol{A}^m(k)^2 + \boldsymbol{B}^m(k)^2}. \tag{3.78}$$

We can therefore write

$$\tan \boldsymbol{D}^m(k) = \frac{\sin \boldsymbol{D}^m(k)}{\cos \boldsymbol{D}^m(k)} = \frac{-\boldsymbol{B}^m(k)}{\boldsymbol{A}^m(k)}. \tag{3.79}$$

Because the matrices are diagonal we can write

$$-\tan \delta_{lm}(k) = \frac{B_{lm}(k)}{A_{lm}(k)} \tag{3.80}$$

where $A_{lm}(k)$, $B_{lm}(k)$, and $\delta_{lm}(k)$ are the diagonal elements of $\boldsymbol{A}^m(k)$, $\boldsymbol{B}^m(k)$, and $\boldsymbol{D}^m(k)$, respectively. This is identical to the definition of the phase shift, Eq. (3.63), presented for the spherical case, but with the m dependence now made explicit for the nonspherical case.

3.3.2 Induced density of states in terms of phase shifts

To derive the density of induced states from phase shifts, the following argument is taken from [15]. If one imagines a very large sphere of radius r_∞, one can argue that r_∞ can be made as large as necessary to contain all charges within it. As $r_\infty \to \infty$, $v(r_\infty) \to 0$ and, therefore, the wavefunctions for scattered states must vanish at r_∞. Using Eq. (3.59) and Eq. (3.60), the boundary condition for free and scattered states can be written as

$$\sum_{lm} \left[kr_\infty - l\frac{\pi}{2} \right] = n_{free}\pi \tag{3.81}$$

and

$$\sum_{lm} \left[kr_\infty - l\frac{\pi}{2} + \delta_{lm}(k) \right] = n_{scatt}\pi. \tag{3.82}$$

It can be assumed that k is continuous since, for a very large radius r_∞, $kr_\infty \gg l$. We can then calculate the number of states induced in the gas $\Delta D(k)$ by the presence of the impurity. If the spin degree of freedom is not suppressed, we have

$$\Delta D(k) = \frac{\mathrm{d}(n_{scatt} - n_{free})}{\mathrm{d}k} = \frac{1}{\pi} \sum_{lm\sigma} \frac{\mathrm{d}\delta^\sigma_{lm}(k)}{\mathrm{d}k}. \tag{3.83}$$

3.4 Energy calculation

We now turn to the details of implementing Eq. (2.28) for the immersion system. First, we define the immersion energy as the energy difference between the free atom / homogeneous electron gas system and the impurity system, in which the atom is immersed in the electron gas.

$$E_{imm} = E_{imp} - E_{hom} - E_{atom} \tag{3.84}$$

Eq. (2.50) can be used to obtain E_{atom} directly from a self-consistent free atom calculation. We must then calculate the difference in energy $E_{imp} - E_{hom}$ for the homogeneous and impurity systems. This consists of the induced kinetic, electrostatic and exchange-correlation energies.

$$E_{imp} - E_{hom} = \Delta T + \Delta C + \Delta E_{xc} \tag{3.85}$$

3.4.1 Induced kinetic energy

The induced kinetic energy ΔT can be written similar to Eq. (2.36) as

$$\begin{aligned} \Delta T &= \sum_{i}^{N} \epsilon_i - \int n(\boldsymbol{r}) v(\boldsymbol{r}) \, \mathrm{d}\boldsymbol{r} \\ &= \Delta T_{bound} + \Delta T_{scatt} \end{aligned} \tag{3.86}$$

where the sum over i runs over *all* states not present in the homogeneous system, both bound and scattered. For bound states, we have

$$\Delta T_{bound} = \sum_{i}^{N_{bound}} \epsilon_i - \int n_B(\boldsymbol{r}) v(\boldsymbol{r}) \, \mathrm{d}\boldsymbol{r} \tag{3.87}$$

where the sum only runs over occupied bound states and n_B is the total bound electron density. Since the wave number k is continous, we have for scattered states

$$\Delta T_{scatt} = \int_0^{k_F} k^2 \Delta D(k) \, \mathrm{d}k - \int n_C(\boldsymbol{r}) v(\boldsymbol{r}) \, \mathrm{d}\boldsymbol{r} \tag{3.88}$$

where $\Delta D(k)$ is the density of states induced in the gas by the presence of the impurity and n_C is the total electron density in the continuum or conduction band.

In the previous two sections, the phase shifts of the radial wave functions were examined. The phase shifts are used to calculate the induced density of states in the electron gas, which appears in the induced kinetic energy above. So, using Eq. (3.83) and

$E = k^2$, the first term in Eq. (3.88) can be rewritten, using integration by parts, as

$$\begin{aligned}\int_0^{k_F} k^2 \Delta D(k)\,\mathrm{d}k &= \frac{1}{\pi}\int_0^{k_F} k^2 \sum_{lm\sigma} \frac{\mathrm{d}\delta^\sigma_{lm}(k)}{\mathrm{d}k}\,\mathrm{d}k \\ &= \frac{1}{\pi}\sum_{lm\sigma}\int_0^{E_F} E\frac{\mathrm{d}\delta^\sigma_{lm}(E)}{\mathrm{d}E}\,\mathrm{d}E \\ &= \frac{1}{\pi}\sum_{lm\sigma} E_F\delta^\sigma_{lm}(E_F) - \frac{1}{\pi}\sum_{lm\sigma}\int_0^{E_F}\delta^\sigma_{lm}(E)\,\mathrm{d}E. \end{aligned} \tag{3.89}$$

Adding the contributions from the bound and scattered states together, we have

$$\begin{aligned}\Delta T = &\sum_i^{N_{bound}} \epsilon_i - \int n(\boldsymbol{r})v(\boldsymbol{r})\,\mathrm{d}\boldsymbol{r} \\ &+ \frac{1}{\pi}\sum_{lm\sigma} E_F\delta^\sigma_{lm}(E_F) - \frac{1}{\pi}\sum_{lm\sigma}\int_0^{E_F}\delta^\sigma_{lm}(E)\,\mathrm{d}E \end{aligned} \tag{3.90}$$

with $n(\boldsymbol{r}) = n_B(\boldsymbol{r}) + n_C(\boldsymbol{r})$. To calculate the second term in ΔT, we first write it as

$$\begin{aligned}\int n(\boldsymbol{r})v(\boldsymbol{r})\,\mathrm{d}\boldsymbol{r} &= \int n(\boldsymbol{r})(v_{ext}(\boldsymbol{r}) + v_H(\boldsymbol{r}) + v_{xc}(\boldsymbol{r}))\,\mathrm{d}\boldsymbol{r} \\ &= \int n(\boldsymbol{r})v_{ext}(\boldsymbol{r})\,\mathrm{d}\boldsymbol{r} + \int n(\boldsymbol{r})v_H(\boldsymbol{r})\,\mathrm{d}\boldsymbol{r} + \int n(\boldsymbol{r})v_{xc}(\boldsymbol{r})\,\mathrm{d}\boldsymbol{r}. \end{aligned} \tag{3.91}$$

We again expand $v_H(\boldsymbol{r})$ and $v_{xc}(\boldsymbol{r})$ as

$$v_H(\boldsymbol{r}) = \sum_\nu v^H_\nu(r)P_\nu(\cos\theta) \tag{3.92}$$

and

$$v_{xc}(\boldsymbol{r}) = \sum_\nu v^{xc}_\nu(r)P_\nu(\cos\theta) \tag{3.93}$$

to write the second and third terms of Eq. (3.91) as

$$\begin{aligned}\int v_H(\boldsymbol{r})n(\boldsymbol{r})\,\mathrm{d}\boldsymbol{r} &= \int \sum_\nu v^H_\nu(r)P_\nu(\cos\theta)\sum_{\nu'} n_{\nu'}(r)P_{\nu'}(\cos\theta)r^2\sin\theta\,\mathrm{d}r\,\mathrm{d}\theta\,\mathrm{d}\phi \\ &= \sum_{\nu\nu'}\int \mathrm{d}\phi\int P_\nu(\cos\theta)P_{\nu'}(\cos\theta)\,\mathrm{d}(\cos\theta)\int v^H_\nu(r)n_{\nu'}(r)r^2\,\mathrm{d}r \\ &= \sum_\nu \frac{4\pi}{2\nu+1}\int v^H_\nu(r)n_\nu(r)r^2\,\mathrm{d}r \end{aligned} \tag{3.94}$$

and

$$\begin{aligned}\int v_{xc}(\boldsymbol{r})n(\boldsymbol{r})\,\mathrm{d}\boldsymbol{r} &= \int \sum_{\nu} v_{\nu}^{xc}(r)P_{\nu}(\cos\theta)\sum_{\nu'} n_{\nu'}(r)P_{\nu'}(\cos\theta)r^2\sin\theta\,\mathrm{d}r\,\mathrm{d}\theta\,\mathrm{d}\phi \\ &= \sum_{\nu\nu'}\int \mathrm{d}\phi\int P_{\nu}(\cos\theta)P_{\nu'}(\cos\theta)\,\mathrm{d}(\cos\theta)\int v_{\nu}^{xc}(r)n_{\nu'}(r)r^2\,\mathrm{d}r \\ &= \sum_{\nu}\frac{4\pi}{2\nu+1}\int v_{\nu}^{xc}(r)n_{\nu}(r)r^2\,\mathrm{d}r. \end{aligned} \tag{3.95}$$

As for the external potential term, we use $P_0(\cos\theta)=1$ to write

$$\int P_l(\cos\theta)\,\mathrm{d}(\cos\theta) = \int P_l(\cos\theta)P_0(\cos\theta)\,\mathrm{d}(\cos\theta)) = \frac{2}{2l+1}\delta_{l,0} = 2$$

and therefore

$$\begin{aligned}\int n(\boldsymbol{r})v_{ext}(\boldsymbol{r})\,\mathrm{d}\boldsymbol{r} &= -Ze^2\int\frac{n(\boldsymbol{r})}{r}\,\mathrm{d}\boldsymbol{r} \\ &= -Ze^2\int\mathrm{d}\phi\int\sin\theta\,\mathrm{d}\theta\int r^2\,\mathrm{d}r\frac{1}{r}\sum_{\nu}n_{\nu}(r)P_{\nu}(\cos\theta) \\ &= -Z4\pi e^2\sum_{\nu}\int n_{\nu}(r)\delta_{\nu,0}r\,\mathrm{d}r \\ &= -Z4\pi e^2\int n_0(r)r\,\mathrm{d}r. \end{aligned} \tag{3.96}$$

We can then write Eq. (3.91) as

$$\int n(\boldsymbol{r})v(\boldsymbol{r})\,\mathrm{d}\boldsymbol{r} = \sum_{\nu}\frac{4\pi}{2\nu+1}\int\left[\left(v_{\nu}^{H}(r)+v_{\nu}^{xc}(r)\right)r^2 - Ze^2r\,\delta_{\nu,0}\right]n_{\nu}(r)\,\mathrm{d}r \tag{3.97}$$

and the induced kinetic energy can finally be written as

$$\begin{aligned}\Delta T = &\sum_{i}^{N_{bound}}\epsilon_i - \sum_{\nu}\frac{4\pi}{2\nu+1}\int\left[\left(v_{\nu}^{H}(r)+v_{\nu}^{xc}(r)\right)r^2 - Ze^2r\delta_{\nu,0}\right]n_{\nu}(r)\,\mathrm{d}r \\ &+\frac{1}{\pi}\sum_{lm\sigma}E_F\delta_{lm}^{\sigma}(E_F) - \frac{1}{\pi}\sum_{lm\sigma}\int_0^{E_F}\delta_{lm}^{\sigma}(E)\,\mathrm{d}E. \end{aligned} \tag{3.98}$$

3.4.2 Induced electrostatic energy

To calculate the induced electrostatic energy ΔC, we first note that the homogeneous background density contribution exactly cancels the positive jellium contribution (see Sec.

3.2.1) to give

$$\begin{aligned}\Delta C &= \frac{1}{2}e^2 \int \frac{\Delta n(\boldsymbol{r})\Delta n(\boldsymbol{r}')}{|\mathbf{r}-\mathbf{r}'|}\,\mathrm{d}\boldsymbol{r}\,\mathrm{d}\boldsymbol{r}' - e\int \Delta n(\boldsymbol{r}) v_{ext}(\boldsymbol{r})\,\mathrm{d}\boldsymbol{r} \\ &= \int \left(\frac{1}{2}v_H(\boldsymbol{r}) - \frac{Ze^2}{r}\right)\Delta n(\boldsymbol{r})\,\mathrm{d}\boldsymbol{r} \\ &= \Delta C_H + \Delta C_Z \end{aligned} \tag{3.99}$$

where $v_H(\boldsymbol{r})$ is given by Eq. (3.46) and $\Delta n(\boldsymbol{r}) = n(\boldsymbol{r}) - n_0$ is the induced electron density due to the presence of the impurity. The first term ΔC_H is the direct Coulomb interaction between the electrons (which is positive and therefore increases the total system energy) and the second term ΔC_Z is the the direct Coulomb interaction between the electrons and the external potential due to the impurity nucleus (which is negative and therefore lowers the total system energy). Using Eq. (3.48), Eq. (3.53) and

$$\int P_l(\cos\theta)P_{l'}(\cos\theta)\,\mathrm{d}(\cos\theta) = \frac{2}{2l+1}\delta_{ll'}$$

we have

$$\begin{aligned}\Delta C_H &= \frac{1}{2}\int v_H(\boldsymbol{r})\Delta n(\boldsymbol{r})\,\mathrm{d}\boldsymbol{r} \\ &= \frac{1}{2}\int \sum_{\nu} v_\nu^H(r)P_\nu(\cos\theta)\sum_{\nu'}\Delta n_{\nu'}(r)P_{\nu'}(\cos\theta)r^2\sin\theta\,\mathrm{d}r\,\mathrm{d}\theta\,\mathrm{d}\phi \\ &= \frac{1}{2}\sum_{\nu\nu'}\int \mathrm{d}\phi\int P_\nu(\cos\theta)P_{\nu'}(\cos\theta)\,\mathrm{d}(\cos\theta)\int v_\nu^H(r)\Delta n_{\nu'}(r)r^2\,\mathrm{d}r \\ &= \frac{1}{2}\sum_{\nu}\frac{4\pi}{2\nu+1}\int v_\nu^H(r)\Delta n_\nu(r)r^2\,\mathrm{d}r \end{aligned} \tag{3.100}$$

where

$$\Delta n_\nu(r) = n_\nu^B(r) + \Delta n_\nu^C(r) \tag{3.101}$$

and where $n_\nu^B(r)$ is given by Eq. (3.42) and $\Delta n_\nu^C(r)$ is given by Eq. (3.33).

Similarly, the second term can be written as

$$\begin{aligned}\Delta C_Z &= -Ze^2 \int \frac{\Delta n(\boldsymbol{r})}{r}\,\mathrm{d}\boldsymbol{r} \\ &= -Z4\pi e^2 \sum_\nu \int \Delta n_\nu(r)\delta_{\nu,0} r\,\mathrm{d}r \\ &= -Z4\pi e^2 \int \Delta n_0(r) r\,\mathrm{d}r \end{aligned} \tag{3.102}$$

giving, for the induced electrostatic energy,

$$\Delta C = \sum_\nu \frac{4\pi}{2\nu+1} \int \left(\frac{1}{2} v_\nu^H(r) r^2 - Ze^2 r \delta_{\nu,0}\right) \Delta n_\nu(r)\,\mathrm{d}r \tag{3.103}$$

where $v_\nu^H(r)$ is again given by Eq. (3.46) and $\Delta n_\nu(r)$ by the sum of Eq. (3.33) and Eq. (3.42).

3.4.3 Induced exchange-correlation energy

The induced exchange-correlation energy is given by

$$\Delta E_{xc} = E_{xc}[n_+, n_-] - E_{xc}[n_0] \tag{3.104}$$

with $E_{xc}[n_+, n_-]$ given in the LSDA by

$$\begin{aligned} E_{xc}[n_+, n_-] &= E_{xc}[n(\boldsymbol{r}), \zeta(\boldsymbol{r})] \\ &= \int \epsilon_{xc}\left(n(\boldsymbol{r}), \zeta(\boldsymbol{r})\right) n(\boldsymbol{r})\,\mathrm{d}\boldsymbol{r} \\ &= \int \sum_\nu \epsilon_\nu^{xc}(r) P_\nu(\cos\theta) \sum_{\nu'} n_{\nu'}(r) P_{\nu'}(\cos\theta) r^2 \sin\theta\,\mathrm{d}r\,\mathrm{d}\theta\,\mathrm{d}\phi \\ &= \sum_{\nu\nu'} \int \mathrm{d}\phi \int P_\nu(\cos\theta) P_{\nu'}(\cos\theta)\,\mathrm{d}(\cos\theta) \int \epsilon_\nu^{xc}(r) n_{\nu'}(r) r^2\,\mathrm{d}r \\ &= \sum_\nu \frac{4\pi}{2\nu+1} \int \epsilon_\nu^{xc}(r) n_\nu(r) r^2\,\mathrm{d}r \end{aligned} \tag{3.105}$$

where we have suppressed the explicit dependence of the exchange correlation energy on the local density and local spin-polarization

$$\epsilon_{xc}\left(n(\boldsymbol{r}), \zeta(\boldsymbol{r})\right) \to \epsilon_{xc}(\boldsymbol{r}) \tag{3.106}$$

For the same reason as for the exhange-correlation potential (see Eq.'s (3.54) and (3.56)) the partial-wave components of the exchange-correlation energy are calculated as

$$\epsilon_\nu^{xc}(r) = \frac{2\nu+1}{2}\int \epsilon_{xc}(\boldsymbol{r})\, P_\nu(\cos\theta)\,\mathrm{d}(\cos\theta). \tag{3.107}$$

We therefore write

$$\epsilon_\nu^{xc}(r) = \sum_{i=1}^{\nu_{max}+1} \frac{2\nu+1}{2} w_i P_\nu(x_i)\epsilon_{xc}(r,\cos^{-1}x_i). \tag{3.108}$$

$E_{xc}[n_0]$ is given by

$$\begin{aligned} E_{xc}[n_0] &= \int \epsilon_{xc}\left(n_0(\boldsymbol{r}),\zeta_0(\boldsymbol{r})\right) n_0(\boldsymbol{r})\,\mathrm{d}\boldsymbol{r} \\ &= 4\pi\epsilon_{xc}(n_0)n_0\int r^2\,\mathrm{d}r \\ &= \epsilon_{xc}(n_0)N \end{aligned} \tag{3.109}$$

which gives the induced exchange-correlation energy as

$$\Delta E_{xc} = \sum_\nu \frac{4\pi}{2\nu+1}\int \left[\epsilon_\nu^{xc}(r)n_\nu(r) - \epsilon_{xc}(n_0)n_0\delta_{\nu,0}\right] r^2\,\mathrm{d}r. \tag{3.110}$$

The immersion energy can finally be written as

$$\begin{aligned} E_{imm} = &\sum_i^{N_B}\epsilon_i + \frac{1}{\pi}\sum_{lm\sigma} E_F\delta_{lm}^\sigma(E_F) - \frac{1}{\pi}\sum_{lm\sigma}\int_0^{E_F}\delta_{lm}^\sigma(E)\,\mathrm{d}E \\ &- \sum_\nu \frac{4\pi}{2\nu+1}\int\left[\left(v_\nu^H(r)+v_\nu^{xc}(r)\right)r^2 - Ze^2r\delta_{\nu,0}\right]n_\nu(r)\,\mathrm{d}r \\ &+ \sum_\nu \frac{4\pi}{2\nu+1}\int\left(\frac{1}{2}v_\nu^H(r)r^2 - Ze^2r\delta_{\nu,0}\right)\Delta n_\nu(r)\,\mathrm{d}r \\ &+ \sum_\nu \frac{4\pi}{2\nu+1}\int\left[\epsilon_\nu^{xc}(r)n_\nu(r) - \epsilon_{xc}(n_0)n_0\delta_{\nu,0}\right]r^2\,\mathrm{d}r - E_{atom}. \end{aligned} \tag{3.111}$$

3.5 Friedel oscillations and the Friedel sum rule

Many of the attempts to circumvent the mathematical difficulties of the many-body problem have involved making various approximations to the screening effects that arise

in many-body systems. A series of publications by J. Friedel in the 1950's [6, 7, 8] showed that an impurity atom in an electron gas will induce oscillations in the electron density in the vicinity of the impurity.

The number of electrons induced in the gas can be found using Eq. (3.83).

$$\Delta N = Z = \int_0^{k_F} \Delta D(k)\,\mathrm{d}k = \int_0^{k_F} \frac{1}{\pi} \sum_{lm\sigma} \frac{\mathrm{d}\delta^\sigma_{lm}(k)}{\mathrm{d}k}\,\mathrm{d}k = \frac{1}{\pi} \sum_{lm\sigma} \delta^\sigma_{lm}(k_F) \tag{3.112}$$

This result is known as the Friedel sum rule and is a statement that the displaced electronic charge in the gas $\Delta N(-e)$ is equal in magnitude to the positive charge Ze of the impurity atom. For impurity systems such as those studied in this work, the displaced charge is essentially drawn in from a reservoir 'beyond (our numerical cutoff for) infinity' and the $1/r$ Coulomb potential of the impurity atom becomes screened by the displaced electronic charge and this charge density must be determined self-consistently.

Another result from the original work of Friedel is that the induced charge density in the vicinity of the impurity oscillates with a wavelength of $\lambda_{Friedel} \approx \pi/k_{Fermi}$. The Friedel sum rule and the Friedel oscillations will be verified in Chapter 5.

3.6 Electric polarizability

The linear dipole polarizability for spherically symmetric atoms has been calculated using perturbative methods in the work of Stott and Zaremba [4], Subbaswamy and Mahan [37], and Senatore and Subbaswamy [38, 39] for rare-gases, alkali-metal ions and other closed-shell metal atoms. For an overview of polarizability calculations within the context of the LDA in density functional theory, see [40].

In this work, we have direct access to calculating the dipole polarizability since we can calculate the polarization directly as

$$\boldsymbol{p} = -e \int \boldsymbol{r} n(\boldsymbol{r})\,\mathrm{d}\boldsymbol{r}. \tag{3.113}$$

Due to the cylindrical symmetry of the density, we again use the expansion

$$n(\boldsymbol{r}) = \sum n_\nu(r) P_\nu(\cos\theta). \tag{3.114}$$

We assume that the external field $\boldsymbol{E}$ is constant and has only a non-vanishing z-component, so that

$$\boldsymbol{E}(\boldsymbol{r}) = E_0\,\hat{z} \tag{3.115}$$

$$\text{and} \qquad \boldsymbol{p} = p\,\hat{z}. \tag{3.116}$$

The polarization can then be written as

$$\begin{aligned}
\boldsymbol{p} &= -e\int \boldsymbol{r} n(\boldsymbol{r})\,\mathrm{d}\boldsymbol{r} \;= p\hat{z} \\
\text{so} \qquad p &= -e\int z n(\boldsymbol{r})\,\mathrm{d}\boldsymbol{r} \\
&= -e\int r\cos\theta \sum_\nu n_\nu(r) P_\nu(\cos\theta)\, r^2 \sin\theta\,\mathrm{d}r\,\mathrm{d}\theta\,\mathrm{d}\phi \\
&= -e\int \mathrm{d}\phi \sum_\nu \int \cos\theta P_\nu(\cos\theta)\,\mathrm{d}(\cos\theta) \int n_\nu(r) r^3\,\mathrm{d}r \\
&= -2\pi e \sum_\nu \frac{2}{2\nu+1}\delta_{\nu,1}\int n_\nu(r) r^3\,\mathrm{d}r \\
&= -e\frac{4\pi}{3}\int n_1(r) r^3\,\mathrm{d}r
\end{aligned} \tag{3.117}$$

which is the required formula. If the external field E_0 is small, we can expand the polarization as a power series in the field

$$p_i = \sum_j \alpha^{(1)}_{ij} E_j + \sum_{jkl} \alpha^{(3)}_{ijkl} E_j E_k E_l + ... \tag{3.118}$$

or rather as

$$p = \alpha^{(1)} E_0 + \alpha^{(3)} E_0^3 + ... \tag{3.119}$$

so that the linear dipole polarizability can be calculated as

$$\alpha^{(1)} \simeq \frac{-4\pi e}{3E_0}\int n_1(r) r^3\,\mathrm{d}r \qquad \text{as} \quad E_0 \to 0. \tag{3.120}$$

The linear electric susceptibility is related to the linear polarizability by the relation

$$\chi^{(1)} = \frac{\alpha^{(1)}}{\epsilon_0} \tag{3.121}$$

where ϵ_0 is the *permittivity of free space*.

4. NUMERICAL IMPLEMENTATION

In this chapter, we discuss the implementation of the iterative procedure used to achieve self-consistent solutions for the systems analyzed and the numerical errors which arise at various points in the calculations.

In this work, there arise a variety of problems which cannot be dealt with by analytic methods alone and we are forced to implement numerical solutions to these problems. This is most prominent in the solution of coupled differential equations such as Eq.'s (3.5). As analytic forms for the solutions are not known, differentiation and integration of the functions must also be performed numerically. When utilizing a computer to perform these tasks, we must inevitably address the limits of the numerical techniques employed and the errors which arise. In the case of the tasks stated above, the most obvious problem comes from the finite (discrete) differences used to approximate infinitesimal (continous) differential elements. Depending on the nature of the nonlinearities inherent in the equations to be solved, these errors can cause drastic deviations from the true physical solutions. These errors will be examined in detail in this chapter.

Another problem comes from the cutoff value used to approximate infinity. The most dramatic example of this shows up in the integral involved with calculating the Hartree potential $v_H(\boldsymbol{r})$ and is a result of the long range nature of the Coulomb interaction. The errors which appear in the Hartree potential can quickly cause instability in the iterative procedure of the Kohn-Sham scheme. In order to prevent this from happening and to ensure the stability of the procedure, we implement a numerical correction to the error in the Hartree potential based on analytic knowledge of its form. This is most important at the beginning of calculations when the densities and potentials are the furthest from self-consistency. Before we can discuss these problems, we must first explain the iterative procedure used.

4.1 Iterative scheme used to find self-consistent solutions

4.1.1 Non spin-polarized systems

To find a self-consistent solution to the Kohn-Sham equations, we employ an iterative scheme as shown in Fig. 4.1. It is performed as follows.

1. Start with a guess for the potential $v_{in}(\boldsymbol{r})$.
2. Use this potential in the Kohn-Sham equation and find the Kohn-Sham eigenstates $\psi(\boldsymbol{r})$ corresponding to this potential.
3. From these Kohn-Sham eigenstates, calculate the total density $n(\boldsymbol{r}) = |\psi(\boldsymbol{r})|^2$.
4. From the density, calculate the output potential $v_{out}(\boldsymbol{r})$. The external term is known analytically. The Hartree term is obtained from a solution of Poisson's equation. The exchange-correlation term comes from the chosen (LDA) parametrization.
5. Use a mixing scheme to find an appropriate input density from the output density $v_n^{out}(\boldsymbol{r}) \rightarrow v_{n+1}^{in}(\boldsymbol{r})$.
6. Iterate until self-consistency is achieved $\frac{\delta v(\boldsymbol{r})}{\delta n_{iter}} = 0$.

One could equivalently start with a guess for the initial density; however, the relative response of the potential in real space is much larger than that of the density. For this reason, it is more convenient to monitor variations in the potential. Self-consistency is achieved when the input and output potentials, for a given iteration, are the same to within some numerical threshold. The most obvious choice for this threshold is when further numerical precision of physical quantities of interest is no longer achieved by further iteration. In this work, we are primarily concerned with effects on the total energy, and so will use this to determine self-consistency. To quantify the degree of self-consistency,

we define the quantity

$$(\Delta V)^2 = \frac{1}{\Omega} \int \left[v_n^{in}(\boldsymbol{r}) - v_n^{out}(\boldsymbol{r}) \right]^2 d\mathbf{r}. \tag{4.1}$$

At self-consistency, $\Delta V = 0$, and so we can extrapolate to find values of physical quantities by appropriate fitting methods. For instance, it is known that the total energy should be a minimum with respect to variations in the potential; therefore, a plot of $E[n]$ vs. $(\Delta V)^2$ should be linear near self-consistency. The total energy can be found be extrapolating this linear plot to a zero value of $(\Delta V)^2$.

It was previously mentioned that the response of the potential is quite large to small variations of the density. This large response can cause the iterative procedure to become unstable very quickly (within a few iterations). This is particularly a problem at the begining of calculations. We must therefore filter this response by mixing the output potential with the previous input potential to find the next input potential. This will be discussed in Sec. 4.2.

4.1.2 Spin-polarized systems

In the spin-polarized formulation of LDA used in this work, the only practical difference from the non spin-polarized calculations is that for the spin-polarized systems, we keep track of two different sets of densities $n_+(\boldsymbol{r})$ and $n_-(\boldsymbol{r})$ and potentials $v^+(\boldsymbol{r})$ and $v^-(\boldsymbol{r})$ as explained in Sec. 2.2.4. We must therefore solve two different sets of Kohn-Sham equations, which doubles the calculation time. It is worthwhile to note that the only part of the potential that depends explicitly on the spin density is the exchange-correlation potential. The Coulomb potential is the same for both spin densities.

4.2 Potential mixing scheme

If we naïvely set the output potential $v^{out}(\boldsymbol{r})$ equal to the next input potential $v^{in}(\boldsymbol{r})$, the large response of the output potential will cause instability in the iterative procedure and we will not achieve self-consistency. To avoid this, we mix the output potential with the previous input potential to slow or filter this large response[5] so that self-consistency can be achieved.

The simplest way to construct the input potential is as follows

$$v^{in}_{n+1}(\boldsymbol{r}) = \alpha v^{out}_{n}(\boldsymbol{r}) + (1-\alpha)\, v^{in}_{n}(\boldsymbol{r}) \tag{4.2}$$

where α is just a constant that we must determine. In order to find the optimal value for α, we must balance two competing requirements. First, we would like α as small as possible to filter the large response of the potential and keep the iterative procedure stable. Second, we would like α as large as possible to speed up the convergence of the iterative procedure and thereby reduce computation time since computation time is a major limiting factor for the calculations performed in this work.

Another factor that needs to be taken into account regarding numerical convergence is the long range of the Coulomb interaction. The Friedel oscillations in the electron density fall off as $1/r^3$. This long range tail of the density oscillations is strongly coupled to variations in the electron density near the impurity. In order to suppress this strong response, we introduce an exponential mixing parameter in addition to the proportional mixing parameter of Eq. (4.2). This is given as

$$\alpha(r) = \alpha e^{-\beta r^2} \tag{4.3}$$

[5]Even though it is known [30] that for higher densities, the resopnse of the gas is smaller than for lower densities, it is still large enough to cause problems in the procedure.

so that our mixing scheme becomes

$$v_{n+1}^{in}(\boldsymbol{r}) = \alpha(r) v_n^{out}(\boldsymbol{r}) + (1 - \alpha(r))\, v_n^{in}(\boldsymbol{r}),$$

or rather

$$v_{n+1}^{in}(\boldsymbol{r}) = v_n^{in}(\boldsymbol{r}) + \alpha e^{-\beta r^2} \left[v_n^{out}(\boldsymbol{r}) - v_n^{in}(\boldsymbol{r}) \right]. \tag{4.4}$$

To speed up convergence, we want to make α large to allow a large change of density in the vicinity of the impurity, while we want to make β large to suppress the response of the tail of Friedel oscillations. However, to achieve convergence of the iterative procedure we want to make α and β both small. One strategy is to start with large values of α and β to avoid instability at the beginning of calculations. After some degree of self-consistency is achieved in the vicinity of the impurity, we can reduce the values of α and β. The values must be found by trial and error. It was found that initial values of 0.04 for α and 0.002 for β were suitable for most immersion calculations. For free atom calculations, a value of 0.5 was used for α and a value of 0 was used for β. It was found that a suitable value for $(\Delta V)^2$ at which to lower the values of α and β was around 10^{-8} - 10^{-9}. At that point α and β were both lowered by 50% or so.

Since we deal with nonspherical systems in this work, it is worthwhile to note that the spherical components of the densities and potentials are the most important as these correspond to the dominant features of the charge distribution. The higher order components cause small rearrangements of the otherwise spherical charge density. For this reason, it turns out to be necessary to filter or mix the spherical component only to stabilize the iterative procedure. This was not necessarily expected.

4.3 Energy eigenvalue search

4.3.1 Bound states

In this work, we study systems with nonspherical symmetry. As the systems under consideration still possess cylindrical symmetry, m_l (throughout and furthermore m) is still a good quantum number. n is also still a good quantum number as there is no coupling present that is strong enough to induce level crossing between primary shells. Since we neglect spin-orbit coupling and deal with spin up and spin down densities separately, m_s (throughout and furthermore σ) is also still a good quantum number. As discussed in Sec. 3.1, in the LSDA we must solve coupled radial equations where the coupling exists between different l-channels only. However, since the coupling again does not cause level crossing between shells, we can associate each individual eigenstate with an l quantum number corresponding to a diagonalization of the Hamiltonian in a new l'-basis. For this reason, we still refer to the individual eigenstates by n, l', m, and σ. We use the more common spectroscopic notation $1s^+$, $1s^-$, $2s^+$, etc. to distinguish eigenstates. If we analyze the nodal structure of the radial wave functions, we find that it is identical to that for the spherical systems, specifically $n_{nodes} = n - l' - 1$.

For a bare Coulomb potential, the lowest energy eigenvalue is given by $-Z^2/n^2$. Since the effect of screening always increases the energy eigenvalues by making the electrons less bound to the (now screened) impurity nucleus, we can use this value as a lower bound when searching for energy eigenvalues. For bound states, we can use a reference energy of zero for the upper energy bound since $\lim_{r\to\infty} v_{eff}(\boldsymbol{r}) = 0$.

The procedure used to find the energy eigenvalues in this work is referred to as the *bisection algorithm* [42]. To explain how it is implemented, we must first outline the basic details of the energy eigenvalue search.

We integrate Eq.'s (3.5) from $r = 0$ outward and from $r = \infty$ inward using the asymptotic limits given by Eq. (3.7). We can identify the bound state energy eigenvalues

with the energy values for which the determinant of Eq's. (3.38) is equal to zero. This condition is equivalent to enforcing the continuity of the radial wavefunction and its first derivative. So, to find the energy eigenvalues, we begin by dividing the total energy range between the upper and lower bounds stated above into discrete intervals and using the lower energy bound as our initial energy guess. We use successively higher energy values (those at the endpoints of the energy intervals just mentioned) as successive guesses and look for roots in the corresponding determinant by watching for an algebraic sign change of the determinant, computed for each energy guess. Once a root in the determinant has been found from it's sign change, we obtain further precision for the energy by using the bisection algorithm, which is now discussed.

When a root is found in the determinant of the system, Eq.'s (3.38), we use the two endpoints of that interval (in which the sign change occurred) as lower and upper bounds for the eigenvalue and try an energy halfway in between these values (the first bisection). If the determinant for the midpoint energy has the same algebraic sign as for the lower bound, then we know the eigenvalue must lie higher in energy and bisect the upper half of the first interval (the second bisection). If the determinant at the midpoint energy has the opposite algebraic sign as the lower bound, then the we know the eigenvalue must lie in the lower half of the first interval and bisect the lower half of the energy range instead (the second bisection). The bisection algorithm is repeated until the desired precision is obtained. Once a particular energy eigenvalue is found to within the desired precision, we continue the energy eigenvalue search from the upper bound of the original energy interval in which the first (n-th) eigenvalue was found. This search process is continued until we reach the upper absolute bound for the energy range or until we no longer need to search because all occupied eigenstates have been found. This process is repeated for each m and σ as we solve a separate set of equations, for coupled l-channels, for each value that m and σ can possess.

The bisection algorithm is not the most quickly converging algorithm, but it is easy to implement and *guaranteed* to converge. The number of decimal places of precision obtained is approximately equal to 2^N where N is the number of bisections performed.

As for the initial division of the total energy search range into discrete intervals, we must find an appropriate interval by trial and error. This is easy to accomplish since we know the nodal structure of the physical solutions and we can check that the lowest occupied eigenstates have been found.

It should also be stated that the choice of matching radius for the inward and outward integrations is important. We must use a value that is large enough to contain the oscillatory behavior near the impurity, but not so large as to begin mixing-in the linearly independent solution for the outward integration. This is due to the nature of the asymptotic behavior used to begin the integrations from zero. The asymptotic behavior of the radial wave functions for very large values of r is such that we begin the inward integration assuming an exponentially decaying solution in only one l-channel. The second, linearly independent solution will *always* eventually be mixed in because of the numerical roundoff errors which always occur in the integration. An obvious choice for this matching radius is the innermost classical turning point, since the oscillatory behavior of the radial wavefunction becomes exponentially decreasing at this point. However, due to the Friedel oscillations in the tail of the potentials, there could be a number of turning points. The actual value used does not matter as long as the diverging solutions are not mixed in. This can easily be verified by a visual inspection of the solution.

In this work, we found that a matching radius of $r_N = 2$ was the best choice[6]. When the matching radius was made much smaller ($r_N \approx 1$), large relative errors in the energy eigenvalues resulted. This is due to the larger (linear) r-mesh for the outer integration not being fine enough for the rapid density fluctuations near the impurity. If the matching

[6]The notation r_N was chosen for the number of points N on the inner mesh, which will be discussed in Sec. 4.4.1.1.

radius was made much larger than this ($r_N \approx 3$), it would cause the diverging solution to get mixed in and very large relative errors in the eigenvalues as well as large errors and discontinuities in the densities and potentials. The numerical errors caused by the finite interval size of the r-space mesh will be discussed in more detail in Sec. 4.4.1.

4.3.2 Scattered states

The immersion systems studied in this work extend to infinity. For this reason, the boundary conditions, Eq's. (3.81) and (3.82), are physically reasonable and appropriate for the purposes of deriving phase shifts, but rather arbitrary in terms of finding scattered eigenvalues. The arbitrarity is due to the arbitrarity of the specific value of the cutoff r_∞ used to approximate infinty in real-space. Essentially, there *are* no boundary conditions on the scattered wave functions. As a result, any value of k is allowed and in fact all values of k, from 0 to k_F, are valid wavenumbers (eigenvalues). Also, the chemical potential of the infinite homogeneous system (at zero temperature) is equal to the chemical potential of the infinite impurity system (at zero temperature) since the system is infinitely larger than the volume around the impurity atom. This was discussed in the derivation of the Kohn-Sham equation in Sec. 2.2. In practice, the Kohn-Sham equations must be solved for enough points in k-space on the interval from 0 to k_F to ensure convergence of physical quantities, such as the energy. The set of points in k-space chosen is referred to, in this work, as the k-mesh. The choice of k-mesh directly affects the numerical precision of physical quantities. This will be discussed in Sec. 4.4.2. The scattered states are, of course, also subject to the same numerical errors associated with the r-mesh parameters as discussed for bound states. Again, this will be discussed in Sec. 4.4.1.

4.4 Numerical errors

Now that we have outlined the basic details regarding the calculation of the bound and scattered wave functions, we return to discuss the details of the numerical errors which arise, as mentioned at the beginning of Chapter 4.

4.4.1 Real-space mesh

The kernel of the procedure performed in this work consists of numerically solving the coupled Eq's. (3.5) in real-space. Another task that arises is the numerical integration and differentiation of several different functions in real-space. In order for these procedures to give accurate results, we must use a small interval to approximate the infinitesimal length elements, or differentials, in the corresponding expressions. The term *mesh* is used in this work to describe these discrete intervals. In particular, the term *r-mesh* is used if the function domain is real-space. The numerical precision of the calculations directly depends on the mesh used. As a result, we must analyze the behavior of the functions to be integrated or differentiated in order to determine appropriate mesh parameters.

4.4.1.1 Mesh parameters

The basic rationale for choosing the r-mesh parameters is the rapidity of the fluctuations in the densities and potentials as these are the basic functions which must be integrated or differentiated. In addition, the density, Eq.'s (3.34) and (3.43), is constructed from the solutions to Eq's. (3.5), which indicates that the behavior of the density results from the behavior of these radial wavefunctions, Eq.'s (3.10) and (3.35).

The first feature of merit is that the wavefunctions, densities and potentials all vary rapidly in the vicinity of the impurity where the core states dominate the density. As a result, we would like to have a very fine mesh near the impurity to ensure accurate integration and differentiation. However, to reduce computation time, we would like a

coarser mesh in regions where we do not need the fine mesh. In the asymptotic region far away from the impurity, the average induced density is zero and the density is dominated by the Friedel oscillations, the amplitude of which falls off like $\sim \frac{1}{r^3}$. For these reasons, we use two different meshes, a fine mesh near the impurity and a coarser mesh further away. This is accomplished by the use of a *logarithmic* (log) mesh. The log mesh begins with a very small interval size very near the impurity which then gradually increases as the distance from the impurity increases. The second mesh does not need to be as fine as the inner mesh and there is no need to have anything more sophisticated than a simple *linear* mesh, in which the intervals are of constant length. The parameters for the log mesh are chosen so that the interval sizes at the matching point for the two meshes are roughly equal. The logarithmic mesh is defined by

$$r_i = r_0 e^{\delta(i-N)} \tag{4.5}$$

where r_0 is the minimum value of r on the log mesh, δ is a scaling parameter which determines the length of the mesh intervals, and N is the total number of points on the log mesh. r_N therefore denotes the maximum value of the log mesh, which is also referred

N_{log}	ΔE	E_{atom}	E_{imm}
600	-76.39529	-76.34485	-0.05044
700	-76.21733	-76.16682	-0.05051
800	-76.08415	-76.03368	-0.05047
900	-75.98074	-75.93035	-0.05039
1000	-75.89814	-75.84780	-0.05034

TABLE 4.1: Numerical errors associated with the core states can be greatly reduced by calculating the impurity system energy and the free atom energy on the same mesh in real-space. The data shown is for a spin-polarized carbon impurity system at 0.0002 background density with the number of electrons in bound states limited to 6 with structure $1s^2\,2s^2\,2p_1^+\,2p_{-1}^+$

to as the *matching radius*. The value of δ is given by

$$\delta = -\frac{1}{N}\ln\left(\frac{r_N}{r_0}\right) \tag{4.6}$$

which varies with the number of points N on the log-mesh or N_{log}.

To find appropriate values of r_0, r_N, and N (and therefore δ), we must examine how these quantities affect the numerical precision of the immersion energy. It is worthwhile to note that if the mesh interval is too large, self-consistency may not be achieved in some situations. This seems to be dependent on the numerical procedure used to solve the coupled nonlinear equations. This is apparent from the observation that a much finer mesh must be used to achieve self-consistency for the same background density than for the spherical calculation.

The second mesh, which is referred to as the linear mesh, begins at the matching radius r_N and extends to the cutoff value r_∞, which is the approximation to infinity used in this work. Like the log-mesh parameters, we must determine a value of r_∞ by examining how this choice affects the numerical precision of the immersion energy. In addition, we must consider how the convergence of the self-consistent procedure is affected as the cutoff must be large enough to provide stability of the procedure. If the cutoff is too small, self-consistency cannot be achieved. This is due to the long-range effects of the Coulomb interaction.

4.4.1.2 Oscillation of induced charge

Since the electron density exhibits Friedel oscillations far away from the impurity, the induced electron density will exhibit the same oscillations because the homogeneous background density is constant. Since the system is infinite, the total charge induced in the system should not depend on the numerical cutoff r_∞ chosen for the r-mesh. In order to calculate the induced charge, we must examine the oscillations of the integrated charge density which result from the Friedel oscillations and use the average value. This is shown

in Fig. 4.5. We note that the dependence of the Hartree energy and exchange-correlation energy on the cutoff r_∞ can be removed in this way.

4.4.2 Momentum space mesh

In order to determine an appropriate mesh in momentum (k) space or *k-mesh*, we must examine the behavior of the functions which must be integrated or differentiated in k-space. The basic quantity that appears in Eq's. (3.34), (3.83), (3.88) and (3.98) is the phase shift $\delta^\sigma_{lm}(k)$.

The behavior of the phase shifts at $l = 0$ needs to be examined to determine the appropriate k-mesh. If the phase shift varies rapidly or the slope of the phase shift varies rapidly, we must use a fine enough k-mesh to calculate induced energies and densities of states accurately.

4.4.3 Cutoff values for l quantum numbers

Another problem that arises comes from the choice of the maximum or cutoff value for the l quantum numbers. For the calculated wavefunctions, we limit the sums over l to l_{max}, whereas for the densities and potenials, we limit the sums over l (ν) to ν_{max}.

r_∞	ΔE	E_{atom}	E_{imm}
90.2	-76.52002	-76.34485	-0.17517
95.59	-76.52200	-76.34485	-0.17715
100.0	-76.52144	-76.34485	-0.17659
104.41	-76.52017	-76.34485	-0.17532
109.8	-76.52096	-76.34485	-0.17611

TABLE 4.2: Oscillation of immersion energy with choice of r-mesh cutoff r_∞. The immersion energy variations are $\sim$ 0.001 Rydbergs. These calculations are for a carbon impurity at 0.0002 background density with 2.9 electrons in the $2p^+$ sub-shell. 600 points were used for the logarithmic r-mesh and 800 points for the linear r-mesh with matching radius $r = 2$.

To decide on an appropriate cutoff value to be used for l_{max}, we must consider several factors. kr_∞ is theoretically a good choice, but tends to neglect low-energy scattering for small values of wavenumber k [41]. In the work of Puska, Nieminen, and Manninen [5], a value of 10 was used for the maximum l. In the work of Song [30], the maximum l value was determined by examing the value of the phase shift for each value of the wavenumber k. When the phase shifts for a given l (and k) were sufficiently small, the behavior of that scattered wavefunction was essentially identical to the free particle states. For this reason, it would not contribute to the induced density, Eq. (3.34), and higher l values (for that particular value of k) could be neglected. So, the maximum l value depended on the particular k value and on the background density n_0.

In the work of Puska, et al. [5] and of Song [30], calculations were performed for spherical systems only. Therefore, the maximum value of l used for the densities and potentials (ν_{max} in this work) was zero.

In this work, nonspherical systems are studied and the coupled equations, Eq's. (3.5), must be solved *simultaneously*. This is a very important distinction from previous work. The numerical complexity and computation time are greatly increased by this. It is

N_k	ΔE	E_{atom}	E_{imm}
81	-76.54565	-76.34485	-0.20080
121	-76.54520	-76.34485	-0.20035
141	-76.54494	-76.34485	-0.20009
161	-76.54466	-76.34485	-0.19982
201	-76.54438	-76.34485	-0.19953

TABLE 4.3: Immersion energies for a carbon impurity. The immersion energy is accurate to within 0.001 Rydbergs for the number of k-mesh points beyond 120 for a given background density. 600 points for the logarithmic r-mesh and 800 points for the linear r-mesh were used for these calculations. The value of r_∞ used was 100. The calculations shown are for 0.002 background density for a nonspherical, spin-polarized system.

for this reason that we must employ a different rationale to decide an appropriate cutoff for l quantum numbers. The coupled system of equations increases linearly in number with l_{max}, but the number of floating point operations involved with solving the system increases as l_{max}^2. This turns out to be *the* major limiting factor affecting computation time in this work. In addition to this, the process of diagonalization of a complex-number matrix, which must be performed on the scattering matrix $\mathbf{S}^m(k)$ to obtain the phase shifts $\delta_{lm}^{\sigma}(k)$, scales as l_{max}^3. This would be the major limiting factor if the value of l_{max} were determined to be sufficiently larger than it was.

In order to decide on a value for l_{max}, we would like to base the decision on theoretical factors alone, but this is not an option as the computation time is impractical if l_{max} is made too large. Furthermore, since we are solving coupled equations, we must specify l_{max} *before* the start of calculations, so the scheme employed by Song is not an option. We could perhaps choose a value of 10, so that results could be compared to the work of Puska, et al., but this turns out not to be practical either. We therefore examine the effect that including (or neglecting) higher values of l has on the immersion energy. Tests were performed for values ranging from 2 to 10.

What was found was that limiting l_{max} to a value of 2 was sufficient to examine the basic features of the solution and could be performed quickly, but did not give precise values for the immersion energy. Limiting l_{max} to a value of 4 turned out to be sufficient both in terms of practical computation time and precision of the immersion energy. In addition, other physical quantities such as the induced density of states $\Delta D(k)$ and the induced density $\Delta n(\boldsymbol{r})$ turned out to show convergence for a value of 4 for l_{max}. If l_{max} was increased to 5 or beyond, the numerical differences in the immersion energy were well below the threshold of absolute error and the relative error associated with other precision limiting factors, such as the choice of mesh size.

To determine the value for the maximum l (ν) value used for densities and potentials

ν_{max}, we first note that the computation time scales linearly with this value, but that for the small ($\sim< 10$) values of l_{max} used in this work, this is still a major limiting factor for computation time. In the work of Salin, et al. [33] and Muiño et al. [34], the cutoff value ν_{max} was limited to 2. This includes the monopole, dipole and quadrupole components of the charge densities and potentials. In order to decide on a value for the maximum ν, we first note that due to the even-cylindrical symmetry of the impurity systems studied in this work, only even components will contribute. This means that the dipole ($l = 1$) component does not contribute and therefore the quadrupole ($l = 2$) component is the first nonspherical term that contributes in the multipole expansion of the densities and potentials, Eq's. (3.4) and (3.19). (For the atomic polarizability calculatoins performed, the dipole ($l = 1$) component is nonzero.) Examination of the effect of the next even-order term ($l = 4$), showed it to be almost negligible and when the greatly increased computation time was taken into account, we decided to neglect this term and all higher order terms. Therefore, for all data presented in this work, a value of 4 for l_{max} and a value of 2 for ν_{max} are used unless otherwise stated.

4.4.4 Numerical corrections to the output potential

If we return to the expression for the Hartree potential, Eq. (3.52),

$$v_\nu^H(r) = \frac{4\pi e^2}{2\nu+1} \int r'^2 \Delta n_\nu(r') \frac{r_<^\nu}{r_>^{\nu+1}} \, \mathrm{d}r'$$

the integral over r' extends to infinity, which in this work is approximated by r_∞. Due to this approximation, severe errors are evident in the output total effective potential. The errors are due almost entirely to this effect. If this is not addressed, these defects will quickly cause instability in the iterative procedure and self-consistency will not be achieved. One way to reduce this effect is to use a very large cutoff for r_∞. This is, however, not practical due to the very large value which must be used for r_∞ to make the defect negligible. Instead, we can numerically correct this defect based on knowledge of

its analytic form.

If we write out the Hartree potential inserting the appropriate limits of integration, we have

$$v_\nu^H(r) = \frac{4\pi e^2}{2\nu+1}\left[\frac{1}{r^{\nu+1}}\int_0^r r'^{2+\nu}\Delta n_\nu(r')\,\mathrm{d}r' + r^\nu\int_r^{r_\infty}\Delta n_\nu(r')\frac{r'^2}{r'^{\nu+1}}\,\mathrm{d}r' + O(r^\nu)\right] \quad (4.7)$$

where the error term comes from the truncation associated with the approximation to infinity

$$O(r^\nu) = r^\nu\int_{r_\infty}^{\infty}\Delta n_\nu(r')\frac{r'^2}{r'^{\nu+1}}\,\mathrm{d}r'. \quad (4.8)$$

It can be seen that the leading term of the Hartree potential varies as $1/r^{\nu+1}$. Therefore, $r^{\nu+1}v_\nu(r) \rightarrow$ constant. A plot of $r^{\nu+1}v_\nu(r)$ vs. $r^{2\nu+1}$ will be linear or close to linear in the error. This error manifests as an offset and slope in the plot. We can then determine this slope and offset numerically and adjust the output potential accordingly. We make the substitution

$$r^{\nu+1}\times v_\nu(r) \longrightarrow r^{\nu+1}\times v_\nu(r) - r\left(m_\nu + \frac{C_\nu}{r_\infty}\right) \quad (4.9)$$

where m_ν is the slope of $r^{\nu+1}v_\nu(r)$ vs. $r^{2\nu+1}$ and C_ν is the y-intercept. For the monopole ($l=0$) component of the potential, this amounts to replacing

$$r\times v_0(r) \longrightarrow r\times v_0(r) - r\left(m_0 + \frac{C_0}{r_\infty}\right). \quad (4.10)$$

For the quadrupole ($l=2$) component of the potential, this becomes

$$r^3\times v_2(r) \longrightarrow r^3\times v_2(r) - r\left(m_2 + \frac{C_2}{r_\infty}\right). \quad (4.11)$$

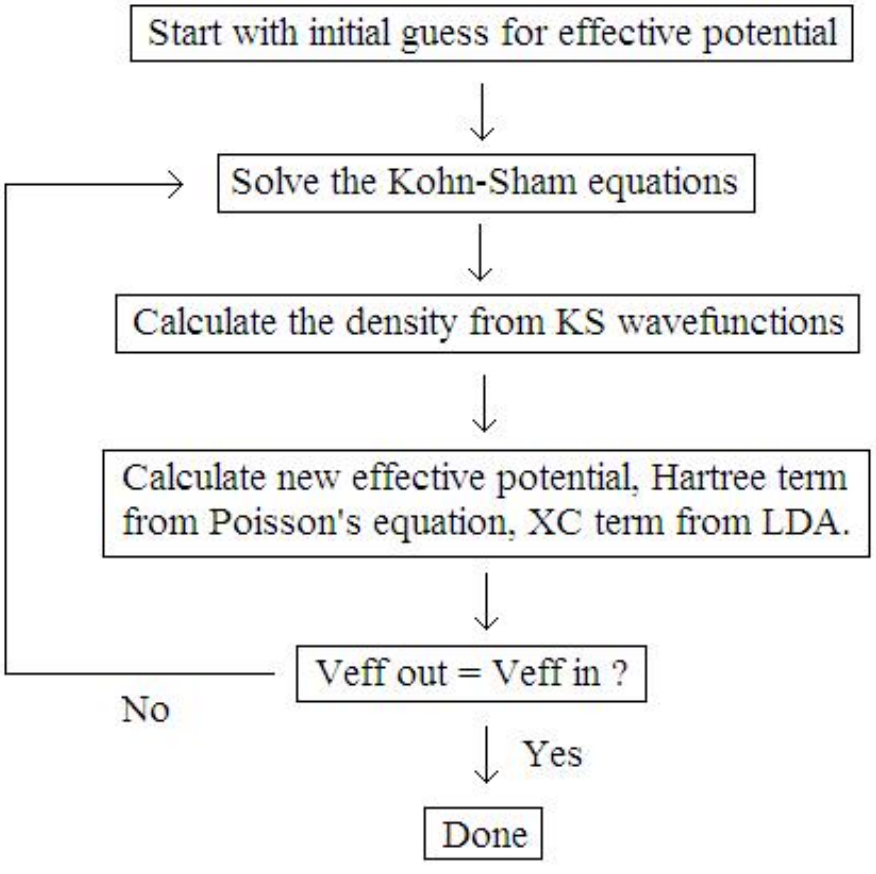

FIGURE 4.1: Iterative scheme used to find self-consistent solutions.

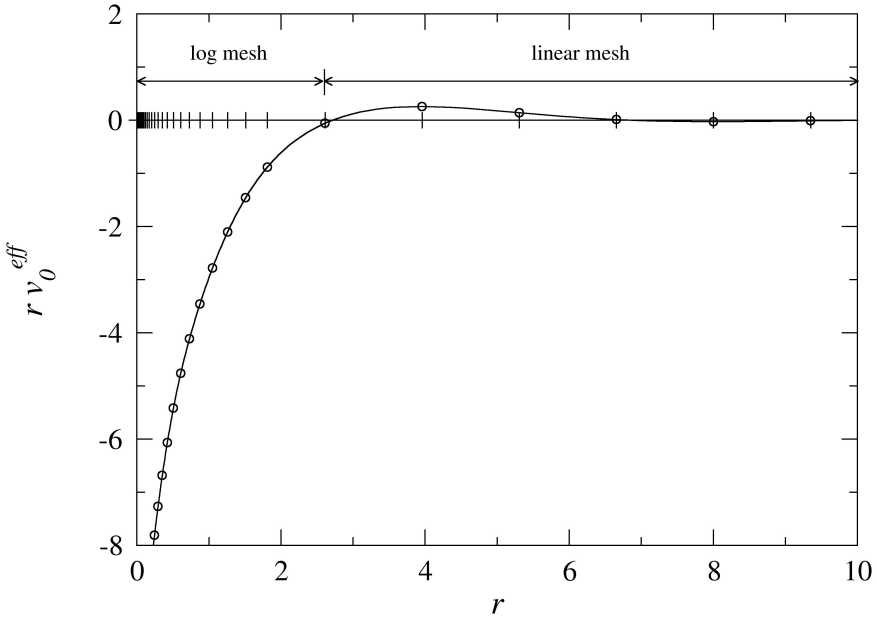

FIGURE 4.2: A logarithmic mesh is used close to the impurity where the potential varies rapidly. This helps reduce errors in the numerical integrations due to rapidly varying densities associated with the core states.

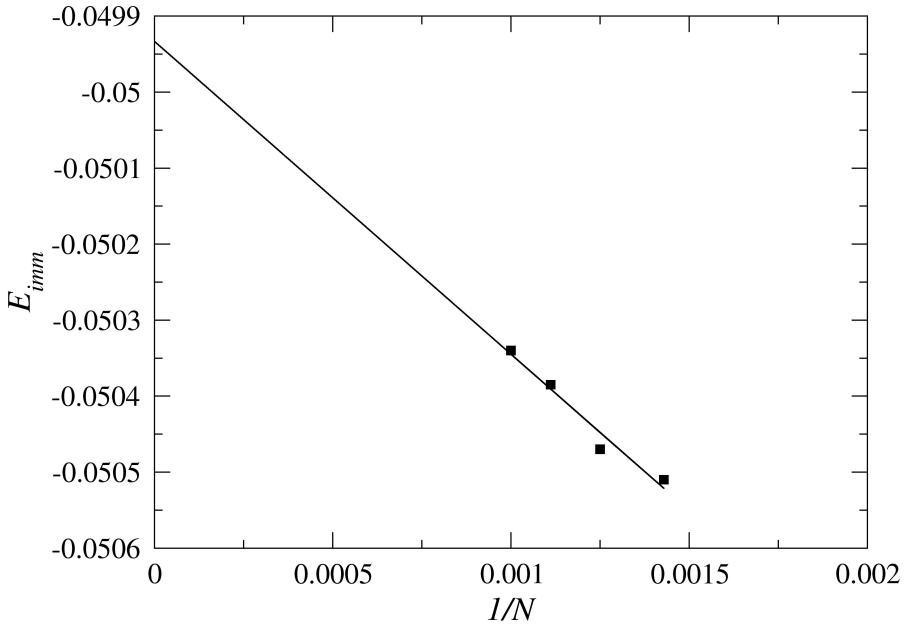

FIGURE 4.3: Immersion energies are found by extrapolating to an infinite number of points N on the logarithmic r-mesh using the data from Table 4.1.

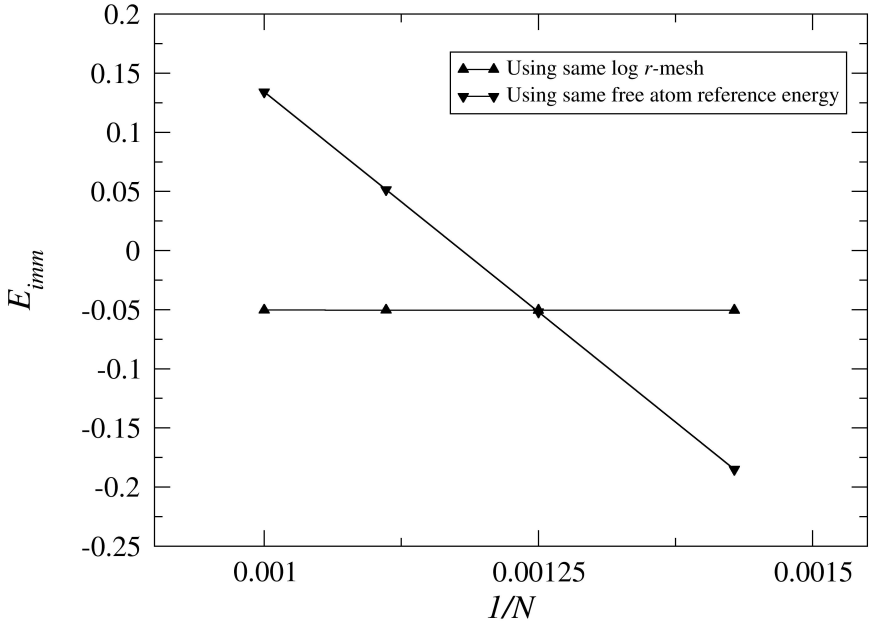

FIGURE 4.4: Numerical errors in the immersion energy can be reduced by using the same r-mesh for the free atom and immersion calculations. Data shown are from Table 4.1.

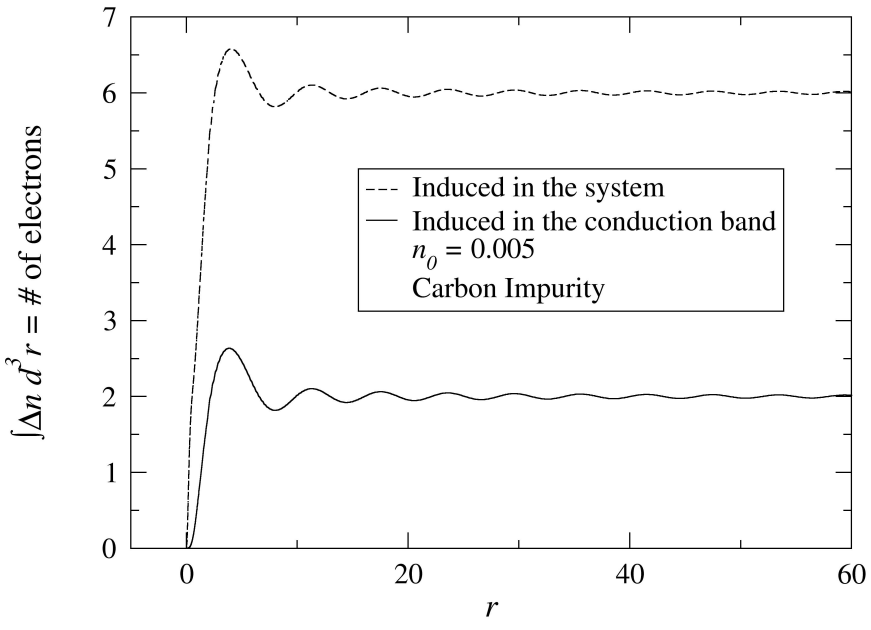

FIGURE 4.5: The total induced charge oscillates as a result of the Friedel oscillations. This creates an error that depends on our choice of cutoff radius r_∞, which is $r = 100$ for most calculations in this work. The effect on the total energy for various symmetries is much smaller than the effect from changes in background density since the spherical components of the density are almost identical for variations of the magnetic quntum number M_L for a given background density. This plot is for a carbon impurity at $n_0 = 0.005$ background density with 4 electrons in bound states.

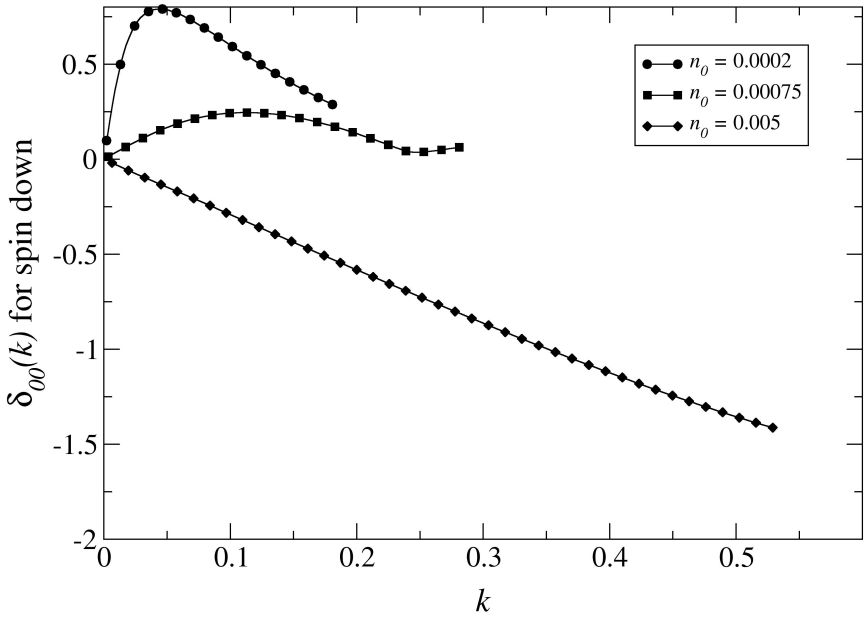

FIGURE 4.6: For low densities, the rapid variation of the spherical phase shift requires the use of a fine k-mesh. These calculations are for a spin up electron in the conduction band of a carbon impurity system.

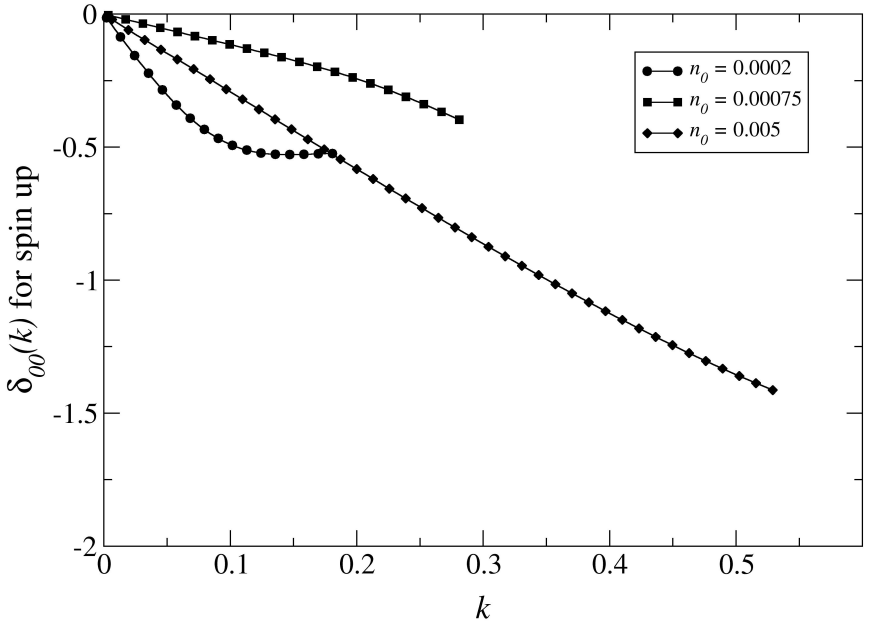

FIGURE 4.7: For low densities, the rapid variation of the spherical phase shift requires the use of a fine k-mesh. These calculations are for a spin down electron in the conduction band of a carbon impurity system.

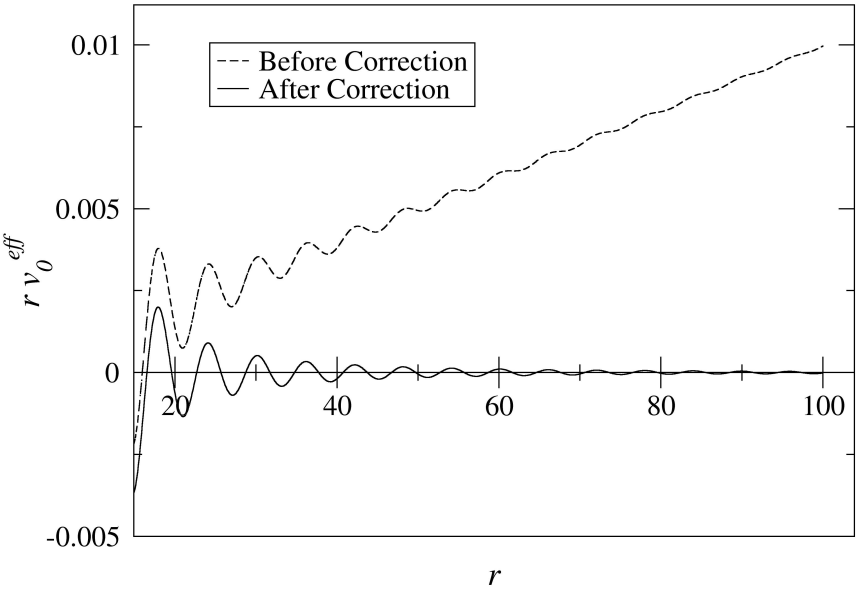

FIGURE 4.8: An example of defects in the spherical component of the output total potential and the total potential after correction. The primary defect arises from the artificial cutoff used for r_∞ and the long range nature of the Coulomb interaction. These data are for spin up electrons in a carbon impurity system of $n_0 = 0.005$ background density.

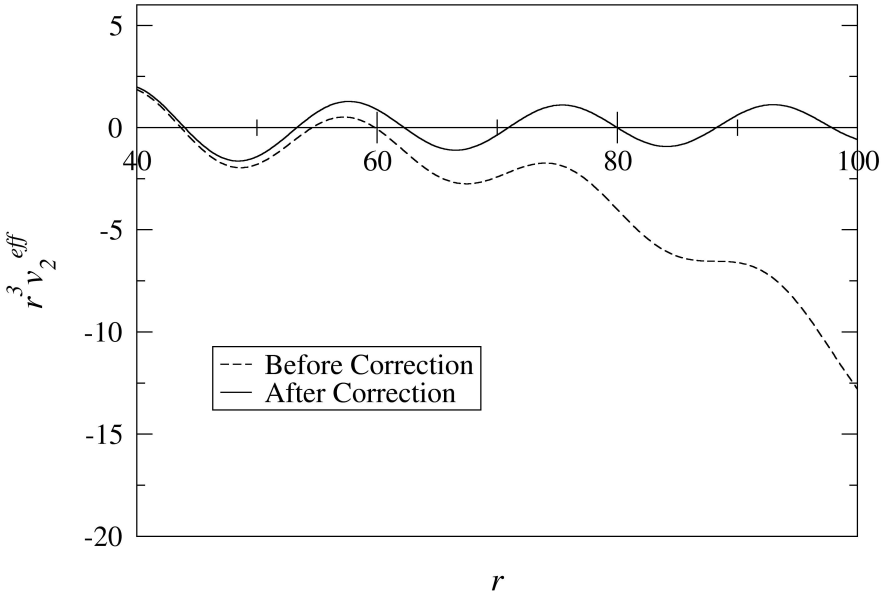

FIGURE 4.9: An example of defects in the quadrupole component of the total output potential and the total potential after correction. The primary defect arises from the artificial cutoff used for r_∞ and the long range nature of the Coulomb interaction. These data are for spin up electrons in a carbon impurity system of $n_0 = 0.005$ background density.

5. RESULTS

For a free atom, the physical quantities that determine the nature of the solutions are the Coulomb charge of the atomic nucleus and the total amount and distribution of electronic charge. The Coulomb potential and potential energy are determined by the total charge density of both the nucleus and orbital electrons. The exchange-correlation potential and potential energy are determined by the total electronic charge.

For impurity systems, the primary physical quantities that determine the nature of the solutions are the charge of the impurity atom and the density of the background electron gas. These, in turn, determine the induced electron density in the vicinity of the impurity. The Coulomb potential and potential energy are determined by the impurity charge and the induced electron density since the homogeneous background density cancels the contribution from the positive 'jellium'. The exchange-correlation potential and potential energy are determined by the induced electron density and the homogeneous background density of the electron gas. The exchange-correlation contribution to the immersion energy is, in fact, the difference in exchange-correlation energy between the homogeneous and impurity systems.

Previous work on atomic immersions has focused on spherical systems [5, 30, 31], so much of this chapter will detail the nonspherical contributions to physical quantities such as the total energy, densities, potentials and phase shifts. In addition, spin-polarization effects will be discussed as well since the total spin-moment helps to distinguish between different solutions.

5.1 Free atom

For free atom calculations performed in this work, the total number of electrons can be chosen to be integral or fractional. Total energies of free neutral and singly-ionized atoms are calculated. By taking the difference between these energies, the ionization energies can be calculated for free atoms.

In addition, the nonspherical solutions allow us to distinguish between solutions with different symmetry properties and to study the effect of symmetry variations on the total energy.

5.1.1 Zero external electric field

The nonspherical calculations performed in this work allow for a more fundamental analysis of atomic structure within the LDA. For free atoms, in the spherical approximation, a partially occupied angular momentum shell will have the (integral) number of electrons in that subshell divided equally (fractionally) among the orbitals, which is not necessarily the ground state, or any physically meaningful state for that matter[7]. Even for spin-polarized calculations, the total number of electrons in a partially occupied shell will still be divided among different m subshells for a given n, l and σ. In contrast, the nonspherical symmetry of the calculations performed in this work allows us to distinguish between the different m states in a given sub-shell and to compare the results obtained with the physical ground state.

Hund's rules [9] allow us to determine the ground state configuration of atoms. This assumes $L - S$ coupling, which is usually true for light atoms. The rules are stated as

1. The ground state configuration has maximum multiplicity or spin S.

[7]The approximations present in the LDA may result in a ground state configuration which has fractionally populated eigenstates, both for spherical and nonspherical systems.

2. For a given value of S, the ground state has maximum L cooresponding to maximum M_L (furthermore M).

3. For atoms with less than half-filled shells, the ground state has minimum J, for atoms with more than half-filled shells, the ground state has maximum J.

where the configuration or *term* is denoted in Russel-Saunders [10] notation as ${}^{2S+1}L_J$. For carbon, which has the structure $1s^2\,2s^2\,2p^2$, the terms, in order of increasing energy are ${}^3P_0 < {}^3P_1 < {}^3P_2 < {}^1D_2 < {}^1S_0$. In the absence of spin-orbit coupling, all of the $L = 1$ (P) terms are equal in energy. Including spin-orbit coupling or not, Hund's 2nd rule indicates that the ground state of carbon has a value of $M = 1$.

For a spherical calculation, there is no distinction between the eigenstates and energy eigenvalues for different m values for a given l. However, in the nonspherical calculations, we can directly vary M by varying the population of the valence electrons between different m states. A neutral, spin-polarized spherical carbon atom would have 2/3's of an electron in the $2p_{-1}$, $2p_0$ and $2p_1$ spin up states resulting in a value of $M = 2/3$. If we examine the total energy as shown in Fig. 5.1, it can be seen that for the free atom, the nonspherical effects tend to raise the energy from the spherical value. It can be seen that the magnitude of these energy effects are small ($\sim 1mR$ or $0.01eV$) for carbon. However this ground state configuration of $M = 2/3$ predicted by the LDA is in contradiction with the ground state configuration of $M = 1$ predicted by Hund's rules.

It is interesting to see that the spherical configuration with $M = 2/3$ extremizes all of the major energy terms, including the kinetic energy, the Coulomb potential energy, the exchange-correlation (potential) energy, and as already mentioned, the total energy. Fig. 5.2 shows the variation of the valence electron energy eigenvalues for a free carbon atom as M is varied. The $2p^+$ $m = -1, 0, 1$ eigenvalues are all equal for the spherical $M = 2/3$ configuration. It is also worthwhile to note that the spherical configuration minimizes the *average* energy eigenvalue of a $2p^+$ state. Fig. 5.3 shows the variation of the kinetic

energy of a free carbon atom as M is varied and that the kinetic energy is maximized for the spherical configuration. Variations of the potential energy terms are shown in Fig. 5.4. The Coulomb potential energy is minimized while the exchange-correlation energy is maximized for the spherical configuration. The variations of the total electron density with M are shown in Fig. 5.5. Note that the quadrupole component of the density disappears for the spherical configuration of $M = 2/3$.

5.1.2 Non-zero external electric field; atomic polarizability

In the work of Stott and Zaremba [4], atomic dipole polarizabilities were calculated within the linear-response theory using a Green's function formalism. As we are solving the nonspherical coupled system, Eq.'s (3.5), we can directly calculate the dipole response of the charge cloud to an applied electric field. This was discussed in Sec. 3.6. We therefore have access to both the linear and nonlinear terms of the dielectric response. The linear dipole polarizability calculated in this way can be compared to that found previously and to experiment [4].

Fig. 5.1 shows that the external electric field causes the ground state symmetry to shift from the spherical to the $M \approx 1$ configuration. In addition, the extrema of the energy eigenvalues shift as well. Fig. 5.2 shows the variation of the valence electron energy eigenvalues with M. The $2p$ spin up $m = 0$ and $|m| = 1$ eigenvalues cross at the new total energy minimum near $M = 1$. It can also be seen that the ground state maximizes the dipole polarizability α. As shown in Fig. 5.3, it is interesting to see that the kinetic energy is now minimized for the ground state of the polar atom, whereas it is maximized for the ground state of the free atom. Fig. 5.4 shows that the trends for the Coulomb energy and exchange-correlation energy are similar for the polar atom and the free atom. The Coulomb energy is minimized for the polar atom and the exchange-correlation energy is maximized for the polar atom. Fig. 5.6 shows the electron density for the ground state of a polar carbon atom while Fig. 5.7 shows the variation in the electron density for a

polar carbon atom as M is varied.

Element	Exp.[8]	NS-VBHL	S-VBHL[9]	KS-XC[8]	KS-X[8]	HF[8]
He	-5.807	-5.741	-	-5.651	-5.447	-5.723
Li	-14.956	-14.791	-14.71	-14.656	-14.349	-14.865
C	-	-75.132	-74.933	-	-	-75.377
Ne	-257.88	-256.82	-256.747	-256.349	-254.986	-257.094

TABLE 5.1: Total energies of free atoms in Rydbergs. It is seen that our results (NS-VBHL) for He, Li, and Ne atoms compare well with experiment and other DFT and Hartree-Fock methods. In the case of a C atom, the energy we found is somewhat lower than the result of Song.

Element	Exp.[8]	NS-VBHL	S-VBHL[9]	KS-XC[8]	KS-X[8]	HF[8]
He	1.807	1.82	-	1.938	1.834	-
Li	0.396	0.433	0.417	0.396	0.331	0.393
C	0.828	0.895	-	-	-	-
Ne	1.585	1.67	1.641	1.657	1.551	1.461

TABLE 5.2: Ionization energies of removing one electron from a free atom, in Rydbergs. It is seen that our results (NS-VBHL) compare well with experiment and with other theoretical approaches, but have much smaller absolute errors than the total energies shown in Table 5.1. This is due to the removal of errors associated with core states since the core density is very similar for neutral and ionized atoms of the same element.

[8]Ref [3]

[9]Ref [30]

Element	Exp.[10]	NS-VBHL	CI[10]	XC[10]	X[10]	CHF[10]
He	1.385	1.640	1.383	1.89	1.98	1.3217
C	11.7	14.310	-	-	-	-
Ne	2.666	3.029	2.676	2.76	3.03	2.365

TABLE 5.3: Linear dipole polarizabilities of free atoms (in a_0^3). For He, where exchange effects are more important, configuration interaction and ordinary Hartree-Fock methods give better results than DFT. No theoretical data could be found for C, but our calculation (NS-VBHL) over-estimates the linear dipole polarizbility, but is in reasonable agreement with experiment.

5.2 Impurity System

For the impurity systems studied in this work, the Friedel oscillations exhibited provide an important numerical verfication that the self-consistent solutions found are the correct physical solutions. In particular, we can use the Friedel sum rule to verify the total induced charge and the Friedel oscillations to verify the asymptotic behavior of the induced electron density in the vicinty of an impurity.

In the case of a carbon impurity, it is found that the number of electrons in bound states depends on the density of the background gas. For low metallic densities, $n_0 \leq 0.001$, 6-7 electrons can be held in bound states. For intermediate densities, $0.001 \leq n_0 \leq 0.004$, the number of bound states can be made to be 6, but only 4 in the ground state. This is due to the presence of a virtual bound state resonance in the conduction band for the structure with only 4 electrons in bound states. For higher densities $0.004 \leq n_0 \leq 0.06$, only 4 electrons are held in bound states with structure $1s^2\,2s^2$ and the resulting densities are spherical.

[10]Ref [4]

5.2.1 Transient behavior during numerical calculation iterations

In order to achieve a self-consistent solution, the errors in the Hartree potential must be corrected throughout the numerical iterations. This was discussed in Sec. 4.4.4. At the beginning of calculations, the impurity system under consideration is generally very far from self-consistency. The potentials and densities are incorrect and the numerical tests, such as charge balance, give incorrect results. If the errors in the Hartree potential are not corrected, the iterative procedure will diverge and self-consistency will not be achieved. If the errors are accounted for, the iterative procedure can be made to converge to the *correct* self-consistent solution. However, during the early iterations of the procedure, the densities and potentials are incorrect. In addition, the numerical tests for the true physical solutions are incorrect as well. This can clearly be seen by inspecting the charge balance of the system. This is done by numerically integrating the densities and by using the phase shifts of the radial wave functions to verify the Friedel sum rule. The Friedel sum rule, Eq. (3.112), states that the total electronic charge induced by the impurity is equal and opposite to the impurity charge. It can be seen from Fig. 5.8 that the Friedel sum rule gives the same results as numerically integrating the total induced electron density at almost every point throughout the calculations. This numerical result, however, is not in agreement with the physical solution during the early iterations of the iterative procedure.

Fig. 5.8 shows an example of how a carbon impurity system evolves to self-consistency. The initial density used to calculate the initial guess for the effective potential is the electron density of a neutral free atom plus the homogenous background gas. The initial effective potential is sufficiently attractive to hold an extra electron in a bound state (beyond that of the neutral atom). This extra electron must be mixed in slowly in order to keep the procedure stable. This transient mixing of the seventh bound state can be seen as the linearly increasing region of the bound state population from iterations 1 to 10 of Fig. 5.8. The number of electrons induced in the conduction band can be seen

to decrease from 0 to -1 during this same period to maintain charge conservation. For the data shown, the background density of 0.002, however, is too high to hold 7 electrons in bound states for a carbon impurity. As a result, the system evolves to a self-consistent solution in which only 4 electrons are held in bound states and 2 electrons are induced in the conduction band by the presence of the impurity. This transient behavior can be seen from iterations 24 through 40. The total number of electrons induced in the system by the impurity at self-consistency is calculated by integrating the total induced charge density and is seen to be in agreement with the Friedel sum rule, calculated from the radial phase shifts.

5.2.2 Friedel Oscillations

In [6, 7, 8], it was shown that an electron gas exhibits oscillations in the density due to the presence of an impurity. These oscillations are known as Friedel oscillations and it was shown that the wavelength of oscillation is independent of the impurity atom and has a value of $\lambda_{Friedel} \approx \pi/k_{Fermi}$. This can be verified by plotting the density vs. $k_{Fermi}r$ and is shown in Fig. 5.9. The amplitude of oscillation can be seen to vary with the background electron gas density, but the wavelength does not. The details of the charge oscillations will be shown more clearly in Sec. 5.2.3.1.

5.2.3 Low background density; symmetry variation of excited state

We first note that for a carbon impurity with 3 electrons held in $2p$ bound states, all of the same spin, the resulting structure will be spherical due to equal populations of available m-symmetry states. These are in addition to the 4 bound $1s$ and $2s$ electrons. Since we would like to analyze nonspherical systems, we limit the number of bound $2p$ electrons to 2 (to make a neutral impurity) and study the effect of symmetry variations by varying the population of different m states within the $2p$ spin up sub-shell. The overall effect of this is to vary M for the impurity atom.

5.2.3.1 Charge densities and potentials

Fig. 5.10 shows the variation of the total induced electron density as M is varied from 0-1 for a neutral carbon impurity. The maximum amplitude of the nonspherical component of the density is seen first to decrease and then to increase again with an amplitude of 0 at the spherical configuration with a value of $M = 2/3$. The spherical component of the induced electron density does not change substantially for these symmetry variations. The total induced spin-density, the electron density induced in the conduction band and the spin-densty induced in the conduction band all show similar features to those of the total induced electron density. One feature of merit is that the *sign* of the density variations changes at $M = 2/3$'s as M is varied. In terms of the electron densities, this is a change in the relative amount of charge in a given region, which could affect chemical bonding in a molecule or solid. In terms of the spin-densities, this causes a change in the anti-ferromagnetic structure resulting from the Friedel oscillations. These data are shown in Fig.'s 5.11 through 5.13.

The trends in the density variations are similar as the background density is increased in this low density range, $0.0002 < n_0 < 0.002$. These data are shown in Fig.'s 5.14 through 5.21.

It can also be seen that the wavelength of the Freidel oscillations decreases as the background density increases, as it should. The actual wavelength of $\lambda_{Freidel} \approx \pi/k_{Fermi}$ was already verified in Sec. 5.2.2. As the distance from the impurity is increased, the induced electron density decreases to zero, indicating that the impurity is completely screened and that the total electron density is equal to that of the homogeneous background gas.

Fig.'s 5.22 through 5.25 show the variation of the densities and spin-densities for the entire low denisty range for the $M = 0$ configuration for a neutral carbon impurity.

5.2.3.2 Phase shifts and density of induced states

If we examine the phase shifts for a neutral carbon impurity at low density ($n_0 = 0.0002$) with $M = 0$ in Fig. 5.26, we note several features. First of all, the very large slope at low k in the $l = 0$, $m = 0$ spin up phase shift indicates the presence of a virtual bound state resonance. The induced conduction band density will have a $3s^+$ state coming down from the conduction band. This is most easily seen as a peak in the induced spin-density, Fig.'s 5.23 and 5.25. Secondly, the $l = 1$ phase shifts indicate that the $m = 0$ spin up scattered states are less screened than the $|m| = 1$ states due to the lack of a bound $2p_0^+$ electron and the presence of bound $2p_{-1}^+$ and $2p_1^+$ electrons. This is evident from the larger slope of the $l = 1$, $m = 0$ spin up phase shift near the Fermi surface.

The opposite trend is seen for the $l = 1$ spin down phase shifts. The $l = 1$, $m = 0$ spin down phase shift has a smaller *negative* slope than the $|m| = 1$ states. This is because there are twice as many unpopulated $|m| = 1$ states ($m = \pm 1$) than $m = 0$ states for the spin down channel and they are therefore less screened. This results in the $l = 1$, $|m| = 1$ spin down phase shifts having a larger negative slope near the Fermi surface as seen in Fig. 5.26.

The last feature of merit is that the $l = 2$ conductions electrons are screened equally for a given spin. This indicates that the nonspherical effects are limited to the low order, s and p, partial-waves. However, it is evident that spin-polarization effects are still important for higher order partial-waves, as the $l = 2$ phase shifts for spin up and spin down electrons have opposite sign. The positive value of the phase shifts for $l = 2$ spin up conduction electrons indicates that they are repelled by the impurity due to the presence of $2p^+$ electrons despite the ability of the impurity to hold more bound electrons. The negative sign of the phase shifts for spin down conduction electrons indicates that they are attracted to the impurity nucleus due to the lack of $2p^-$ electrons.

To vary M for the neutral impurity atom from 0 to 1, the population of the $2p_0^+$

state is varied from 0 to 1 while the population of the $2p^+_{-1}$ state is varied from 1 to 0. So, the $2p^+_0$ population increases as M increases. If we look at Fig. 5.27, we can see that the slope of the phase shift for the $l = 1$, $m = 0$ spin up conduction electrons decreases near the Fermi level as M increases, indicating that this channel is more effectively screened by the bound $2p^+_0$ electron as the population of that state is increased. Conversely, we can also see in Fig. 5.27 that the slope of the phase shift for the $l = 1$, $m = -1$ spin up conduction electrons increases near the Fermi level as M increases, indicating that this channel is less effectively screened by the bound $2p^+_{-1}$ electron as the population of that state is decreased. We see similar trends for the $l = 1$ spin down conduction electrons in Fig. 5.28. This indicates that the spin down conduction electron are screened by the bound spin up electrons due to the Coulomb effects, but the *sign* of the phase shift is different due to the exchange effects within the spin-polarized LDA. Variations of the lowest order phase shifts for the low density range are shown in Fig.'s 5.29 through 5.32.

5.2.3.3 Immersion energies

In the work of Stott and Zaremba [4], it was indicated that immersion energies for light atoms in an electron gas should exhibit a minimum for very low background densities.

It can be seen that for the $M = 0$ configuration, the immersion energy vs. density curve exhibits a decrease in slope as the density decreases, but no minimum is observed although the data suggests that a minimum may exist at still lower densities, shown in Fig. 5.33. As M is increased from 0 to 1, this curvature decreases and eventually disappears altogether. At a value of $M = 1$, the immersion energy vs. density curve is completely linear and no evidence of a minimum can be seen.

The behavior of the immersion energy as a function of M, for a given density, is seen to be linear for a neutral carbon impurity over the entire low density range. This is in contrast to the behavior for a free neutral carbon atom, as shown in Fig. 5.1. This indicates that, in the LDA, the presence of the background electron gas changes the nature

of the solution, even for very low gas densities, where the properties should approach that of the free atom.

It is also interesting to note that the M-symmetry variation causes the immersion energy for a neutral carbon impurity to change from negative to positive as M is varied from $0 - 1$. This indicates that adsorption of the impurity into the electron gas is energetically favorable for lower M values and not favorable for higher M values.

Fig.'s 5.34 and 5.35 show that the variation of the kinetic energy with M for a neutral carbon impurity shows the same trend as for a free atom; the spherical configuration maximizes the kinetic energy. The valence electron energy eigenvalues also cross at the spherical configuration and minimze the avergage $2p^+$ energy eigenvalue. If we examine the variation of the Coulomb energy with M for the carbon impurity system, as shown in Fig. 5.36, we see that the trend is also similar to that for the free atom; the spherical configuration minimizes the Coulomb energy. The spherical configuration, however, is no longer the minimum total energy configuration. We do see that the variation of the exchange-correlation energy with M is quite different than it was for the free atom. The scale of the exchange-correlation energy variation is much larger as well. In fact, the scale of the exchange-correlation energy can be seen to be the same as that of the immersion energy variations. It appears that the exchange-correlation energy contribution to the immersion energy is the dominant term in causing the $M = 0$ configuration to become the lowest energy configuration for a neutral carbon impurity.

The last feature of merit is that the spherical configuration maximizes the spin-polarization of the carbon impurity system, whereas the spin-polarization of the free carbon atom is constant with M-symmetry variations. This data is shown in Fig. 5.37. We have defined the spin-polarization here as the difference between the total number of spin up and spin down electrons in the system, $\Delta N = N_+ - N_-$.

5.2.4 Low background density; variation of sub-shell population

In the previous section, Sec. 5.2.3, we studied the effect of varying the M quantum number for a neutral carbon impurity atom in an electron gas. We will now investigate the effect of varying the valence population of the impurity atom. We populate the $2p^+$ $m = 1$ and $2p^+$ $m = -1$ states with 1 electron and the $2p^+$ $m = 0$ state with a variable number of electrons between 0 and 1. This means that the impurity atom will maintain a value of $M = 0$ as the valence population is varied. This was chosen since the $M = 0$ configuration was found to be the lowest energy for all neutral carbon impurity systems studied in this work. We will study the effect of this variation on the structure and energy of the impurity systems.

5.2.4.1 Charge densities and potentials

In Fig. 5.38, the variation of the total induced electron density for a carbon impurity at 0.0002 background density is shown for variations in the valence population. For the neutral impurity with only two $2p$ electrons, it is seen that the amplitude of the spherical component of the Friedel oscillations is smallest. This is due to the near complete screening of the impurity nucleus by the electrons induced in the vicinity of the impurity. However, the neutral carbon impurity can hold more electrons in bound states due to the extended distribution of the induced charge. As additional electronic charge is added to the impurity, the induced electronic charge near the impurity is greater than the impurity charge and the response of the electron gas can be seen as the increased amplitude of the spherical component of the Friedel oscillations around the impurity. However, the quadrupole component of the total induced electron density can be seen to decrease in amplitude since the carbon impurity system approaches a spherical configuration as the valence occupation approaches an equal distribution in the m sub-shell channels.

If we look at the induced spin-density in Fig. 5.39, we see similar trends to those for the total induced electron density. However, one important difference is the variation

in the spin-density due to the virtual bound state resonance in the spin down channel that arises near a valence population of 2.5. This is due to the $2p^-$ bound states merging into the conduction band as the valence population is increased in the spin up channels since the $2p^-$ states are higher in energy than the $2p^+$ states. This can clearly be seen in Fig. 5.40. Due to this effect, it was not possible to achieve good convergence for a $2p$ population near 2.5.

If we examine the spherical component of the induced electron density in the conduction band, shown in Fig. 5.41, we can see the effect of the virtual bound state resonance as a peak near the impurity. We can also see the effect on the induced spin-density in the conduction band, shown in Fig. 5.42.

5.2.4.2 Phase shifts and density of induced states

If we examine the $l =$ phase shifts, shown in Fig. 5.43, several features are evident. With only 2 electrons in the valence, the $l = 0$, $m = 0$ spin up phase shift shows the presence of the $3s^+$ virtual bound state evident as the steep slope at low k values. As the valence population is increased, this feature disappears as that state is pushed beyond the Fermi surface. The $l = 0$, $m = 0$ spin up phase shift drops to its lowest value of negative slope near a valence population of 2.5 when the $2p^-$ states merge into the conduction band. As the valence population is increased further, the $l = 0$, $m = 0$ spin up phase shift increases to a slightly less negative slope.

For the $l = 0$, $m = 0$ spin down phase shift, a different trend is evident. The slope is initially negative for a valence population of 2 and increases near 2.5 when the $2p^-$ states merge into the conduction band. The slope then decreases as the $2p^-$ state is pushed further into the conduction band. All of this shows that the $l = 0$ phase shifts are not completely screened from the $l = 1$ states and that the Coulomb effects between these channels are still important.

If we examine the $l = 1$ spin up phase shifts, shown in Fig. 5.44, the same types of

features are evident. There is, of course, no virtual bound state resonance indicated in the $l = 1$ spin up channels from the $3s^+$ state. We do, however, see similar trends in terms of the $2p^-$ states merging into the conduction band. All of the $l = 1$ spin up phase shifts have a positive slope for a valence population of 2. As the valence population is increased, we see a dramatic decrease in the slope near a population of 2.5 as the $2p^-$ states merge into the conduction band. As the valence population is increased further, the slope over most of the range of k increases as the virtual bound state resonance is pushed beyond the Fermi level.

For the $l = 1$ spin down phase shifts, shown in Fig. 5.45, the opposite trend from the $l = 1$ spin up phase shifts is evident. For a valence population of 2, the $l = 1$ spin down phase shifts show a negative slope. As the valence population is increased, the slope becomes positive near a population of 2.5 as the $2p^-$ state merge into the conduction band. As the valence population is increased further, the slope decreases back to a negative value. All of this behavior can be seen clearly if we examine the induced density of states in the conducton band, shown in Fig. 5.46. The induced density of states in the spin up channel is initially positive for a valence population of 2. As the valence population is increased, the induced density of states in the spin up channel becomes negative near a valence population of 2.5 when the $2p^-$ states merge into the conduction band. As the valence population is increased further the induced density of states in the spin up channel becomes positive again. The opposite trend is seen in the spin down channel. For a valence population of 2, the induced density of states in the spin down channel is initially negative. As the valence population is increased, the induced density of states in the spin down channel becomes positive near a valence population of 2.5 when the $2p^-$ states merge into the conduction band. As the valence population is increased further, the induced density of states in the spin down channel becomes negative again.

5.2.4.3 Immersion energies

If we examine the variation of the immersion energy with the valence population, we can use Janak's theorem [44] as a test for physical verification. Janak's theorem states that

$$\frac{\mathrm{d}E_{imm}}{\mathrm{d}n} = E_n - E_{Fermi} \tag{5.1}$$

where n is the population of the state which is being varied. Fig. 5.47 shows the variation of the immersion energy with the valence population for a carbon impurity at 0.0002 background density. The bottom graph shows the numerical derivative of E_{imm} vs. $n_{2p_0^+}$ using different approximations and shows $E_{n_{2p_0^+}} - E_{Fermi}$. The data shows good agreement with Janak's theorem. It appears that the discrepancies are due due to the approximations in the numerical differentiation. Fig. 5.48 shows the variation in the immersion energy with the valence population for the low density range $0.0002 \leq n_0 \leq 0.00075$. For densities greater than 0.0005, it was not possible to achieve convergence for a valence population greater than 2.3. It is again seen that the data are in good agreement with Janak's theorem.

5.2.5 High background density

We have seen that nonspherical effects are important for impurities at low metallic densities. In this section, we will show that the nonspherical effects are quenched beyond the low density range previously studied. For background densities higher than 0.001, the ground state for a carbon impurity system has only 4 electrons in bound states. The resulting structure $1s^2\,2s^2$ is spherical.

5.2.5.1 Charge densities and potentials

Fig. 5.49 shows the variation in the total induced electron density for higher background densities. Data for lower densities is shown for comparison. For the spherical component of the density, the variation looks continuous. For the quadrupole compo-

nent, however, it can be seen that the contribution is effectively zero for 0.002 background density and above. The lower inset shows the scale of the nonspherical term, which is essentially noise due to the numerical nature of the differential equation solver routine.

In Fig. 5.50, the total induced spin-density is shown for the higher density range. Again, low density data is also shown for comparison. One major difference in the spherical component of the spin density is the presence of a peak centered around $r \simeq 17$ for the lower density system. This is again due to the presence of the virtual bound state resonance coming from the $3s^+$ state in the conduction band at very low densities. For densities of 0.002 and higher, it can be seen that there is no peak from such a state and the Friedel oscillations dominate the density in the same region. For the nonspherical terms, it is again seen that the quadrupole term is essentially zero for background densities higher than 0.002. It can also be seen that the spin-polarization effects are largely quenched above a background density of 0.005. This is apparent from the decrease in the amplitude of the total induced spin-density as the background density is increased.

Fig. 5.51 shows the induced electron density in the conduction band for higher background densities. For background densities higher than 0.002, a peak is seen near the impurity resulting from the $2p$ states that have merged into the conduction band for these densities.

If we examine the induced spin-density in the conduction band, shown in Fig. 5.52, we see essentially the exact same data for the spherical term of the total induced electron density since the bound $1s$ and $2s$ electrons form closed shells. For the nonspherical term, we again see that for background densities higher than 0.002 the quadrupole term is essentially zero. One feature of merit is the decrease of the spin moment near the impurity as the background density is increased.

5.2.5.2 Phase shifts and density of induced states

Fig. 5.53 shows the phase shifts for the higher density impurity systems. For the $l = 0$ spin up and spin down channels, the phase shifts are almost identical for a given density and remain almost unchanged as the density increases. The slopes are negative and almost constant. The negative contribution to the induced density of states is due to the presence of the two $1s$ and two $2s$ bound states.

The $l = 1$ phase shifts show a decrease in the spin-polarization as the background density increases. The $l = 1$ spin up channel has a steep slope at lower background densities that indicates the presence of a peak in the induced density of states, shown in Fig. 5.54. As the background density increases, the slope decreases, but remains noticeable near the Fermi level. The slope of the phase shift for the $l = 1$ spin down channel is initially very small for lower background densities. As the background density increases, the slope of the phase shift for the $l = 1$ spin down channel increases. For lower values of the background density, the $l = 1$ spin up channel has a much larger slope than the $l = 1$ spin down channel. As the background density increases, the two spin channels for $l = 1$ approach equal values for the phase shifts and therefore equal values for the induced density of states.

5.2.5.3 Spin-polarization

Fig. 5.55 shows the variation of the spin-polarization for the ground state impurity system for the entire background density range studied in this work. It is interesting to note that there is a sharp increase in the difference between the number of spin up and spin down electrons in the system for very low densities. This is due to the presence of the $3s^+$ virtual bound state resonance previously mentioned.

5.2.5.4 Immersion energies

Fig. 5.56 shows the variation of the immersion energy for the higher background density range. This data is shown for verification and is in excellent agreement with the results of Song.

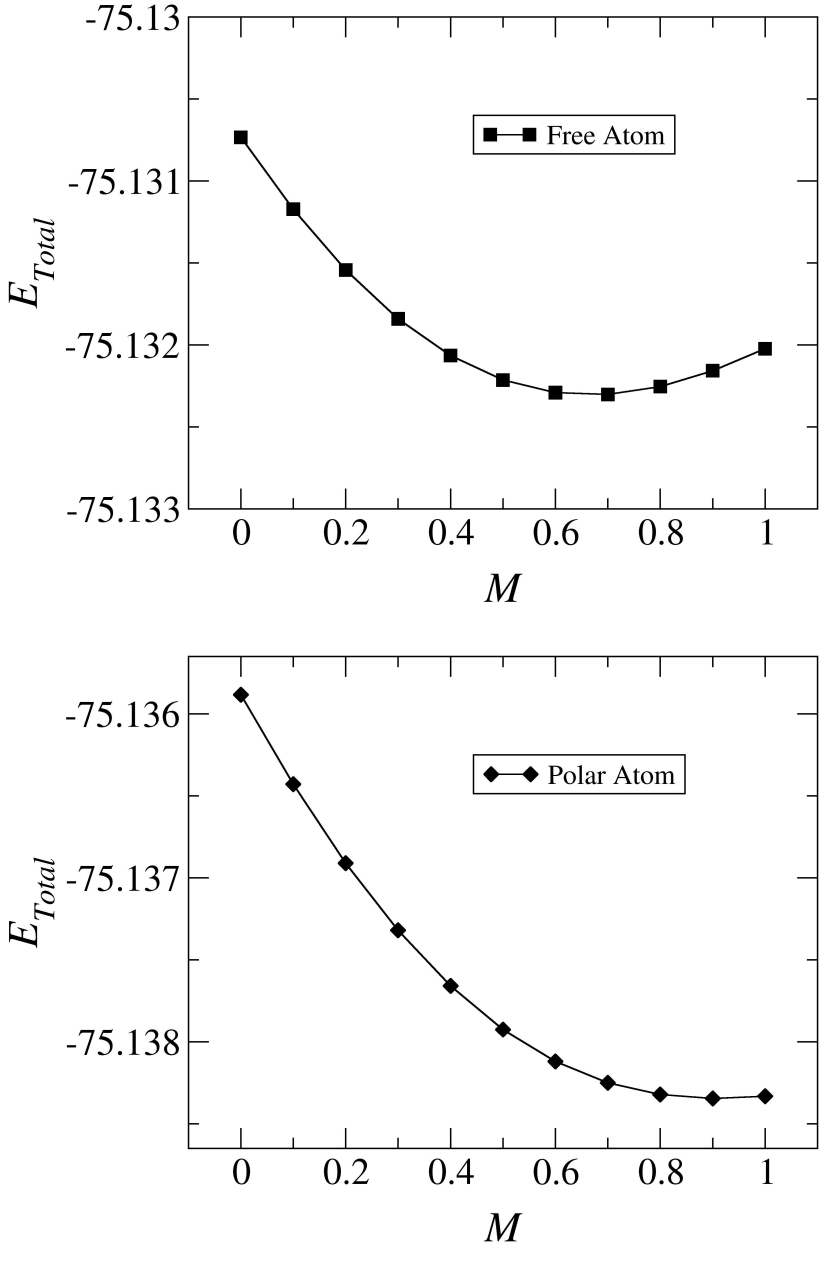

FIGURE 5.1: The LDA violates Hund's 2nd rule for a free atom, which states that the ground state configuration maximizes M. The upper graph shows the variation of the total energy for a free carbon atom, which shows a minimum at the spherical configuration of $M = 2/3$. The lower graph shows the variation of the total energy for a polar atom; the minimum is very close to $M = 0.9$. The electric field value used is $E = 0.03$ with a cutoff of $r = 7$.

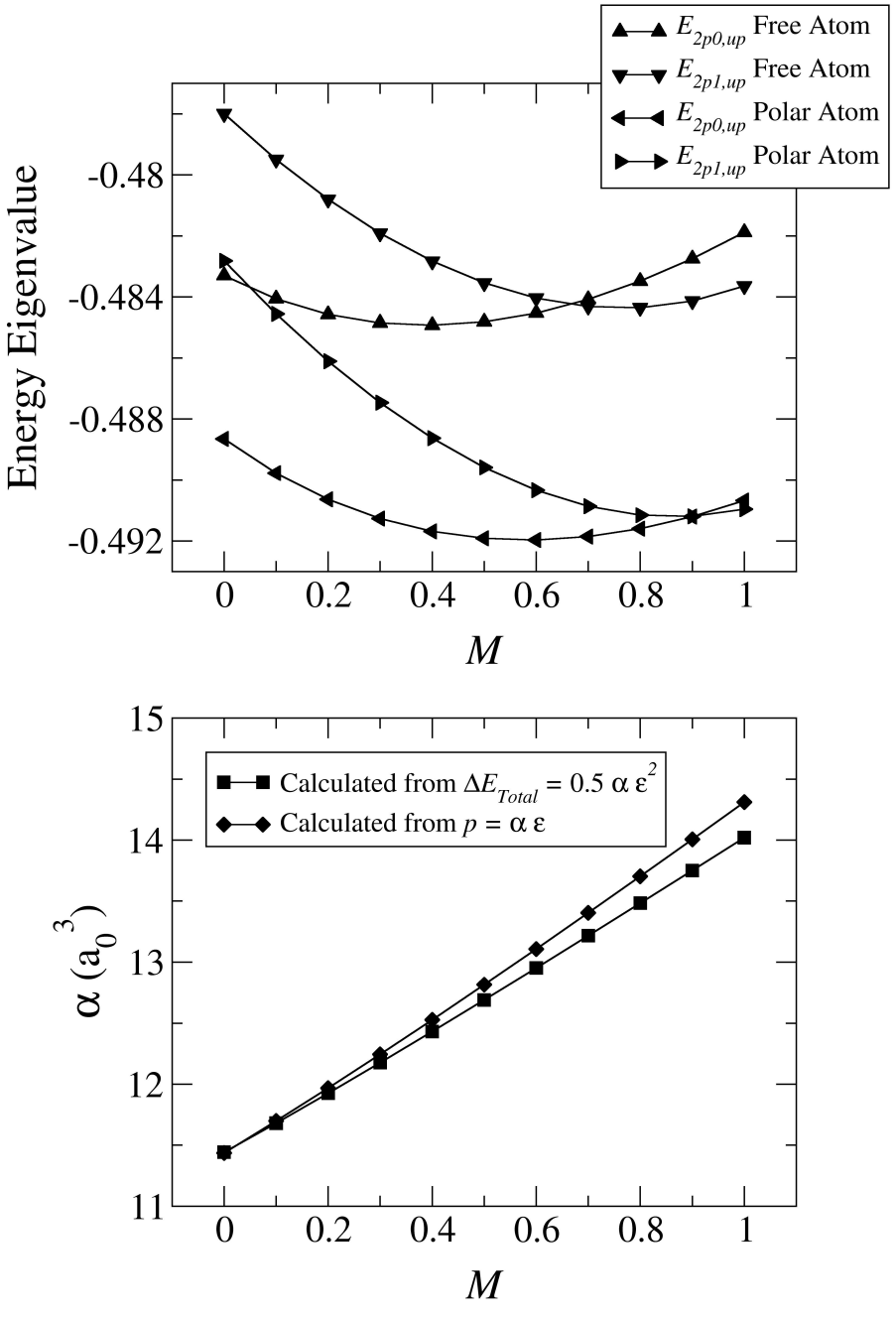

FIGURE 5.2: Variation of the $2p^+$ energy eigenvalues and dipole polarizability as M is varied from $0-1$ for a free carbon atom. The electric field value used is $E_0 = 0.03$ with a cutoff value of $r = 7$. The data shown are converged for r-mesh parameters. It is seen in Fig. 5.1 that the LDA ground state for a free carbon atom is spherical. It is seen above that the 3 $2p_m^+$ energy eigenvalues are therefore equal for the ground state. For a polar carbon atom, the ground state is no longer spherical, but is still the configuration that makes the 3 $2p_m^+$ energy eigenvalues equal.

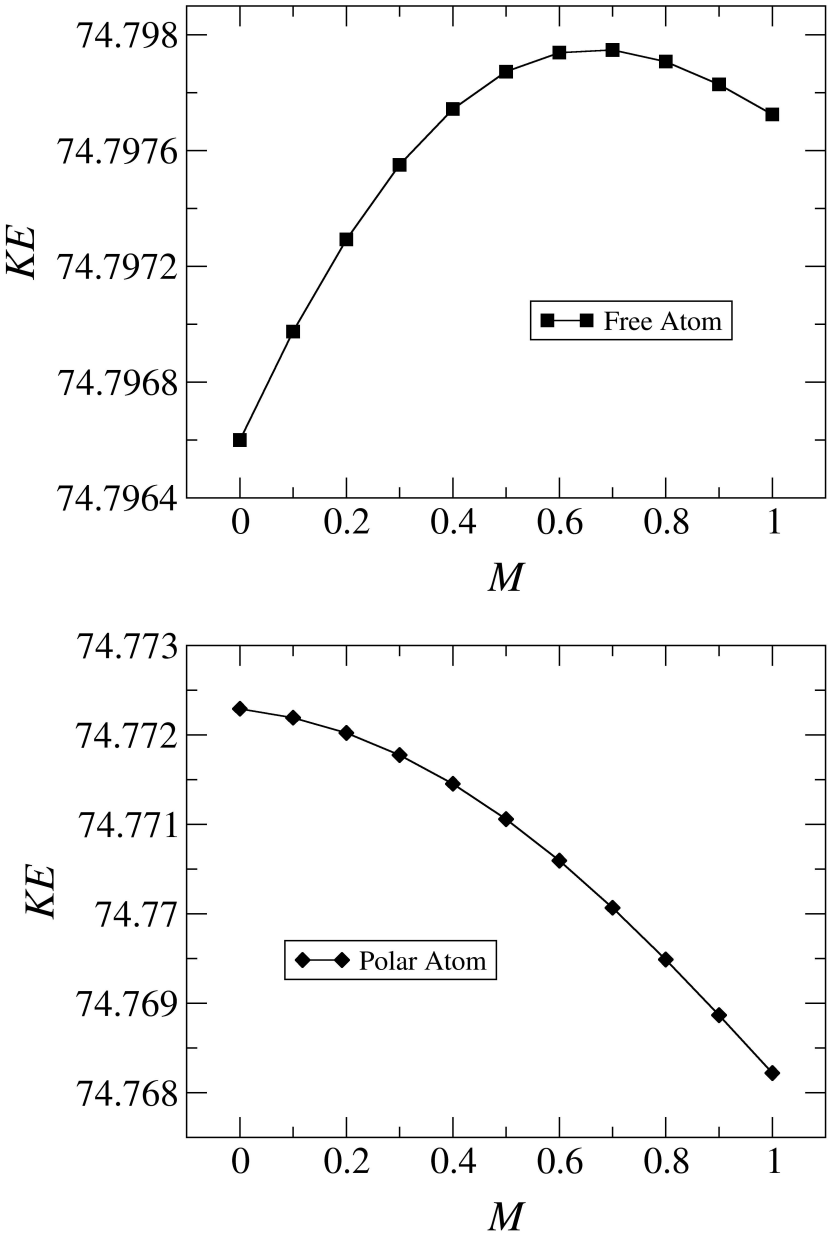

FIGURE 5.3: Variation of the kinetic energy for free and polar carbon atoms as M is varied from $0-1$. It is seen that for the free atom, the kinetic energy is maximized for the ground state with $M = 2/3$, while for the polar atom, the ground state of $M \approx 1$ is a minimum of the kinetic energy. The value of electric field used was 0.03 with a cutoff of $r = 7$. The number of points on the r-mesh is $N_{lin} = 700$ and $N_{log} = 700$.

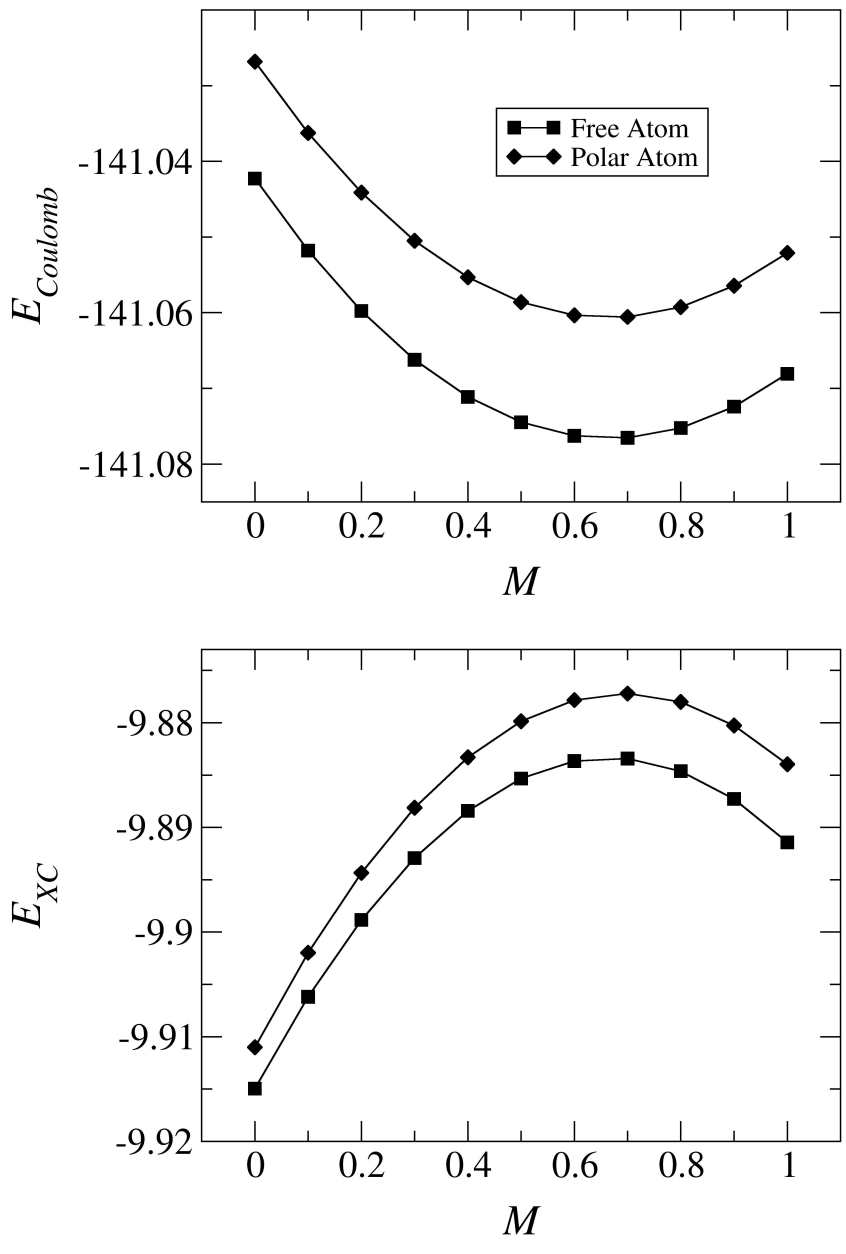

FIGURE 5.4: Variation of the Coulomb energy and the exchange-correlation energy for free and polar carbon atoms as M is varied from $0-1$. The Coulomb energy is minimized for $M = 2/3$ for both free and polar atoms. The exchange-correlation energy is maximized for $M = 2/3$ for both free and polar atoms. The value of electric field used was 0.03 with a cutoff of $r = 7$. The number of points on the r-mesh is $N_{lin} = 700$ and $N_{log} = 700$.

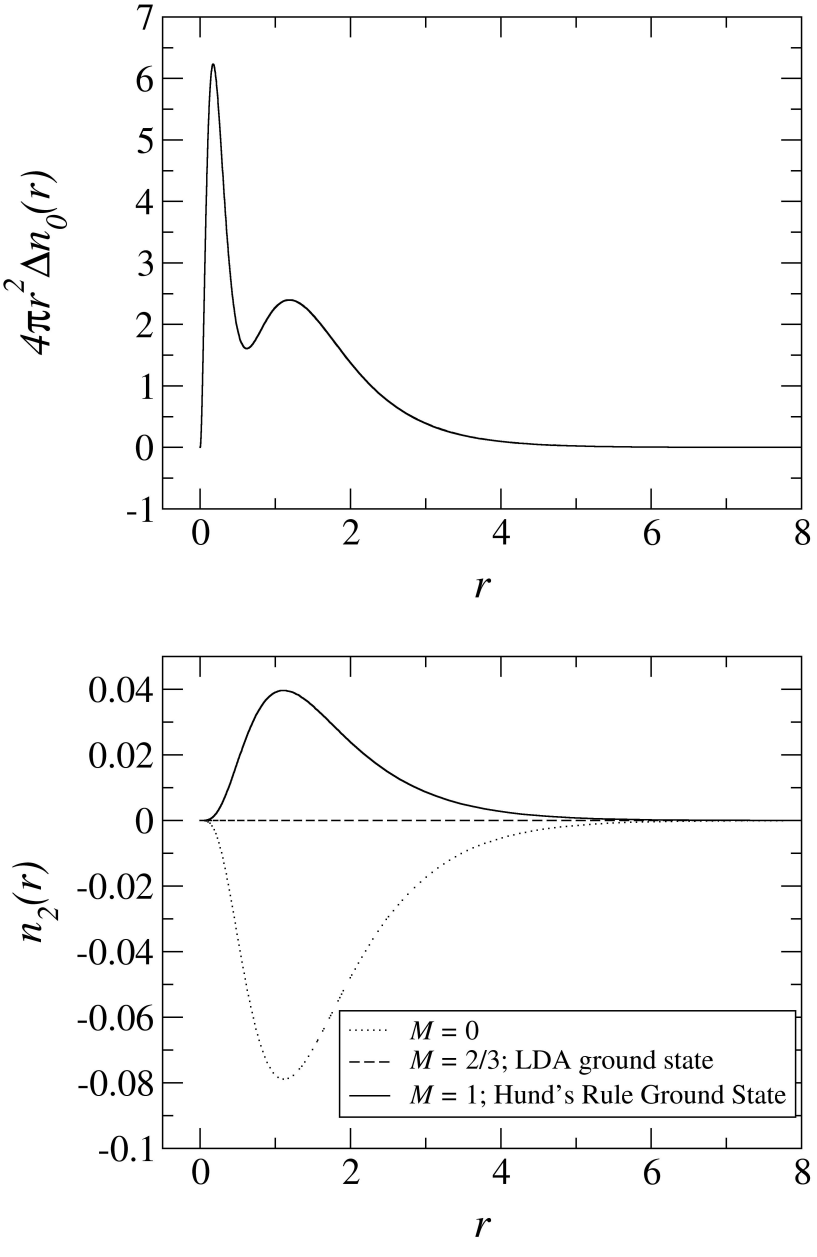

FIGURE 5.5: Spherical (monopole) and nonspherical (quadrupole) components of the electron density for a free carbon atom. The quadrupole component of the density vanishes for the LDA ground state, but not according to Hund's rules. In the absence of an external electric field, the dipole component of the electron density is zero.

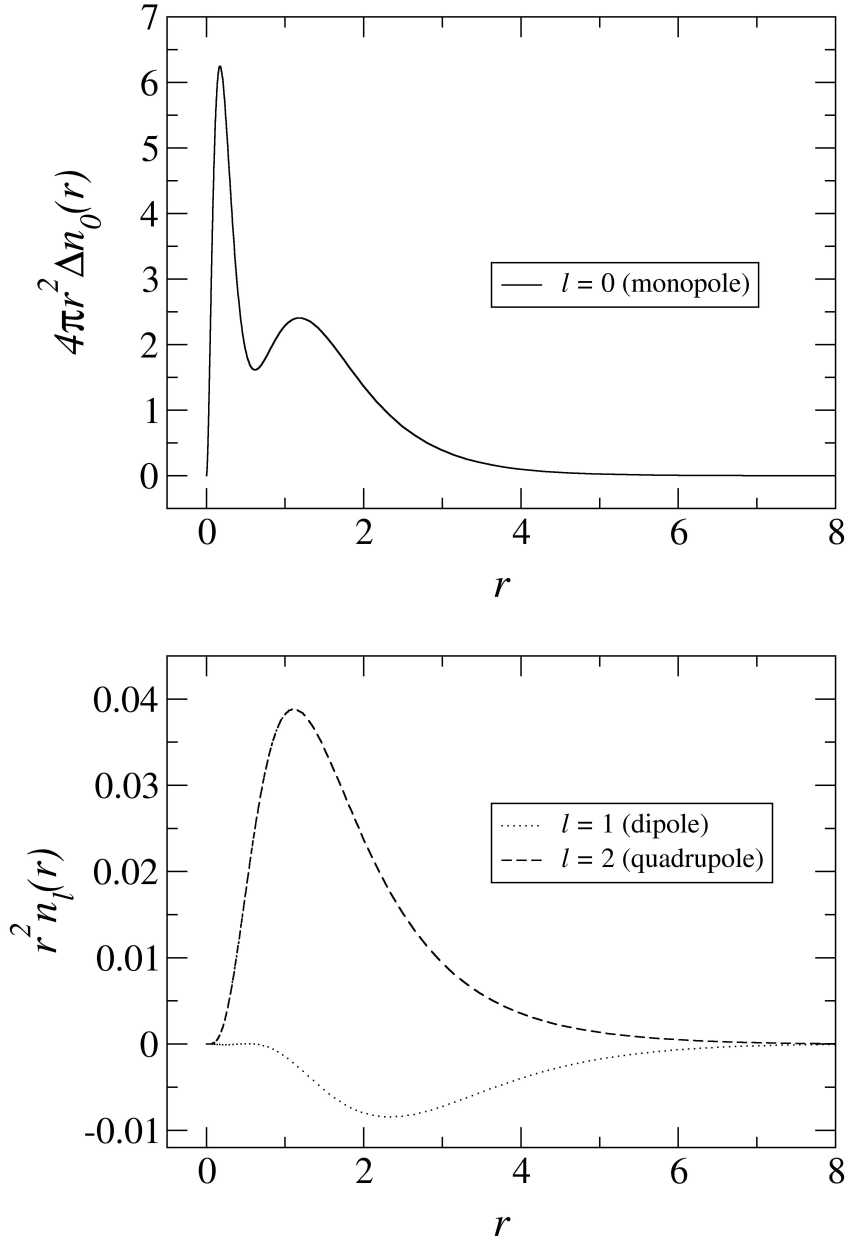

FIGURE 5.6: Spherical (monopole) and nonspherical (dipole and quadrupole) components of the electron density for a free carbon atom in an external electric field. The field value used was $E_0 = 0.03$ with a cutoff value of $r = 10$.

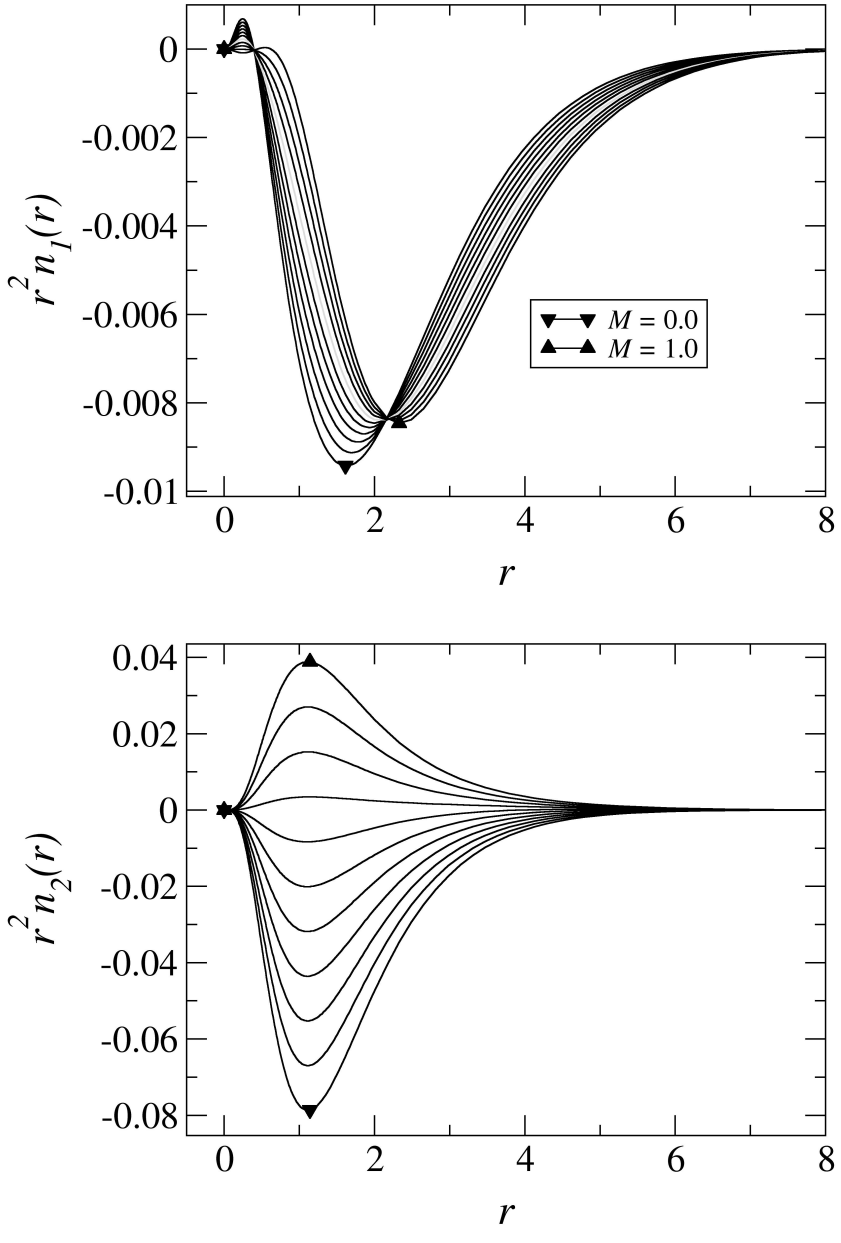

FIGURE 5.7: Nonspherical (dipole and quadrupole) components of the electron density for a free carbon atom in an external electric field. The field value used was $E_0 = 0.03$ with a cutoff value of $r = 7$.

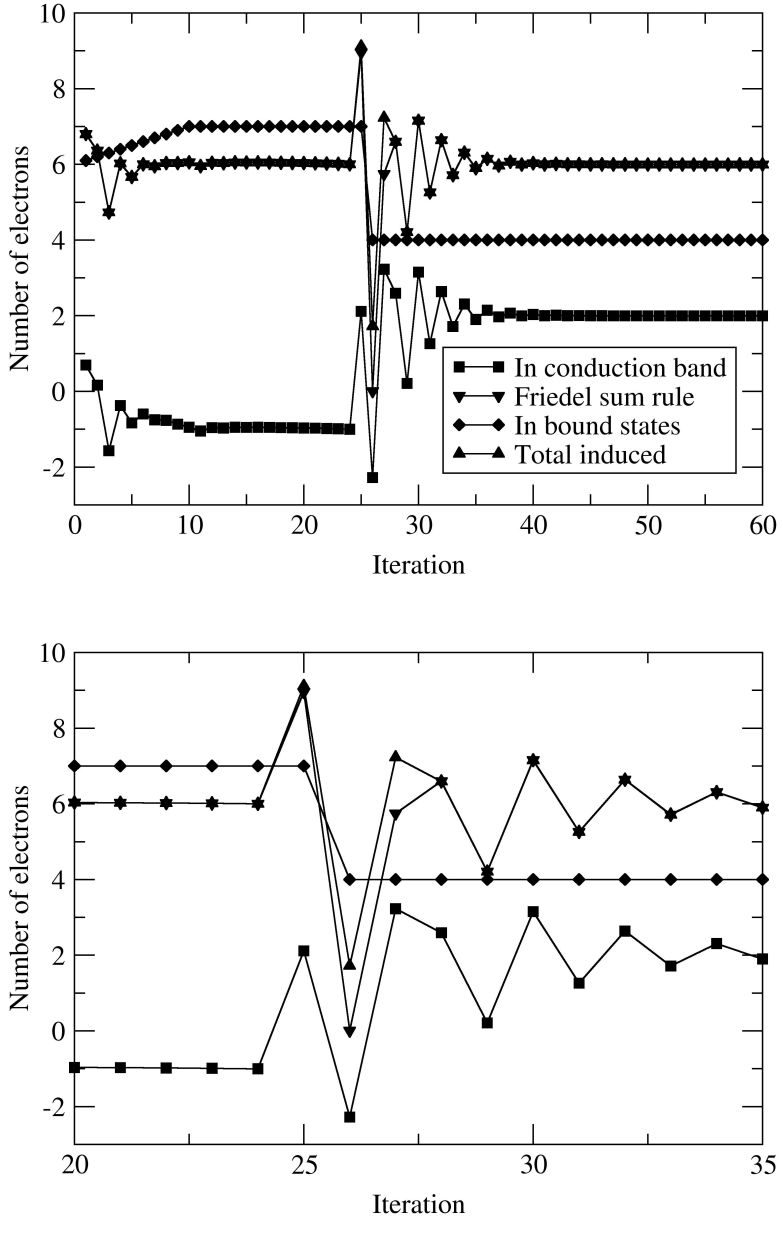

FIGURE 5.8: Variation of the number of electrons for a carbon impurity at 0.002 background density during the iterative procedure. Initially 6 electrons are placed into bound states while a $7th$ is mixed in. This helps to stabilize the iterative procedure at the beginning. However, this value of background density is too high to hold 7 electrons in bound states and a transition occurs from 7 to 4 electrons being held in bound states as the system settles to the ground state. This is for a nonspherical, spin-polarized impurity system.

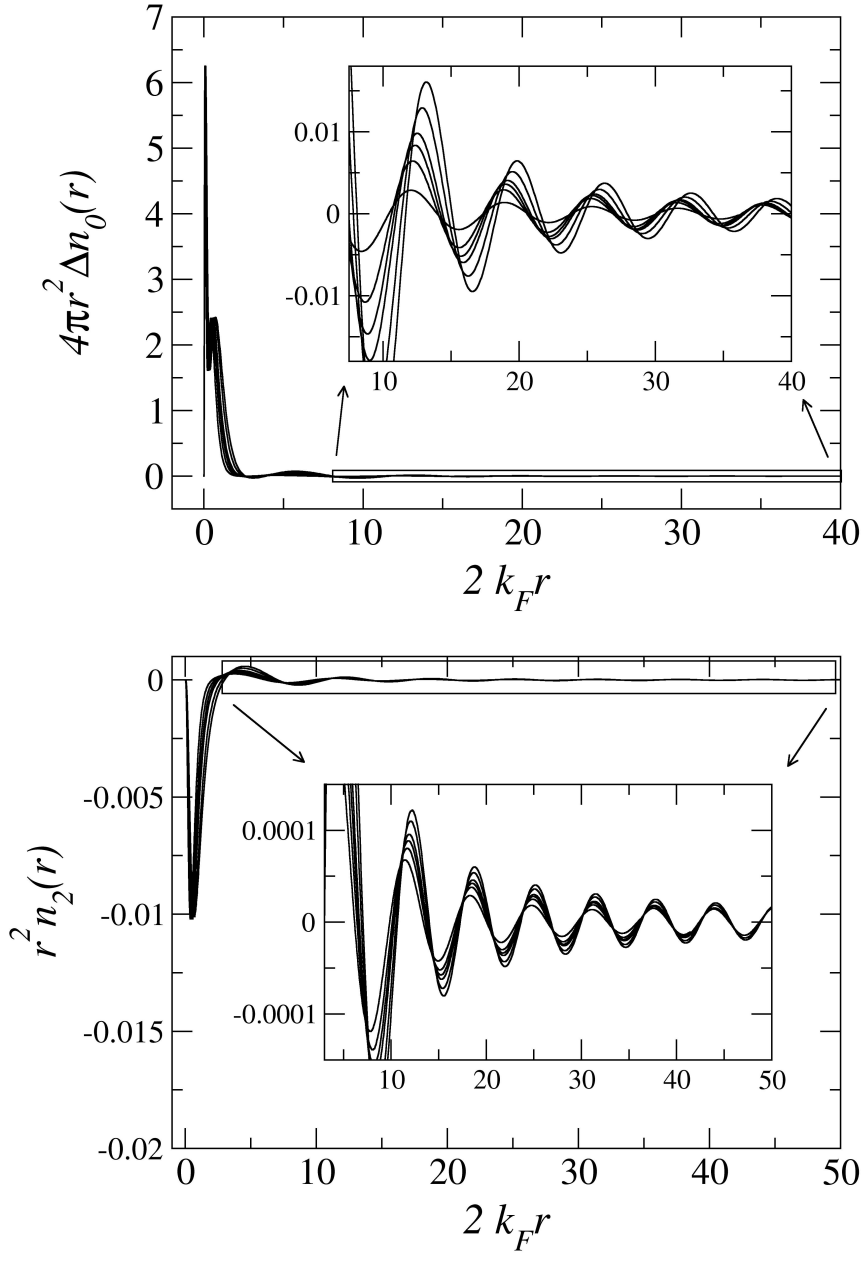

FIGURE 5.9: Behavior of the Friedel oscillations for a carbon impurity for the density range $0.0002 - 0.001$ with the number of electrons in bound states limited to 6. This shows that the wavelength of the Friedel oscillations is independent of the background density.

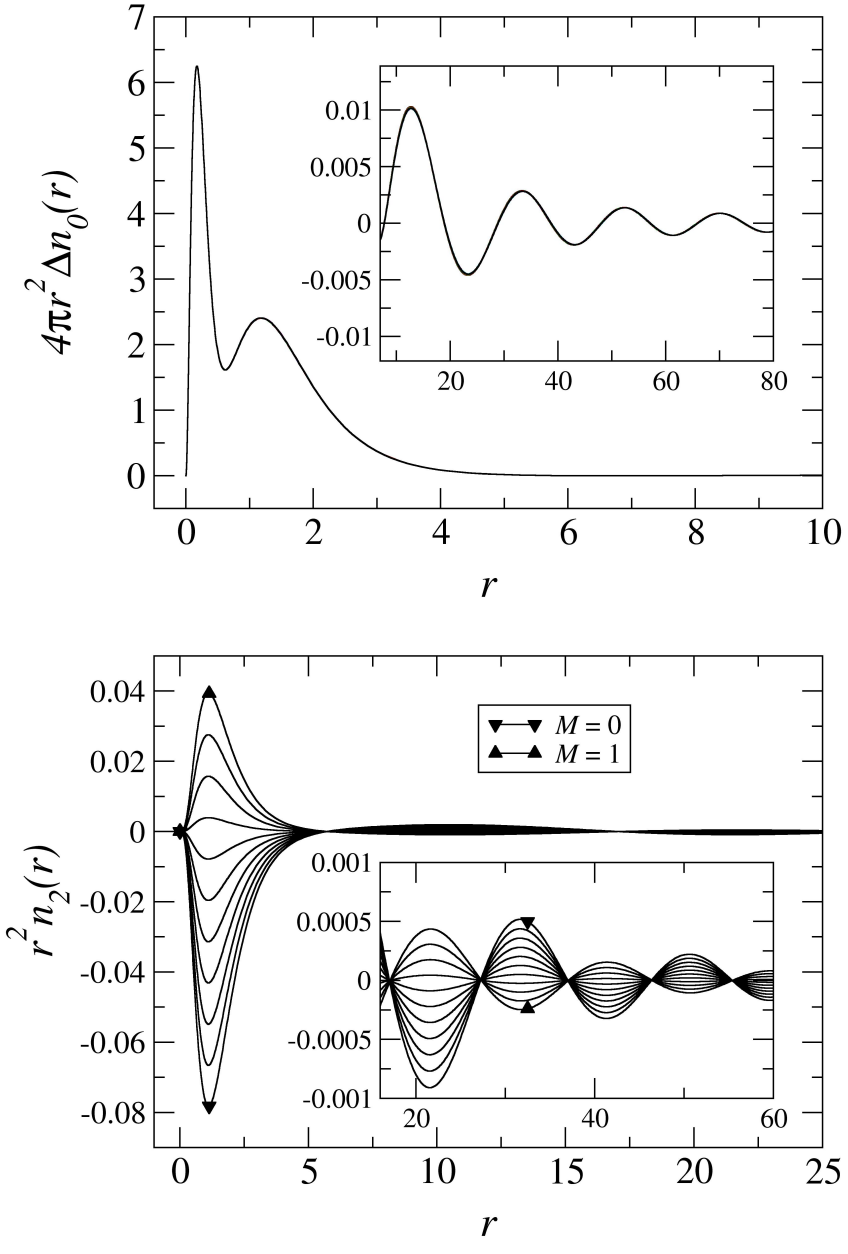

FIGURE 5.10: Variation in the total electron density as M is varied from $0 - 1$ at $n_0 = 0.0002$ background density for a neutral carbon impurity.

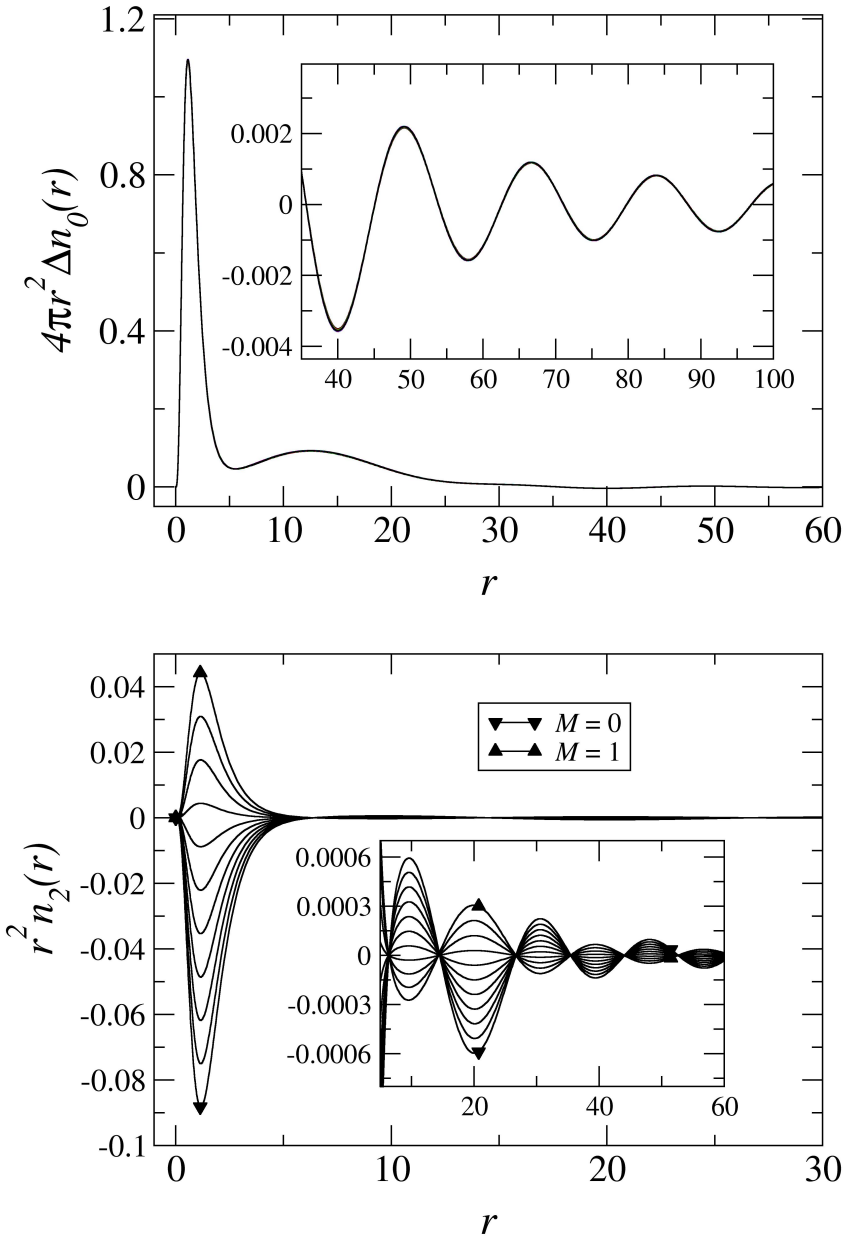

FIGURE 5.11: Variation in the total spin-density as M is varied from $0-1$ at $n_0 = 0.0002$ background density for a neutral carbon impurity.

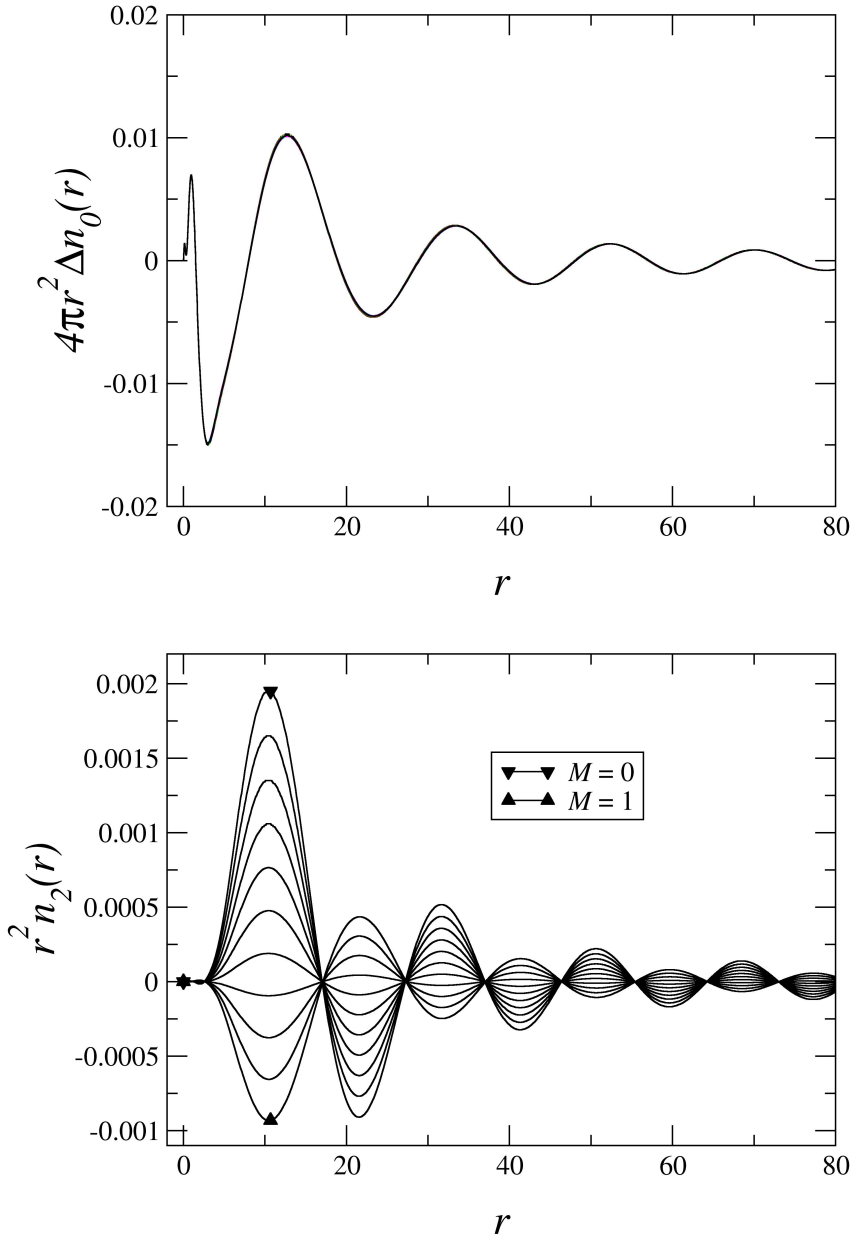

FIGURE 5.12: Variation in the conduction band electron density as M is varied from $0 - 1$ at $n_0 = 0.0002$ background density for a neutral carbon impurity.

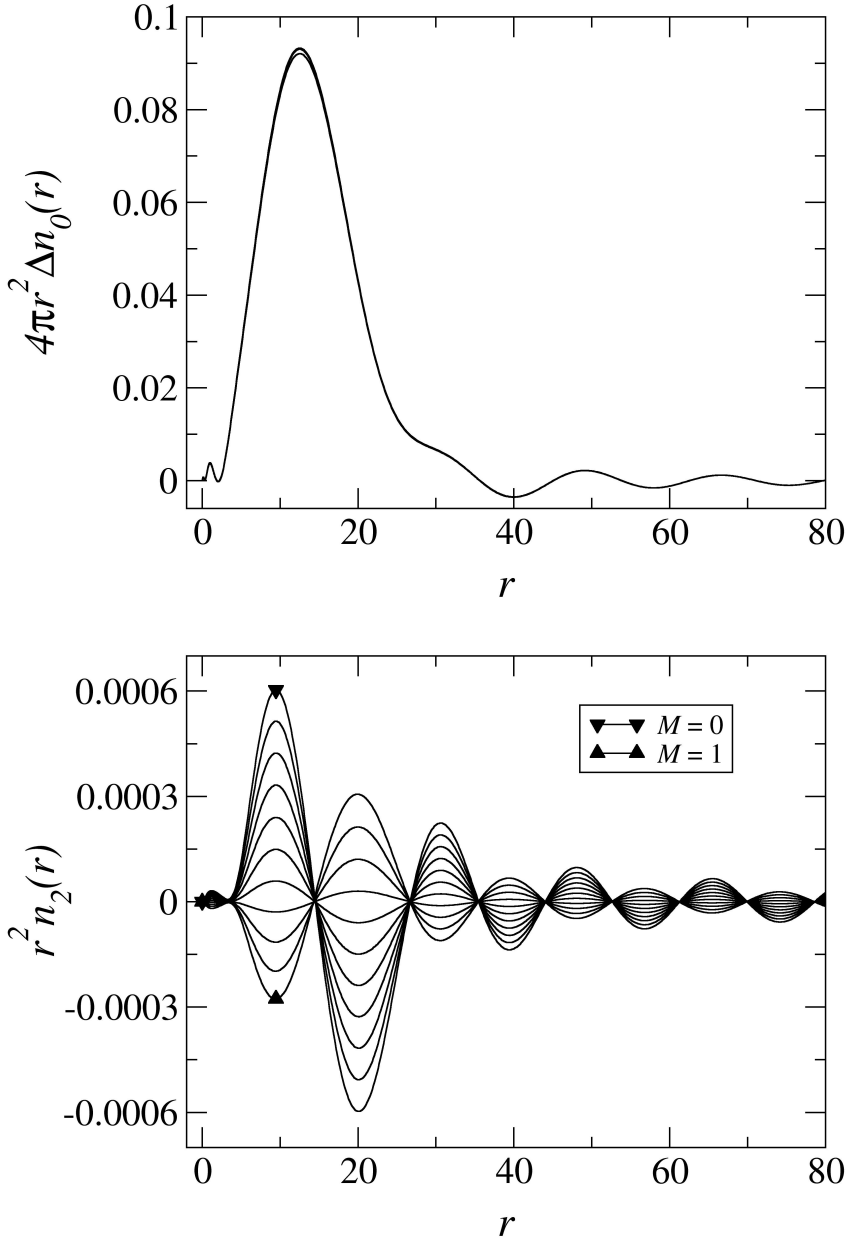

FIGURE 5.13: Variation in the conduction band spin-density as M is varied from $0 - 1$ at $n_0 = 0.0002$ background density for a neutral carbon impurity.

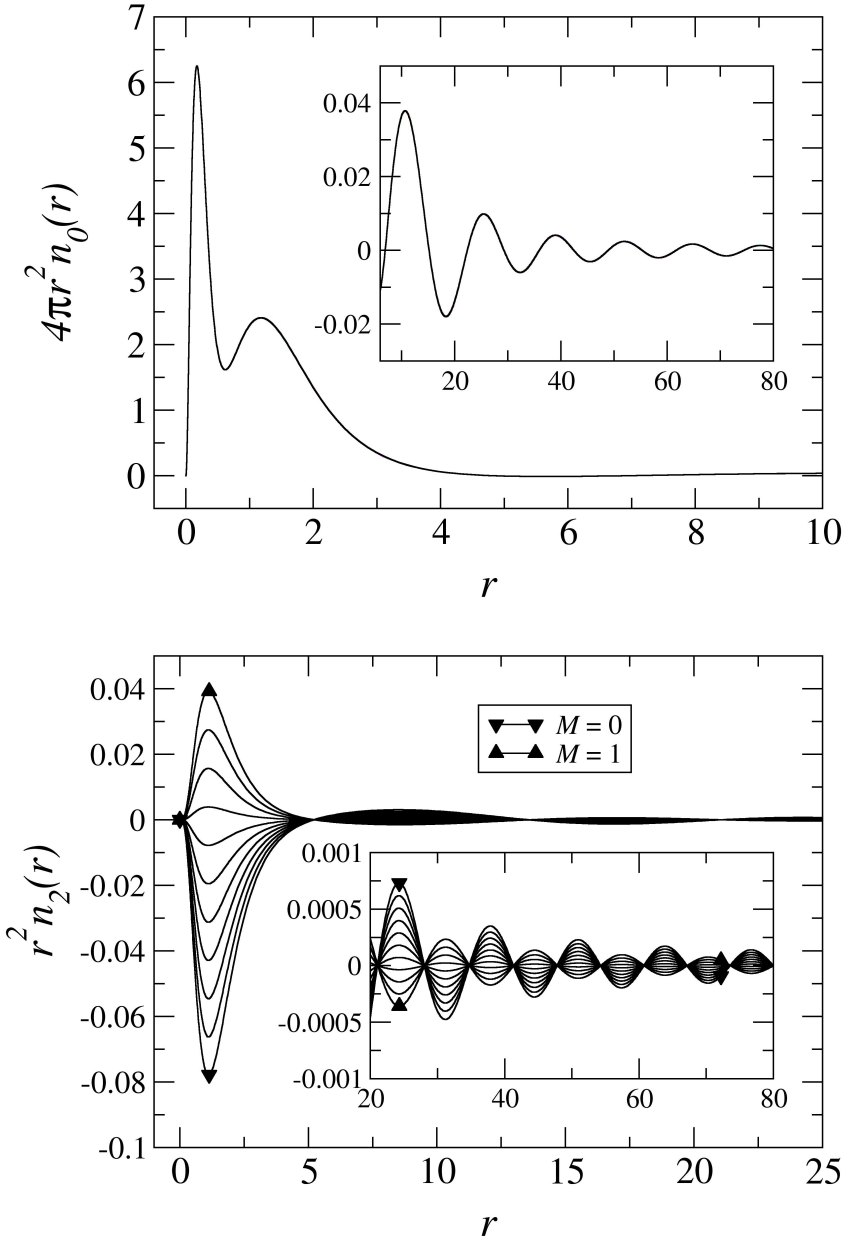

FIGURE 5.14: Variation in the total electron density as M is varied from $0 - 1$ at $n_0 = 0.0005$ background density for a neutral carbon impurity.

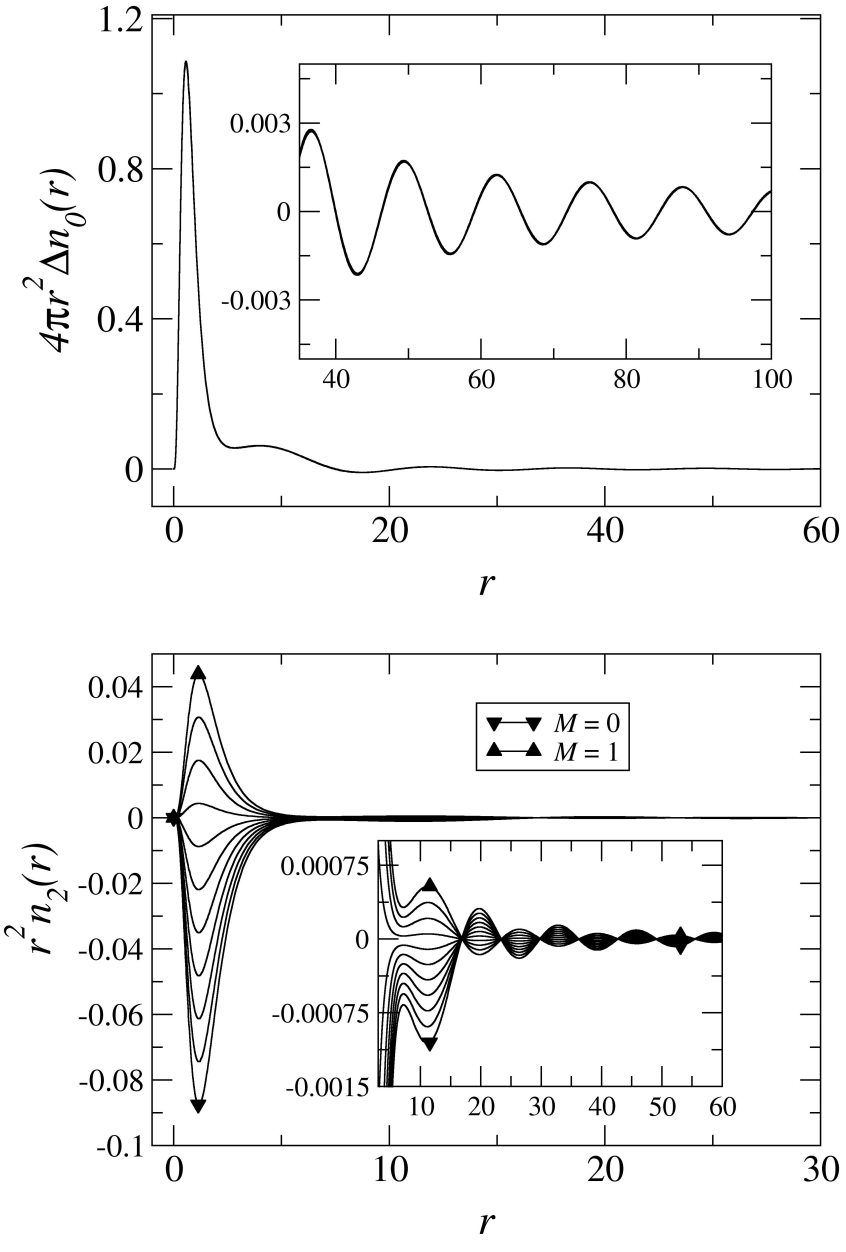

FIGURE 5.15: Variation in the total spin-density as M is varied from $0-1$ at $n_0 = 0.0005$ background density for a neutral carbon impurity.

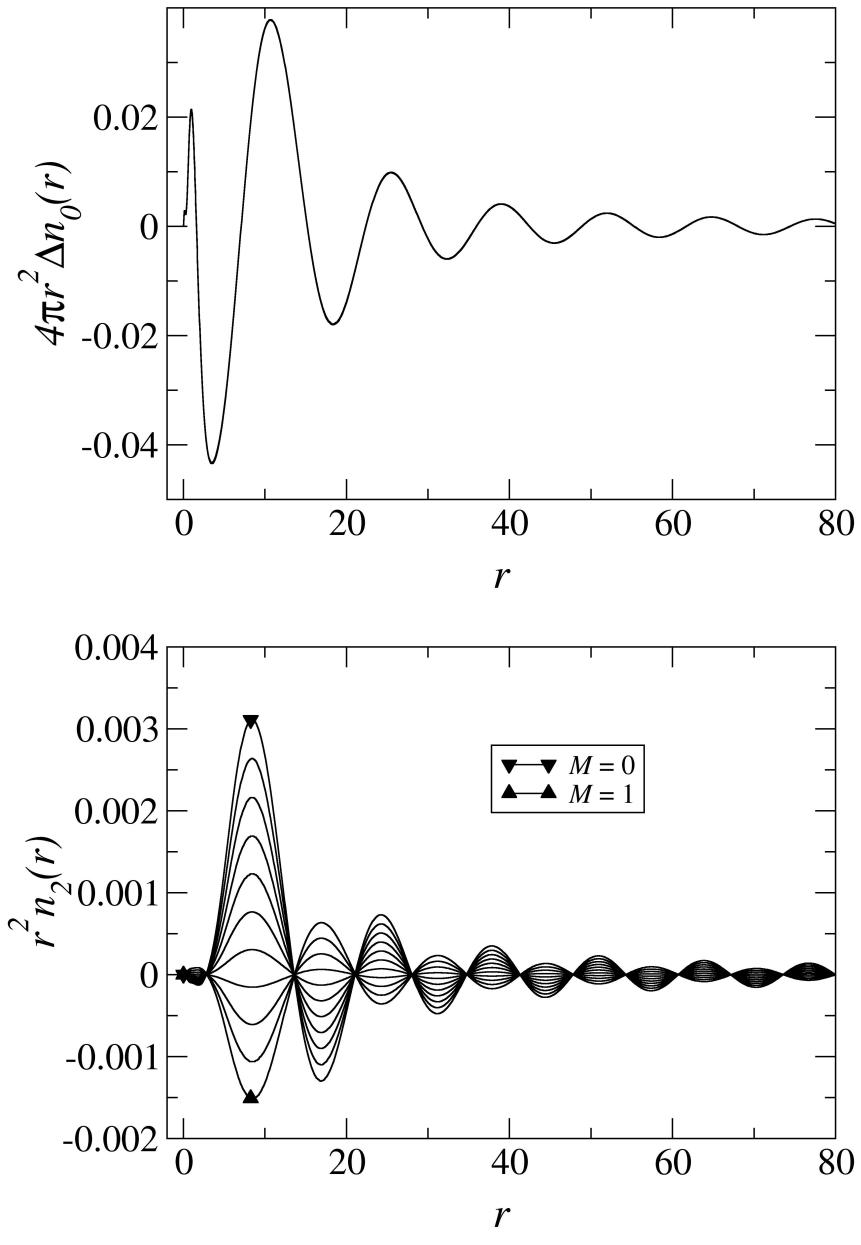

FIGURE 5.16: Variation in the conduction band electron density as M is varied from $0 - 1$ at $n_0 = 0.0005$ background density for a neutral carbon impurity.

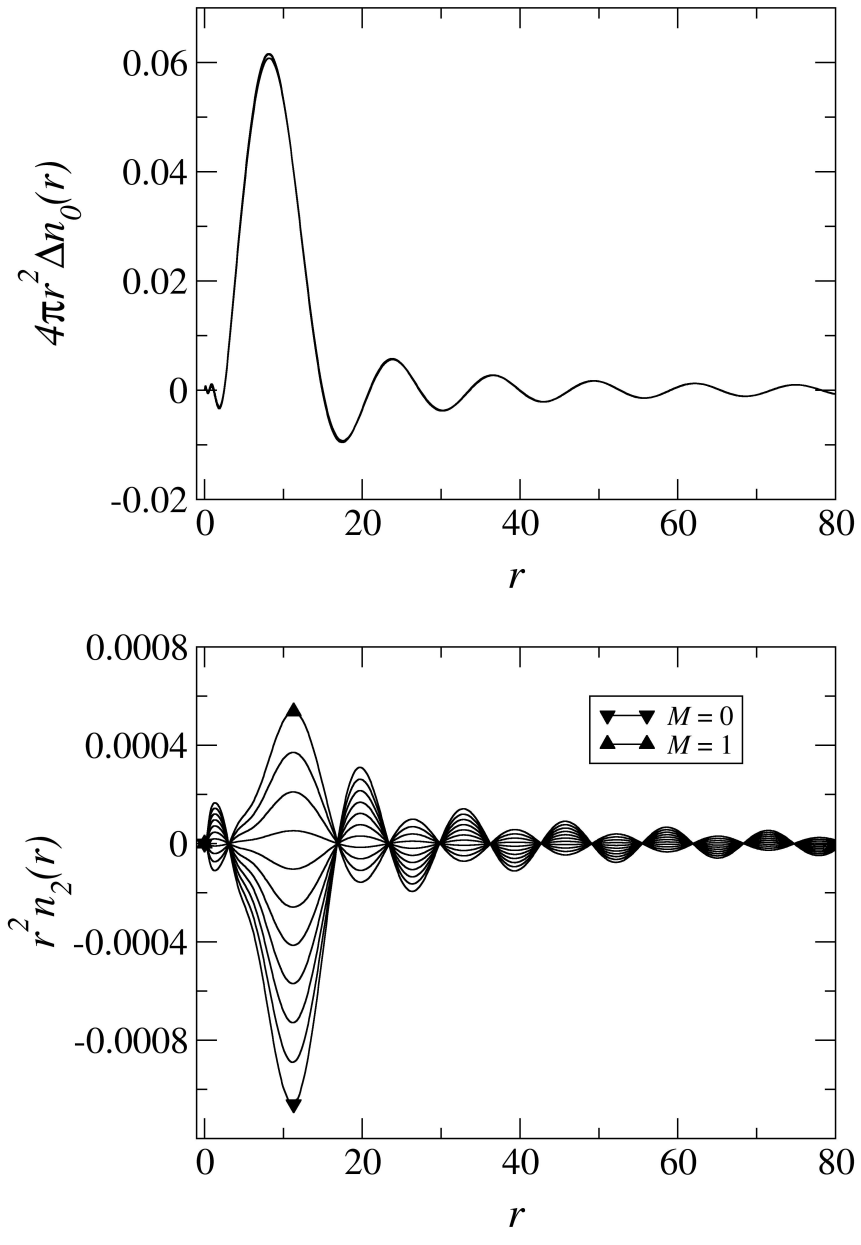

FIGURE 5.17: Variation in the conduction band spin-density as M is varied from $0 - 1$ at $n_0 = 0.0005$ background density for a neutral carbon impurity.

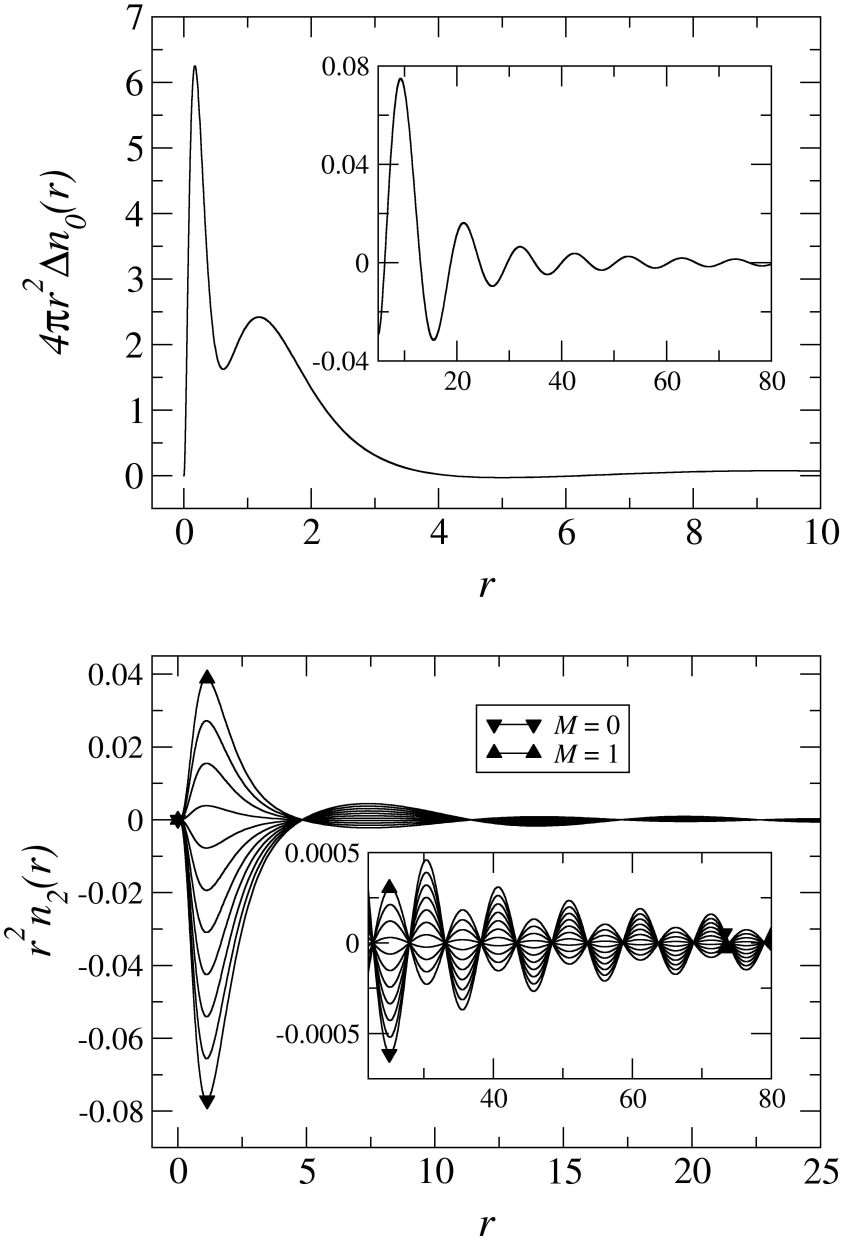

FIGURE 5.18: Variation in the total electron density as M is varied from $0-1$ at $n_0 = 0.001$ background density for a neutral carbon impurity.

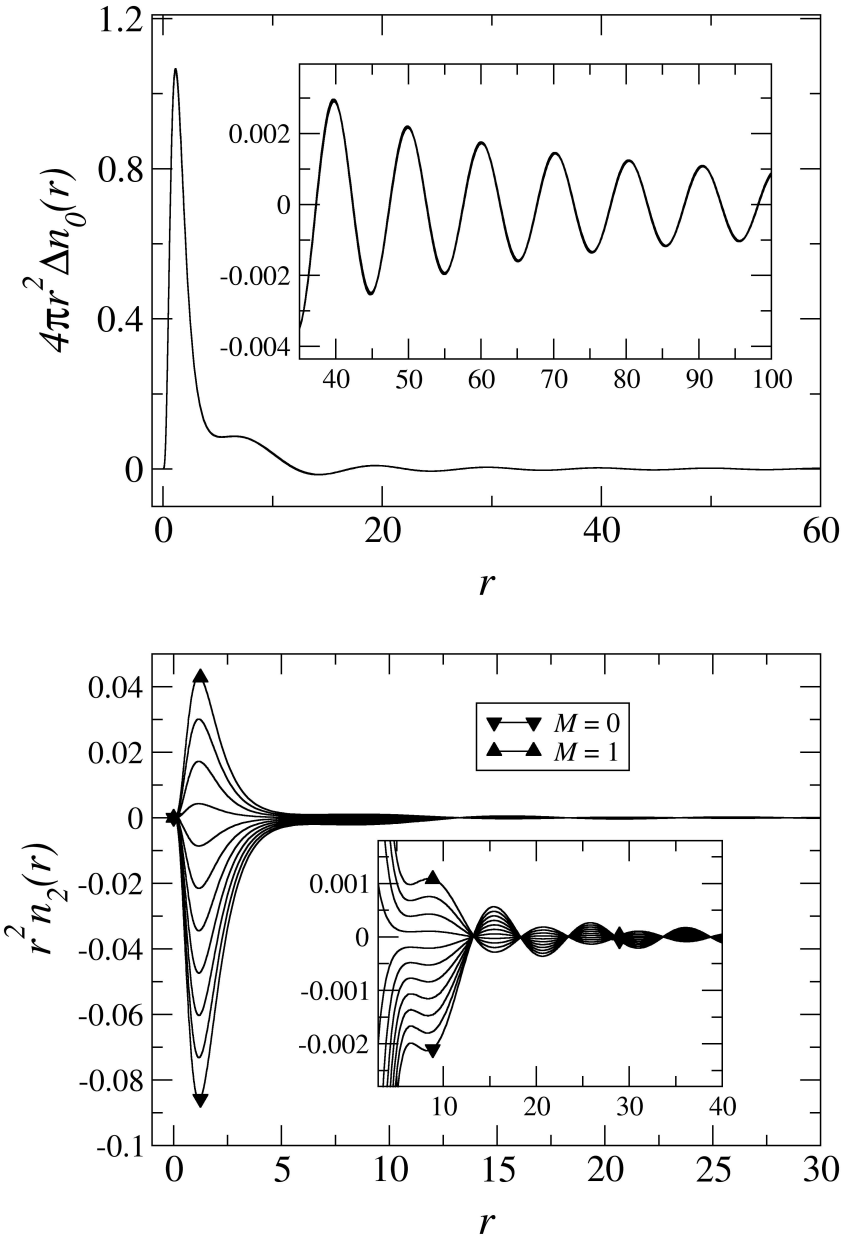

FIGURE 5.19: Variation in the total spin-density as M is varied from $0-1$ at $n_0 = 0.001$ background density for a neutral carbon impurity.

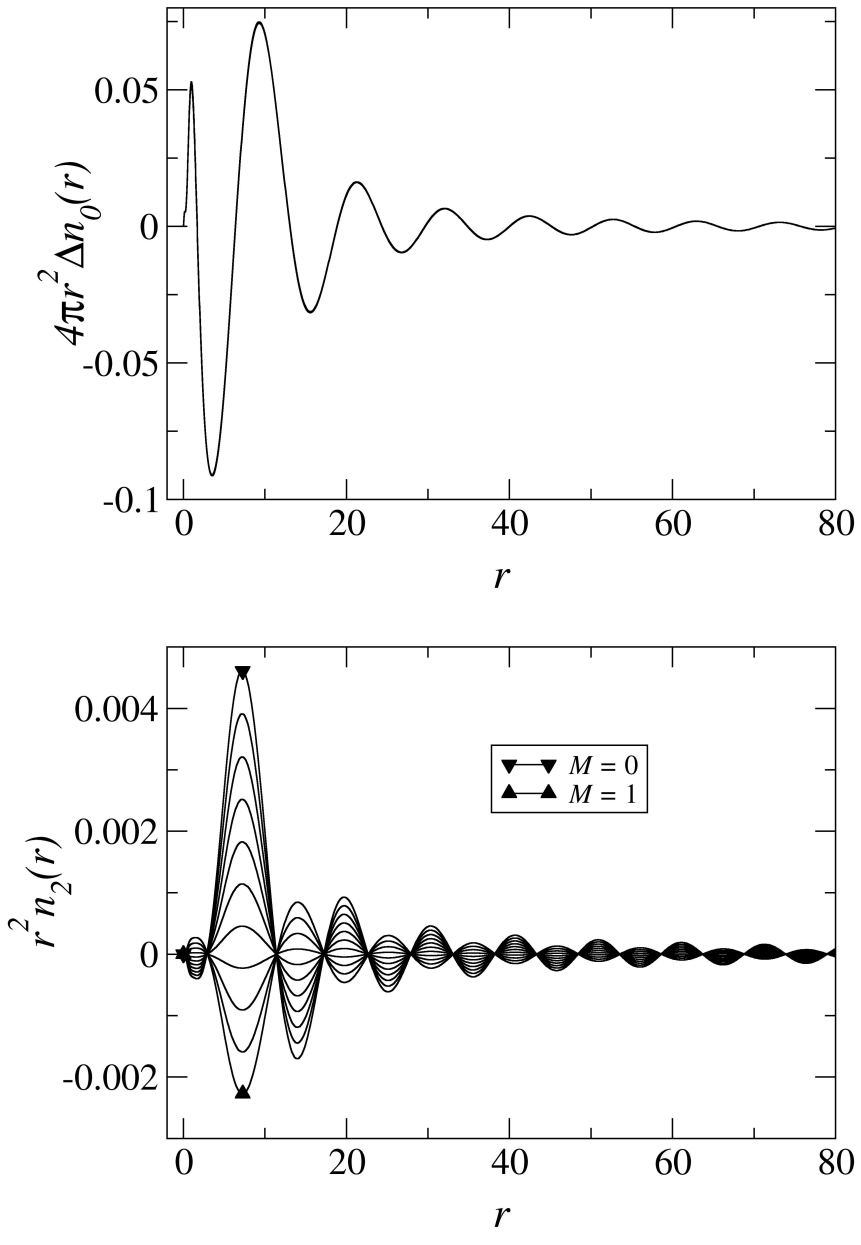

FIGURE 5.20: Variation in the conduction band electron density as M is varied from $0 - 1$ at $n_0 = 0.001$ background density for a neutral carbon impurity.

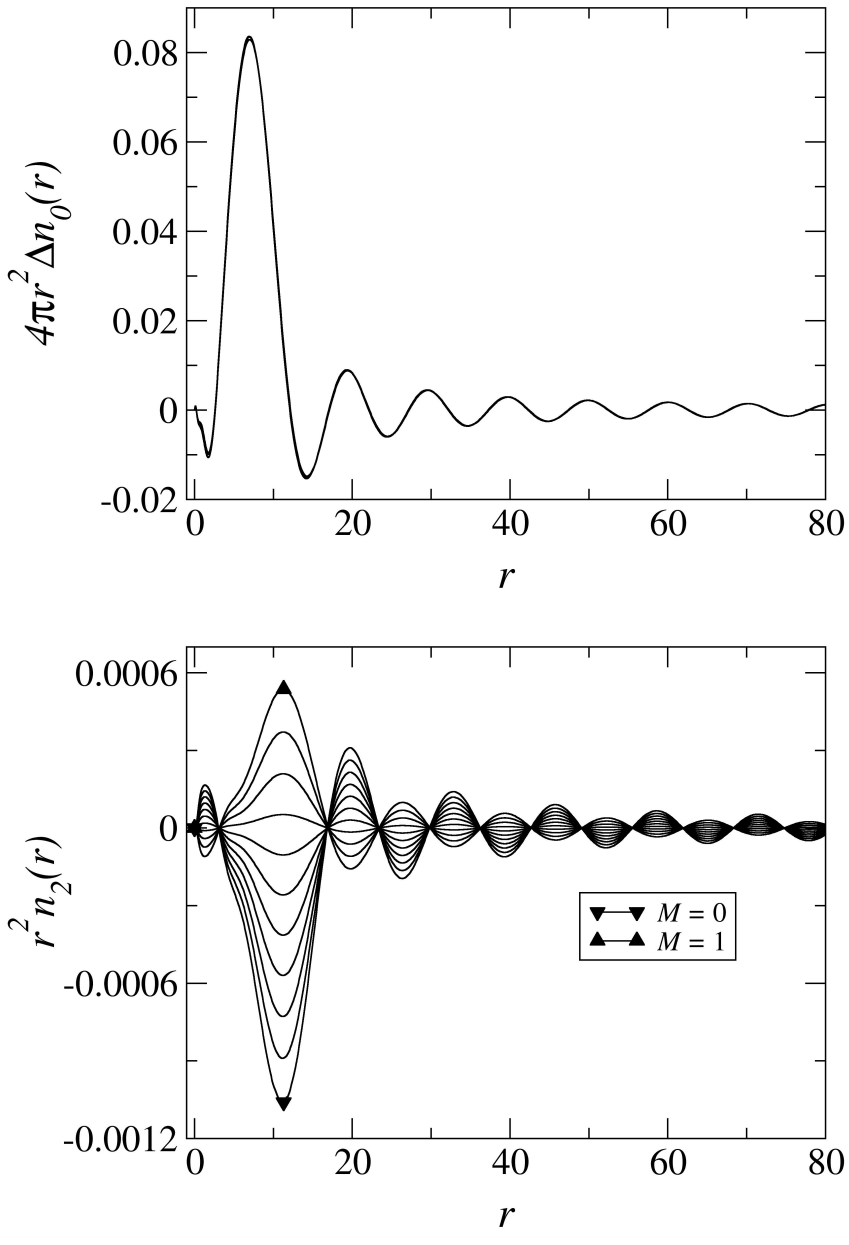

FIGURE 5.21: Variation in the conduction band spin-density as M is varied from $0 - 1$ at $n_0 = 0.001$ background density for a neutral carbon impurity.

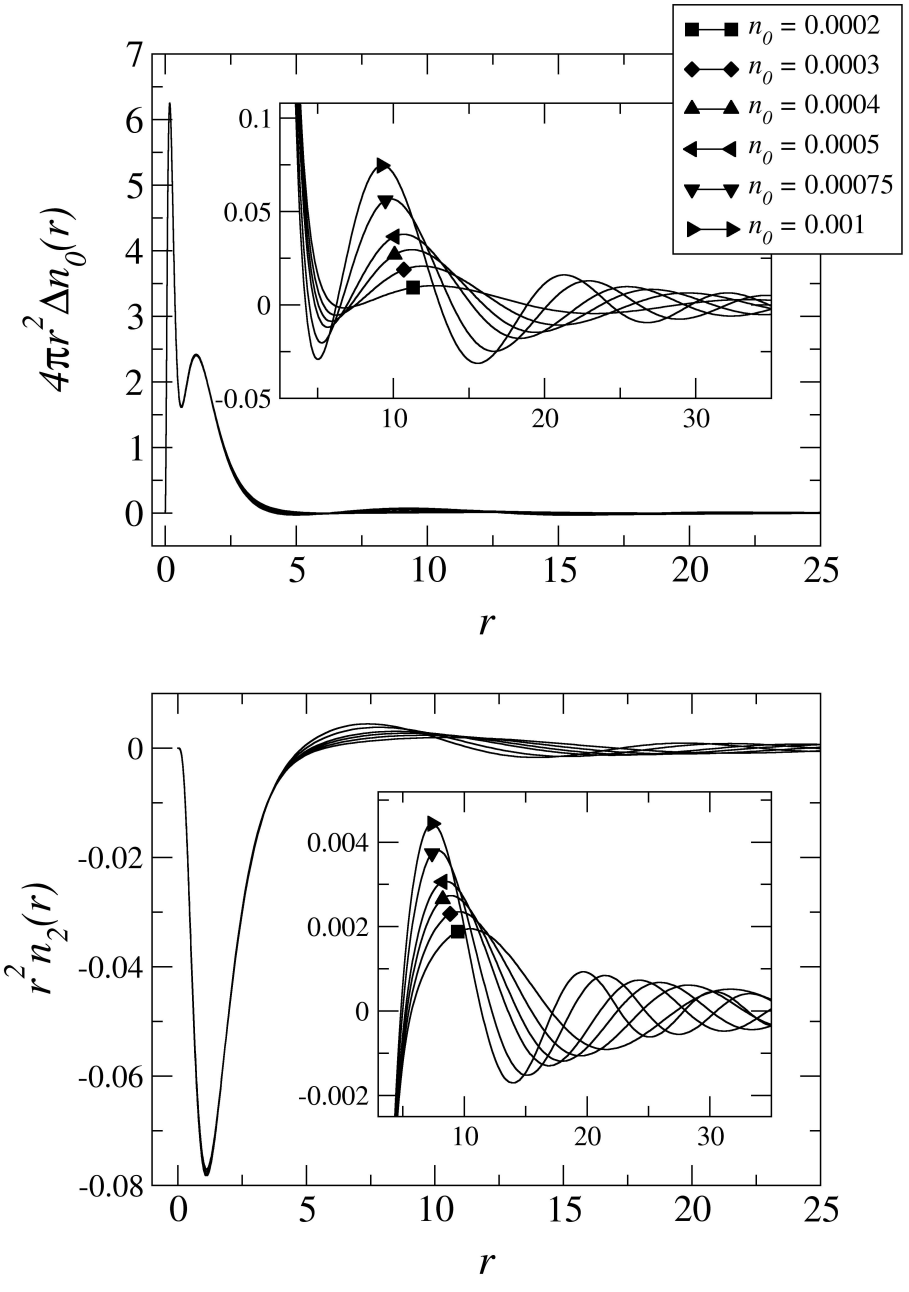

FIGURE 5.22: Induced electron density for a carbon impurity at low densities where the number of electrons in bound states has been limited to 6 with $M = 0$. The Friedel oscillations are seen to have an increasing amplitude as the background density is increased for both the spherical and nonspherical components of the electron density.

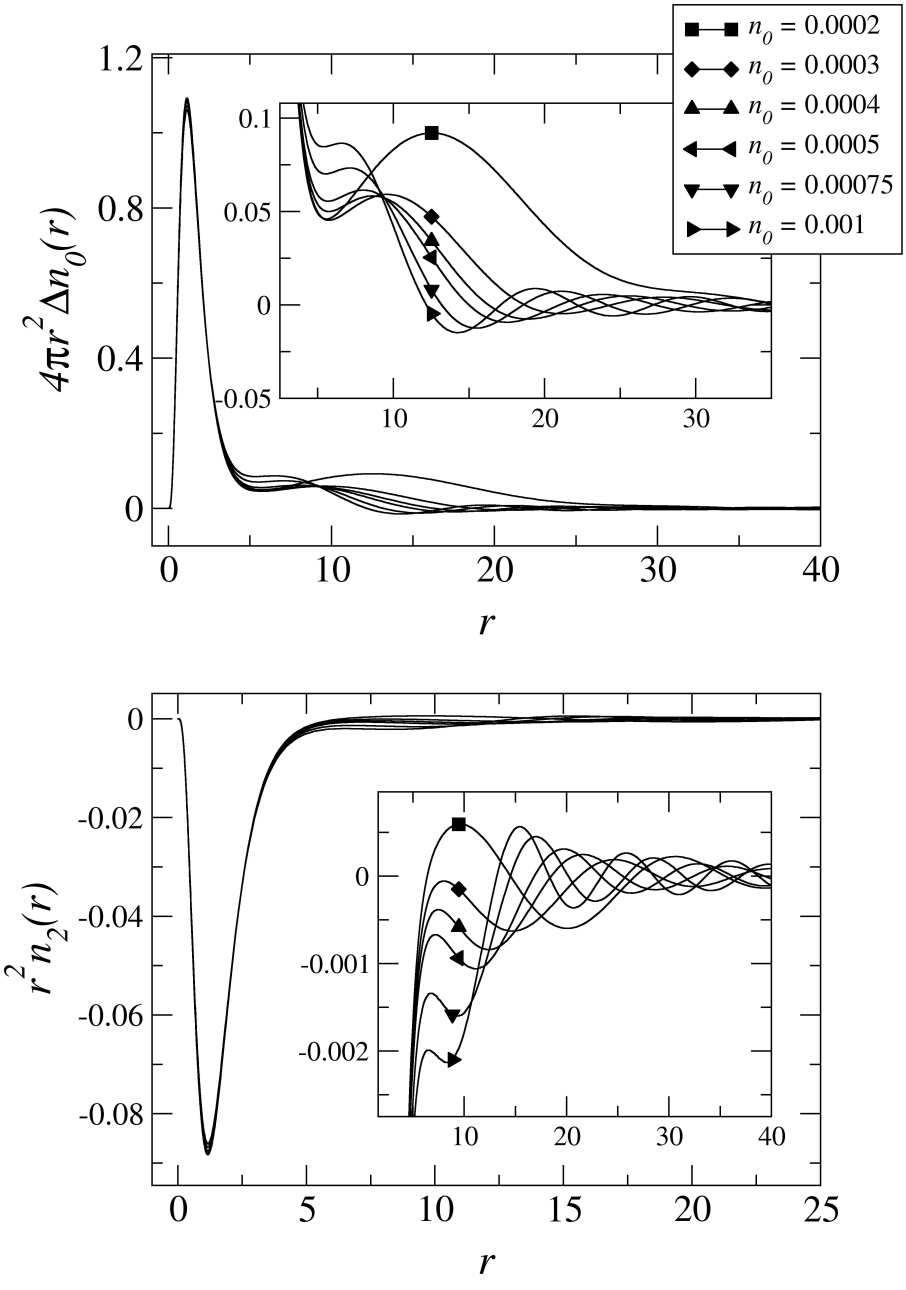

FIGURE 5.23: Induced spin-density for a carbon impurity at low background densities where the number of electrons in bound states has been limited to 6 with $M = 0$. There is a peak in the spherical spin-density due to a virtual bound state in the spin up channel at low density. As this peak disappears at higher densities, the Friedel oscillations are seen to begin closer to the impurity.

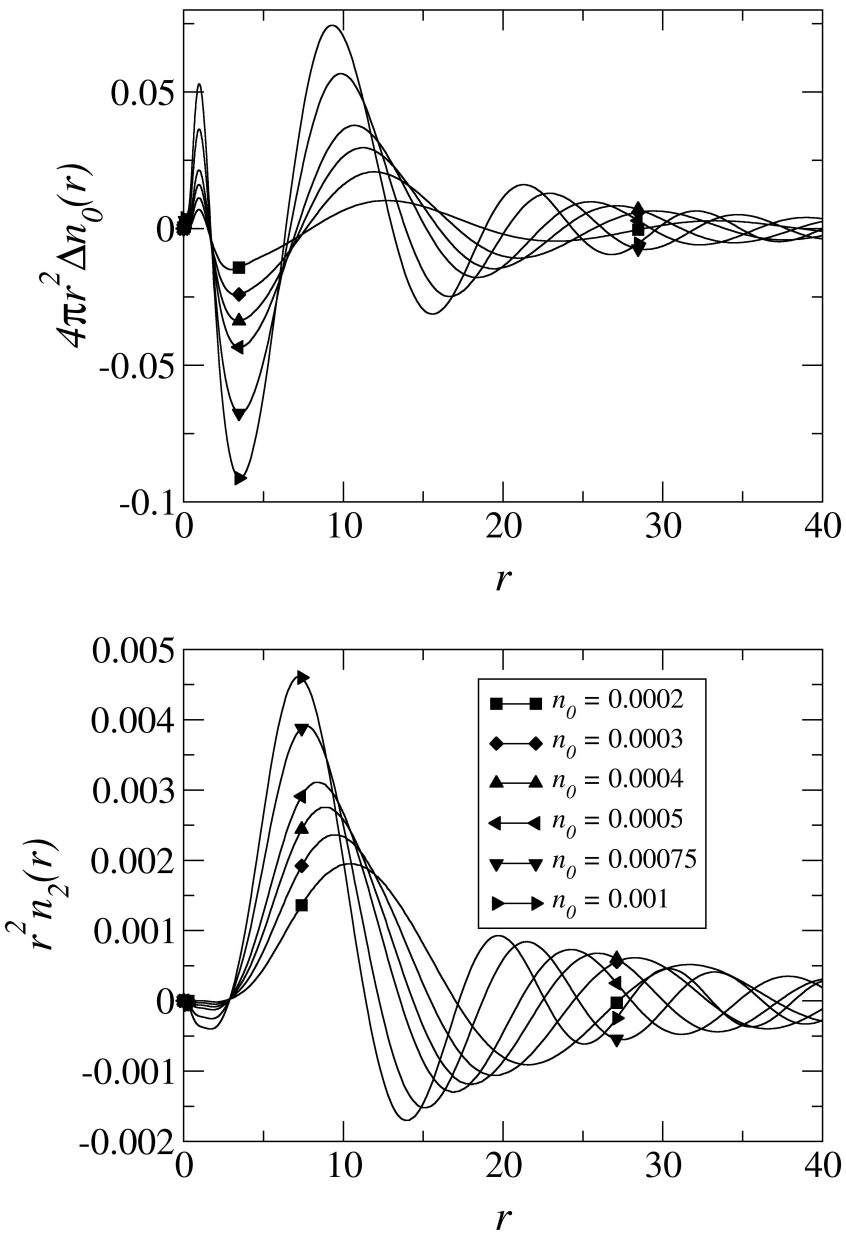

FIGURE 5.24: Induced density in the conduction band for a carbon impurity at low background densities where the number of electrons in bound states has been limited to 6 with $M = 0$. The increase in amplitude and decrease in wavelength of the Friedel oscillations with increasing background density is clearly seen.

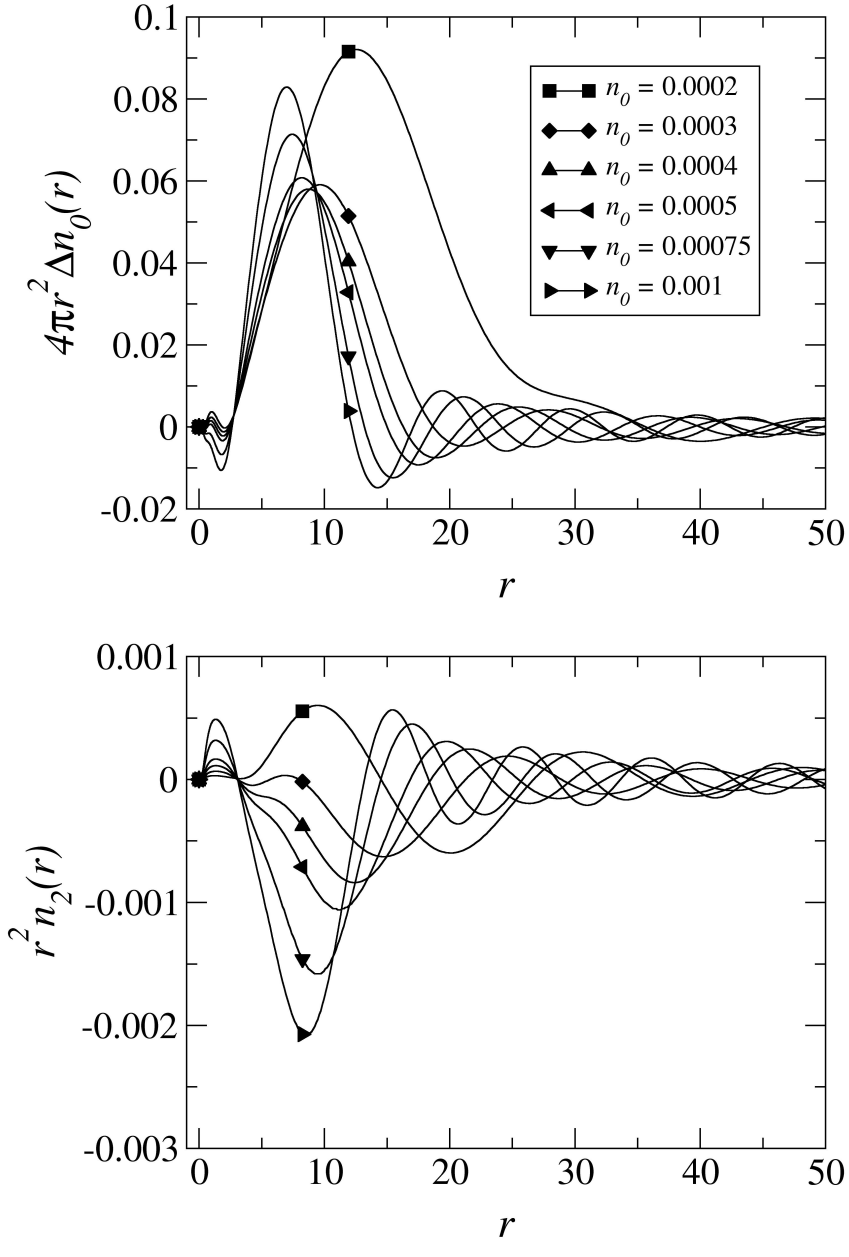

FIGURE 5.25: Induced spin-density in the conduction for a carbon impurity at low background densities where the number of electrons in bound states has been limited to 6 with $M = 0$. There is a peak in the spherical spin density due to a virtual bound state in the spin up channel at low density.

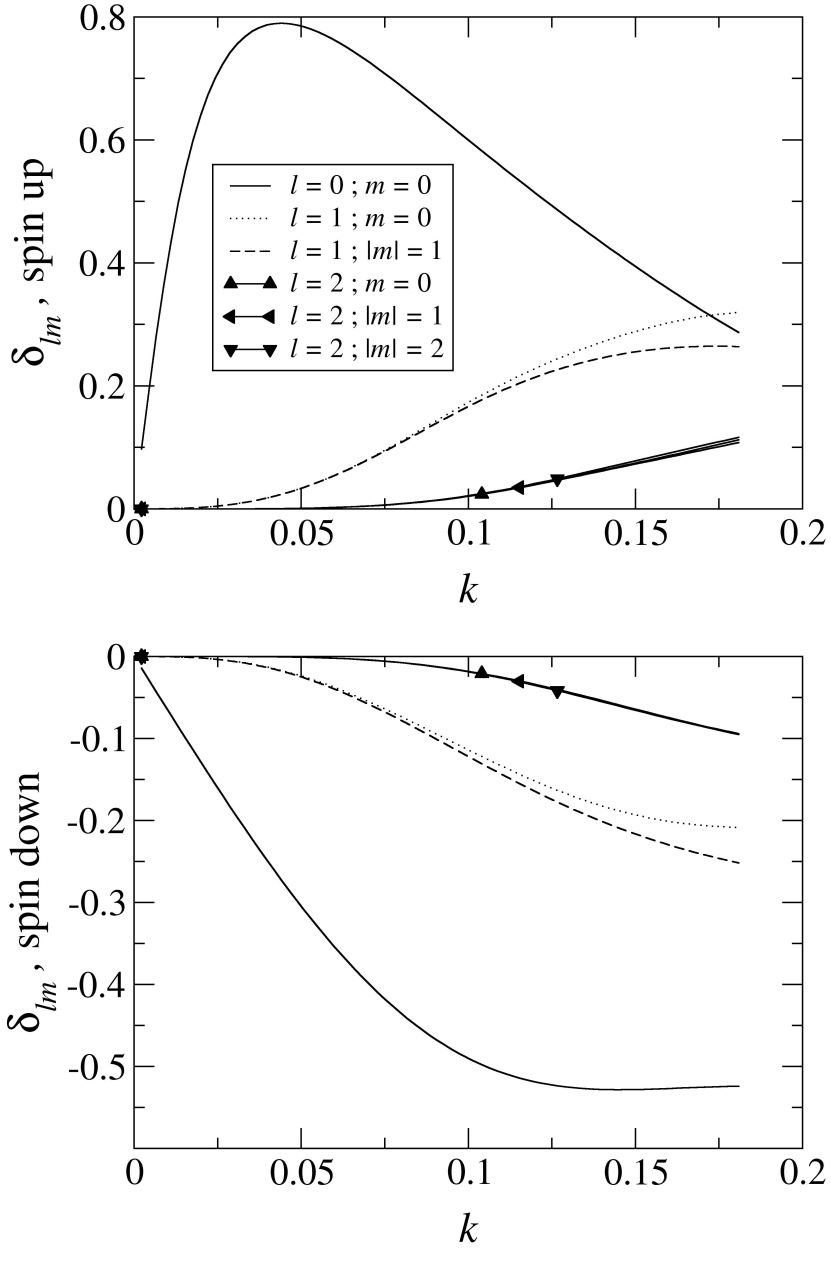

FIGURE 5.26: Phase shifts for $l = 0, 1, 2$ conduction electrons scattered from a neutral carbon impurity at 0.0002 background density with $M = 0$. The very large slope at the bottom of the conduction band indicates a virtual bound state resonance for the $l = 0$ spin up channel at this low density. It is also seen that the $l = 2$ states are affected roughly equally, indicating that the nonspherical effects are less pronounced than for lower-order partial-waves.

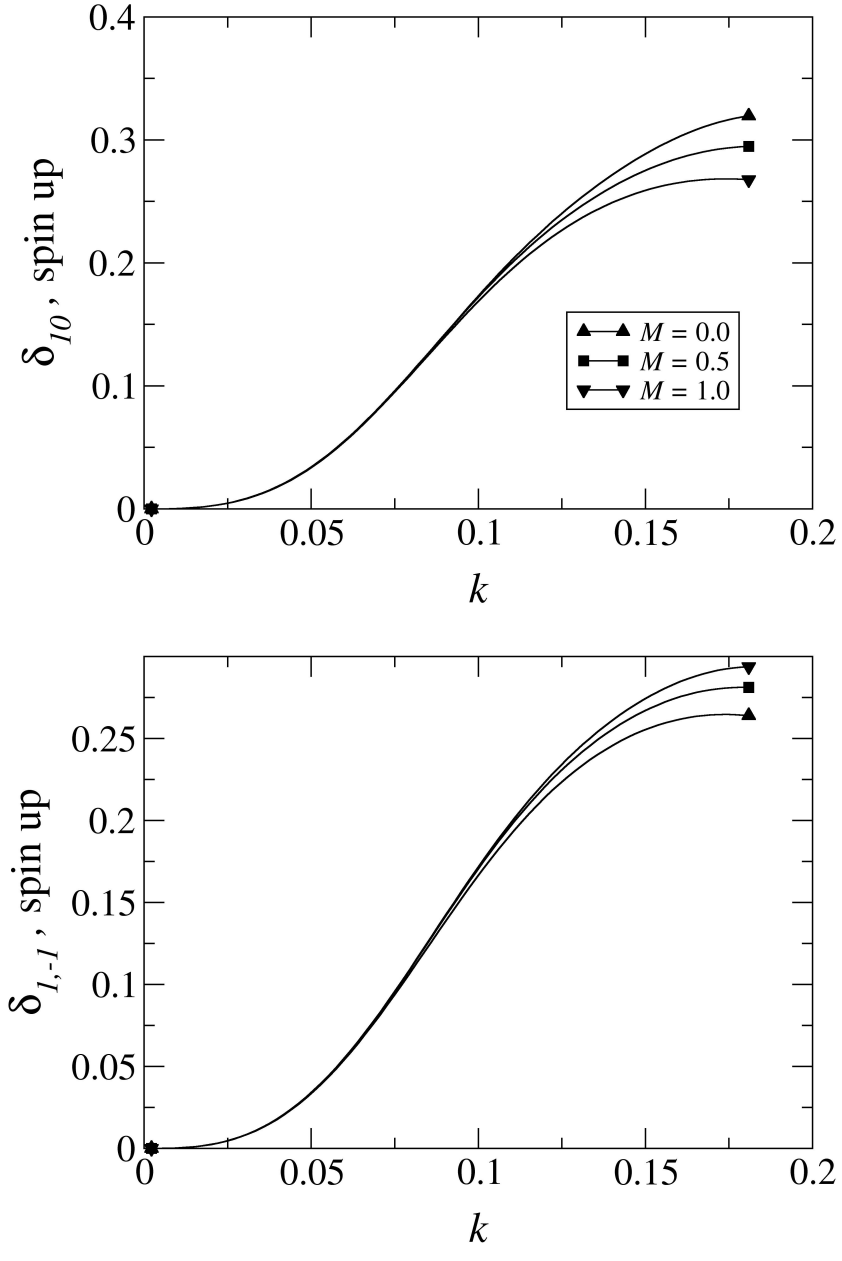

FIGURE 5.27: Phase shifts for $l = 1$ spin up electrons in the conduction band as M is varied for a neutral carbon impurity at 0.0002 background density. As M ranges from $0-1$, the population of the $2p_0^+$ varies from $1-0$ and the phase shift of the $l = 1$ $m = 0$ spin up channel is seen to decrease, indicating a smaller contribution to the induced density of states in the conduction band. The opposite trend is seen for the $l = 1$ $m = +/-1$ spin up channel.

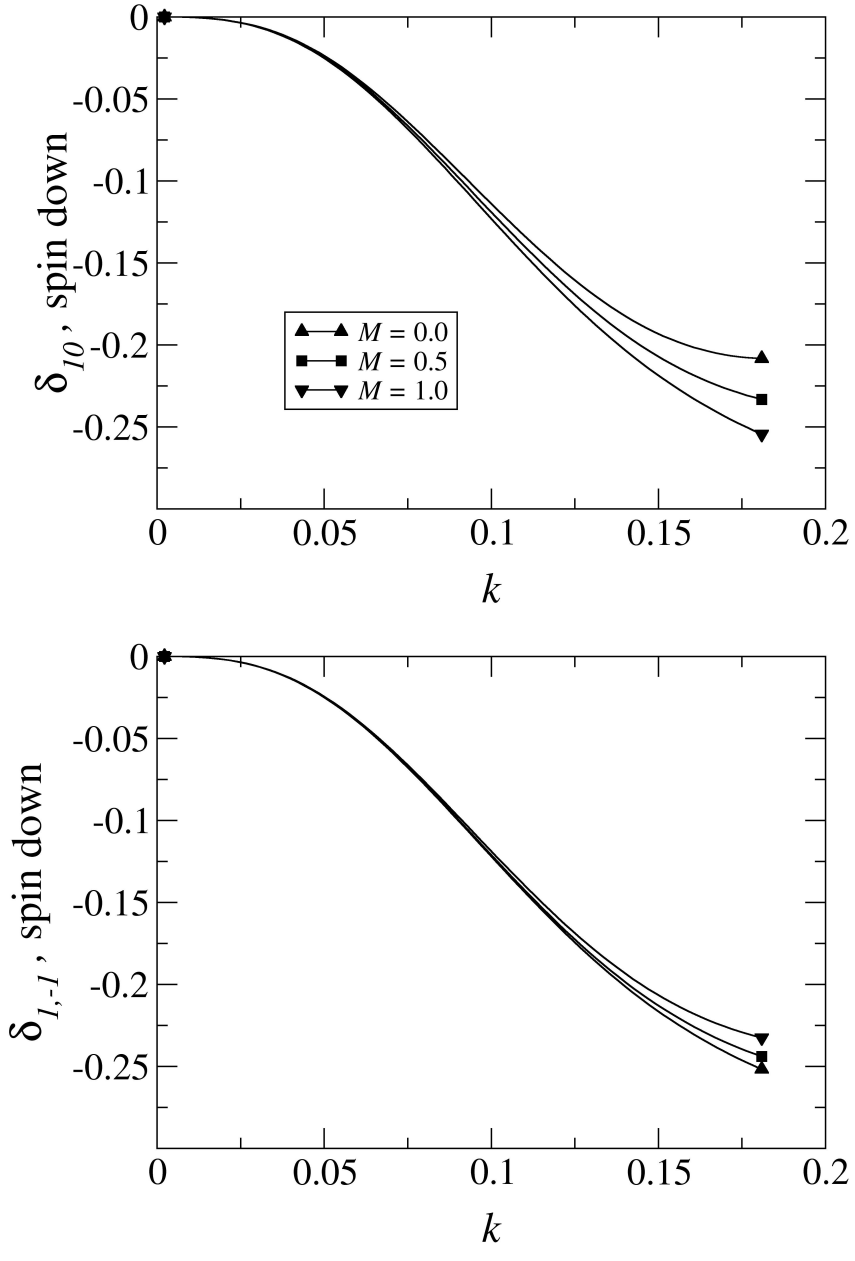

FIGURE 5.28: Phase shifts for $l = 1$ spin down electrons in the conduction band as M is varied for a neutral carbon impurity at 0.0002 background density. As M ranges from $0 - 1$, the population of the $2p_0^+$ varies from $1 - 0$ and the phase shift of the $l = 1$ $m = 0$ spin down channel is seen to decrease, indicating a larger negative contribution to the induced density of states in the conduction band. The opposite trend is seen for the $l = 1$ $m = +/-1$ spin down channel.

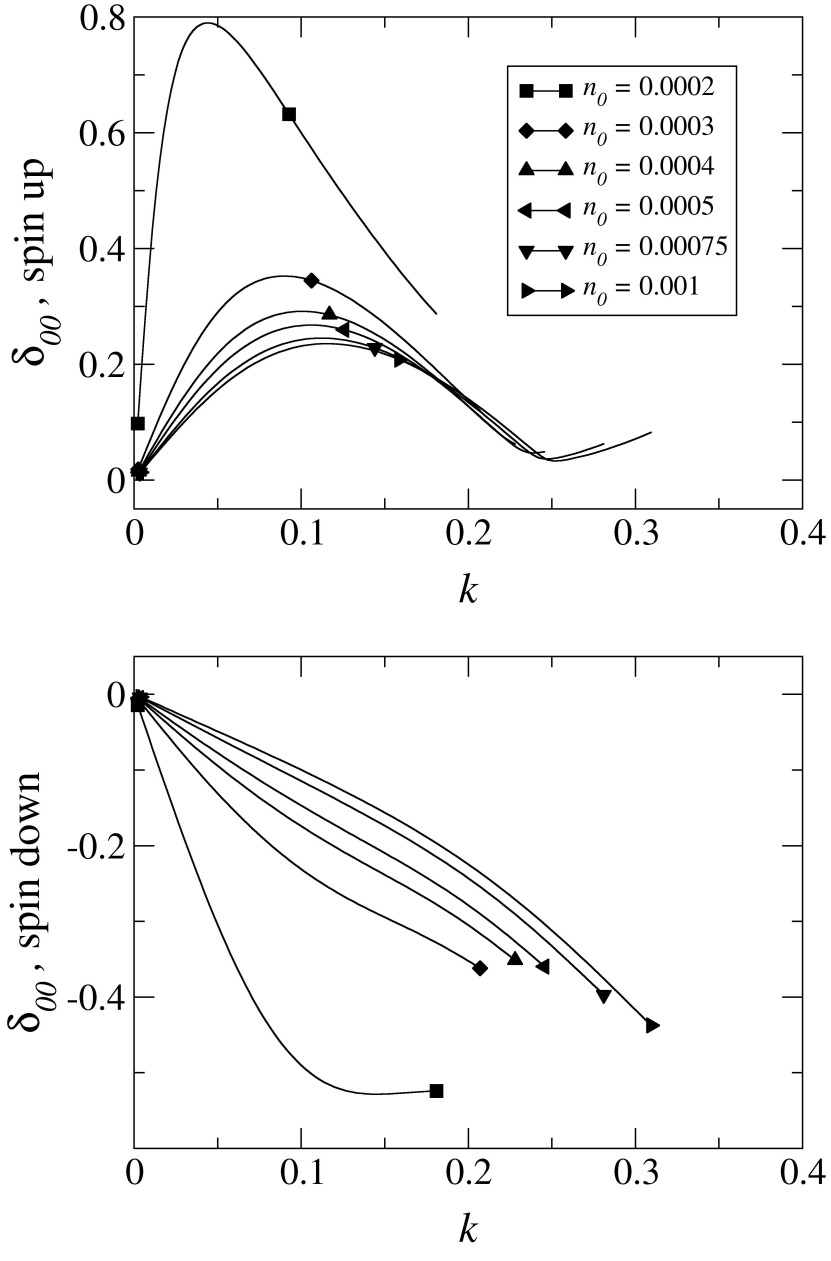

FIGURE 5.29: Phase shifts for $l = 0$, $m = 0$ conduction electrons scattered from a neutral carbon impurity with $M = 0$ for low background densities. The large slope near the bottom of the conduction band can be seen to decrease in magnitude dramatically as the background density is increased, for both spin up and spin down electrons, indicating a quenching of spin-polarization effects.

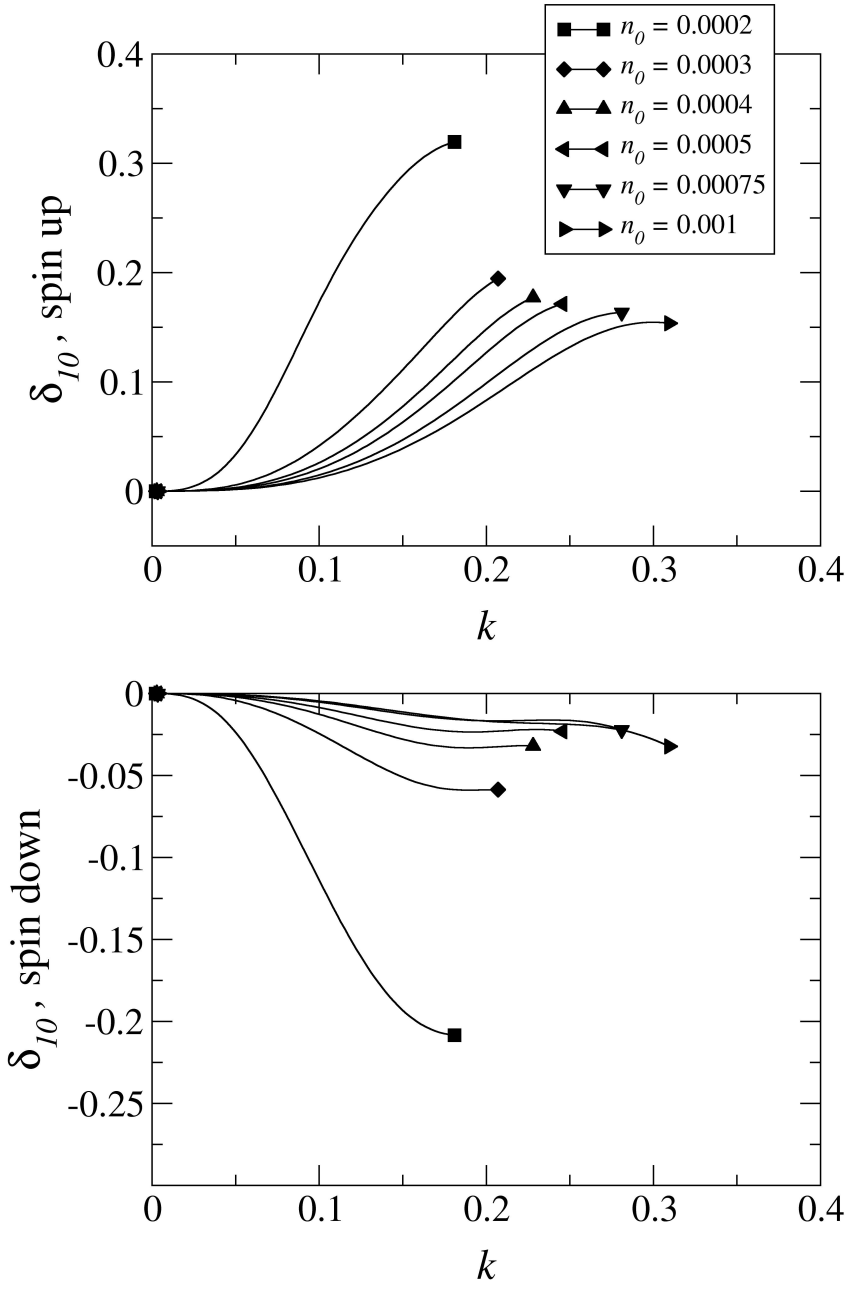

FIGURE 5.30: Phase shifts for $l = 1$, $m = 0$ conduction electrons scattered from a neutral carbon impurity with $M = 0$ for low background densities. As the background density is increased, the phase shift near the Fermi level decreases, indicating a smaller contribution to the partial wave decomposition of the Friedel sum rule and a quenching of nonspherical effects.

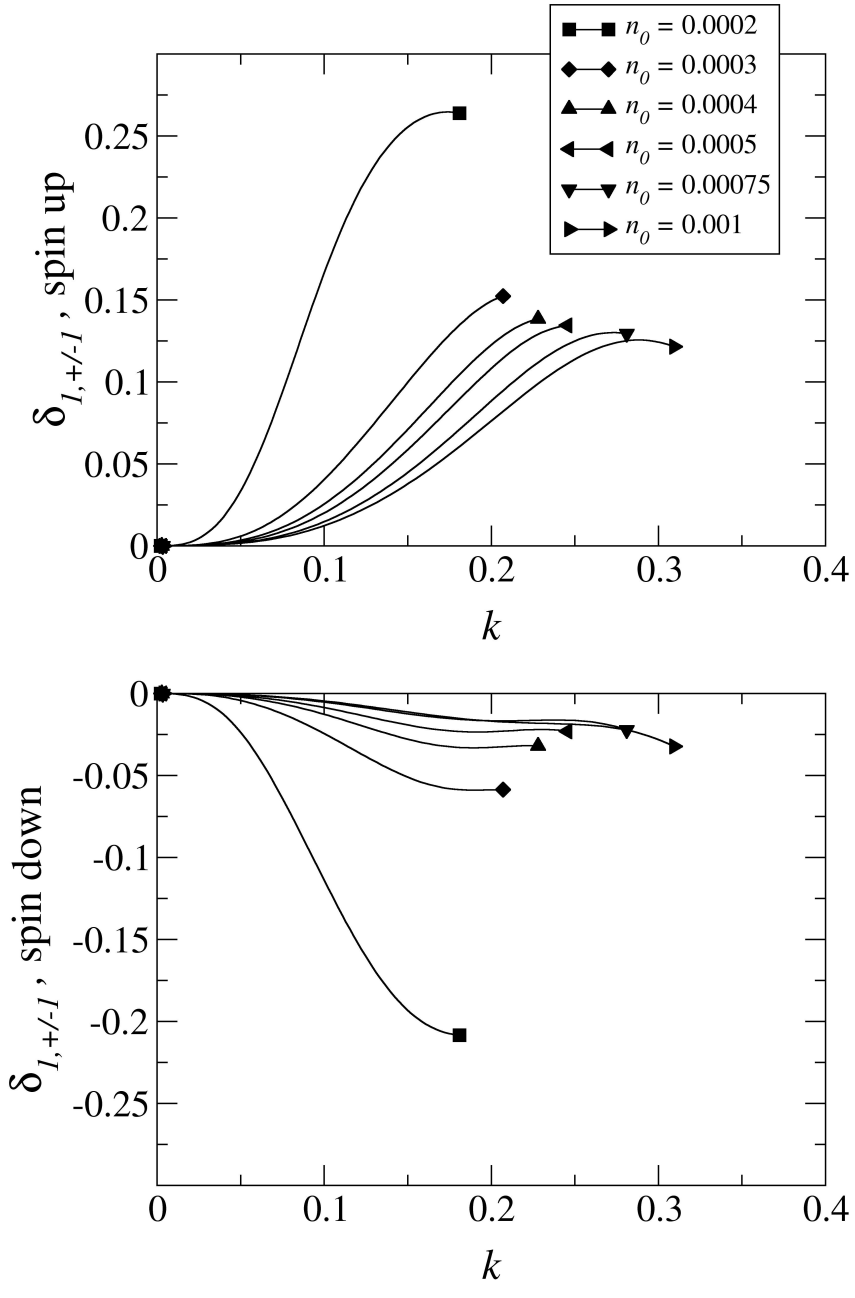

FIGURE 5.31: Phase shifts for $l = 1$, $|m| = 1$ conduction electrons scattered from a neutral carbon impurity with $M = 0$ for low background densities. As the background density is increased, the phase shift near the Fermi level decreases, indicating a smaller contribution to the partial wave decomposition of the Friedel sum rule and a quenching of nonspherical effects.

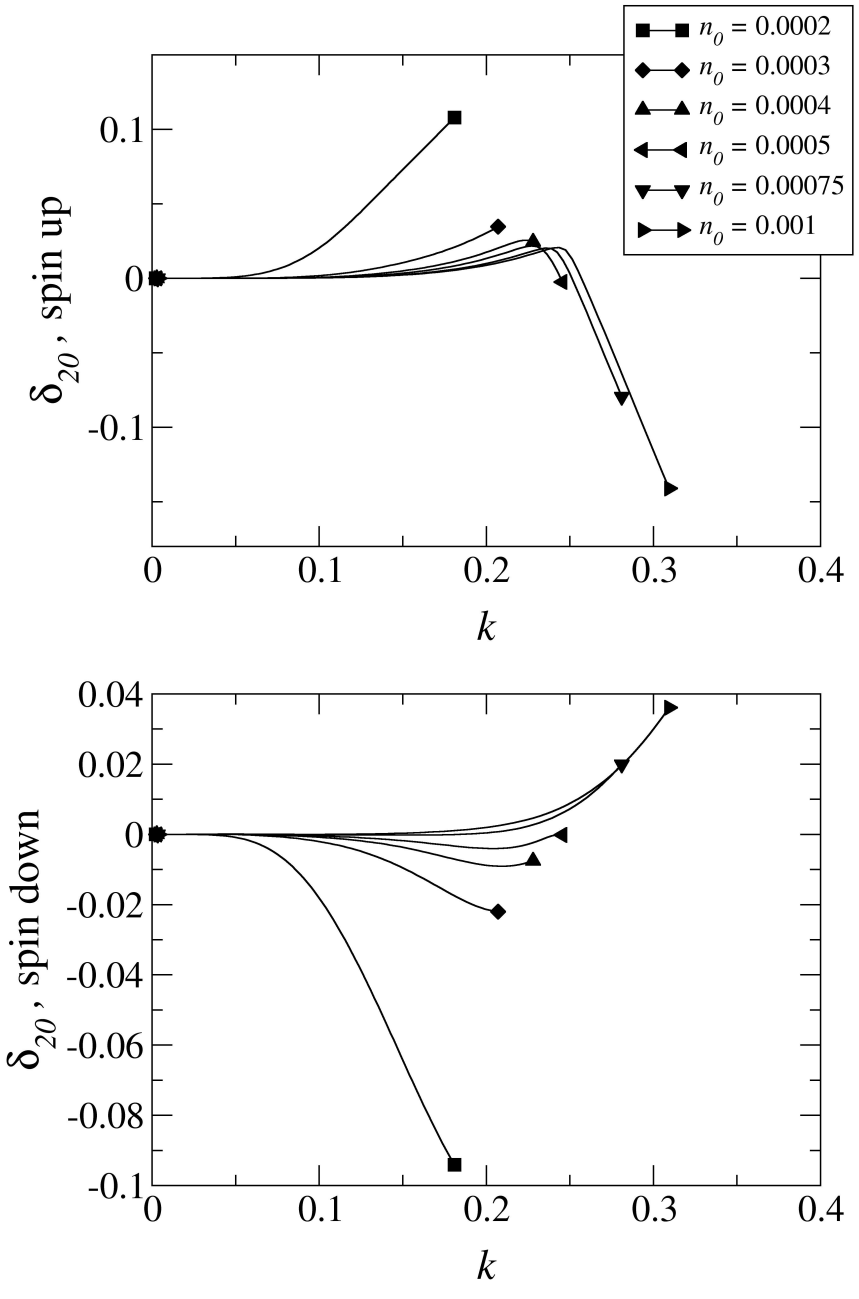

FIGURE 5.32: Phase shifts for $l = 2$, $m = 0$ for conduction electrons from a neutral carbon impurity with $M = 0$ at low background densities.

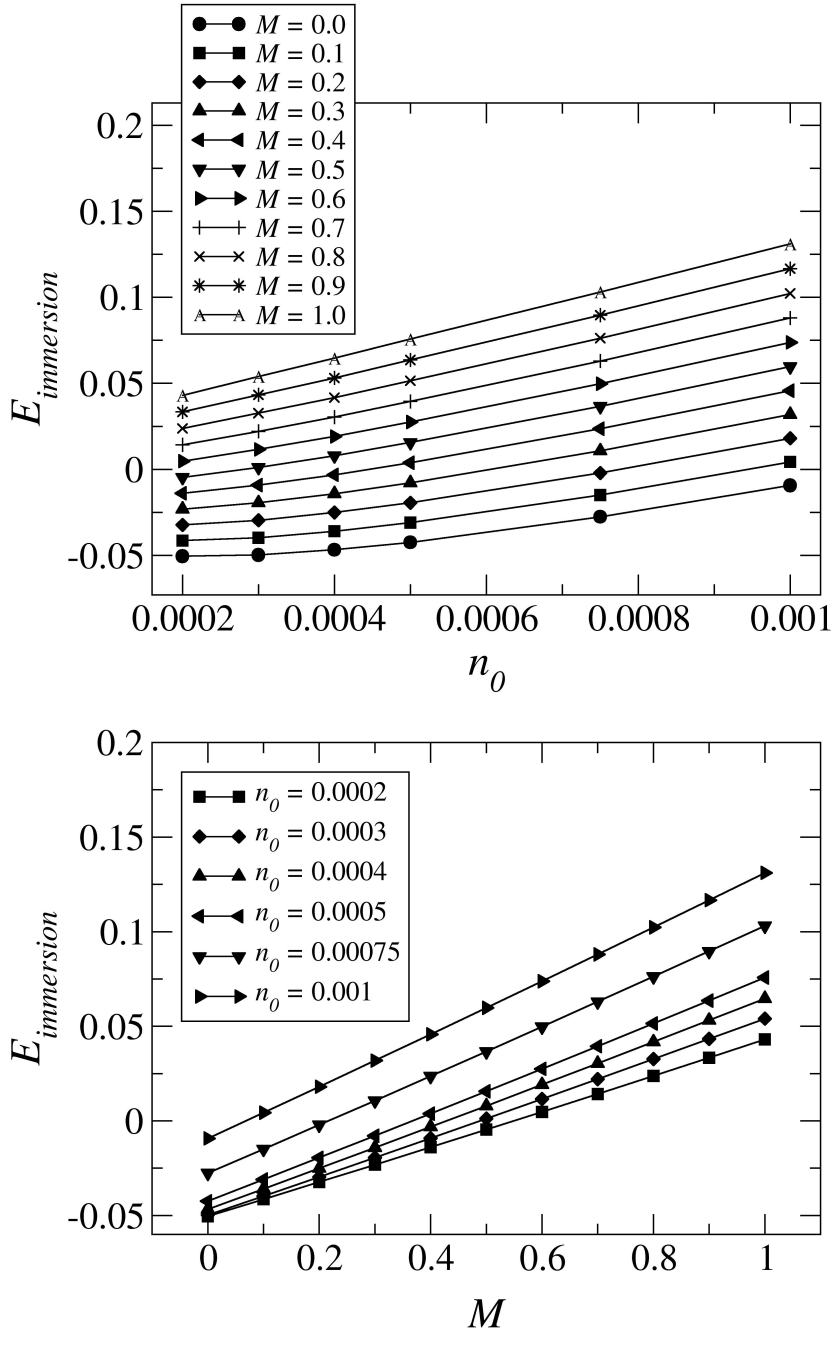

FIGURE 5.33: Variation in the immersion energy as M is varied from $0 - 1$ and the background density is varied from $n_0 = 0.0002$ to 0.001 for a neutral carbon impurity. Note that the differences in the immersion energy with variations of the background density are much larger than errors in the energy associated with the approximation to infinity, r_∞, discussed in Sec. 4.4.1.2. Also note that there is no minimum observed in any of the plots.

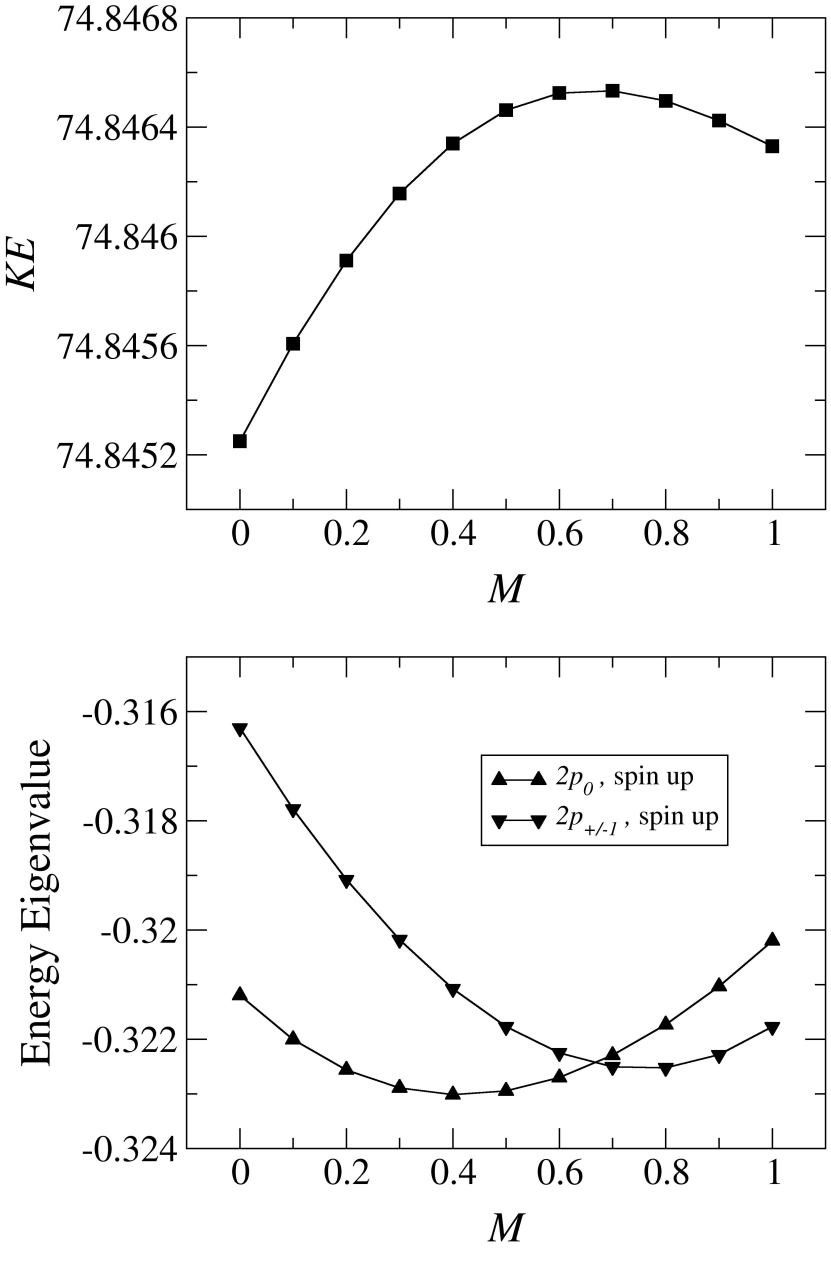

FIGURE 5.34: Variation in the kinetic energy and $2p$ spin up energy eigenvalues as M is varied from $0-1$ for a neutral carbon impurity at 0.0002 background density. The trends seen here are identical to those for a free carbon atom.

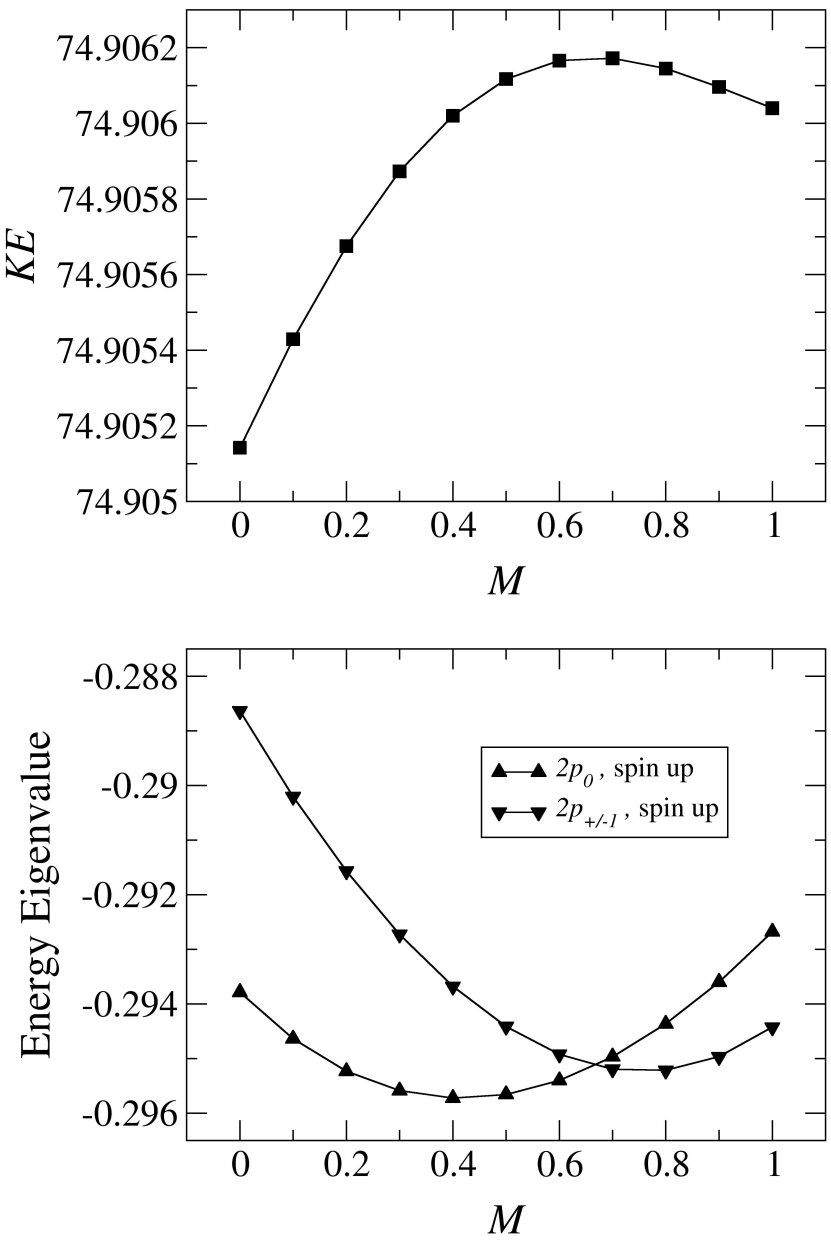

FIGURE 5.35: Variation in the kinetic energy and $2p$ spin up energy eigenvalues as M is varied from $0-1$ for a neutral carbon impurity at 0.0005 background density. The trends seen here are identical to those for a free carbon atom.

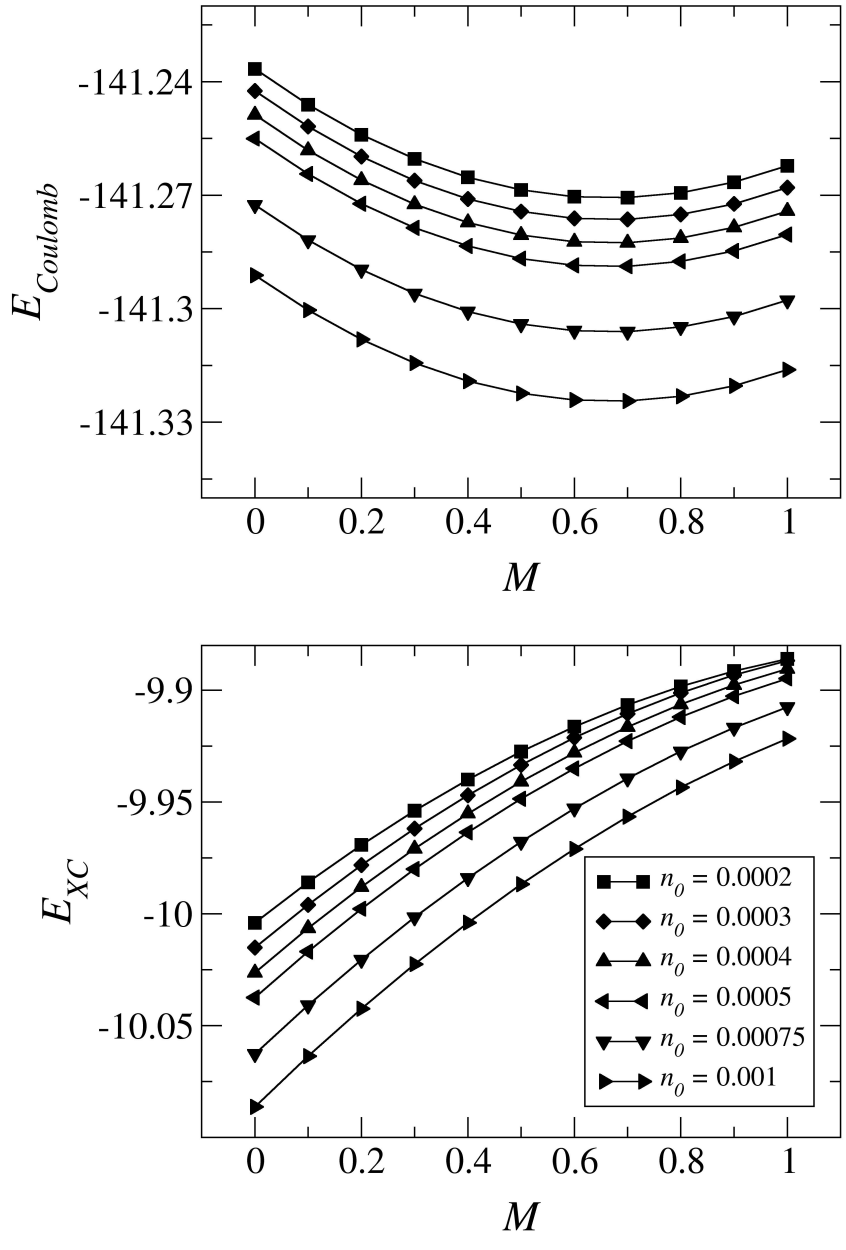

FIGURE 5.36: Variation in the Coulomb and Exchange-correlation energies as M is varied from $0-1$ and the background density is varied from $n_0 = 0.0002$ to 0.001 for a neutral carbon impurity. For the Coulomb energy, the trend is identical to that for a carbon atom. The exchange-correlation energy, however, is seen to have a minimum for the ground state ($M = 0$) for a neutral carbon impurity, whereas the exchange-correlation energy for a free carbon atom has a *maximum* for the ground state ($M = 2/3$). Note the large difference in scale.

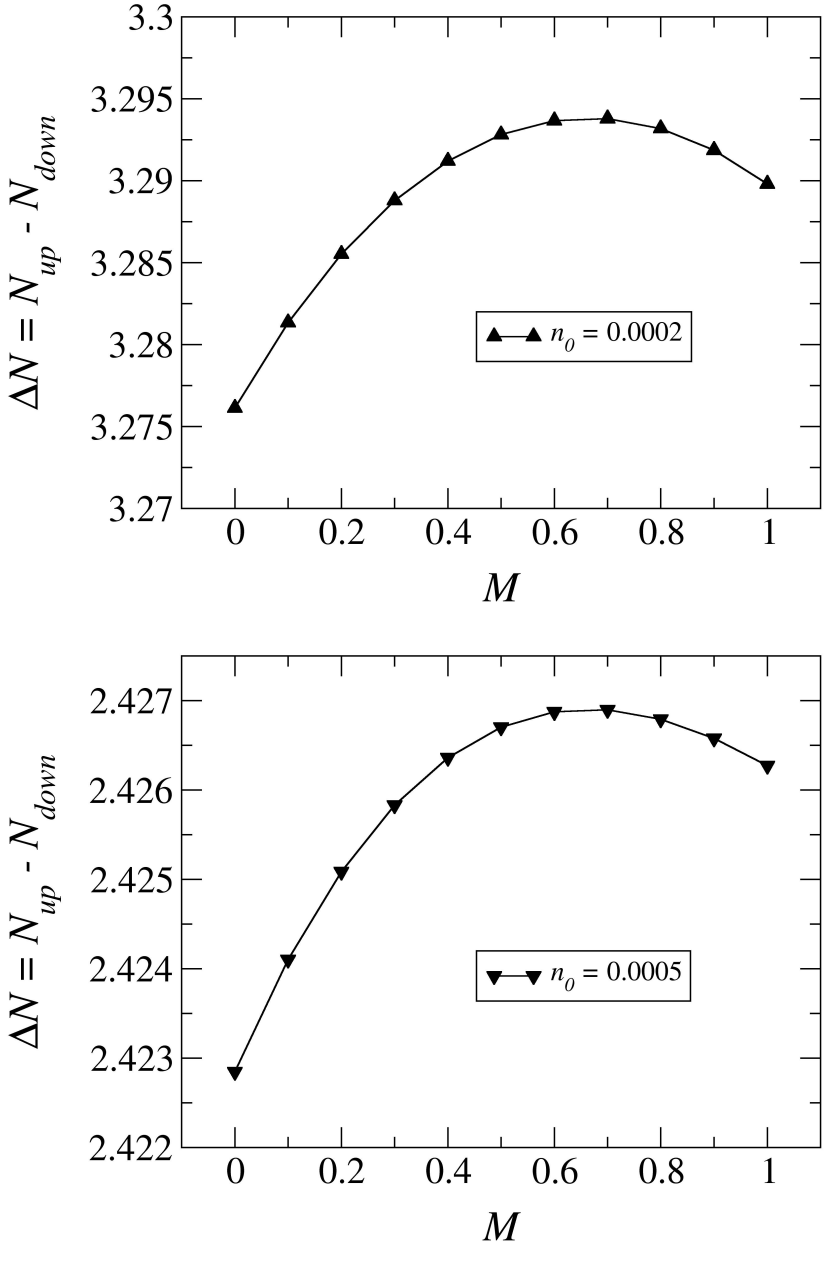

FIGURE 5.37: Variation in the spin-polarization as M is varied from $0-1$ for a neutral carbon impurity at low background densities. The degree of spin-polarization is minimized for the ground state ($M=0$) of a neutral carbon impurity.

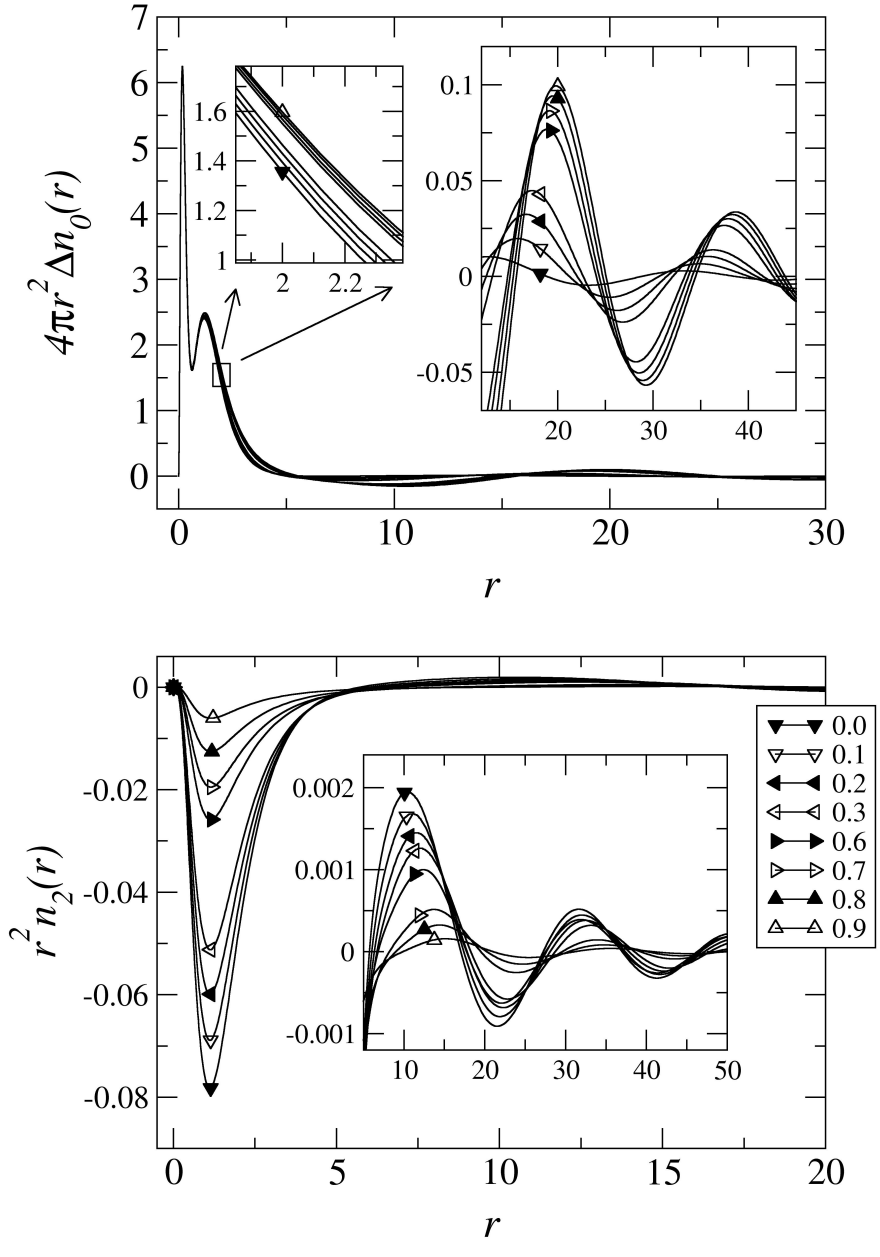

FIGURE 5.38: Variation of the total electron density as the population of the $2p$ sub-shell is varied. The data shown is for a carbon impurity at 0.0002 background density with 1 electron in the $2p_1^+$ and $2p_{-1}^+$ states and a variable fractional population in the $2p_0^+$ state. As the $2p^+$ sub-shell population is increased, the impurity atom is less screened from the gas since there is a surplus of negative charge near the impurity and the Friedel oscillations in the spherical component of the density increase as a result. However, as the $2p^+$ sub-shell population is increased, the impurity atom also becomes more spherical and the nonspherical component of the Friedel oscillations decrease as a result.

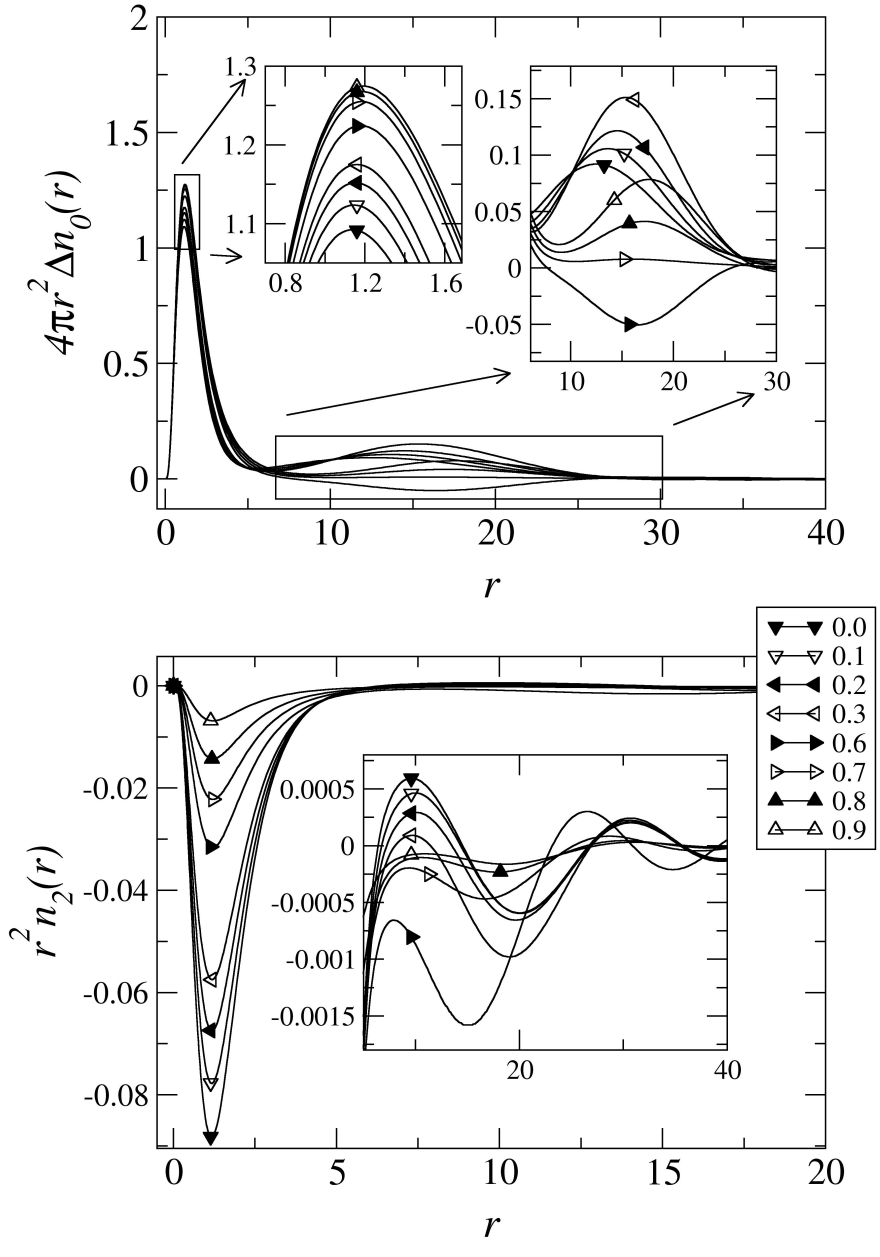

FIGURE 5.39: Variation of the spin-density as the population of the $2p$ sub-shell is varied. The data shown is for a carbon impurity at 0.0002 background density with 1 electron in the $2p_1^+$ and $2p_{-1}^+$ states and a variable fractional population in the $2p_0^+$ state. As the $2p^+$ sub-shell population is increased, the impurity atom is less screened from the gas since there is a surplus of negative charge near the impurity and the amplitude of the spherical component of the spin density increases as a result. However, as the $2p^+$ sub-shell population is increased, the impurity atom also becomes more spherical and the nonspherical component of the spin density decreases as a result. A large variation in the spherical spin density can be seen associated with the presence of a virtual bound state resonance at very low background densities.

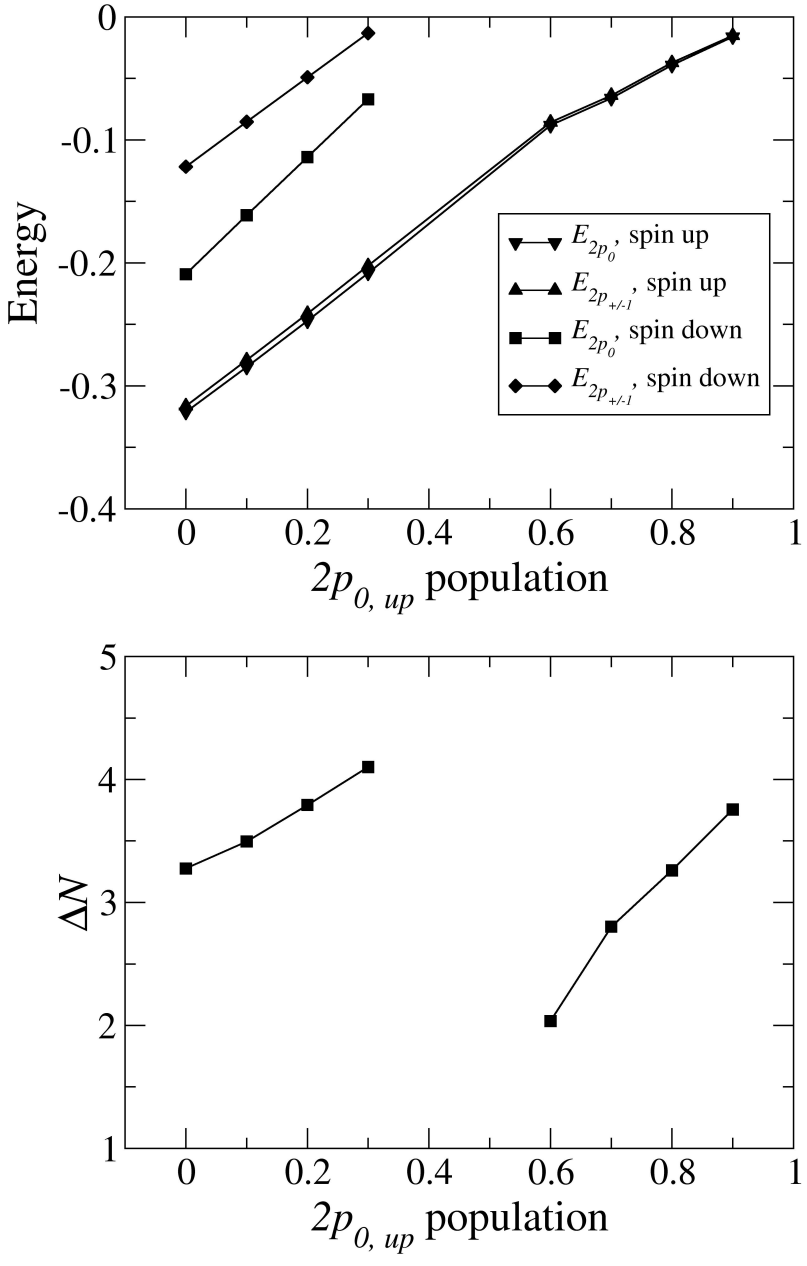

FIGURE 5.40: Variation of the $2p$ energy eigenvalues for a carbon impurity at 0.0002 background density as the $2p$ population is varied. The $2p_1^+$ population and $2p_{-1}^+$ population =1, while the $2p_0^+$ population is varied. As the $2p$ (all spin up) population is increased, the $2p$ spin down eigenstates merge into the conduction band and the spin-polarization drops before increasing again.

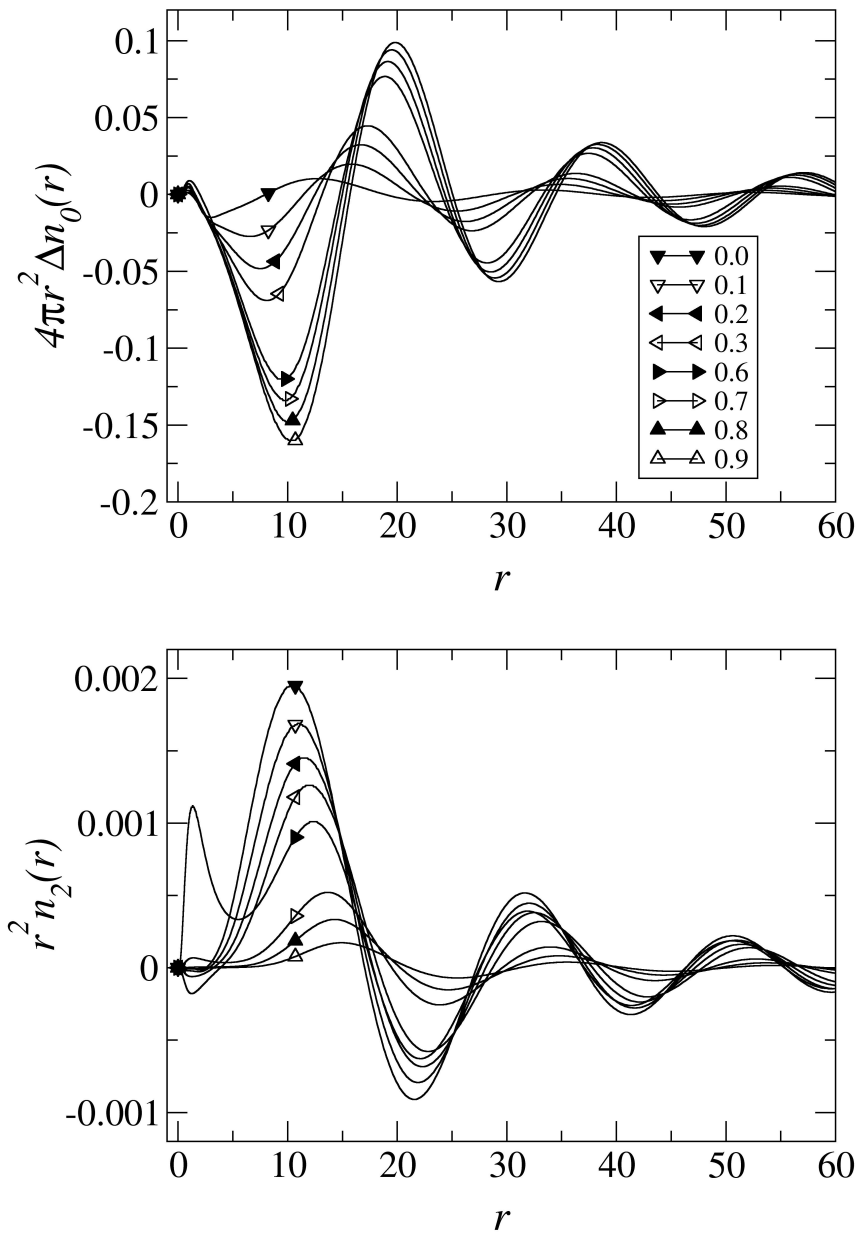

FIGURE 5.41: Variation of the electron density in the conduction band as the population of the $2p$ sub-shell is varied for a carbon impurity. The data shown is for 0.0002 background density with 1 electron in the $2p_1^+$ and $2p_{-1}^+$ states and a variable fractional population in the $2p_0^+$ state. It is seen that the magnitude of the Friedel oscillations increases as the $2p$ population increases and the excess charge on the impurity increases.

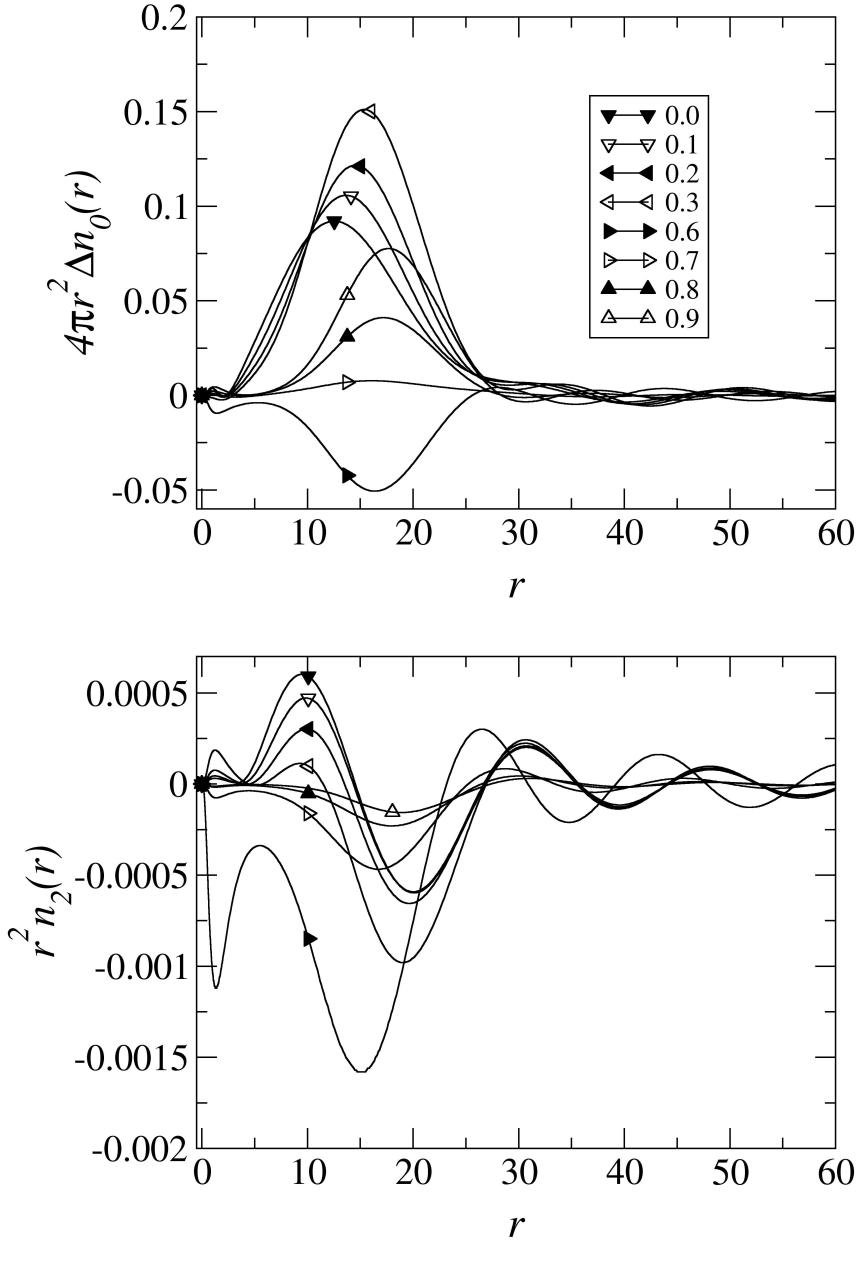

FIGURE 5.42: Variation of the spin-density in the conduction band as the population of the $2p$ sub-shell is varied for a carbon impurity. The data shown is for 0.0002 background density with 1 electron in the $2p_1^+$ and $2p_{-1}^+$ states and a variable fractional population in the $2p_0^+$ state. The variation in the large peak in the spin-density is due to the merging of the $2p^-$ states into the conduction band.

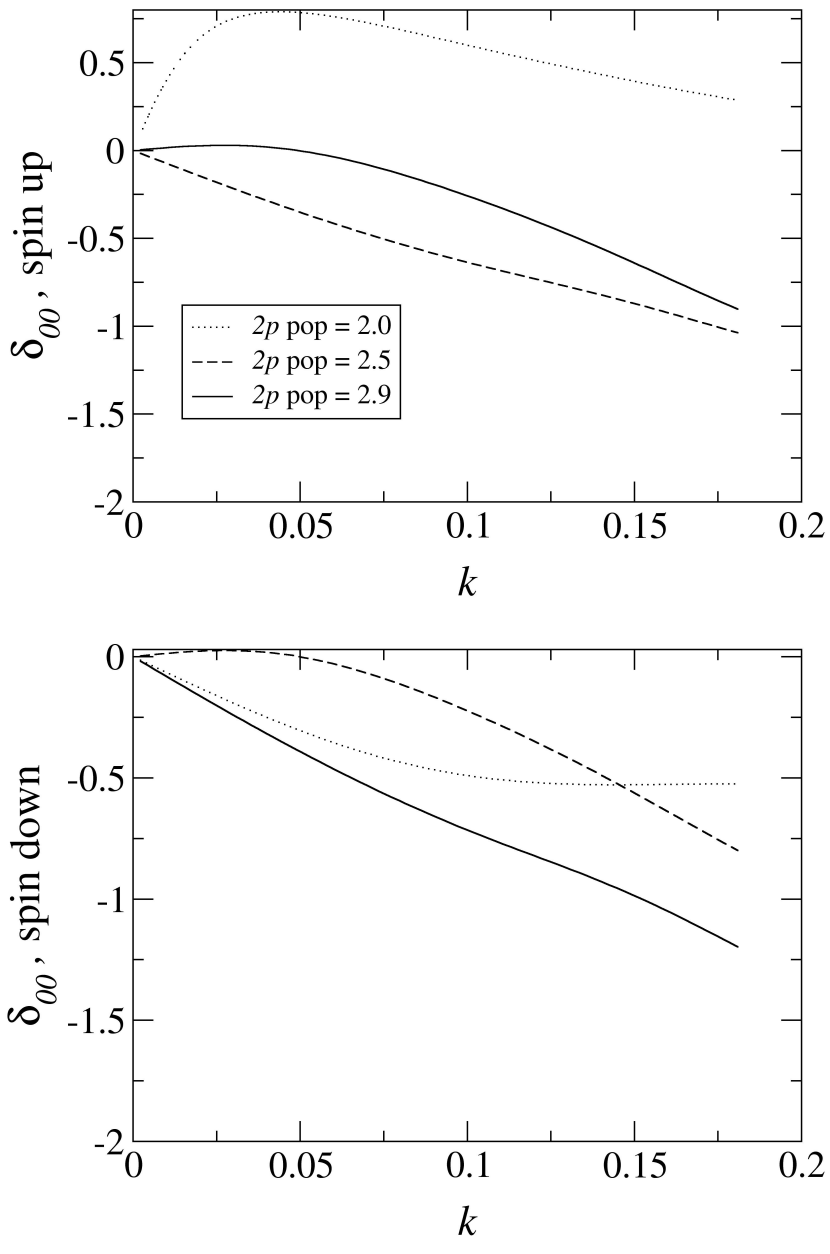

FIGURE 5.43: Variation of the $l = 0$ phase shifts as the population of the $2p$ sub-shell is varied. The data shown is for a carbon impurity at 0.0002 background density with 1 electron in the $2p_1^+$ and $2p_{-1}^+$ states and a variable fractional population in the $2p_0^+$ state. As the $2p^-$ states merge into the conduction band, the spin up phase shift first decreases and then increases again as the resonance moves higher into the conduction band as the $2p$ population is increased further. The opposite trend is seen for spin down electrons.

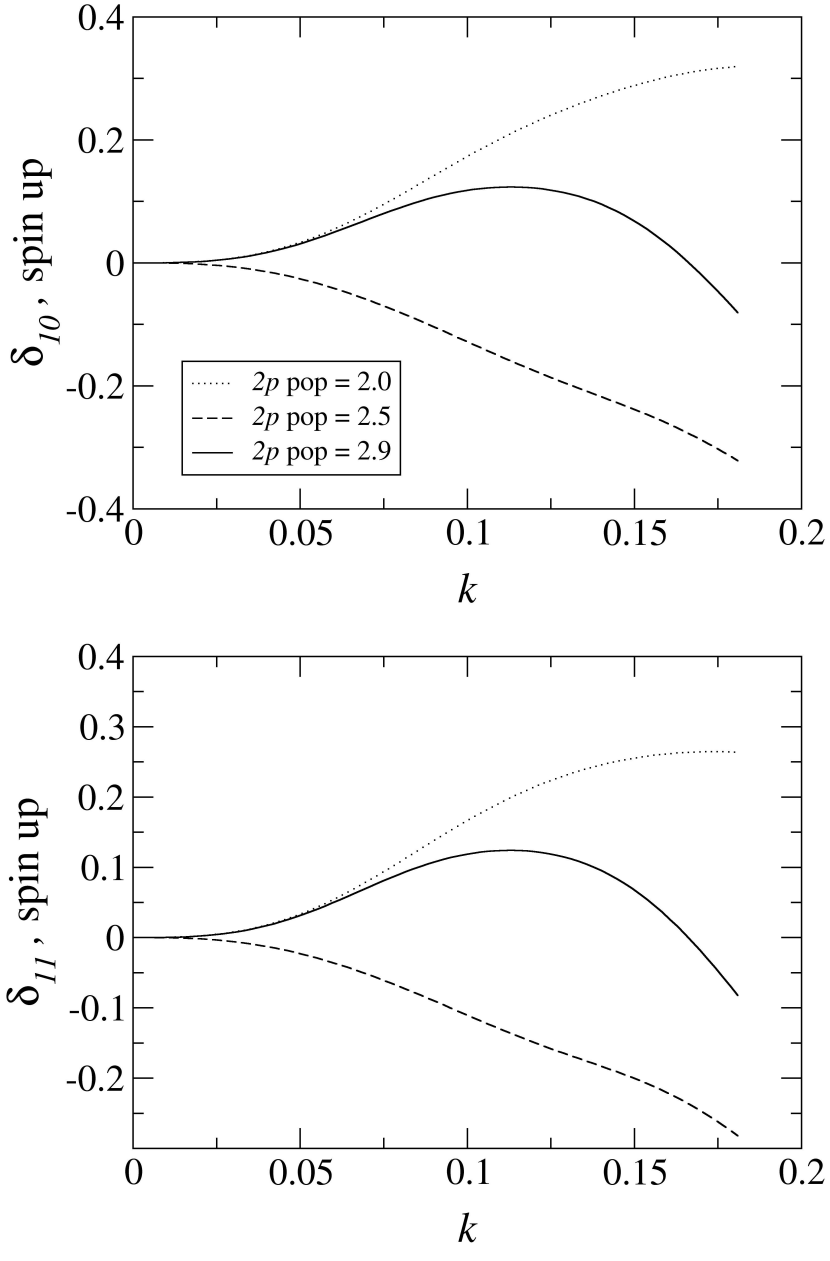

FIGURE 5.44: Variation of the $l = 1$ spin up phase shifts as the population of the $2p$ sub-shell is varied. The data shown is for a carbon impurity at 0.0002 background density with 1 electron in the $2p_1^+$ and $2p_{-1}^+$ states and a variable fractional population in the $2p_0^+$ state. As the $2p^-$ states merge into the conduction band, the spin up phase shift first decreases and then increases again as the resonance moves higher into the conduction band as the $2p$ population is increased further.

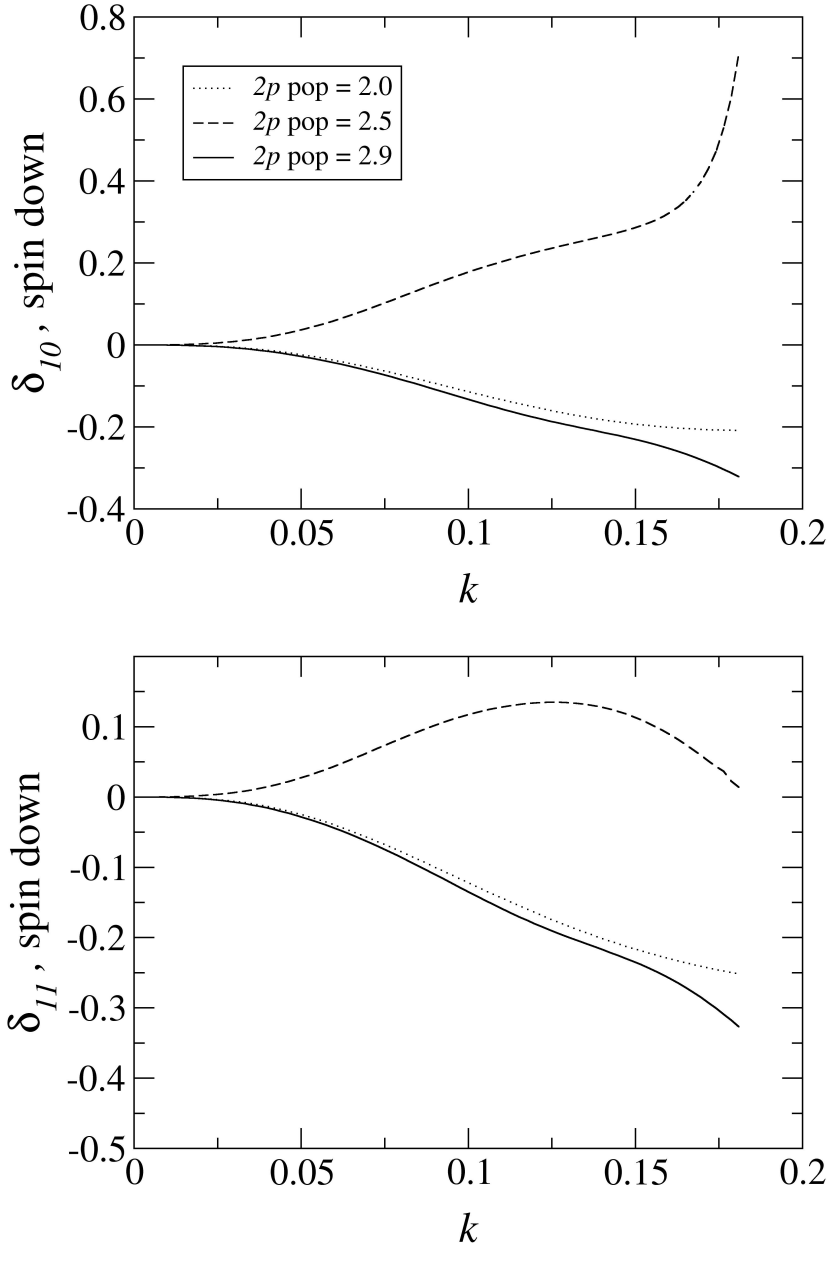

FIGURE 5.45: Variation of the $l = 1$ spin down phase shifts as the population of the $2p$ sub-shell is varied. The data shown is for a carbon impurity at 0.0002 background density with 1 electron in the $2p_1^+$ and $2p_{-1}^+$ states and a variable fractional population in the $2p_0^+$ state. As the $2p^-$ states merge into the conduction band, the spin down phase shift first increases and then decreases again as the resonance moves higher into the conduction band as the $2p$ population is increased further.

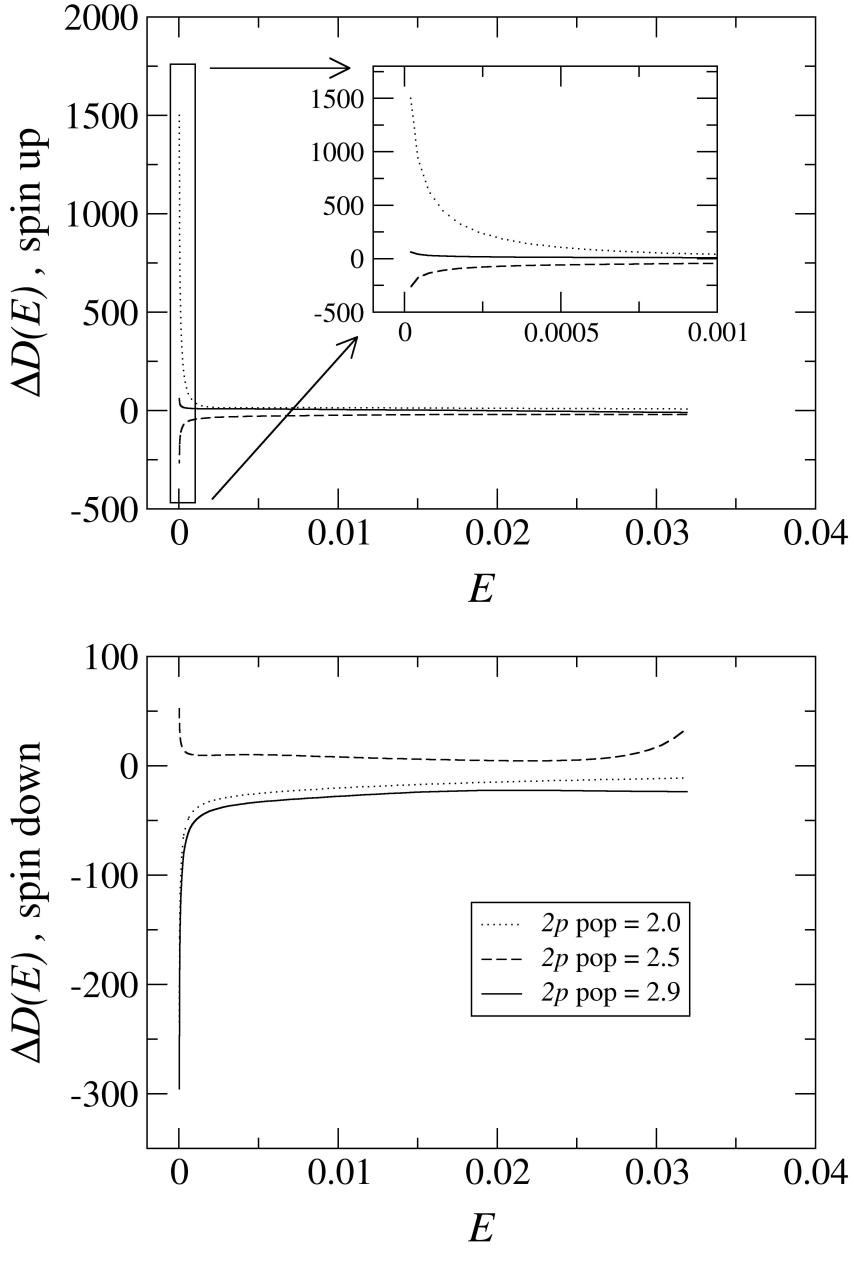

FIGURE 5.46: Variation of the induced density of states in the conduction band as the population of the $2p$ sub-shell is varied. The data shown is for a carbon impurity at 0.0002 background density with 1 electron in the $2p_1^+$ and $2p_{-1}^+$ states and a variable fractional population in the $2p_0^+$ state. As the $2p^-$ states merge into the conduction band, the spin up density of states first decreases and then increases again as the resonance moves higher into the conduction band as the $2p$ population is increased further. The opposite trend is seen for the spin down density of states.

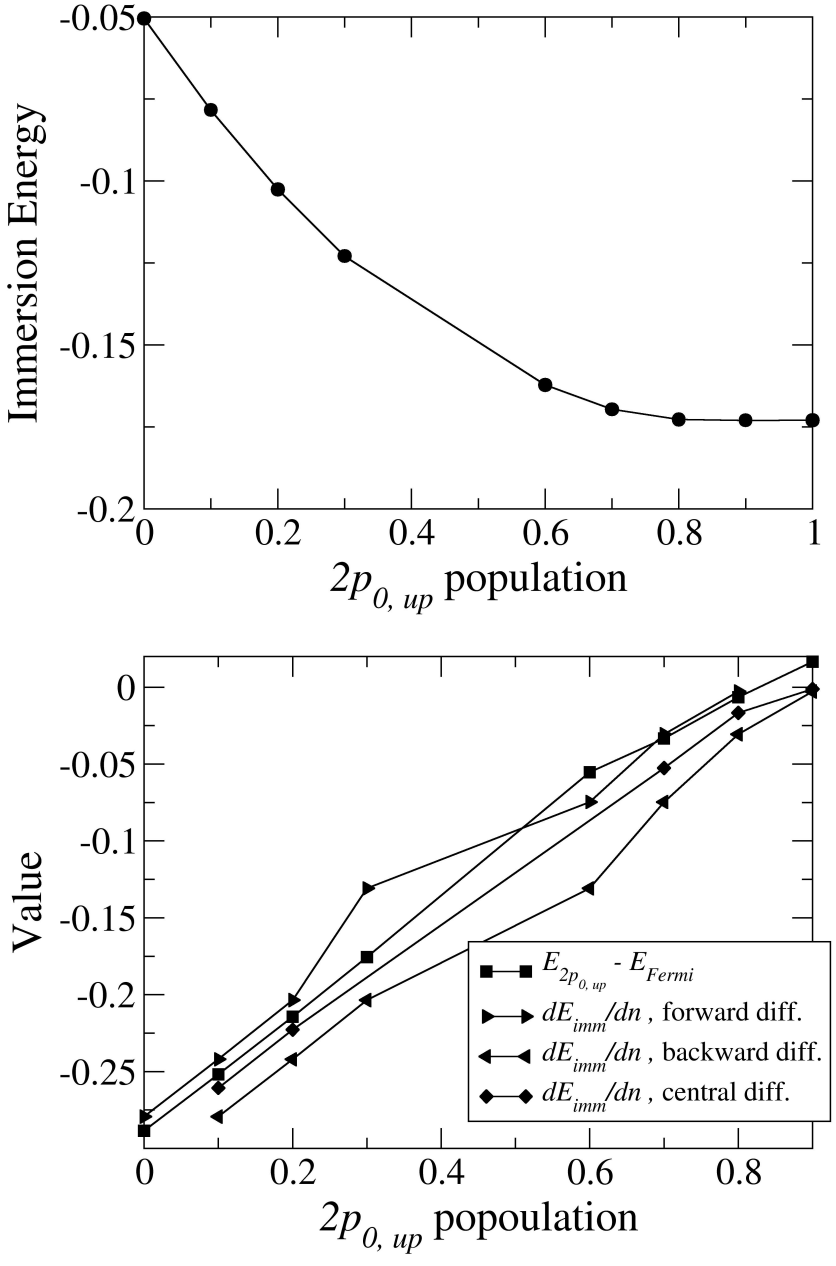

FIGURE 5.47: Variation of the immersion energy as the $2p$ population is varied for a carbon impurity at 0.0002 background density. We were not able to achieve self-consistency around a $2p$ population of 2.5 due to the very shallow $2p^-$ virtual bound state resonance in the conduction band. It was also difficult to achieve self-consistency for a $2p$ population near 3.0 due to the flatness of the upper plot. Good agreement with Janak's theorem is seen.

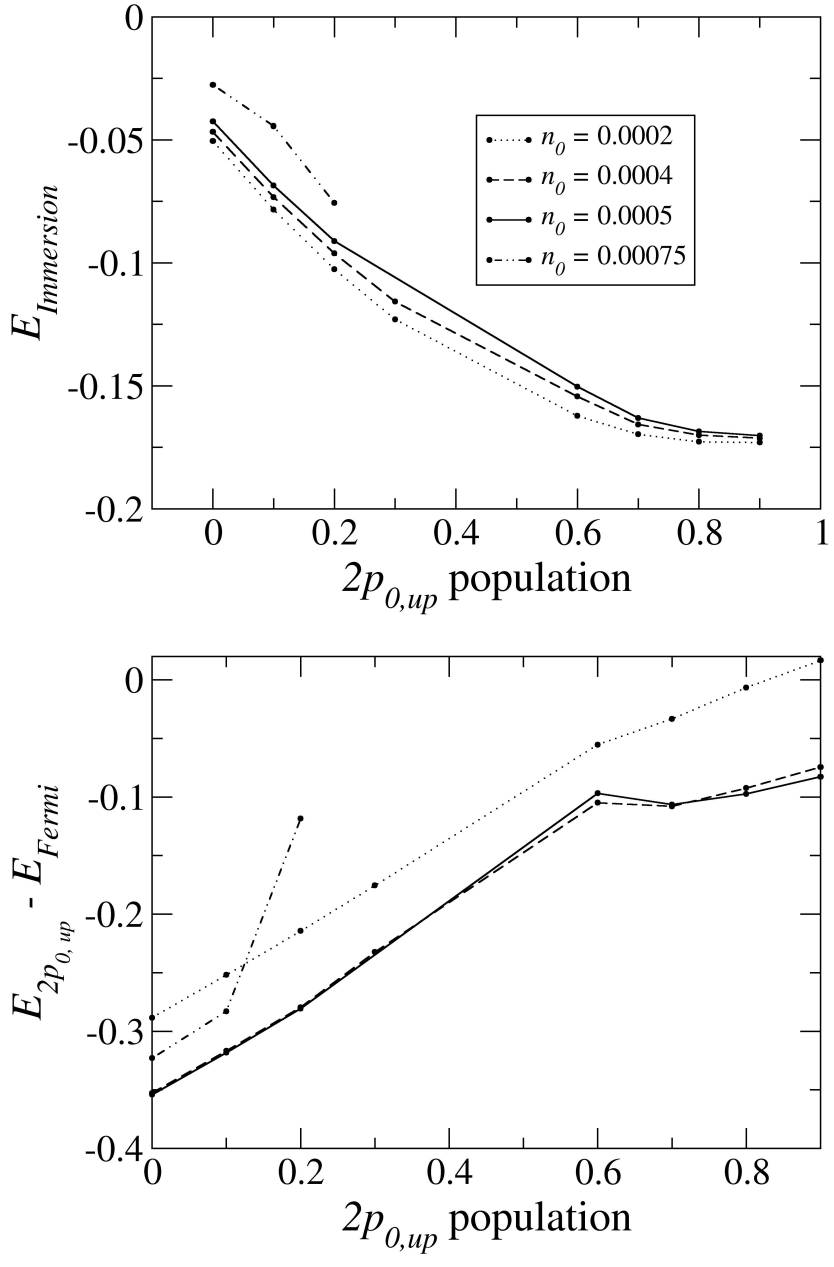

FIGURE 5.48: Variation of the immersion energy as the $2p$ population is varied for a carbon impurity at low background densities. The trends are seen to be similar to that for 0.0002 background density, in agreement with Janak's theorem.

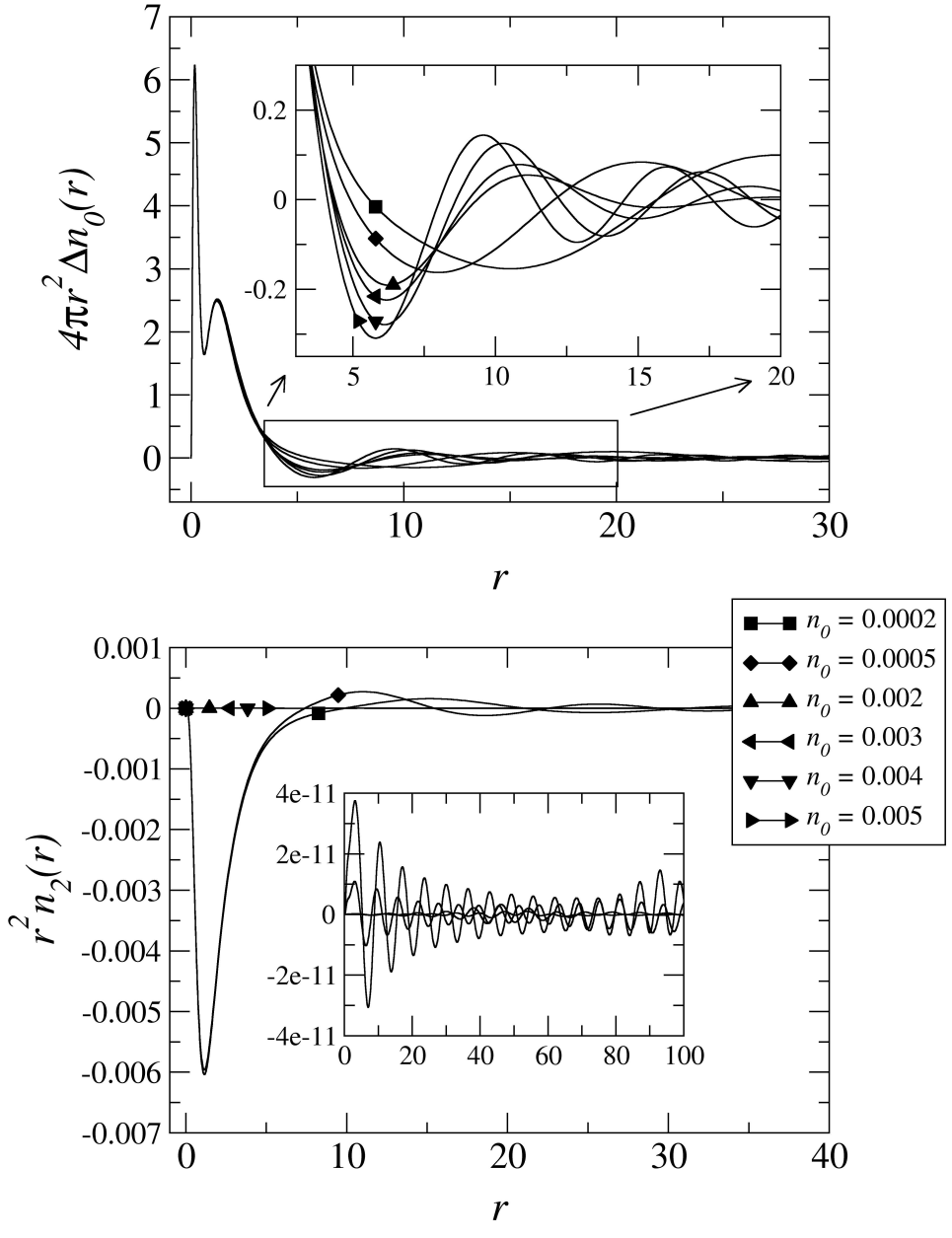

FIGURE 5.49: Total electron density for a carbon impurity at low to mid-range metallic densities, $0.0002 \leq n_0 \leq 0.005$. The lower inset shows the nonspherical component for $0.002 \leq n_0 \leq 0.005$ only. It is seen that the nonspherical component is quenched for background densities of 0.002 and greater.

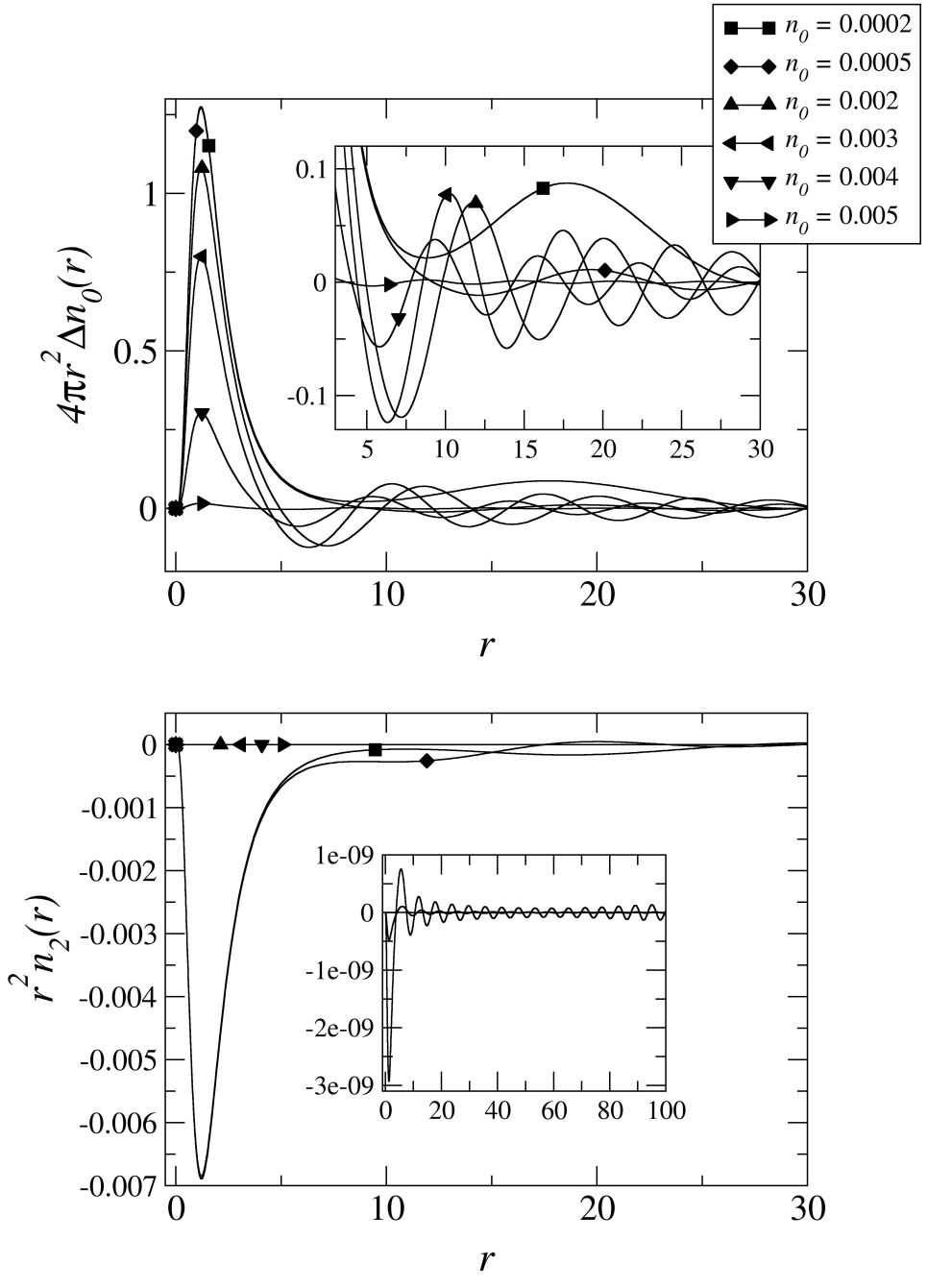

FIGURE 5.50: Spin-density for a carbon impurity at low to mid-range metallic (background) densities, $0.0002 \leq n_0 \leq 0.005$. The lower inset shows the nonspherical component for $0.002 \leq n_0 \leq 0.005$ only. It is seen that the nonspherical component is quenched for background densities of 0.002 and greater. It is also seen that there is a large peak for very low background density due to the $3s^+$ virtual bound state resonance, and that the Friedel oscillations extend much closer to the impurity for higher densities.

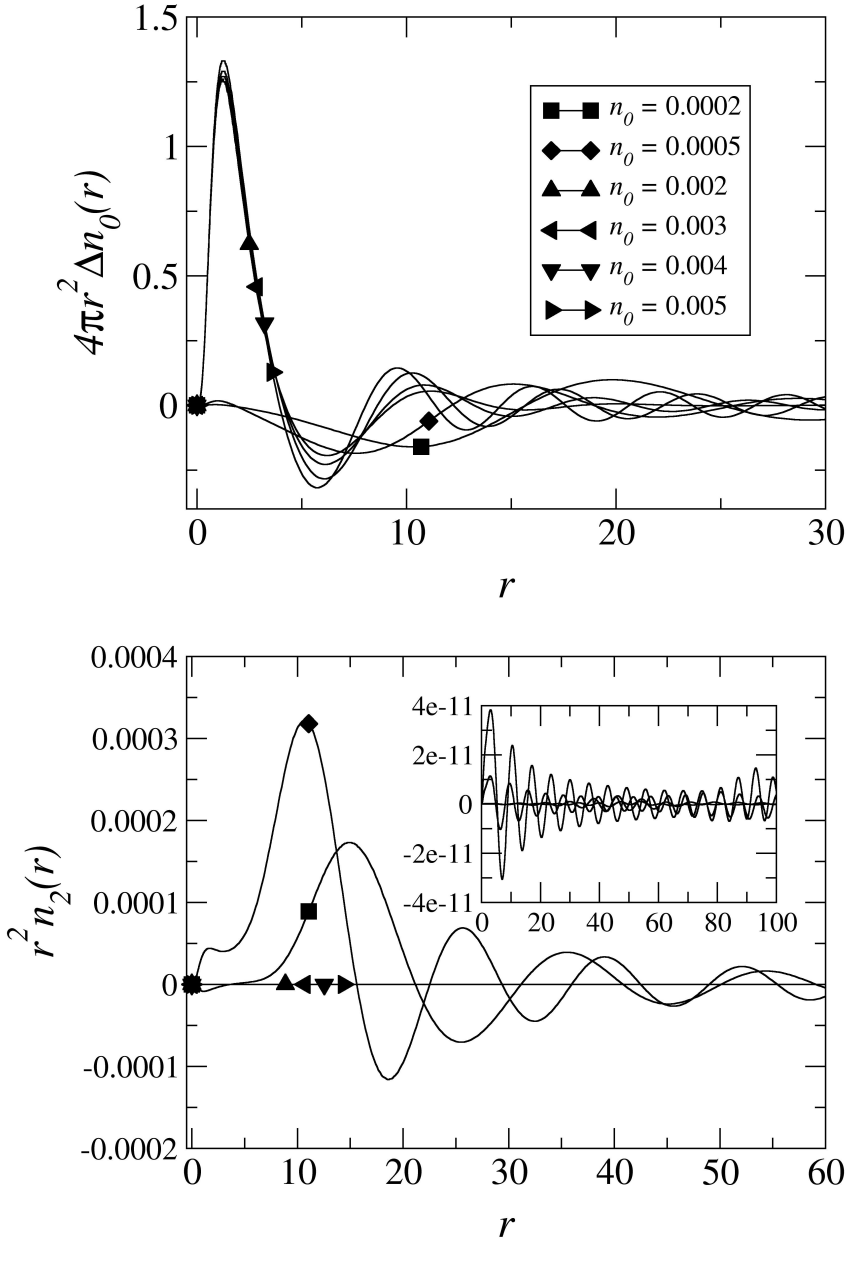

FIGURE 5.51: Induced density in the conduction band for a carbon impurity at low to mid-range metallic (background) densities, $0.0002 \leq n_0 \leq 0.005$. The lower inset shows the nonspherical component for $0.002 \leq n_0 \leq 0.005$ only. It is seen that the nonspherical component is quenched for background densities of 0.002 and greater. It is also seen that there is a peak in the conduction band density for higher background densities due to the $2p^+$ virtual bound state resonance which is absent for lower densities for which $2p$ bound states exist.

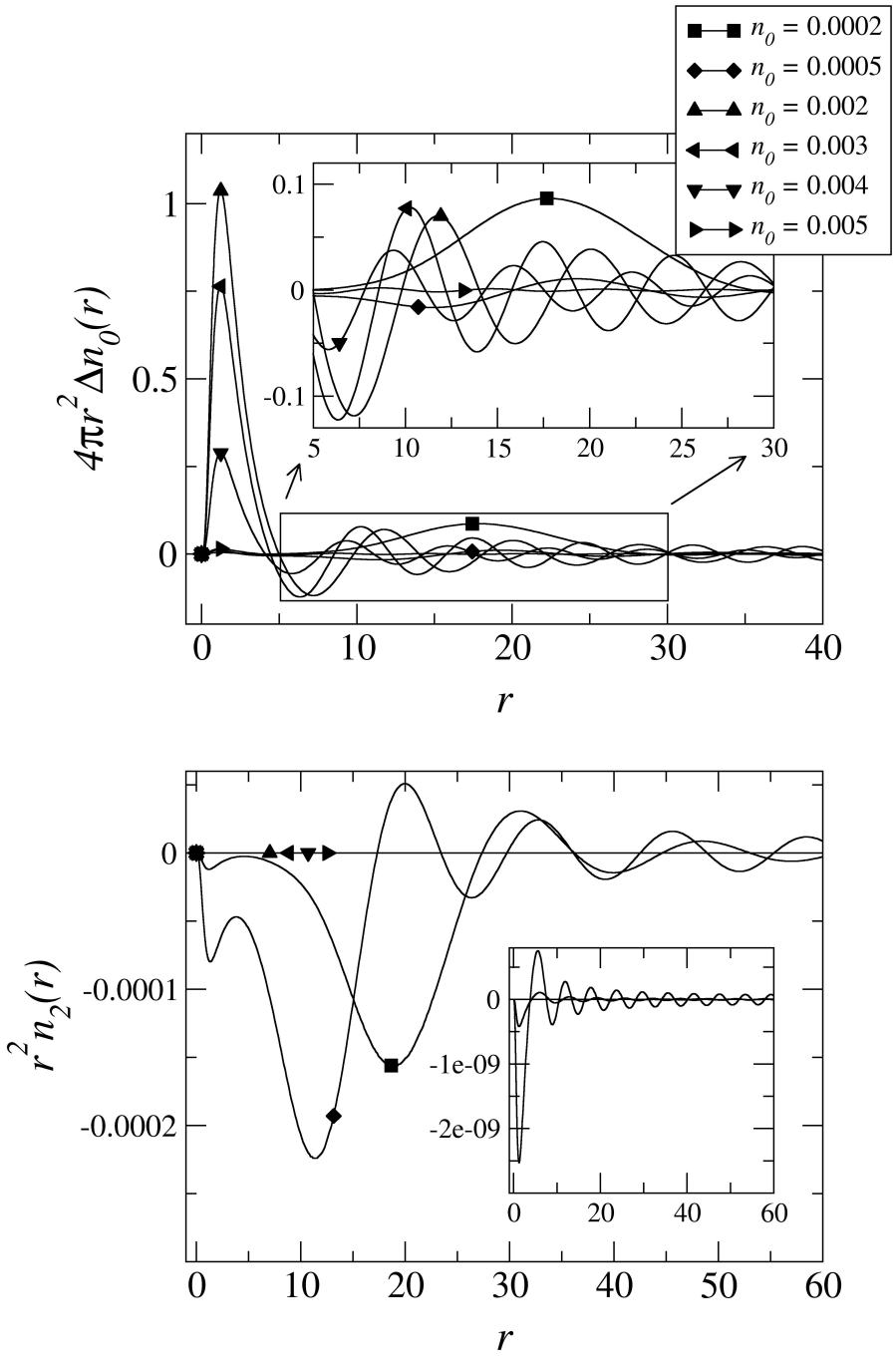

FIGURE 5.52: Spin-density in the conduction band for a carbon impurity at low to mid-range metallic (background) densities, $0.0002 \leq n_0 \leq 0.005$. The lower inset shows the nonspherical component for $0.002 \leq n_0 \leq 0.005$ only. It is seen that the nonspherical component is quenched for background densities of 0.002 and greater. It is also seen that the spin-polarization effects are quenched as the background density increases.

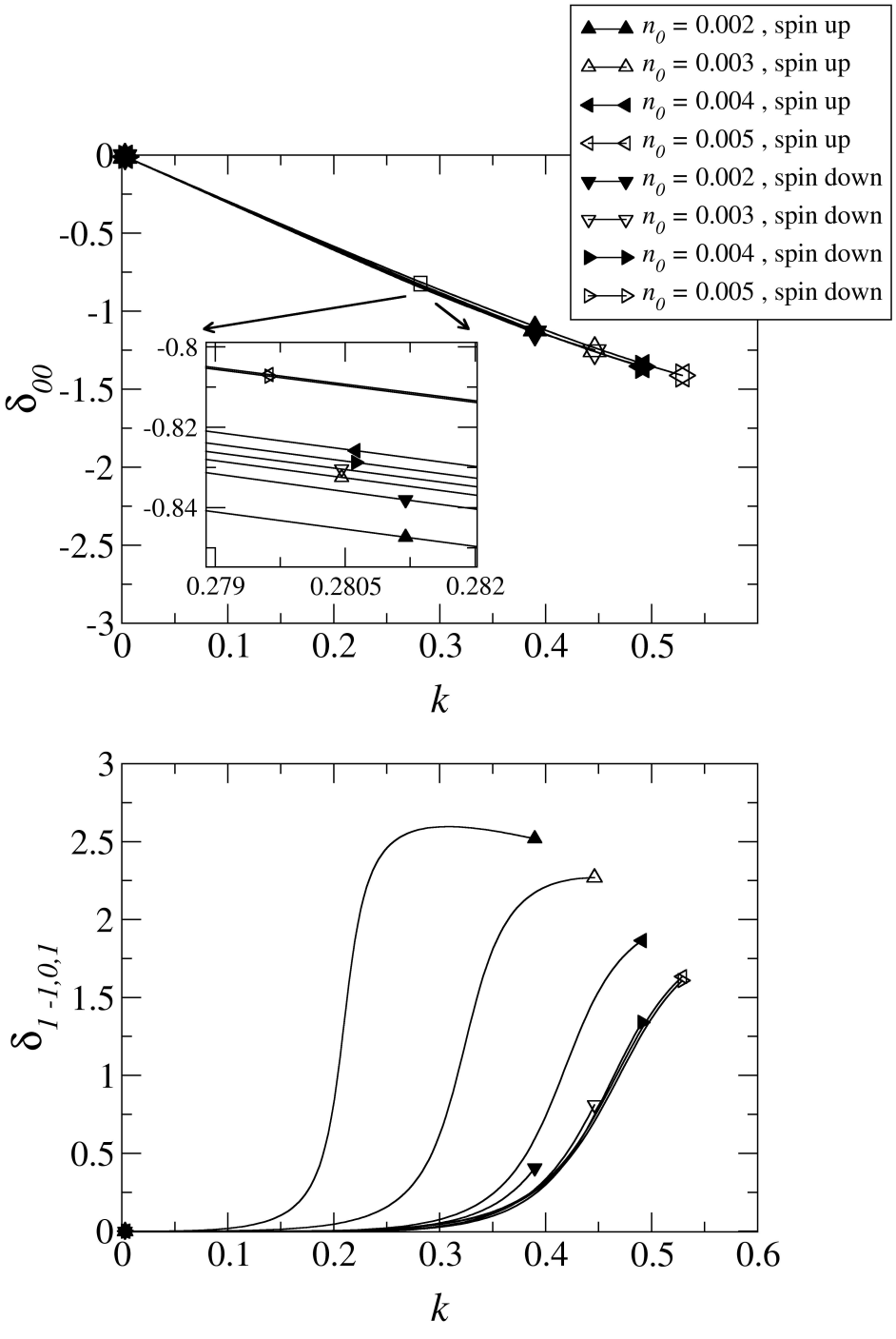

FIGURE 5.53: Phase shifts for $l = 0, 1$ electrons in the conduction band for a carbon impurity at mid-range metallic (background) densities, $0.002 \leq n_0 \leq 0.005$. A virtual bound state resonance can be seen in the $2p^+$ state for densities slightly higher than $n_0 = 0.001$. It is also seen that the spin-polarization effects are quenched as the background density is increased. At 0.005 background density, the spin-polarization effects are completely quenched and the spin up and spin down phase shifts are equal.

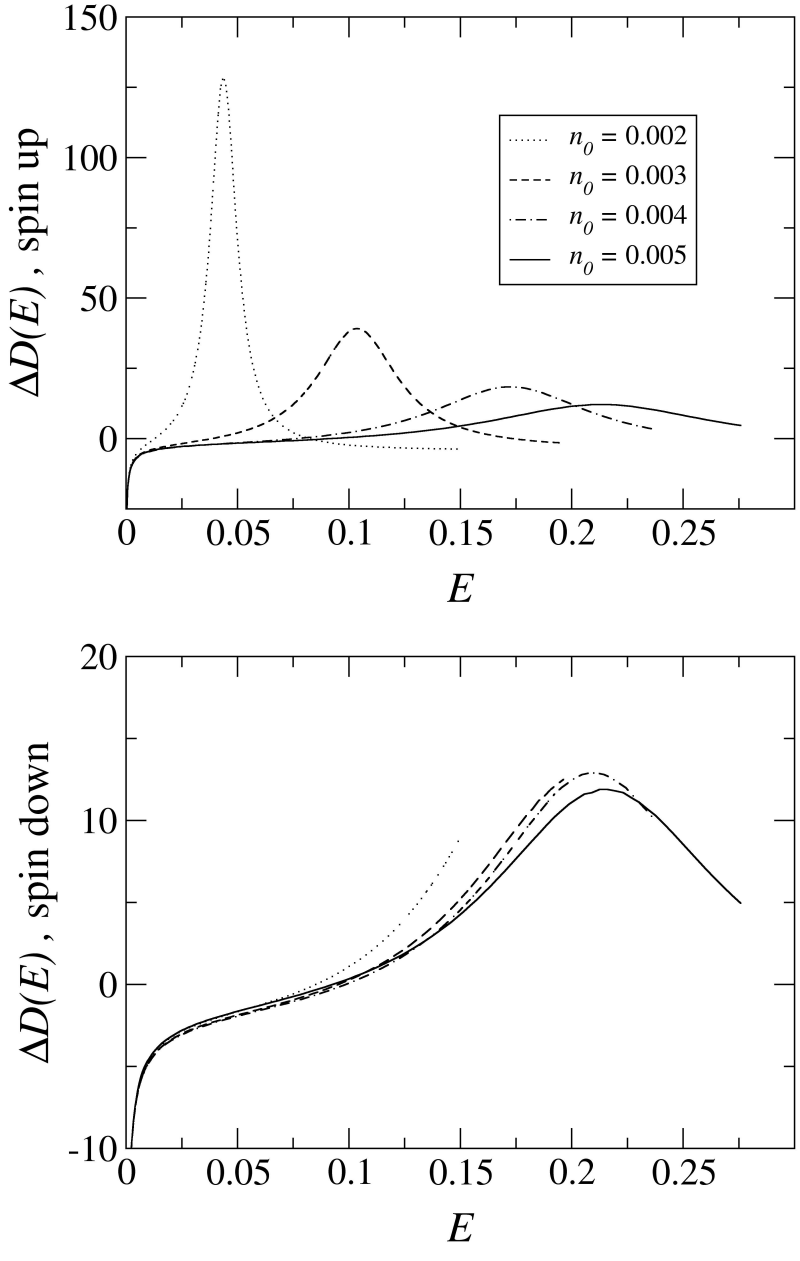

FIGURE 5.54: Induced density of states in the conduction band for a carbon impurity at mid-range metallic (background) densities, $0.002 \leq n_0 \leq 0.005$. The $2p^+$ virtual bound state resonance peak is seen to decrease as the background density is increased. For this background density range, the nonspherical effects are quenched and these data are in excellent agreement with the work of Song.

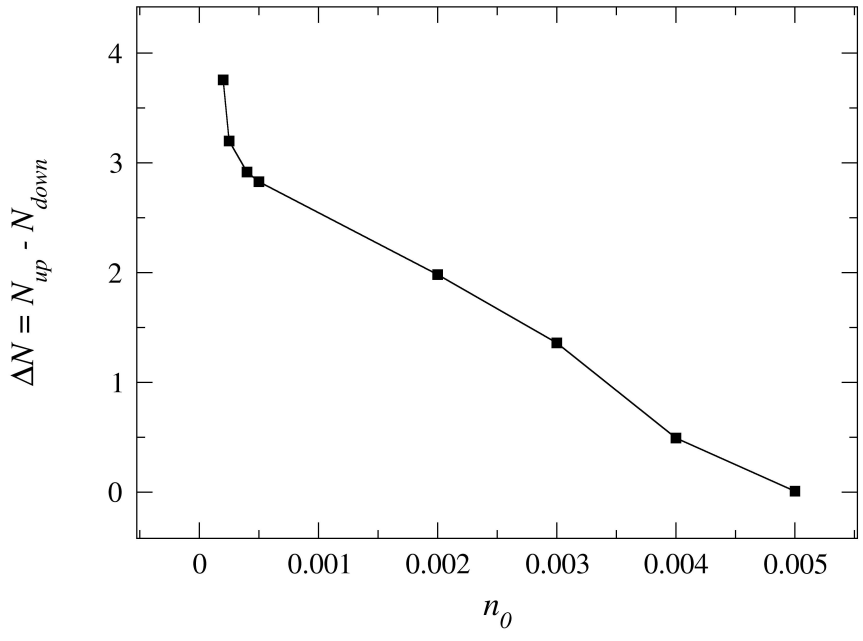

FIGURE 5.55: Variation of the spin-polarization of the ground state for the entire density range studied. The dramatic upturn at very low density has not been shown in prior work and results from the $3s^+$ virtual bound state in the conduction band.

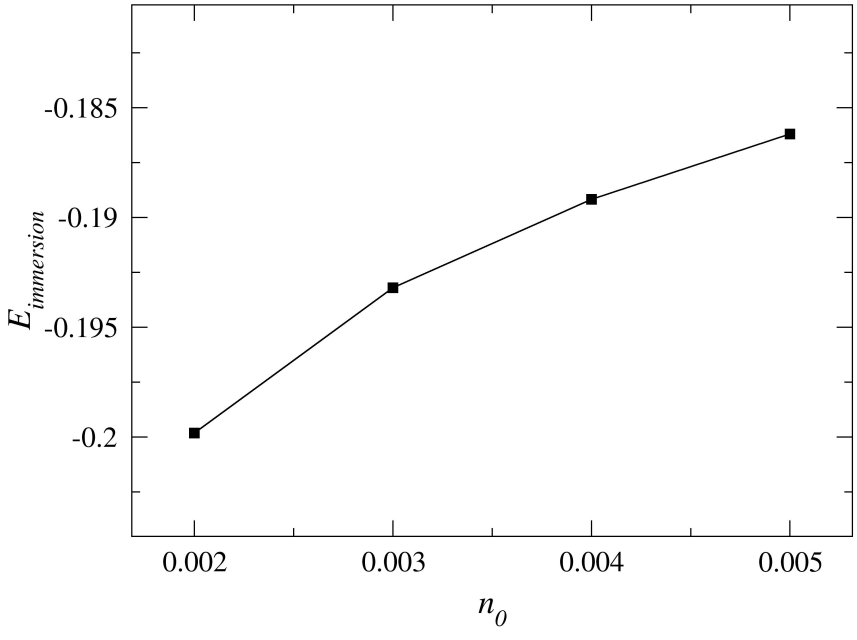

FIGURE 5.56: Variation of the immersion energy for the background density range $0.002 \leq n_0 \leq 0.005$. For this background density range, the nonspherical effects are quenched and these data are in excellent agreement with the work of Song.

6. DISCUSSION

In the work of Tong and Sham [3], a self-consistent density functional scheme with an interpolation for the exchange-correlation energy between the schemes of Wigner [24] and of Gell-Mann and Brueckner [17] in the LDA was used to calculate the total energies and ionization energies of spherical atoms including both noble gas and rare earth atoms. These calculations were compared with results from Hartree-Fock theory. No calculations were performed for nonspherical atoms.

In this work, we have included nonspherical effects into a self-consistent density functional scheme using the spin-polarized formulation of the LDA with the interpolation scheme proposed by Von Barth, Hedin, and Lundqvist [12, 26]. For the case of spherical atoms, the results of this work are in very good agreement with the results from the previous studies [3, 30] and with experiment. However, for the case of nonspherical atoms, we found that the ground state predicted by the LDA is in disagreement with the actual physical ground state predicted by Hund's rules for light atoms. We also elucidated the manner in which Hund's rules are violated and what the effects on the total energy are in relation to angular momentum symmetry variations. What was found was that Hund's rules predict a value of $M_L = 1$ for a free carbon atom, while the LDA predicts a value of $M_L = 2/3$ (spherical) for a free carbon atom. The magnitude of the energy errors due to the nonspherical effects are smaller than the errors associated with the LDA for spherical atoms and so the results in this work, even for nonspherical atoms, are in good agreement with the previous results for total energy calculations.

The nature of the LDA is such that rapid variations in the electron density cause large errors in the exchange-correlation energy and therefore the total energy. For free atoms, these errors are larger for core states where the electron density varies most rapidly. These errors can be removed by calculating ionization energies in which the errors asso-

ciated with the core states are subtracted out. The results in this work do show smaller absolute errors for ionization energies than for total free atom energies. This is a good verification of the basic theory.

Atomic polarizabilities are also calculated for light atoms. The results of direct calculations of polarizabilities in this work are in good agreement with the results of Stott and Zaremba [4] where a perturbative approach is used.

In the work of Puska, et al. [5], of Song [30] and of Nazarov, et al. [31], a spherical approximation was used to perform atomic immersion calculations in an electron gas. In the work of Puska, et al. and of Nazarov, et al., the interpolation scheme of Gunnarson and Lundqvist [28] was used. In the work of Song, the interpolation scheme of Von Barth, Hedin, and Lundqvist was used, as in this work. The range of electron gas densities studied was approximately that of ordinary metals, $\approx 1.8 < r_S < 8$, or $0.0005 < n_0 < 0.06$ where r_S is the Wigner-Seitz radius and where n_0 is the density of the electron gas. These studies looked at very light atoms, primarily H, He, Li, and Be, which are all spherical due to the presence of only s-orbital electrons. Some work was performed for impurity systems with p-orbital electrons, primarily B, C, N, and O. No studies of impurity systems with d-orbital electrons were performed in these works.

In this work, to study nonspherical effects in impurity systems, we begin by studying the simplest interesting case, that of a single carbon impurity. For electron gas densities greater than 0.002, a carbon impurity has only s-orbital electrons held in bound states, the nonspherical effects are quenched and the results presented in this work are in excellent agreement with the work of Song. For electron gas densities of 0.0005 and lower, a carbon impurity in the ground state has a spherical configuration due to a fully occupied $2p^+$ subshell. For this reason, in this work, the number of valence electrons is limited in order to study the effects of the nonspherical terms. What was found is that the presence of the electron gas changes the nature of a neutral impurity atom when compared to a free

neutral atom, even for very low background densities, $n_0 \leq 0.0002$, where the impurity solution should approach that of the free atom. This is due in part to the availability of charge provided by the 'infinite' electron gas and may in part be due to errors inherent in the LDA. It was also found that a spherical approximation tends to extremize the various energy terms for both free and immersed atoms. In the case of a neutral carbon atom, the degree of spin-polarization is held constant by the choice of angular momentum symmetry. For a carbon impurity, the degree of spin-polarization $\Delta N = N_+ - N_-$ is found to be a local maximum for the spherical configuration while the $M_L = 0$ configuration yields the minimum degree of spin-polarization ΔN over the range $0 \leq M_L \leq 1$. A free neutral carbon atom is found to have an energy minimum for a spherical configuration while for immersed atoms an energy minimum is found for $M_L = 0$.

All of this work has been performed with the goal of eventually understanding the quenching of the orbital moment and the violation of Hund's rules for metallic iron. It is hoped that this study will elucidate the value and limitations of the approach taken by DFT and approximations inherent in the LDA. Future work will require studying atoms with d-orbital electrons where $L - S$ coupling does not hold in order to study magnetic effects like those seen for metallic iron.

BIBLIOGRAPHY

1. P. Hohenberg, W. Kohn, Phys. Rev. **136**, B864 (1964)
2. W. Kohn, L.J. Sham, Phys. Rev. **140**, 4A, A1133 (1965)
3. B.Y. Tong, L.J. Sham, Phys. Rev. **144**, 1 (1966)
4. M.J. Stott, E. Zaremba, Phys. Rev. A, **21**, 12 (1980)
5. M.J. Puska, R.M. Nieminen, M. Manninen, Phys. Rev. B **24**, 3037 (1981)
6. J. Friedel, *Philos. Mag.* **43**, 153-89 (1952)
7. J. Friedel, Adv. Phys. **3**, 446-507 (1953)
8. J. Friedel, *Nuovo Cimento* **7**, 287-311 (1958)
9. F. Hund, Zeitschrift fr Physik, **33**, 345-371 (1925)
10. H. N. Russell and F. A. Saunders, Astrophysical Journal, **61**, 38 (1925)
11. R.M. Dreizler, E.K.U. Gross, *Density Functional Theory*, Springer-Verlag (1990)
12. U. von Barth, L. Hedin, J. Phys. C: Solid St. Phys. **5**, 1629-42 (1972)
13. M.M. Pant, A.K. Rajagopal, Solid State Comm. **10**, 1157 (1972)
14. A.K. Rajagopal, J. Callaway, Phys. Rev. B **7**, 1912 (1973)
15. Gerald D. Mahan, *Many-Particle Physics*, Kluwer Academic, Plenum (2000)
16. C. Kittel, *Quantum Theory of Solids*, Wiley (1987)
17. M. Gell-Mann, K. Brueckner, Phys. Rev. **106**, 364 (1957)
18. K. Sawada, K.A. Brueckner, N. Fukada, and R. Brout, Phys. Rev. **108**, 507 (1957)
19. J. Hubbard, Proc. Royal Soc. London Ser. **A 243**, 336 (1957)
20. P. Nozieres, D. Pines, Phys. Rev. **111**, 442 (1958)
21. J.J. Quinn, R.A. Ferrel, Phys. Rev. **112**, 812 (1958)
22. L. Onsager, L. Mittag, M.J. Stephen, Ann. Phys. **18**, 71 (1966)
23. W.J. Carr, A.A. Maradudin, Phys. Rev. **133**, A371 (1964)
24. E. Wigner, Phys. Rev. **46**, 1002 (1934)

25. S. Lundqvist, N.H. March *Theoy of the Inhomogeneous Electron Gas*, Plenum (1983)

26. L. Hedin, B.I. Lundqvist, J. Phys. C; Solid St. Phys. **4**, 2064-83 (1971)

27. K.S. Singwi, A. Sjölander, M.P. Tosi, and R.H. Land, Phys. Rev. B **1**, 1044 (1970)

28. O. Gunnarson, B.I. Lundqvist, Phys. Rev. B **13** 4272 (1976)

29. D.M. Ceperley, B.J. Alder, Phys. Rev. Lett. **45**, 566 (1980)

30. J.H. Song, *Impurities in a Homogeneous Electron Gas*, Ph.D. Thesis, Oregon State University (2005)

31. V.U. Nazarov, C.S. Kim, Y. Takada, Phys. Rev. B, **72**, 233205 (2005)

32. A.P. Albus, *Immersion Energies of Atoms in Jellium*, M.S. Thesis, Oregon State University (1999)

33. A. Salin, A. Arnau, P.M. Echenique, E. Zaremba, Phys. Rev. B **59**, 4, 2537-48 (1999)

34. R.D. Muiño, A. Salin, Phys. Rev. B **60**, 3, 2074-83 (1999)

35. J.D. Jackson, *Classical Electrodynamics, 3rd Edition*, John Wiley & Sons (1999)

36. M. Abramowitz, I.A. Stegun, *Handbook of Mathematical Functions*, Dover (1965)

37. K.R. Subbaswamy, G.D. Mahan, J. Chem. Phys. **84**, 3317 (1986)

38. G. Senatore, K.R. Subbaswamy, Phys. Rev. A **34**, 3619 (1986)

39. G. Senatore, K.R. Subbaswamy, Phys. Rev. A **35**, 2440 (1987)

40. G.D. Mahan, K.R. Subbaswamy, *Local Density Theory of Polarizability*, Springer (1990)

41. J.J. Sakurai, *Modern Quantum Mechanics*, Benjamin/Cummings (1985)

42. W. Press, B. Flannery, S. Teukolsky, W. Vetterling, *Numerical Recipes: The Art of Scientific Computing*, Cambridge University Press (1986)

43. J.H. Wilkinson, C. Reinsch, *Handbook for Automatic Computation, Vol. II*, Springer-Verlag (1971)

44. J.F. Janak, Phys. Rev. B **18**, 7165 (1978)

APPENDICES

A APPENDIX Rydberg Atomic Units

Definition of system of units (with m = mass of electron)

$$\hbar = \frac{e^2}{2} = 2m = 1 \tag{A.1}$$

Unit of length

$$a_0 = \frac{\hbar^2}{me^2} = 1 \simeq 0.529 \cdot 10^{-10}\,\mathrm{m} \tag{A.2}$$

Unit of energy

$$E_R = \frac{e^2}{2a_0} = \frac{me^4}{2\hbar^2} = 1\mathrm{Ryd} \simeq 13.60\,\mathrm{eV} \tag{A.3}$$

Unit of time

$$t_0 = \frac{\hbar}{E_R} = 1 \simeq 4.84 \cdot 10^{-17}\,\mathrm{s} \tag{A.4}$$

Unit of elementary charge

$$q_0 = \frac{e}{\sqrt{2}} = 1 \simeq 1.133 \cdot 10^{-19}\,\mathrm{C} \tag{A.5}$$

Unit of electric field

$$E_0 = 1 \simeq 3.636 \cdot 10^{11}\,\frac{\mathrm{V}}{\mathrm{m}} \tag{A.6}$$

Unit of magnetic field

$$B_0 = 1 \simeq 3.324 \cdot 10^{5}\,\mathrm{T} \tag{A.7}$$

B APPENDIX Boundary conditions for potentials as $r \to 0$.

In order to integrate the coupled radial equation, Eq.'s (3.5), it is first necessary to find the appropriate boundary conditions. The general technique here was mentioned in [33] and shown in more detail in [30].

The system of equations that we must solve is given by

$$\left[\frac{\mathrm{d}^2}{\mathrm{d}r^2} + \epsilon_i - \frac{l(l+1)}{r^2}\right] u_{ilm}(r) = \sum_{l'} U^m_{ll'}(r) u_{il'm}(r) \tag{B.1}$$

where the coupling terms have the form

$$U^m_{ll'}(r) = \int Y^*_{lm}(\hat{\boldsymbol{r}}) v(\boldsymbol{r}) Y_{l'm}(\hat{\boldsymbol{r}})\, \mathrm{d}\hat{\boldsymbol{r}}. \tag{B.2}$$

To find a set of linearly independent solutions $u^{(j)}_{lm}(r)$, we must find their behavior at small r. Due to the cylindrical symmetry, the potential is expanded as

$$v(\boldsymbol{r}) = \sum_l v_l(r) P_l(\cos\theta) \tag{B.3}$$

where $P_l(\cos\theta)$ is a Legendre polynomial. Inserting the expansion, Eq. (B.3), into Eq. (B.2), we have

$$U^m_{ll'}(r) = \int [Y^*_{lm}(\hat{\boldsymbol{r}}) v_0(r) P_0(\cos\theta) Y_{l'm}(\hat{\boldsymbol{r}}) + Y^*_{lm}(\hat{\boldsymbol{r}}) v_1(r) P_1(\cos\theta) Y_{l'm}(\hat{\boldsymbol{r}}) \tag{B.4}$$

$$+ Y^*_{lm}(\hat{\boldsymbol{r}}) v_2(r) P_2(\cos\theta) Y_{l'm}(\hat{\boldsymbol{r}}) + ...]\, \mathrm{d}\hat{\boldsymbol{r}}. \tag{B.5}$$

We note that

$$\int Y^*_{lm}(\hat{\boldsymbol{r}}) P_{l''} Y_{l'm}(\hat{\boldsymbol{r}})\, \mathrm{d}\hat{\boldsymbol{r}} = \beta_{l''} \delta_{(l-l'')+2i,l'} \tag{B.6}$$

where $i = 0, 1, 2...$ up to $l' \leq (l + l'')$.

Next, we make use of the fact that

$$\lim_{r\to 0} v_l(r) \sim \begin{cases} r^l & \text{if} \quad l \neq 0 \\ -\frac{Z}{r} & \text{if} \quad l = 0 \end{cases} \tag{B.7}$$

and insert this into Eq. (B.2) to write

$$\lim_{r\to 0} U^m_{ll'}(r) = \alpha_0 \frac{1}{r}\delta_{l,l'} + \alpha_1 r \int Y^*_{lm}(\hat{\boldsymbol{r}}) P_1(\cos\theta) Y_{l'm}(\hat{\boldsymbol{r}}) + \alpha_2 r^2 \int Y^*_{lm}(\hat{\boldsymbol{r}}) P_2(\cos\theta) Y_{l'm}(\hat{\boldsymbol{r}}) + ... \tag{B.8}$$

$$= \gamma_0 \frac{1}{r}\delta_{l,l'} + \gamma_1 r \delta_{l\pm 1,l'} + \gamma_2 r^2 \delta_{l\pm 2,l'} + ... \tag{B.9}$$

where we have kept only the lowest order terms in r for each coupling term l' and where the γ_l are just the constants of proportionality from Eq. (B.7) (α_l) combined with the constants resulting from the integrations in Eq. (B.8) (β_l).

Next, we use the form of the solutions at small r for sphericallly symmetric potentials

$$\lim_{r\to 0} u_{lm}(r) = A r^{l+1} \tag{B.10}$$

and insert this and Eq. (B.9) into the right side of Eq. (B.1) to write

$$\lim_{r\to 0} \sum_{l'} U^m_{ll'}(r) u^{(l')}_{l'm}(r) = \gamma_0 \frac{1}{r} r^{l+1} + \gamma_1 r^{l+3} + \gamma_1 r^{l+1} + \gamma_2 r^{l+5} + \gamma_2 r^{l+1} + \gamma_3 r^{l+7} + \gamma_3 r^{l+1} + \gamma_4 r^{l+9} + \gamma_4 r^{l+1} + ... \tag{B.11}$$

It is now evident that the coupling terms have the form

$$\begin{aligned} r^{l+1} &\quad \text{if } j < l \\ r^{2j+l+1} &\quad \text{if } j \geq l. \end{aligned} \tag{B.12}$$

where $j = 0, 1, 2, ...l_{max}$. We can finally write down the power series form of the linearly independent solutions (for small r) used to begin the outward integrations of the coupled equations as we have shown that they follow the form of the coupling terms, Eq.'s (B.11) and (B.12).

$$u^{(j)}_{lm}(r) \sim_{r\to 0} r^{j+|l-j|+1} \sum_{i=1}^{\infty} b^l_i r^{i-1} \tag{B.13}$$

C APPENDIX Singular Value Decomposition (SVD)

Singular value decomposition (SVD) is a matrix decomosition used for matrices that are singular or very close to singular. For these matrices, other matrix decompositions, such as Gauss-Jordan elimination, will fail. It is used in many areas of mathematics, science, and information science. In the context of this work, it is used as an eigenvalue decomposition for a system with 0-value eigenvalues, such as a system of homogeneous equations, Eq.'s (3.38). If A is a real $m \times n$ matrix, the SVD of A is given by

$$A = U \cdot D \cdot V^T \tag{C.1}$$

where U is an $m \times m$ orthogonal matrix, V is an $n \times n$ orthogonal matrix, and D is a diagonal matrix with elements $s_1 > s_2.s_3 > ... > s_i$ where i is the smaller of m and n. The s_i are called the *singular values* of A and the columns of U are the left-singular vectors of A and the columns of U are the right-singular eigenvectors of A. The left-singular vectors are eigenvectors of AA^T, while the right-singular vectors are eigenvectors of A^TA.

To make things a little clearer, suppose that

$$A \cdot x = b \tag{C.2}$$

where x and b are vectors and we assume that A is singular. The *nullspace* of A is defined as the subspace of x such that $A \cdot x = 0$. The range is defined as the subspace of b that is obtained by mapping from x with A. The dimension of the range is found by subtracting the dimension of the nullspace from m (assuming $m \geq n$). This is also equal to the rank of A. If A is non-singular, its range spans the space of b. If A is singular, its rank is less than m by the dimension of the nullspace as stated above and the singular values $s_i + 1 = s_i + 2 = ... = s_m = 0$.

Let us suppose that A is singular and $b = 0$. Any column of V, which corresponds to a 0 singular value s_j is therefore a solution of $A \cdot x = 0$. The general solution in this

case is then given by

$$x = \alpha_1 v_i + \alpha_2 v_{i+1} + \alpha_3 v_{i+2} + ... + \alpha_{n-i} v_n \tag{C.3}$$

where v_j is a column of V and

$$\alpha_1^2 + \alpha_2^2 + \alpha_3^2 + ... + \alpha_{n-i}^2 = 1. \tag{C.4}$$

If $A \cdot x = b$ with $b \neq 0$, the solutions can be found from

$$x = V \cdot \Sigma \cdot U^T \cdot b \tag{C.5}$$

where Σ is the diagonal matrix whose elements are the inverses of the singular values s_i.

$$\Sigma = \text{diag}\left(\frac{1}{s_i}\right) \tag{C.6}$$

It should be noted that if a value of s_i is zero, $1/s_i$ must be set equal to zero. The reader can refer to [42] or [43] for more details.

Let us consider an example. First of all, it is easy to construct a singular matrix. Just make one or more rows some constant multiple of another row.

$$A = \begin{pmatrix} 1 & 2 & 4 & 7 \\ 3 & 6 & 4 & 9 \\ 3 & 6 & 12 & 21 \\ 6 & 12 & 8 & 18 \end{pmatrix} \tag{C.7}$$

In this case, the third row is 3 times the first and the fourth row is twice the second. The dimension of A is 4 and the rank of A is therefore 2 since the last 2 rows are equivalent to the first 2. The dimension of the nullspace is also 2. Using the Java implementation of the SVD as based on LAPACK (which is what was used in this work), we have

$$U = \begin{pmatrix} 0.222764 & 0.224446 & -0.936089 & -0.154068 \\ 0.317415 & -0.315036 & 0.145257 & -0.882553 \\ 0.668293 & 0.673339 & 0.312030 & 0.051356 \\ 0.634830 & -0.630072 & -0.072628 & 0.441277 \end{pmatrix} \tag{C.8}$$

$$D = \begin{pmatrix} 37.009447 & 0 & 0 & 0 \\ 0 & 6.348293 & 0 & 0 \\ 0 & 0 & 0 & 0 \\ 0 & 0 & 0 & 0 \end{pmatrix}, \text{ and} \tag{C.9}$$

$$V = \begin{pmatrix} 0.188840 & -0.390826 & 0.443871 & 0.783947 \\ 0.377680 & -0.781653 & -0.438653 & -0.232294 \\ 0.412297 & 0.421708 & -0.650151 & 0.479038 \\ 0.807285 & 0.241736 & 0.433434 & -0.319359 \end{pmatrix}. \tag{C.10}$$

We can check that the decomposition is correct by computing

$$U \cdot D \cdot V^T = \begin{pmatrix} 1 & 2 & 4 & 7 \\ 3 & 6 & 4 & 9 \\ 3 & 6 & 12 & 21 \\ 6 & 12 & 8 & 18 \end{pmatrix} = A. \tag{C.11}$$

We can also verify that the last 2 columns of V are the eigenvectors corresponding to the nullspace.

$$A \cdot v_3 = \begin{pmatrix} 1 & 2 & 4 & 7 \\ 3 & 6 & 4 & 9 \\ 3 & 6 & 12 & 21 \\ 6 & 12 & 8 & 18 \end{pmatrix} \cdot \begin{pmatrix} 0.443871 \\ -0.438653 \\ -0.650151 \\ 0.433434 \end{pmatrix} = \begin{pmatrix} -0.000001 \\ -0.000003 \\ -0.000003 \\ -0.000006 \end{pmatrix} \simeq 0 \tag{C.12}$$

$$A \cdot v_4 = \begin{pmatrix} 1 & 2 & 4 & 7 \\ 3 & 6 & 4 & 9 \\ 3 & 6 & 12 & 21 \\ 6 & 12 & 8 & 18 \end{pmatrix} \cdot \begin{pmatrix} 0.783947 \\ -0.232294 \\ -0.479038 \\ -0.319359 \end{pmatrix} = \begin{pmatrix} -0.000002 \\ -0.000002 \\ -0.000006 \\ -0.000004 \end{pmatrix} \simeq 0 \tag{C.13}$$

We can see that the last 2 columns of V are indeed eigenvectors with eigenvalues of 0 (within the precision used), corresponding to the nullspace. It is also worthwhile to note that the columns v_j of V are orthonormal.